

Winter 2001

Measurement of Virtual Compton Scattering Below Pion Threshold at Invariant Four- Momentum Transfer Squared $Q^2=1.(\text{GEV}/\text{C})^2$

Christopher Jutier
Old Dominion University

Follow this and additional works at: https://digitalcommons.odu.edu/physics_etds

Recommended Citation

Jutier, Christopher. "Measurement of Virtual Compton Scattering Below Pion Threshold at Invariant Four-Momentum Transfer Squared $Q^2=1.(\text{GEV}/\text{C})^2$ " (2001). Doctor of Philosophy (PhD), dissertation, Physics, Old Dominion University, DOI: 10.25777/4fe7-c262
https://digitalcommons.odu.edu/physics_etds/108

This Dissertation is brought to you for free and open access by the Physics at ODU Digital Commons. It has been accepted for inclusion in Physics Theses & Dissertations by an authorized administrator of ODU Digital Commons. For more information, please contact digitalcommons@odu.edu.

**MEASUREMENT OF VIRTUAL COMPTON
SCATTERING BELOW PION THRESHOLD
AT INVARIANT FOUR-MOMENTUM
TRANSFER SQUARED $Q^2=1$. (GEV/C)²**

by

Christophe Jutier
Diplôme d'Etudes Approfondies (DEA degree), June 1996.
Université Blaise Pascal, Clermont-Ferrand, France

A Dissertation Submitted to the Faculty of
Old Dominion University in Partial Fulfillment of the
Requirement for the Degree of

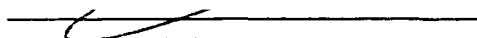
DOCTOR OF PHILOSOPHY

PHYSICS

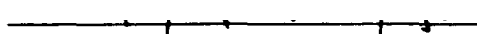
OLD DOMINION UNIVERSITY
December 2001

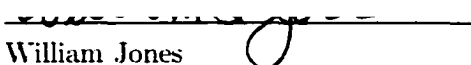
Approved by:


Charles Hyde-Wright (Director)


Bernard Michel


Pierre-Yves Bertin


Anatoly Radyushkin


William Jones


Charles Sukenik

ABSTRACT

MEASUREMENT OF VIRTUAL COMPTON SCATTERING BELOW PION THRESHOLD AT INVARIANT FOUR-MOMENTUM TRANSFER SQUARED $Q^2=1. (\text{GEV}/c)^2$

Christophe Jutier

Old Dominion University, 2001

Director: Dr. Charles Hyde-Wright

Experimental Virtual Compton Scattering (VCS) off the proton is a new tool to access the Generalized Polarizabilities (GPs) of the proton that parameterize the response of the proton to an electromagnetic perturbation. The Q^2 dependence of the GPs leads, by Fourier transform, to a description of the rearrangement of the charge and magnetization distributions. The VCS reaction $\gamma^* + p \rightarrow p + \gamma$ was experimentally accessed through the reaction $e + p \rightarrow e + p + \gamma$ of electroproduction of photons off a cryogenic liquid Hydrogen target. Data were collected in Hall A at Jefferson Lab between March and April 1998 below pion threshold at $Q^2=1.$ and $1.9 (\text{GeV}/c)^2$ and also in the resonance region. Both the scattered electron and the recoil proton were analyzed with the Hall A High Resolution Spectrometer pair while the signature of the emitted real photon is obtained with a missing mass technique. A few experimental and analysis aspects will be treated. Cross-sections were extracted from the data set taken at $Q^2=1. (\text{GeV}/c)^2$ and preliminary results for the structure functions $P_{LL} - P_{TT}/\epsilon$ and P_{LT} , which involve the GPs, were obtained.

© Copyright by
Christophe Jutier
2002
All Rights Reserved

Acknowledgements

I wish to thank first and foremost Dr. Charles Hyde-Wright for being my advisor over the years that it took me to complete this Ph.D. work. Not only did he advise me on many occasions and taught me nuclear physics but he also gave me the opportunity to work on various subjects. His patience and consistency over time matched my temperament and fitted my studying and working habits. These traits prevented me from giving up when discouragement was in sight. I also want to thank him for trying to bond more tightly two sides of an ocean as he took me as a student on a joint degree adventure between the American Old Dominion University and the French Université Blaise Pascal. My thankful thought goes to Dr. Pierre-Yves Bertin who initiated the project and acted as co-advisor from the French side. This gave me the opportunity to come to live for a while in the United-States of America, a dream, an experience, a discovery.

I also want to thank all the members of my thesis committee who agreed to fulfill this function and who put up with me fairly often. I particularly wish to thank Dr. Bernard Michel who traveled from France for my defense in unusual international circumstances.

I then would like to thank all the members, either researcher, post-Doc or student, of the VCS collaboration from Clermont-Ferrand and Saclay, France and last but not least Gent, Belgium. It was nice going back there from time to time to work and exchange ideas. It also helped me cope with my situation of graduate student in America.

People working in or for Hall A and more globally at Jefferson Lab at every level deserve my thanks too since the Virtual Compton Scattering experiment,

from which my thesis work was made possible, could not have successfully run without their help. Their accessibility for question was valuable for my work. People at Old Dominion University also provided a nice environment.

On the personal side, I wish to say that a beginning is a very delicate time. Know then that my American life started speedily. As of the day of this writing, only a few scattered people still know and/or remember this time. I wish to thank the French community at the lab and the Americans that shared this time that I would qualify of blessed.

Then, soon enough, things deteriorated and dark ages came. From this swamp period, I wish to thank those who shared a piece of my life. I address special thanks to Sheila for her friendly support and to Pascal for being a good friend and for showing perseverance and character.

To those concerned, thank you very much for the fantastic triumvirate resonance peak period.

Finally I wish to express my deepest thanks to Ludy without whom I would not have lived what I lived and done what I did. Her help and support is a blessing.

Despite this happy tone, I want to finish by quoting Kant: "What does not kill you makes you stronger." I feel stronger today than yesterday. But sometimes, just sometimes, I heard my heart bleeding.

Table of Contents

List of Tables	x
List of Figures	xiii
1 Introduction	1
2 Nucleon structure	3
2.1 Elastic Scattering and Form Factors	3
2.2 Real Compton Scattering	10
3 A new insight : Virtual Compton Scattering	20
3.1 Electroproduction of a real photon	20
3.2 BH and VCS amplitudes	22
3.3 Multipoles and Generalized Polarizabilities	25
3.4 Low energy expansion	27
3.5 Calculation of Generalized Polarizabilities	30
3.5.1 Connecting to a model	30
3.5.2 Gauge invariance and final model	31
3.5.3 Polarizabilities expressions	32
3.6 Dispersion relation formalism	34
4 VCS experiment at JLab	42
4.1 Overview	42
4.2 Experimental requirements	43
4.3 Experimental set-up	43
4.4 Experimental method	44
5 the CEBAF machine at Jefferson Lab	48
5.1 Overview	48
5.2 Injector	50
5.3 Beam Transport	51

6	Hall A	52
6.1	Beam Related Instrumentation	52
6.2	Cryogenic Target and other Solid Targets	58
6.2.1	Scattering chamber	58
6.2.2	Solid targets	58
6.2.3	Cryogenic Target	59
6.3	High Resolution Spectrometer Pair	66
6.4	Detectors	70
6.4.1	Scintillators	72
6.4.2	Vertical Drift Chambers	75
6.4.3	Calorimeter	77
6.5	Trigger	79
6.5.1	Overview	79
6.5.2	Raw trigger types	79
6.5.3	Trigger supervisor	83
6.6	Data Acquisition	83
7	Calibrations	87
7.1	Charge Evaluation	88
7.1.1	Calibration of the VtoF converter	88
7.1.2	Current calibration	96
7.1.3	Charge determination	100
7.2	Scintillator Calibration	102
7.2.1	ADC calibration	102
7.2.2	TDC calibration	103
7.3	Vertical Drift Chambers Calibration	103
7.4	Spectrometer Optics Calibration	106
7.5	Calorimeter Calibration	108
7.6	Coincidence Time-of-Flight Calibration	112
8	Normalizations	117
8.1	Deadtimes	118
8.1.1	Electronics Deadtime	118
8.1.2	Prescaling	120
8.1.3	Computer Deadtime	122
8.2	Scintillator Inefficiency	125
8.2.1	Situation	125
8.2.2	Average efficiency correction	127
8.2.3	A closer look	129
8.2.4	Paddle inefficiency and fitting model	136

8.3	VDC and tracking combined efficiency	143
8.4	Density Effect Studies	145
8.4.1	Motivations	145
8.4.2	Data extraction	146
8.4.3	Data screening, boiling and experimental beam position dependence	148
8.4.4	Boiling plots and conclusions	154
8.5	Luminosity	158
9	VCS Events Selection	161
9.1	Global aspects and pollution removal	162
9.1.1	Coincidence time cut	162
9.1.2	Collimator cut	165
9.1.3	Vertex cut	166
9.1.4	Missing mass selection	168
9.2	Chasing the punch through protons	170
9.2.1	Situation after the spectrometer in the Electron arm	170
9.2.2	Zone 1: elastic	172
9.2.3	Zone 2: Bethe-Heitler	183
9.2.4	Zone 3: pion	189
10	Cross-section extraction	194
10.1	Average <i>vs.</i> differential cross-section	194
10.2	Simulation method	196
10.3	Resolution in the simulation	199
10.4	Kinematical bins	199
10.5	Experimental cross-section extraction	202
11	Cross-section and Polarizabilities Results	205
11.1	Example of polarizability effects	205
11.2	First pass analysis	207
11.3	Polarizabilities extraction	208
11.4	Iterated analysis	209
11.5	Discussion	210
12	Conclusion	218
	Appendix A Units	222
	Appendix B Spherical harmonics vector basis	225

TABLE OF CONTENTS

ix

Bibliography

226

Vita

229

List of Tables

I	Electron and hadron spectrometers central values for VCS data acquisition below pion threshold at $Q^2 = 1.0 \text{ GeV}^2$	45
II	Hall A High Resolution Spectrometers general characteristics .	68
III	Electron spectrometer collimator specifications	69
IV	Proportions of tracking results	144

List of Figures

1	Elastic electron-nucleon scattering	4
2	World data prior to CEBAF for the electric and magnetic proton form factors	7
3	Polarization transfer data for the ratio $\mu_p G_{Ep}/G_{Mp}$	9
4	Real Compton Scattering off the nucleon	10
5	Cauchy's loop used for the integration of the Compton amplitude.	17
6	FVCS and BH diagrams	21
7	Dispersion relation predictions at $Q^2 = 1 \text{ GeV}^2$	39
8	Results for the unpolarized structure functions $P_{LL} - P_{TT}/\epsilon$ and P_{LT} for $\epsilon = 0.62$ in the Dispersion Relation formalism	41
9	Schematic representation of the experimental set up	44
10	Hadron arm settings	46
11	Overview of the CEBAF accelerator	49
12	Beamline elements (part 1)	53
13	Beamline elements (part 2)	54
14	BCM monitor	56
15	User monitor	57
16	Schematic of available targets	60
17	Diagram of a target loop	62
18	Hall A high resolution spectrometer pair	67
19	Electron arm detector package	71
20	Hadron arm detector package	72
21	Scintillator detector package	74
22	VDC detector package	75
23	Particle track in a VDC plane	76
24	Preshower-shower detector package	78
25	Simplified diagram of the trigger circuitry	81
26	Hall A data acquisition system	86
27	Readout electronics for the upstream cavity diagram	88
28	VtoF converter calibration: EPICS signal <i>vs.</i> VtoF counting rate	92
29	Residual plot from the VtoF converter calibration	93

30	Relative residual plot from the VtoF converter calibration	94
31	Upstream BCM cavity current calibration coefficient	99
32	Drift time spectrum in a VDC plane	105
33	Drift velocity spectrum in a VDC plane	106
34	Examples of ADC pedestal spectra	109
35	2-D plot of energies deposited in the Preshower <i>vs.</i> Shower counters	111
36	Spectrum of energy in the calorimeter over momentum	112
37	Wide <i>tc_cor</i> spectrum for run 1589	115
38	Zoom on the true coincidence peak	116
39	Electronics deadtimes	119
40	Electronics deadtimes as functions of beam current	121
41	Computer Deadtimes	124
42	Time evolution of the average trigger efficiency corrections	130
43	Electron <i>S1</i> scintillator inefficiencies	131
44	Electron <i>S2</i> scintillator inefficiencies	132
45	Check of paddle overlap regions in the Electron <i>S2</i> plane	134
46	Inefficiencies in an overlap region in the Electron <i>S1</i> plane	135
47	Inefficiency of the right side of paddle 4 of the Electron <i>S1</i> scintillator as a function of both <i>x</i> and <i>y</i> trajectory coordinates	137
48	Iso-inefficiency curve for the right side of paddle 4 of the Electron scintillator <i>S1</i>	139
49	Weighed <i>y</i> distribution for the right side of paddle 4 of the Electron scintillator <i>S1</i>	140
50	Inefficiency model for the right side of paddle 4 of the Electron scintillator <i>S1</i>	141
51	Raw counting rates for run number 1636	149
52	Boiling screening result for run number 1636	150
53	Fit of beam position dependence for run number 1636	151
54	Comparison of the yield before and after average beam position correction for run number 1636	152
55	Determination of beam position dependence for run number 1687	153
56	Raw boiling plot	155
57	Corrected boiling plot	157
58	<i>tc_cor</i> spectrum for run 1660	162
59	Visualization of the punch through protons problem	164
60	Electron and Hadron collimator variables plots	165
61	<i>d</i> spectra after coincidence time and Hadron collimator cuts	167
62	M_X^2 spectra: succession of VCS events selection cuts	168
63	M_X^2 spectrum after all cuts are applied	169
64	Electron coordinates in the first scintillator plane	171

65	Four raw spectra in zone 1 of the Electron arm	173
66	Four spectra in zone 1 after preselection cut	174
67	The pollution is definitely from coincidence events	176
68	The VCS events almost stand apart from the elastic pollution	177
69	Collimator variables in zone 1	178
70	2-D plot of the discriminative variables d and h_{ycol}	179
71	Final selection cuts in zone 1	180
72	Interpretation of the pollution	181
73	Four raw spectra in zone 2 of the Electron arm	184
74	Four spectra in zone 2 after preselection cut	184
75	The pollution is definitely from coincidence events	185
76	The Bethe-Heitler pollution is really close to the VCS events	185
77	Collimator variables in zone 2	186
78	2-D plot of the discriminative variables d and h_{ycol}	187
79	Final selection cuts in zone 2	188
80	Four raw spectra in zone 3 of the Electron arm	190
81	Four spectra in zone 3 after preselection cut	190
82	The pollution is definitely from coincidence events	191
83	The pollution is very close to the VCS events	191
84	Collimator variables in zone 3	192
85	2-D plot of the discriminative variables d and h_{ycol}	192
86	Final selection cuts in zone 3	193
87	Comparison between simulation and experimental data	200
88	VCS in the laboratory frame	201
89	Example of polarizability effects	206
90	$ep \rightarrow ep\gamma$ cross-section results after first pass analysis	211
91	Relative difference between $ep \rightarrow ep\gamma$ experimental cross-section and calculated BH+Born cross-sections after first pass analysis	212
92	Polarizabilities extraction after first pass analysis	213
93	$ep \rightarrow ep\gamma$ cross-section results after third pass analysis	214
94	Relative difference between $ep \rightarrow ep\gamma$ experimental cross-section and calculated BH+Born cross-sections after third pass analysis	215
95	Polarizabilities extraction after third pass analysis	216
96	Comparison between $ep \rightarrow ep\gamma$ cross-section results after third pass analysis and various models	217
97	Q^2 evolution of the P_{LL}/G_E and P_{LT}/G_E structure functions	221

Chapter 1

Introduction

The subject of this thesis is the study of the $ep \rightarrow ep\gamma$ reaction, which is commonly referred to as Virtual Compton Scattering (VCS). The data in this study were taken with a 4 GeV electron beam incident on a cryogenic liquid Hydrogen target. The reaction $ep \rightarrow ep\gamma$ was specified by measuring the scattered electron and recoil proton in two high resolution spectrometers in Jefferson Lab Hall A. The scattering kinematics constrained the invariant mass $W = \sqrt{s}$ of the final photon + proton system to lie below pion production threshold. Also the central invariant momentum transfer squared from the electron was 1 GeV^2 .

One of the fundamental question of subatomic physics is the description of the internal structure of the nucleon. Despite many efforts, the non perturbative structure of Quantum Chromo-Dynamics (QCD) has not yet been understood. New experimental data are then needed to guide theoretical approaches, to exclude some scenarios or to constrain the models. The electromagnetic probe is a privileged tool for an exploration. Indeed, electrons are point-like, they are not sensitive to the strong interaction (QCD), and their interaction (QED) is well known. This clean probe provides a pure image of the probed hadron.

Traditionally, the electromagnetic structure of the nucleon has been investigated with elastic electron scattering, deep inelastic scattering and Real Compton Scattering (RCS). Elastic electron scattering off the nucleon gives access to form

This dissertation follows the form of *the Physical Review*.

factors which describe its charge and magnetization distributions, while RCS allows the measurement of its electric and magnetic polarizabilities which describe the nucleon's abilities to deform when it is exposed to an electromagnetic field.

Recently, interest has emerged to study nucleon structure using Virtual Compton Scattering [1]. In VCS, a virtual photon is exchanged between an electron and a nucleon target, and the nucleon target emits a real photon. In contrast to RCS, the energy and momentum of the virtual photon can be varied independently of each other. In this respect, VCS can provide new insights on the nucleon internal structure.

Below pion threshold, VCS off the proton gives access to new nucleon structure observables, the generalized polarizabilities (GPs) [2], named so because they amount to a generalization of the polarizabilities obtained in RCS. These GPs, functions of the square of the four-momentum Q^2 transferred by the electron, characterize the response of the proton to the electromagnetic excitation of the incoming virtual photon. In this way, one studies the deformation of the charge and magnetization distributions measured in electron elastic scattering, under the influence of an electromagnetic field perturbation. As the energy of the probe increases, VCS is not only a precise tool to access global information on the proton ground state, but also its excitation spectrum, providing therefore a new test of our understanding of the nucleon structure.

Experimentally, the VCS process can be accessed through the electroproduction of a real photon off the proton, which is difficult to measure. Cross-sections are suppressed by a factor $\alpha_{QED} \simeq 1/137$ with respect to the purely elastic case, and the emission of a neutral pion which decays into two photons creates a physical background which may prevent the extraction of the VCS signal. That's why, despite the great wealth of information potentially available from VCS, there has been only one VCS measurement, in 1995-1997 at the Mainz Microtron accelerator (MAMI) in Germany [3]. This first experiment studied VCS below pion threshold at $Q^2 = 0.33 \text{ GeV}^2$, and results have been published in [4].

The combination of CEBAF high duty-cycle accelerator and Hall A high precision spectrometers made it possible to also study VCS at Jefferson Lab.

Chapter 2

Nucleon structure with elastic electromagnetic probes

The exclusive reaction $ep \rightarrow ep\gamma$ has a close relation to elastic electron scattering and also appears as a generalization of Real Compton Scattering on the proton ($\gamma p \rightarrow \gamma p$) at low energy of the outgoing real photon. I propose here to make a description of these mechanisms.

2.1 Elastic Scattering and Form Factors

Elastic electron scattering at high energy (incident electron energy at the GeV level) from a nuclear target is illustrated in Fig. 1 in the case of a nucleon target but the nucleon could be replaced with any nucleus without affecting the global idea. In this process, a virtual photon of wavelength $\lambda = \frac{h}{q}$, q being here the magnitude of the momentum vector, is coherently absorbed by the entire nucleus. This wavelength is determined by the kinematics of the scattering event (incident energy, scattering angle).

Let us now define a quantity that is will be extensively used throughout this thesis. This quantity is noted Q^2 . It is the opposite of the four-momentum squared of the virtual photon and therefore the square of the momentum transfer between the electron and the proton subtracted by the square of the energy transfer.

If the virtual photon's wavelength is large compared to the nuclear size (Q^2 small), then the elastic scattering process is only sensitive to the total charge and magnetic moment of the target (global properties). However, as the wavelength shortens (larger Q^2), the cross-section becomes sensitive to the internal structure of the target nucleus.

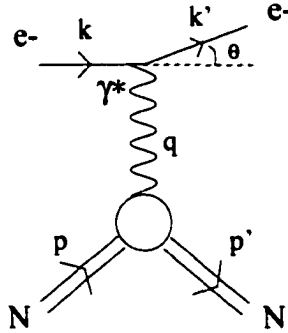


FIG. 1: Elastic electron scattering off the nucleon diagram in the one photon exchange approximation. θ is the scattering angle of the electron. k is the incident electron four-momentum. $k = (E, \vec{k})$ where E is the incident energy. Corresponding primed quantities are for the scattered electron. Similar quantities are defined for the proton using the letter p . q is the four-momentum transfer between the incident electron and the nucleon target. We have $q = k - k' = p' - p$ and the mass of the virtual photon is $q^2 = -Q^2 < 0$.

The comparison between the elastic cross-section on a scalar particle and the elastic cross-section on a **pointlike** scalar particle gives access to the charge distribution of this particle as explained below:

$$\frac{d\sigma}{d\Omega} = \left(\frac{d\sigma}{d\Omega} \right)_{Mott} \frac{E'}{E} |F(q^2)|^2. \quad (1)$$

In Eq. 1, $\left(\frac{d\sigma}{d\Omega} \right)_{Mott}$ is the known differential elastic cross-section for electron scattering off a static pointlike spin 0 target. Its expression as a function of incident electron energy E (with momentum k) and scattering angle θ is the following:

$$\left(\frac{d\sigma}{d\Omega} \right)_{Mott} = \frac{Z^2 \alpha_{QED}^2 E^2}{4k^4 \sin^4 \frac{\theta}{2}} \left(1 - \beta^2 \sin^2 \frac{\theta}{2} \right) \quad (2)$$

where $\beta = \frac{k}{E}$, Z is the charge of the target in units of the elementary charge and α_{QED} is the fine structure constant or the measure of the strength of the electromagnetic interaction.

In the non relativistic limit, Eq. 2 recovers the Rutherford cross-section:

$$\left(\frac{d\sigma}{d\Omega}\right)_{Rutherford} = \frac{Z^2 \alpha_{QED}^2}{16T^2 \sin^4 \frac{\theta}{2}} \quad (3)$$

where T is the kinetic energy of the incoming electron.

In the ultra relativistic limit when the mass of the electron is negligible with respect to its momentum, which is the case in this thesis, Eq. 2 takes the following form:

$$\left(\frac{d\sigma}{d\Omega}\right)_{Mott} = \frac{Z^2 \alpha_{QED}^2 \cos^2 \frac{\theta}{2}}{4E^2 \sin^4 \frac{\theta}{2}} \quad (4)$$

where Z is the charge of the target in units of the elementary charge and α_{QED} is the fine structure constant or the measure of the strength of the electromagnetic interaction. Appendix A gives more information on α_{QED} and the system of units in use in this thesis.

The second factor in Eq. 1 is the target recoil correction term that arises when the target is not infinitely heavy:

$$\frac{E'}{E} = \frac{1}{1 + 2 \frac{E}{m_{tg}} \sin^2 \frac{\theta}{2}} \quad (5)$$

For an infinitely massive target this term evaluates to 1 as one can see when taking the limit of the expression when the mass of the target m_{tg} goes to infinity.

Information on the target structure is contained in the term $|F(q^2)|$, called form factor, which is the Fourier transform of the charge distribution of the target [5].

Elastic electron scattering off the proton

The electron-proton scattering case is described in the review of De Forest and Walecka (Ref. [6]). In this case the cross-section can be written:

$$\left(\frac{d\sigma}{d\Omega}\right)_{Mott} \frac{E'}{E} \left[\left(F_1^2(q^2) - \frac{q^2}{4m_p^2} F_2^2(q^2) \right) - \frac{q^2}{2m_p^2} (F_1(q^2) + F_2(q^2))^2 \tan^2 \left(\frac{\theta}{2} \right) \right] \quad (6)$$

where F_1 and F_2 are two independent form factors (called Pauli and Dirac form factors respectively) that parameterize the detailed structure of the proton represented by the blob in Fig. 1. (See also later Eq. 59.) The fact that we have two form factors for the proton comes from its spin 1/2 nature. Letting q^2 go to zero, the conditions $F_1(0) = 1$ and $F_2(0) = \kappa_p = 1.79$ are obtained: $F_1(0)$ is the proton charge in units of the elementary charge and $F_2(0)$ is the experimental anomalous magnetic moment of the proton in units of nuclear magneton [7].

In order to eliminate interference terms such as the product $F_1 \times F_2$, one can introduce the following linear combinations of F_1 and F_2 :

$$G_E(q^2) = F_1(q^2) + \frac{q^2}{4m_p} F_2(q^2) \quad (7)$$

$$G_M(q^2) = F_1(q^2) + F_2(q^2) \quad (8)$$

Eq. 6 can then be rewritten as:

$$\frac{d\sigma}{d\Omega} = \left(\frac{d\sigma}{d\Omega} \right)_{Mott} \frac{E'}{E} \left[\frac{G_E^2(q^2) + \tau G_M^2(q^2)}{1 + \tau} + 2\tau G_M^2(q^2) \tan^2\left(\frac{\theta}{2}\right) \right] \quad (9)$$

with $\tau = -q^2/4m_p = Q^2/4m_p$. One can even further decouple G_E and G_M by rearranging the terms:

$$\frac{d\sigma}{d\Omega} = \left(\frac{d\sigma}{d\Omega} \right)_{Mott} \frac{E'}{E} \left[G_E^2(q^2) + \frac{\tau}{\epsilon} G_M^2(q^2) \right] \left(\frac{1}{1 + \tau} \right) \quad (10)$$

where

$$\epsilon = 1/(1 + 2(1 + \tau) \tan^2(\frac{\theta}{2})) \quad (11)$$

is the virtual photon longitudinal polarization.

In the Breit frame defined by $\vec{p}' = -\vec{p}$, it is possible to show [5] that G_E is the Fourier transform of the charge distribution of the proton and G_M the Fourier transform of the magnetic moment distribution. That's why G_E and G_M are called the electric and magnetic form factors respectively.

One procedure to determine these form factors experimentally is to measure the angular distribution of the scattered electrons from the elastic $ep \rightarrow ep$ reaction. The separation of G_E and G_M is achieved by measuring the cross-section at

a given Q^2 value but for different kinematics (beam energy and scattering angle). Indeed, one obtains in that manner different linear combinations of G_E and G_M that allow their extraction. This technique is called the Rosenbluth method [8].

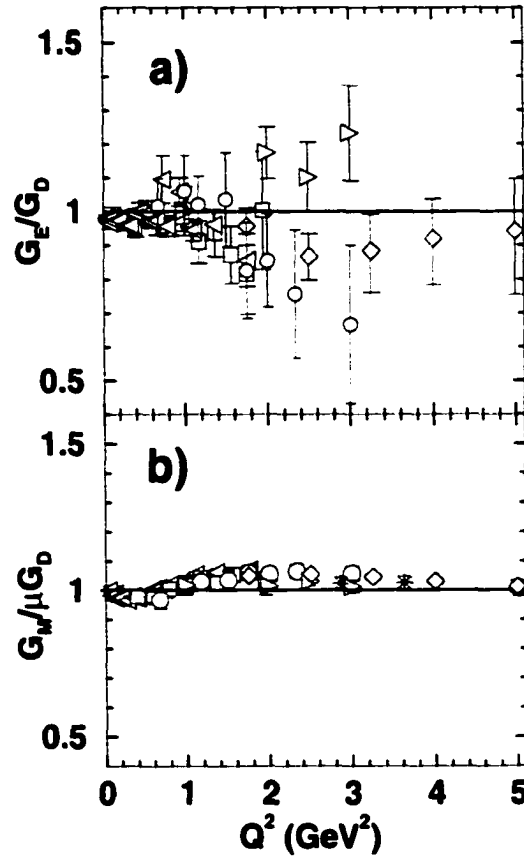


FIG. 2: World data prior to CEBAF for (a) G_{Ep}/G_D and (b) $G_{Mp}/\mu_p G_D$ as functions of Q^2 (see [10] for references). The precise extraction of G_{Mp} indicates it nicely follows the dipole model. The same conclusion is less clear for G_{Ep} .

Since the mid-fifties, many experiments were done in that direction [9]. Fig. 2 presents a compilation of the world data prior to CEBAF [10] for the proton electric and magnetic form factors. The two form factors are normalized to the dipole form factor $G_D = \left(1 + \frac{Q^2}{0.71 (\text{GeV}^2)}\right)^{-2}$. As shown in this figure, the experimental values of G_E are reproduced within 20% by the dipole model while

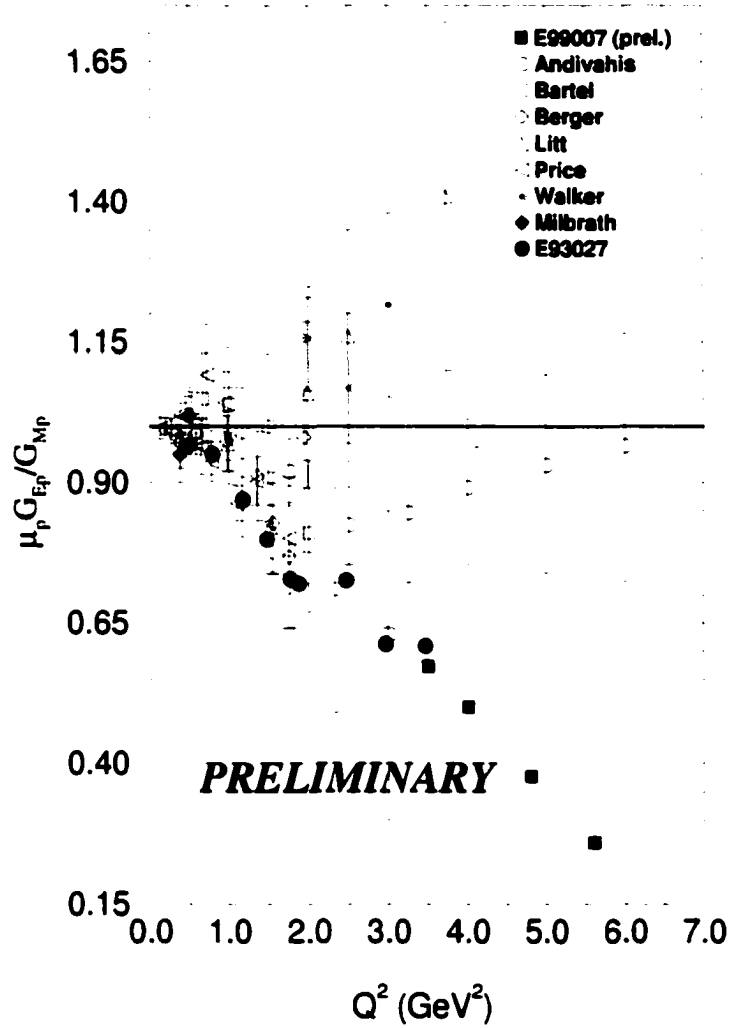
G_M follows more closely this model. If the dipole model is valid, it reveals that the charge and magnetization distributions has an approximate exponential form in space variables: $\rho(r) = e^{-\frac{r}{r_0}}$ where $r_0 = 0.234$ fm [12].

More recently, an alternative method to extract the electric term has been implemented. Indeed with increasing Q^2 , the magnetic term is enhanced by the factor τ and becomes the dominant term, making the extraction of the electric term difficult. The new method aims at measuring the interference term $G_{Ep}G_{Mp}$ via recoil polarization. In the one-photon exchange approximation, the scattering of longitudinally polarized electrons results in a transfer of polarization to the recoil proton with only two non-zero components, P_t perpendicular to, and P_l parallel to the proton momentum in the scattering plane. The former is proportional to the product $G_{Ep}G_{Mp}$ of the form factors while the latter is proportional to G_{Mp}^2 so that the ratio of the two components can be used to extract the ratio of the electric to magnetic form factors:

$$\frac{G_{Ep}}{G_{Mp}} = -\frac{P_t}{P_l} \frac{E + E'}{2m_p} \tan\left(\frac{\theta}{2}\right). \quad (12)$$

This method was experimentally implemented at CEBAF in 1998 where data were taken for Q^2 values between 0.5 GeV² and 3.5 GeV². Fig. 3 presents the data points obtained after analysis for the ratio $\mu_p G_{Ep}/G_{Mp}$ as solid blue points. In this figure is also presented additional data points obtained in 2000 during an extension up to $Q^2 = 5.6$ GeV² of the experiment. The newest points are displayed as solid red points.

The precision of the data points from the previous two sets of data is such that it can be concluded that the electric form factor exhibits a significant deviation from the dipole model implying a charge distribution in the proton that extends farther in space than previously thought.



Fri Sep 21 15:01:41 2001 Oliver Gayou

FIG. 3: Ratio $\mu_p G_{Ep}/G_{Mp}$ as a function of Q^2 : Polarization transfer data are indicated by solid symbols. Specific CEBAF data are shown with solid blue circles and red squares [10][11]. Previous Rosenbluth separation data are displayed with open symbols (see [10] for references). The precision of the CEBAF data points allows the conclusion that G_{Ep} falls faster with Q^2 than the dipole model. This implies that the charge distribution in the proton extends farther in space than previously thought.

2.2 Real Compton Scattering and electric and magnetic polarizabilities

Real Compton Scattering (RCS) refers to the reaction $\gamma p \rightarrow \gamma p$ illustrated in Fig. 4. At low energy, it is a precision tool to access global information on the nucleon ground state and its excitation spectrum.

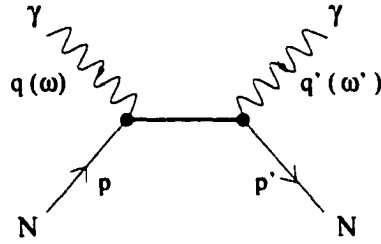


FIG. 4: Real Compton Scattering off the nucleon. The kinematics are described by the initial and final photon four-momenta $q = (\omega, \vec{q})$ and $q' = (\omega', \vec{q}')$ and the initial and final proton four-momenta p and p' . ϵ and ϵ' are the photon polarization vectors. We have $q^2 = q'^2 = q \cdot \epsilon = q' \cdot \epsilon' = 0$. The description of the proton initial and final state carries also a spin projection label.

Kinematics and notations

For the description of the RCS amplitude, one requires two kinematical variables. One can choose the energy of the initial photon ω , and the scattering angle between the initial photon and the scattered photon, $\cos \theta = \hat{q} \cdot \hat{q}'$, or the pair of variables ω and ω' , the latter being the energy of the final photon which is linked to ω by the scattering angle through the relation

$$\frac{\omega'}{\omega} = \frac{1}{1 + \frac{\omega}{m_p}(1 - \cos \theta)}, \quad (13)$$

or still the two invariant variables ν and t defined as:

$$\nu = \frac{s - u}{4m_p} \quad (14)$$

$$t = (q - q')^2 \quad (15)$$

with

$$s = (q + p)^2 \quad (16)$$

$$u = (q - p')^2 \quad (17)$$

where the Mandelstam variables s , u and t are defined using four-momenta. In the case of RCS, these last three variables are related by the property that

$$s + u + t = 2m_p^2 . \quad (18)$$

We also have in the case of RCS for the variables ν and t the following expressions in the Lab frame:

$$\nu = \frac{1}{2} [\omega + \omega']_{lab} \quad \text{and} \quad t = -2 [\omega \omega' (1 - \cos \theta)]_{lab} . \quad (19)$$

These variables ν and t will be used again for VCS in section 3.6. Note that the variable ν should not be confused with the common deep inelastic variable defined by $\nu = q \cdot p / m_p$ which would be the energy of the incoming photon in the RCS case and the energy transfer between the electron and the proton in the VCS case.

RCS amplitude structure

In Fig. 4, there are $2^4 = 16$ combinations of the initial and final proton spin projections. Assuming parity (P) and time reversal (T) invariance, the amplitude $T = \epsilon'^{\mu*} T_{\mu\nu} \epsilon^\nu$ for Compton scattering on the nucleon can be expressed in terms of just six invariant amplitudes A_i [13] as:

$$T_{\mu\nu} = \sum_{i=1}^6 \alpha_{i\mu\nu} A_i(\nu, t) \quad (20)$$

where $\alpha_{i\mu\nu}$ are six known kinematic tensors, and $A_i(\nu, t)$ are six unknown complex scalar functions of ν and t . These amplitudes can be constructed to have no kinematical singularities or kinematical constraints, *e.g.* $q^\mu \alpha_{i\mu\nu} = 0$.

Gauge invariance (charge conservation) implies that:

$$q'^\mu T_{\mu\nu} = T_{\mu\nu} q^\nu = 0 . \quad (21)$$

Note that the Lorentz index ν will be used extensively in relation to the initial photon vertex while the index μ will refer to the outgoing photon vertex.

Because of the photon crossing invariance ($T_{\mu\nu}(q', q) = T_{\nu\mu}(-q, -q')$), the invariant amplitudes A_i satisfy the relations:

$$A_i(\nu, t) = A_i(-\nu, t) . \quad (22)$$

The total amplitude is separated into four parts. The spin dependent terms are set aside from the spin independent terms. A distinction is also made between the Born terms and the Non-Born terms. The Born terms are associated with a propagating nucleon in the intermediate state in the on-shell regime. It is specified by the global properties of the nucleon: mass, electric charge and anomalous magnetic moment. The Non-Born part contains the structure-dependent information. We therefore write the total amplitude:

$$T = T^{B, \text{nospin}} + T^{NB, \text{nospin}} + T^{B, \text{spin}} + T^{NB, \text{spin}} . \quad (23)$$

In order to parameterize our lack of knowledge of the nucleon internal structure, the amplitude is expanded in a power series in ω to obtain a **low-energy expansion**. Sometimes a power series in the cross-even parameter $\omega\omega'$ is preferred to define the parameterization but ω' can always be expanded in powers of ω using Eq. 13.

Low energy theorem

Low energy theorems are model independent predictions based upon a few general principles. They are an important starting point in understanding hadron structure. In their separate articles, M. Gell-Mann and M. L. Goldberger[14] on the one hand and F. E. Low[15] on the other hand present their work on this subject. Based on the requirement of gauge invariance, Lorentz invariance, and crossing invariance, the low energy theorem for RCS uniquely specifies the terms in the low energy scattering amplitude up to and including terms linear in the frequency of the photon.

In the limit $\omega \rightarrow 0$, corresponding to wavelengths much larger than the nucleon size, the effective interaction of the electromagnetic field with the proton is described by the charge e and the external coulomb potential Φ :

$$H_{eff}^{(0)} = e\Phi \quad (24)$$

From Eq. 24, as well as directly from the scattering amplitude, one can determine the leading term of the spin independent part of the scattering amplitude, which comes from the Born part and reproduces the classical Thomson amplitude off the nucleon:

$$T^{B, no spin} = T^{Thomson} + \mathcal{O}(\omega^2) = -2(Ze)^2 \vec{\epsilon}^{i*} \cdot \vec{\epsilon} + \mathcal{O}(\omega^2) \quad (25)$$

where e is the elementary charge and $Z = 1$ for the proton and 0 for the neutron respectively. Note that $\mathcal{O}(\omega^2)$ could have been replaced by $\mathcal{O}(\omega)$ since there is no term linear in ω beyond the Thomson term. This amplitude leads to the following Thomson cross-section:

$$\left(\frac{d\sigma}{d\Omega}\right)_{Thomson} = \left(\frac{\alpha_{QED}}{m_p}\right)^2 \left(\frac{1 + \cos^2\theta}{2}\right). \quad (26)$$

This cross-section can also be retrieved by classical means (J.D. Jackson[16]). An integration over θ yields a total cross-section value of $\sigma = 0.665$ barn for Thomson scattering off electrons and only $\sigma = 0.297 \mu\text{barn}$ when scattering off protons due to the much heavier mass of the proton.

The order $\mathcal{O}(\omega)$ interaction is given by the proton magnetic moment:

$$H_{eff}^{(1)} = -\vec{\mu} \cdot \vec{H}. \quad (27)$$

The corresponding amplitude, leading term of the spin dependent part of the amplitude comes also from the Born contribution:

$$\begin{aligned} \frac{1}{8\pi m_p} T_{fi}^{B, spin} &= -ir_0 \frac{\nu}{2m_p} \left(Z^2 \vec{\sigma} \cdot \vec{\epsilon}^{i*} \times \vec{\epsilon} + (\kappa + Z)^2 \vec{\sigma} \cdot \vec{s}^{i*} \times \vec{s} \right) \\ &+ ir_0 Z \frac{\kappa + Z}{2m_p} (\omega' \vec{\sigma} \cdot \hat{q}' \vec{s}^{i*} \cdot \vec{\epsilon} - \omega \vec{\sigma} \cdot \hat{q} \vec{\epsilon}^{i*} \cdot \vec{s}) \\ &+ \mathcal{O}(\omega^2) \end{aligned} \quad (28)$$

where $r_0 = \alpha_{QED}/m_p$, κ is the anomalous magnetic moment component, and where the two magnetic vectors \vec{s} and \vec{s}' are defined as $\vec{s} = \hat{q} \times \vec{\epsilon}$ and $\vec{s}' = \hat{q}' \times \vec{\epsilon}'$.

Eq. 25 and Eq. 28 taken at the $\mathcal{O}(\omega)$ order ($\omega' = \omega$) define the first two terms in the power series expansion in ω of the amplitude for Compton scattering off the nucleon. The coefficients of this expansion are expressed in terms of the global properties of the nucleon: mass, charge and magnetic moments. When the sum of the two amplitude terms is squared, only the first two terms in the obtained cross-section development are kept to respect the order of the amplitude development: the first term is the Thomson cross-section and the second term is the interference between the Thomson amplitude and the linear term in ω of the total amplitude. This constitutes the low energy theorem for RCS.

Higher order terms

As ω increases, one starts to see the internal structure of the nucleon. The electromagnetic field of the probing photon, creates distortions in the nucleon's charge and current distributions that translate into oscillating multipoles. The response of the nucleon to such a perturbation is summarized by a set of electromagnetic polarizabilities described in details in the article of D. Babusci *et al.*[17].

In this discussion about higher order terms, the Born contribution will be left aside. The higher order terms from $T^{B, \text{nospin}}$ and $T^{B, \text{spin}}$ will not be explicitly stated to bring the focus on the contribution from the Non-Born terms which include the nucleon structure.

The leading order of T^{NB} appears at the order $\mathcal{O}(\omega^2)$ and arises from the spin independent part of the Non-Born amplitude. This order is parameterized in terms of two new structure constants, the electric and magnetic polarizabilities of the nucleon:

$$\frac{1}{8\pi m_p} T^{(2), NB, \text{nospin}} = (\alpha_E \vec{\epsilon}^{*\prime} \cdot \vec{\epsilon} + \beta_M \vec{s}' \cdot \vec{s}) \omega \omega' + \mathcal{O}(\omega^3) . \quad (29)$$

This is in accordance with the effective dipole interaction of the nucleon with

external electric and magnetic fields (\vec{E} and \vec{H}) which can be written as:

$$H_{eff}^{(2), nospin} = -\frac{1}{2}4\pi [\alpha_E \vec{E}^2 + \beta_M \vec{H}^2] \quad (30)$$

where α_E and β_M are identified as the dipole electric and magnetic polarizabilities such that the external fields \vec{E} and \vec{H} induce a polarization $\vec{P} = 4\pi \alpha_E \vec{E}$ and magnetization $\Delta\vec{\mu} = 4\pi \beta_M \vec{H}$.

Now investigating the spin-dependent part of the Non-Born part of the amplitude, it starts at order $\mathcal{O}(\omega^3)$ and can be connected to the effective spin-dependent interaction of order $\mathcal{O}(\omega^3)$ which is:

$$H_{eff}^{(3), spin} = -\frac{1}{2}4\pi \left(\gamma_{E1} \vec{\sigma} \cdot \vec{E} \times \dot{\vec{E}} + \gamma_{M1} \vec{\sigma} \cdot \vec{H} \times \dot{\vec{H}} \right. \\ \left. - 2\gamma_{E2} E_{ij} \sigma_i H_j + 2\gamma_{M2} H_{ij} \sigma_i E_j \right) \quad (31)$$

where

$$E_{ij} = \frac{1}{2} (\nabla_i E_j + \nabla_j E_i) \quad \text{and} \quad H_{ij} = \frac{1}{2} (\nabla_i H_j + \nabla_j H_i) \quad (32)$$

and where $\dot{\vec{E}}$ and $\dot{\vec{H}}$ are the time derivative of the fields. In Eq. 31, γ_{E1} and γ_{M1} describe the spin dependence of the dipole electric and magnetic photon scattering $E1 \rightarrow E1$ and $M1 \rightarrow M1$, whereas γ_{E2} and γ_{M2} describe the dipole-quadrupole amplitudes $M1 \rightarrow E2$ and $E1 \rightarrow M2$ respectively. The spin dependent part of the Non-Born amplitude can be expressed in terms of those four spin polarizabilities γ_{E1} , γ_{E2} , γ_{M1} and γ_{M2} as:

$$\frac{1}{8\pi m_p} T^{(3), NB, spin} = i\omega^3 [- (\gamma_{E1} + \gamma_{M2}) \vec{\sigma} \cdot \vec{\epsilon}^{**} \times \vec{\epsilon} \\ + (\gamma_{E2} - \gamma_{M1}) (\vec{\sigma} \cdot \hat{q}^{**} \times \hat{q} \vec{\epsilon}^{**} \cdot \vec{\epsilon} - \vec{\sigma} \cdot \vec{\epsilon}^{**} \times \vec{\epsilon} \hat{q}^{**} \cdot \hat{q}) \\ + \gamma_{M2} (\vec{\sigma} \cdot \vec{s} \vec{\epsilon}^{**} \cdot \hat{q} - \vec{\sigma} \cdot \vec{s}^{**} \vec{\epsilon} \cdot \hat{q}') \\ + \gamma_{M1} (\vec{\sigma} \cdot \vec{\epsilon}^{**} \times \hat{q} \vec{\epsilon} \cdot \hat{q}' - \vec{\sigma} \cdot \vec{\epsilon} \times \hat{q}' \vec{\epsilon}^{**} \cdot \hat{q} \\ - 2\vec{\sigma} \cdot \vec{\epsilon}^{**} \times \vec{\epsilon} \hat{q}' \cdot \hat{q}) \\] + \mathcal{O}(\omega^4). \quad (33)$$

Finally, the effective interaction of $\mathcal{O}(\omega^4)$ has the form :

$$H_{eff}^{(4), nospin} = -\frac{1}{2}4\pi (\alpha_{E\nu} \dot{\vec{E}}^2 + \beta_{M\nu} \dot{\vec{H}}^2) - \frac{1}{12}4\pi (\alpha_{E2} E_{ij}^2 + \beta_{M2} H_{ij}^2) \quad (34)$$

where the quantities $\alpha_{E\nu}$ and $\beta_{M\nu}$ in Eq. 34, called dispersion polarizabilities, describe the ω -dependence of the dipole polarizabilities, whereas α_{E2} and β_{M2} are the quadrupole polarizabilities of the nucleon.

To summarize, the Compton amplitude to the order $\mathcal{O}(\omega^4)$ is parameterized by ten polarizabilities which have a simple physical interpretation in terms of the interaction of the nucleon with an external electromagnetic field. Note that a generalization of six of those polarizabilities (α_E , β_M , γ_{E1} , γ_{M1} , γ_{E2} and γ_{M2}) will appear to the lowest order in the low-energy expansion of the VCS amplitude.

Differential cross-section

From the scattering amplitude, one can write the differential cross-section of RCS in the lab frame as:

$$\frac{d\sigma}{d\Omega} = \frac{1}{4} \Phi^2 |T_{\mu\nu}|^2, \text{ with } \Phi = \frac{1}{8\pi m_p} \frac{\omega'}{\omega}. \quad (35)$$

For low energy photons, Eq. 35 becomes :

$$\begin{aligned} \frac{d\sigma}{d\Omega}(\omega, \theta) &= \frac{d\sigma^B}{d\Omega}(\omega, \theta) \\ &- \frac{e^2}{4\pi m_p} \left(\frac{\omega'}{\omega}\right)^2 (\omega\omega') \left[\frac{\alpha_E + \beta_M}{2} (1 + \cos\theta)^2 + \frac{\alpha_E - \beta_M}{2} (1 - \cos\theta)^2 \right] \\ &+ \mathcal{O}(\omega^4) \end{aligned} \quad (36)$$

where $\frac{d\sigma^B}{d\Omega}$ is the exact Born cross-section that describes the RCS process on a pointlike nucleon.

This equation shows that the forward ($\theta = 0^\circ$) and backward ($\theta = 180^\circ$) cross-sections are sensitive mainly to $\alpha_E + \beta_M$ and $\alpha_E - \beta_M$ respectively, whereas the 90° cross-section is sensitive only to α_E .

The sum $\alpha_E + \beta_M$ is independently constrained by a model-independent sum rule, the Baldin sum rule [18] :

$$\alpha_E + \beta_M = \frac{1}{2\pi^2} \int_0^\infty \frac{\sigma_\gamma(\omega)}{\omega^2} d\omega = 13.69 \pm 0.14 [17] \quad (37)$$

where σ_γ is the total photo-absorption cross-section on the proton.

α_E and β_M could in principle be separated by studying the RCS angular distributions. However, at small energies ($\nu < 40\text{MeV}$), the structure effects are very small, and hence statistical errors are large. So one has to go to higher energies where one must take into account higher order terms and use models. We will see in the next paragraph how to minimize any model dependence in the extraction of the polarizabilities from the data by using dispersion relation formalism.

Dispersion relations

Using analytical properties in ν of the Compton amplitude, one can write Cauchy's integral formula for the amplitudes defined in Eq. 23:

$$A_i(\nu, t) = \frac{1}{2\pi i} \oint_C \frac{A_i(\nu', t)}{\nu' - \nu - i\epsilon} d\nu' \quad (38)$$

where C is the loop represented in Fig. 5.

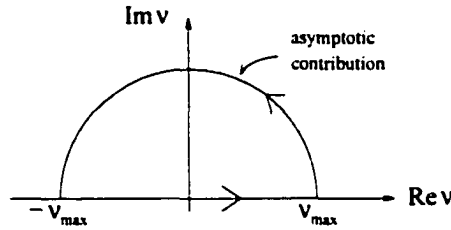


FIG. 5: Cauchy's loop used for the integration of the Compton amplitude.

Eq. 38 gives fixed- t unsubtracted dispersion relations for $A_i(\nu, t)$ [19] :

$$\text{Re}A_i(\nu, t) = A_i^B + \frac{2}{\pi} \mathcal{P} \int_{\nu_{thr}}^{\nu_{max}} \frac{\nu' \text{Im}A_i(\nu', t)}{\nu'^2 - \nu^2} d\nu' + A_i^{as}(\nu, t) \quad (39)$$

where A_i^B are the Born contributions (purely real), \mathcal{P} represents the principal part of the integral, ν_{thr} represents the pion production threshold and finally A_i^{as} is the asymptotic contribution representing the contribution along the finite semi-circle of radius ν_{max} in the complex plane.

The high energy behavior of the A_i for $\nu \rightarrow \infty$ and fixed t makes the unsubtracted dispersion integral of Eq. 39 to diverge for the A_1 and A_2 amplitudes. To

avoid this divergence problem, Drechsel *et al.*[20] introduced subtracted dispersion relations *i.e.* dispersion relations at fixed t that are once subtracted at $\nu = 0$:

$$\text{Re}A_i(\nu, t) - A_i(0, t) = [A_i^B(\nu, t) - A_i^B(0, t)] + \frac{2}{\pi}\nu^2\mathcal{P} \int_{\nu_{thr}}^{+\infty} \frac{\text{Im}A_i(\nu', t)}{\nu'(\nu'^2 - \nu^2)} d\nu' \quad (40)$$

To determine the t -dependence of the subtraction functions $A_i(0, t)$, one has to write subtracted dispersion relation for the variable t [20]. This leads to denote some constants:

$$a_i = A_i(0, 0) - A_i^B(0, 0) . \quad (41)$$

These quantities are then directly related to the polarizabilities:

$$\alpha_E + \beta_M = -\frac{1}{2\pi}(a_3 + a_6) \quad (42)$$

$$\alpha_E - \beta_M = -\frac{1}{2\pi}a_1 \quad (43)$$

$$\gamma_0 \equiv \gamma_{E1} + \gamma_{E2} + \gamma_{M1} + \gamma_{M2} = -\frac{1}{2\pi m_p}a_4 \quad (44)$$

$$\gamma_{M2} - \gamma_{E1} = -\frac{1}{4\pi m_p}(a_5 + a_6) \quad (45)$$

$$\gamma_{E1} + 2\gamma_{M1} + \gamma_{M2} = -\frac{1}{4\pi m_p}(2a_4 + a_5 - a_6) \quad (46)$$

$$\gamma_\pi \equiv \gamma_{E2} - \gamma_{E1} + \gamma_{M1} - \gamma_{M2} = -\frac{1}{2\pi m_p}(a_2 + a_5) \quad (47)$$

A_4 , A_5 and A_6 obey unsubtracted dispersion relations (Eq. 39), so $a_{4,5,6}$ can be calculated exactly:

$$a_{4,5,6} = \frac{2}{\pi} \int_{\nu_{thr}}^{+\infty} \frac{\text{Im}A_{4,5,6}(\nu', t=0)}{\nu'} d\nu' . \quad (48)$$

These dispersion relations are very useful since the imaginary part of each Compton amplitude is related by the optical theorem to a multipole decomposition of the $\gamma N \rightarrow X$ photo-absorption amplitude. In particular the dispersion integral for $a_3 + a_6$ is equal to the dispersion integral over the forward spin independent Compton amplitude, yielding the Baldin sum rule (Eq. 37). Similarly, the dispersion integral over the forward spin dependent Compton amplitude yields the Gerasimov-Drell-Hearn sum rule[21][22]:

$$\int_{\nu_{thr}}^{+\infty} \frac{\sigma^{3/2} - \sigma^{1/2}}{\omega} d\omega = 2\pi^2 \alpha_{QED} \frac{\kappa^2}{m_p^2} \quad (49)$$

where $\sigma^{3/2}$ and $\sigma^{1/2}$ are the inclusive photoproduction cross-sections when the photon helicity is aligned and anti-aligned with the target polarization and where ω is the photon energy.

Since a_3 is related to $\alpha_E + \beta_M$ by Eq. 42, a_3 can be fixed by the Baldin's sum rule and a value for a_6 . For A_1 and A_2 , the unsubtracted dispersion relations do not exist, so a_1 and a_2 will be determined from a fit to the Compton scattering data where the fit parameters will be $\alpha_E - \beta_M$ and γ_π .

Thus, subtracted dispersion relations can be used to extract the nucleon polarizabilities from RCS data with a minimum of model dependence. Predictions in the subtracted dispersion relation formalism are shown and compared with the available Compton data on the proton below pion threshold in Ref. [20].

Recent results

The most recent Compton and pion photoproduction experiments [23][24] are analyzed in a subtracted dispersion relation formalism at fixed t therefore with a minimum of model dependence. They yield the following results:

$$\alpha_E = 12.1 \pm 0.3 \mp 0.4 (10^{-4} fm^3) \quad (50)$$

$$\beta_M = 1.6 \pm 0.4 \pm 0.4 (10^{-4} fm^3) \quad (51)$$

$$\gamma_\pi = -36.1 \pm 2.1 \mp 0.4 \pm 0.8 (10^{-4} fm^4) \quad (52)$$

The first uncertainty includes statistics and systematic experimental uncertainties, the second includes the model dependent uncertainties from the dispersion theory analysis.

Chapter 3

A new insight : Virtual Compton Scattering

3.1 Electroproduction of a real photon

Virtual Compton Scattering (VCS) generally refers to any process where two photons are involved and where at least one of them is virtual. The virtuality of the photon can be characterized by its four-momentum squared. This four-momentum square quantity is frame independent and is equal to the square of the particle's mass. Whereas this mass is zero for real photons, the mass squared of a virtual photon is negative for electron scattering and positive for electron-positron production.

Virtual photons are not actual particles but can be seen as the carrier of the electromagnetic force during interactions between charged particles. This leads me to restrict the meaning of VCS that can be found in this document. Virtual refers to the initial state: a space-like virtual photon is absorbed by a proton target which returns to its initial state by emitting one real photon. Explicitly, Virtual Compton Scattering off the proton refers to the reaction

$$\gamma^* + p \rightarrow p' + \gamma \quad (53)$$

where γ^* stands for an incoming virtual photon of four-momentum squared q^2 , p

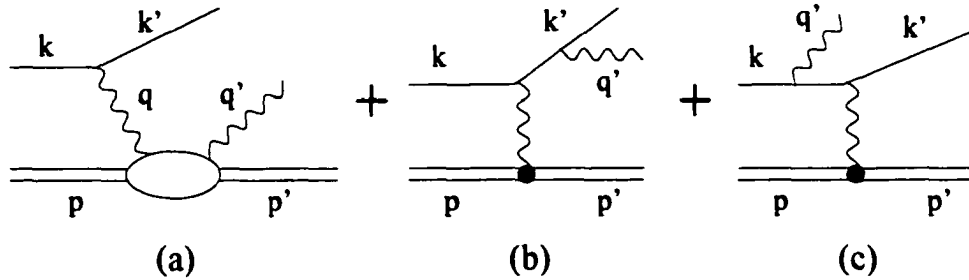


FIG. 6: (a) FVCS diagram and (b,c) BH diagrams. On those diagrams, k and k' indicate initial and final electron four-momentum, p and p' are used for the proton, q' for the final real photon and q for the virtual photon in the VCS case.

for the target proton, p' for the recoil proton and finally γ for the emitted real photon of four-momentum q' .

The VCS reaction is experimentally accessed through the

$$e + p \rightarrow e' + p' + \gamma \quad (54)$$

reaction. In this electroproduction of a real photon on a proton target, an electron scatters off a proton while a real photon γ is emitted.

Due to the way we access the VCS process, we actually have interference between two processes, indistinguishable if only the initial and final states are considered. Those two processes are the Full Virtual Compton Scattering (FVCS) process on the one hand and the Bethe-Heitler (BH) process on the other hand.

In Fig. 6, the main diagrams of the reaction we are interested in are drawn, in the one photon exchange approximation. The first diagram illustrates the FVCS process in which a virtual photon of quadri-momentum $q = k - k'$ is exchanged between the electron and the proton target. The target emits a real photon of four-momentum q' . This process is simply the VCS process where the electronic current is added.

The last two diagrams of Fig. 6 present the BH process. A virtual photon of four-momentum $q - q'$ is exchanged. The electron emits a photon of four-momentum q' , either before or after emission of the virtual photon. Pre- and

post-radiations are illustrated but are part of the same Bremsstrahlung radiation process. BH is in fact elastic scattering off the proton with Bremsstrahlung radiation by the electron.

When the photon is emitted close to the incident or scattered electron direction, the BH process dominates. Furthermore, in nearly all cases, there is a strong interference with the VCS process. Indeed electrons are light particles and so radiate easily at the energy of this experiment of 4 GeV.

The $ep \rightarrow ep\gamma$ five-fold differential cross-section has the form:

$$\frac{d^5\sigma_{ep \rightarrow ep\gamma}}{dk'_{lab}(d\Omega_e)_{lab}(d\Omega_p)_{CM}} = \frac{(2\pi)^{-5}}{32m_p} \left(\frac{k'_{lab}}{k_{lab}}\right) \frac{q'}{\sqrt{s}} \times \mathcal{M} \equiv \Psi q' \mathcal{M} \quad (55)$$

where \mathcal{M} is the square of the coherent sum of the invariant FVCS and BH amplitudes:

$$\mathcal{M} = \frac{1}{4} \sum_{spins} |T^{FVCS} + T^{BH}|^2. \quad (56)$$

The flux and phase space factor Ψ is defined here as:

$$\Psi = \frac{(2\pi)^{-5}}{32m_p} \left(\frac{k'_{lab}}{k_{lab}}\right) \frac{1}{\sqrt{s}}, \quad (57)$$

with k_{lab} and k'_{lab} the energy in the Lab frame of the incident and scattered electron respectively, $s = (p + q)^2$ the usual Mandelstam variable and finally q' the real photon energy in the virtual photon+proton center of mass frame.

3.2 BH and VCS amplitudes

Bethe-Heitler amplitude

In this subsection, the BH process amplitude is examined. It is exactly calculable from Quantum Electro-Dynamics (QED) up to the precision of our knowledge of the proton elastic form factors. Therefore no new information is contained in this term.

In the one photon exchange approximation and in Lorentz gauge, the BH amplitude can be written in the following form, making use of Feynman rules:

$$T^{BH} = -\frac{e^3}{(q - q')^2} \epsilon'^*_{\mu} L^{\mu\nu} \bar{u}(p') \Gamma_{\nu}(p', p) u(p) \quad (58)$$

where p and p' are the proton initial and final four-momentum, $u(p)$ and $u(p')$ are the initial and final proton spinors, ϵ' is the polarization vector of the final photon and Γ is the vertex defined as :

$$\Gamma^\nu(p', p) = F_1((p' - p)^2)\gamma^\nu + i\frac{F_2((p' - p)^2)}{2m_p}\sigma^{\nu\rho}(p' - p)_\rho \quad (59)$$

with:

$$\sigma^{\nu\rho} = \frac{i}{2}(\gamma^\nu\gamma^\rho - \gamma^\rho\gamma^\nu) \quad (60)$$

and F_1 and F_2 the proton elastic form factors with the experimental conditions

$$F_1(0) = 1 \quad \text{and} \quad F_2(0) = \kappa_p = 1.79 .$$

The leptonic tensor is:

$$L^{\mu\nu} = \bar{u}(k') \left(\gamma^\mu \frac{\gamma \cdot (k' + q') + m_e}{(k' + q')^2 - m_e^2} \gamma^\nu + \gamma^\nu \frac{\gamma \cdot (k - q') - m_e}{(k - q')^2 + m_e^2} \gamma^\mu \right) u(k) \quad (61)$$

where $u(k')$ and $u(k)$ are the final and initial electron spinors.

The post- and pre-radiation have been added inside the leptonic tensor. The structure of this current can easily be seen. The spinors take care of the external lines of the electron. The Dirac γ^μ matrix describe the structureless vertex related to the emitted real photon. In turn the γ^ν matrix describe the vertex attached to the virtual photon. The remaining terms are the propagators of the electron between the two vertices.

The proton current $\bar{u}(p')\Gamma_\nu(p', p)u(p)$ can also be understood in a similar manner. The two spinors take care of the proton external lines and $\Gamma_\nu(p', p)$ describes the vertex on the proton line. This vertex takes into account the proton structure by means of the proton form factors.

One can now finish building the BH amplitude by adding the polarization vector of the final photon, by adding the virtual photon propagator and by completing the vertices (multiplying each of them by $i e$).

It can be foreseen that the cross-section of this process is going to be reduced by a factor $\alpha_{QED} \simeq 1/137$ with respect to the elastic cross-section. Indeed no photon is radiated in the elastic process and it is the additional vertex in the BH process that will diminish the cross-section by two orders of magnitude.

Virtual Compton amplitude

The Full Virtual Compton Scattering amplitude has an expression similar to the Bethe-Heitler:

$$T^{FVCS} = \frac{e^3}{q^2} \epsilon'_\mu{}^* H^{\mu\nu} \bar{u}(k') \gamma_\nu u(k) \quad (62)$$

where $H^{\mu\nu}$ is a generic definition of the hadronic tensor in Fig. 6(a).

The leptonic tensor is reduced to what is on the right of the hadronic tensor, which is the initial and final electron spinors and a structureless vertex. The polarization vector of the real photon ϵ' is attached to the hadronic tensor via the index μ . The four-momentum of the virtual photon is now q yielding a different virtual photon propagator in the amplitude. Finally the definition of the hadronic tensor is chosen so that the multiplicative factor e^3 can be factorized for convenience.

The next step is to parameterize the hadronic tensor to translate what is happening on the nucleon side. But first, one can split the hadronic tensor into two terms since one of them, the Born term, is also fully calculable. The idea is to isolate in this term the contribution of the special case of a propagating proton in the intermediate state (between the two photons). The second term called Non-Born term includes everything else and specifically the contributions from all resonance and continuum excitations that can be created in the intermediate state.

Doing so, we write:

$$H^{\mu\nu} = H_B^{\mu\nu} + H_{NB}^{\mu\nu} \quad (63)$$

where H_B stands for the Born term, the proton contribution, and H_{NB} for the Non-Born term.

The Born term is defined by:

$$\begin{aligned} H_B^{\mu\nu} = & \bar{u}(p') \Gamma^\mu(p', p' + q') \frac{\gamma \cdot (p' + q') + m_p}{(p' + q')^2 - m_p^2} \Gamma^\nu(p' + q', p) u(p) \\ & + \bar{u}(p') \Gamma^\nu(p', p - q') \frac{\gamma \cdot (p - q') + m_p}{(p - q')^2 - m_p^2} \Gamma^\mu(p - q', p) u(p) \end{aligned} \quad (64)$$

The first term in this sum is for the s -channel configuration while the second is for the u -channel. The initial and final states are propagating protons whence the

proton spinors. One of the two vertices is for the virtual photon while the other is for the emitted real photon. Both include the proton structure. The remaining components of this tensor are proton propagators.

The Born term is the Bremsstrahlung from the proton and also includes the proton-antiproton pair excitation. (It resembles the BH term but with a more complicated vertex structure.)

One can show that $q'_\mu H_B^{\mu\nu} = H_B^{\mu\nu} q_\nu = 0$. (Some terms vanish individually whereas, for the other terms, the s - and u -channels compensate each other.) The Born term H_B is then gauge invariant. As the full amplitude is constrained to be gauge invariant, H_{NB} is gauge invariant as well.

3.3 Multipole expansion of H_{NB} and Generalized Polarizabilities

If we sum up what we have so far, we can say that the amplitude of the process we have access to experimentally is the coherent sum of the BH and the FVCS amplitudes. In turn FVCS can be written as the sum of the Born term and the non-Born term. Both BH and Born terms are calculable if one knows the proton form factors. There is therefore nothing new so far. We now need a parameterization of the unknown part, H_{NB} .

We are going to use the multipole expansion so as to take advantage of angular momentum and parity conservation following the steps of Guichon *et al.* [25]. We are going to do this expansion in the photon+proton center of mass frame. We introduce the reduced multipoles:

$$H_{NB}^{(\rho'L',\rho L)S}(q',q) = \frac{1}{\mathcal{N}} \frac{1}{2S+1} \sum_{\sigma,\sigma',M,M'} (-1)^{1/2+\sigma'+L+M} \begin{pmatrix} \frac{1}{2} & \frac{1}{2} & S \\ -\sigma' & \sigma & s \end{pmatrix} \begin{pmatrix} L' & L & S \\ M' & -M & s \end{pmatrix} \int d\vec{q}' d\vec{q} V_\mu^*(\rho', L', M'; \vec{q}') H_{NB}^{\mu\nu}(\vec{q}'\sigma', \vec{q}\sigma) V_\nu(\rho, L, M; \vec{q}). \quad (65)$$

The normalization factor $\mathcal{N} = 8\pi\sqrt{p_0 p'_0}$ is here for later convenience. The basis vectors $V^\mu(\rho, L, M; \vec{q})$ are defined in Appendix B. The Clebsch-Gordan coefficients

are the same as in Ref. [27]. In the above equation, L (resp. L') represents the angular momentum of the initial (resp. final) electromagnetic transition whereas S differentiates between the spin-flip ($S=1$) or non spin-flip ($S=0$) transition at the nucleon side.

The index ρ can take *a priori* four values: $\rho = 0$ (charge), $\rho = 1$ (magnetic transition), $\rho = 2$ (electric transition) and $\rho = 3$ (longitudinal). Nevertheless gauge invariance relates the charge and longitudinal multipoles according to:

$$|\vec{q}'|H_{NB}^{(3L', \rho L)S} + q'_0 H_{NB}^{(0L', \rho L)S} = 0 \quad (66)$$

$$|\vec{q}|H_{NB}^{(\rho' L', 3L)S} + q_0 H_{NB}^{(\rho' L', 0L)S} = 0 \quad (67)$$

We have now our parameterization of H_{NB} : it can be expressed by a sum over all the possible multipoles weighted by the appropriate factors. The explicit formula is contained in Ref. [25], Eq. 72.

In the following we are going to restrain ourselves to the case where the outgoing real photon energy q' has small values. The adjective small is used here in accordance with a low energy expansion of the amplitude, development that will be exposed in the next section. The order of magnitude is still the MeV. In such a case, and as a consequence of the multipole expansion, the lowest order term in H_{NB} is entirely determined by the $L' = 1$ multipoles (Ref. [25]).

As indicated in Ref. [25], one needs only six generalized polarizabilities to parameterize the low energy behavior of H_{NB} . They are defined by:

$$P^{(11,02)1}(q) = \lim_{q' \rightarrow 0} \frac{1}{|\vec{q}'||\vec{q}|^2} H_{NB}^{(11,02)1}(q', q) \quad (68)$$

$$P^{(11,11)S}(q) = \lim_{q' \rightarrow 0} \frac{1}{|\vec{q}'||\vec{q}|} H_{NB}^{(11,11)S}(q', q) \quad (69)$$

$$P^{(01,01)S}(q) = \lim_{q' \rightarrow 0} \frac{1}{|\vec{q}'||\vec{q}|} H_{NB}^{(01,01)S}(q', q) \quad (70)$$

$$P^{(01,12)1}(q) = \lim_{q' \rightarrow 0} \frac{1}{|\vec{q}'||\vec{q}|^2} H_{NB}^{(01,12)1}(q', q) \quad (71)$$

3.4 Low energy expansion

Before exposing how the Generalized Polarizabilities (GPs) parameterize the cross-section, I would like to discuss about the expansion upon the energy of the real photon q' of the BH and VCS amplitudes.

From subsection 3.2, we can recall the denominators of the electron propagators appearing in the leptonic tensor part of the BH amplitude. They were: $(k' + q')^2 - m_e^2$ and $(k - q')^2 - m_e^2$. Developing the expressions, it is simple to obtain that:

$$(k' + q')^2 - m_e^2 = k'^2 + q'^2 + 2k' \cdot q' - m_e^2 = 2k' \cdot q' \quad (72)$$

$$(k - q')^2 - m_e^2 = -2k \cdot q' \quad (73)$$

since the square of a four-momentum equals the square of the particle mass.

Likewise, recalling the proton propagators appearing in the VCS amplitude in subsection 3.2, we find that:

$$(p' + q')^2 - m_p^2 = 2p' \cdot q' \quad (74)$$

$$(p - q')^2 - m_p^2 = -2p \cdot q' . \quad (75)$$

This leads to the fact that the BH and VCS amplitudes can be developed as power series in the energy q' in the following way:

$$T^{BH} = \frac{T_{-1}^{BH}}{q'} + T_0^{BH} + T_1^{BH} q' + \mathcal{O}(q'^2) \quad (76)$$

$$T^{Born} = \frac{T_{-1}^{Born}}{q'} + T_0^{Born} + T_1^{Born} q' + \mathcal{O}(q'^2) . \quad (77)$$

It was shown by Guichon *et al.* in Ref.[2] that H_{NB} is a regular function of the four-vector q'^μ . Stated otherwise H_{NB} has a polynomial expansion of the form:

$$H_{NB}^{\mu\nu} = a^{\mu\nu}(q) + b_\alpha^{\mu\nu}(q)q'^\alpha + \mathcal{O}(q'^2) . \quad (78)$$

From the low energy theorem Guichon *et al.* proved that $a^{\mu\nu} = 0$ (Ref. [25] or Ref. [26]). This shows that the expansion of H_{NB} , the unknown part of the VCS amplitude, starts at order q' :

$$T^{NB} = T_1^{NB} q' + \mathcal{O}(q'^2) . \quad (79)$$

We can now rewrite \mathcal{M} , first introduced in subsection 3.1,

$$\mathcal{M} = \frac{1}{4} \sum_{spins} |T^{FVCS} + T^{BH}|^2 \quad (80)$$

$$= \frac{1}{4} \sum_{spins} |T^{BH} + T^{Born} + T^{NB}|^2 \quad (81)$$

$$= \frac{1}{4} \sum_{spins} |T^{BH+Born} + T^{NB}|^2 \quad (82)$$

as

$$\mathcal{M} = \frac{\mathcal{M}_{-2}}{q'^2} + \frac{\mathcal{M}_{-1}}{q'} + \mathcal{M}_0 + \mathcal{M}_1 q' + \mathcal{O}(q'^2) . \quad (83)$$

\mathcal{M}_0 is the first term in the expansion that includes a contribution from T^{NB} . It is an interference term between the leading order term in T^{NB} and the leading order term in $(T^{BH} + T^{Born}) \equiv T^{BH+Born}$. Moreover the first two terms in Eq. 83 are entirely due to T^{BH} and T^{Born} . Indeed, one can check those two facts by calculating:

$$\begin{aligned} |T^{BH+Born} + T^{NB}|^2 &= \left[\frac{T_{-1}^{BH+Born}}{q'} + T_0^{BH+Born} + T_1^{BH+Born} q' + T_1^{NB} q' + \mathcal{O}(q'^2) \right]^2 \\ &= \left(\frac{T_{-1}^{BH+Born}}{q'} \right)^2 + 2 \frac{T_{-1}^{BH+Born} T_0^{BH+Born}}{q'} \\ &\quad + \left(T_0^{BH+Born} \right)^2 + 2 T_{-1}^{BH+Born} T_1^{BH+Born} \\ &\quad + 2 T_{-1}^{BH+Born} T_1^{NB} + \mathcal{O}(q') . \end{aligned} \quad (84)$$

We can also add and subtract the contribution of $(T^{BH+Born})^2$ to \mathcal{M} at all orders so as to end up with the following reformulation of Eq. 83:

$$\mathcal{M} = \mathcal{M}^{BH+Born} + (\mathcal{M}_0 - \mathcal{M}_0^{BH+Born}) + (\mathcal{M}_1 - \mathcal{M}_1^{BH+Born}) q' + \mathcal{O}(q'^2) . \quad (85)$$

This reformulation explicitly puts aside the BH and Born contributions at all orders in the first term. The next term in the equation, namely $\mathcal{M}_0 - \mathcal{M}_0^{BH+Born}$, will be renamed $\mathcal{M}_0^{NonBorn}$ and is the lowest order term that includes a contribution from the Non-Born amplitude and will be parameterized by the generalized polarizabilities.

We can summarize what we have seen in the previous subsections and the present one by the following expression of the VCS cross-section:

$$d^5\sigma_{ep\rightarrow e\gamma}(q, q', \epsilon, \theta, \varphi) = d^5\sigma^{BH+Born}(q, q', \epsilon, \theta, \varphi) + \Psi q' \mathcal{M}_0^{NonBorn}(q, \epsilon, \theta, \varphi) + \mathcal{O}(q'^2) \quad (86)$$

where q and q' are the magnitudes of the virtual and real photon momenta
 ϵ is the virtual photon polarization (Eq. 11)
 θ is the angle between the real and virtual photon in the CM frame
 φ is the angle between the electron and the photon-proton plane.

In the zero-energy limit of the final photon, the cross-section is independent of the dynamical nucleon structure. Indeed, this information is contained in $\mathcal{M}_0^{NonBorn}(q, \epsilon, \theta, \varphi)$, which is parameterized by six independent Generalized Polarizabilities (GPs), functions of Q^2 .

Those polarizabilities are fundamental quantities that characterize the response of a composite system to static or slowly varying external electric or magnetic fields. They can be seen as transition form factors from the nucleon ground state to the electric- or magnetic-dipole polarized nucleon. Their Q^2 dependence reflects the spatial variations of the polarization of the internal structure of the proton induced by an external electromagnetic field.

They are denoted $P^{(\rho'L',\rho L)S}$ where the label was already explained in section 3.3. One has two non-spin flip GPs, $P^{(01,01)0}$ and $P^{(11,11)0}$ proportional to α_E and β_M at $Q^2 = 0$ respectively, and four spin flip GPs, $P^{(11,11)1}$, $P^{(11,00)1}$, $P^{(11,02)1}$, $P^{(01,12)1}$.

In an unpolarized measurement, $\mathcal{M}_0^{NonBorn}(q, \epsilon, \theta, \varphi)$ can be written as:

$$\mathcal{M}_0^{NonBorn}(q, \epsilon, \theta, \varphi) = v_{LL}(\theta, \varphi, \epsilon)[P_{LL}(q) - P_{TT}(q)/\epsilon] + v_{LT}(\theta, \varphi, \epsilon)P_{LT}(q) \quad (87)$$

where $v_{LL}(\theta, \varphi, \epsilon)$, $v_{LT}(\theta, \varphi, \epsilon)$ are known kinematical factors, and $P_{LL}(q)$, $P_{TT}(q)$ and $P_{LT}(q)$ are structure functions. One has:

$$P_{LL} = -2\sqrt{6} m_p G_E P^{(01,01)0} \quad (88)$$

$$P_{TT} = 3G_M q^2 \left[\sqrt{2} P^{(01,12)1} - P^{(11,11)1}/\tilde{q}_0 \right] \quad (89)$$

$$P_{LT} = \sqrt{\frac{3}{2}} \frac{m_p q}{\tilde{Q}} G_E P^{(11,11)0} + \frac{\sqrt{3} \tilde{Q}}{2} \frac{G_M}{q} \left[P^{(11,00)1} + \frac{q^2}{\sqrt{2}} P^{(11,02)1} \right] \quad (90)$$

where $\tilde{q}_0 = m_p - \sqrt{m_p^2 + q^2}$ and $\tilde{Q}^2 = -2 m_p \tilde{q}_0$.

In those formulas, one can see the interference between the Non-Born term and the BH+Born term through the products of the polarizabilities with the electric or magnetic form factors.

3.5 Calculation of Generalized Polarizabilities in a phenomenological resonance model

3.5.1 Connecting to a model

The purpose of this section is to relate the generalized polarizabilities to a dynamic model of the VCS amplitude [28]. The explicit model we consider as a starting point is a resonance model of Todor & Roberts [29]. In this model, the VCS amplitude is computed by a series of Feynman diagrams, each of which describes the real or virtual photoexcitation and decay of a series of resonances.

For example, if the intermediate state is a spin $1/2^+$ resonance.

$$H_{NB}^{\mu\nu} = \bar{u}(p') \Gamma^\mu(p', p' + q'; N^*) \frac{\gamma \cdot (p' + q') + M_r}{(p' + q')^2 - M_r^2 + i\Gamma_r M_r} \Gamma^\nu(p' + q', p; N^*) u(p) \quad (\text{s-channel}) \quad (91)$$

$$+ \bar{u}(p') \Gamma^\nu(p', p - q'; N^*) \frac{\gamma \cdot (p - q') + M_r}{(p - q')^2 - M_r^2 + i\Gamma_r M_r} \Gamma^\mu(p - q', p; N^*) u(p) \quad (\text{u-channel}) \quad (92)$$

where the two first vertices read:

$$\Gamma^\mu(p', p' + q'; N^*) = T_1(q^2; N^*) \gamma^\mu - i \frac{T_2(q^2; N^*)}{m_p + M_r} \sigma^{\mu\rho} q'_\rho \quad (93)$$

$$\Gamma^\nu(p' + q', p; N^*) = T_1(q^2; N^*) \gamma^\nu + i \frac{T_2(q^2; N^*)}{m_p + M_r} \sigma^{\nu\alpha} q_\alpha \quad (94)$$

where T_1 and T_2 are the transition form factors of resonance N^* .

A correct model would include all resonances with spin 1/2 and 3/2 as we couple a spin 1/2 proton with the $L' = 1$ multipolarity of the final photon.

In the big picture, we want to perform a simultaneous fit of the parameters of the resonance model of VCS to $ep \rightarrow ep\gamma$ data below and above pion threshold in order to extract experimental polarizabilities with constraints of all data and full freedom of higher order terms.

In the following subsections, I shall analytically calculate four of the six needed multipoles from Eq. 91 and 92 for spin $1/2^+$ resonances as a function of the transition form factors T_i and express the corresponding polarizabilities as a function of Q^2 .

3.5.2 Gauge invariance and final model

The goal of this subsection is to check on gauge invariance. It is relatively easy to check that the Born term of the VCS amplitude is gauge invariant. One just has to calculate $H_B^{\mu\nu} q_\nu$ and $H_B^{\mu\nu} q'_\mu$. Some terms will not vanish but will compensate each other because of the fact that the resonance we consider is the proton itself.

This simple cancellation does not happen when we consider excited resonances. Nevertheless we want to insure gauge invariance for each resonance. For that purpose, it has been decided to alter the vertices expressions [30].

$H_{NB}^{\mu\nu} q_\nu = 0$ condition

When calculating $H_{NB}^{\mu\nu} q_\nu$, we are led to calculate $\Gamma^\nu q_\nu$, where Γ^ν is the vertex related to the virtual photon. In our model, we have so far:

$$\Gamma^\nu = T_1(q^2)\gamma^\nu + i\frac{T_2(q^2)}{m_p + M_r}\sigma^{\nu\alpha}q_\alpha . \quad (95)$$

The second term will vanish when we multiply by q_ν since $\sigma^{\nu\alpha}$ is antisymmetric whereas $q_\alpha q_\nu$ is symmetric. The other term does not so. We are going to change the structure of the vertex so that we do have $H_{NB}^{\mu\nu} q_\nu = 0$. Now defining Γ^ν to be:

$$\Gamma^\nu = T_1(q^2)(\gamma^\nu - \not{A}\frac{q^\nu}{q^2}) + i\frac{T_2(q^2)}{m_p + M_r}\sigma^{\nu\alpha}q_\alpha \quad (96)$$

one can check that we do have gauge invariance.

$H_{NB}^{\mu\nu}q'_\mu = 0$ condition

Here we are dealing with the other vertex, the one related to the real photon. While calculating $H_{NB}^{\mu\nu}q'_\mu$, we are led to evaluate $\Gamma^\mu q'_\mu$. In our model, we have so far:

$$\Gamma^\mu = T_1(0)\gamma^\mu - i\frac{T_2(0)}{m_p + M_r}\sigma^{\mu\rho}q'_\rho. \quad (97)$$

When multiplying by q'_μ , the second term will vanish by symmetry. Now if we constrain our model with $T_1(0) = 0$, it is sufficient to insure gauge invariance. Another attempt would be to relate $T_1(0)$ to $T_2(0)$. This possibility arise when we don't constrain $T_1(0)$ to be zero, calculate $P^{(01,01)1}$ and $P^{(11,11)1}$ and try to retrieve the properties shown in Ref. [25] that those polarizabilities should vanish when Q^2 goes to zero. After calculations it turns out that the only common solution for $P^{(01,01)1} = 0$ and $P^{(11,11)1} = 0$ is $T_1(0) = 0$.

3.5.3 Polarizabilities expressions

$P^{(01,01)1}$ polarizability

The definition of the multipole corresponding to this polarizability is:

$$H_{NB}^{(01,01)1} = \frac{1}{8\pi\sqrt{p_0p'_0}} \frac{1}{3} \sum_{\sigma,\sigma',M,M'} (-1)^{\frac{1}{2}+\sigma'+1+M} \begin{pmatrix} \frac{1}{2} & \frac{1}{2} & 1 \\ -\sigma' & \sigma & s \end{pmatrix} \begin{pmatrix} 1 & 1 & 1 \\ M' & -M & s \end{pmatrix} \int d\hat{q}' d\hat{q} V_\mu^*(0, 1, M'; \hat{q}') H_{NB}^{\mu\nu} V_\nu(0, 1, M; \hat{q}). \quad (98)$$

The first step in this present method is to calculate the integral in the previous definition. It is obtained by contracting the H_{NB} tensor with the spherical harmonics vectors and then by integrating over the directions of \vec{q} and \vec{q}' . This is the longest part of the calculation since the expression to be integrated is fairly complicated. The next step consists in summing over the spin and orbital momentum projections. And finally, the last step is to take the limit of the calculated reduced multipole when the emitted real photon energy in the CM frame q' goes to zero.

The result, after all calculations are performed, for the contribution from a

$N \rightarrow N^*(\frac{1}{2}+) \rightarrow N$ to the total polarizability is:

$$P^{(01,01)1}(Q^2) = \frac{2}{3} \frac{1}{m_p(m_p^2 - M_r^2)} \sqrt{\frac{1+\tau}{1+2\tau}} T_2(0) \left(T_1(Q^2) - Q^2 \frac{T_2(Q^2)}{(m_p + M_r)^2} \right) \quad (99)$$

where $\tau = \frac{Q^2}{4m_p^2}$.

This polarizability vanishes as Q^2 goes to zero. Note also that Q^2 must be evaluated at the $q' \rightarrow 0$ point.

$P^{(11,11)1}$ polarizability

The definition of the corresponding multipole is:

$$H_{NB}^{(11,11)1} = \frac{1}{8\pi\sqrt{p_0 p'_0}} \frac{1}{3} \sum_{\sigma, \sigma', M, M'} (-1)^{\frac{1}{2} + \sigma' + 1 + M} \left\langle \begin{array}{cc|c} \frac{1}{2} & \frac{1}{2} & 1 \\ -\sigma' & \sigma & s \end{array} \right\rangle \left\langle \begin{array}{cc|c} 1 & 1 & 1 \\ M' & -M & s \end{array} \right\rangle \int d\hat{q}' d\hat{q} V_\mu^*(1, 1, M'; \hat{q}') H_{NB}^{\mu\nu} V_\nu(1, 1, M; \hat{q}) \quad (100)$$

and the final answer in this polarizability case is:

$$P^{(11,11)1}(Q^2) = -\frac{2}{3} \frac{1}{\sqrt{1+\tau}\sqrt{1+2\tau}} \times \frac{T_2(0)}{(m_p + M_r)^2 (M_r - m_p)} \left(\frac{M_r - m_p}{m_p} T_1(Q^2) - 2\tau (T_1(Q^2) + T_2(Q^2)) \right) \quad (101)$$

where $\tau = \frac{Q^2}{4m_p^2}$. This polarizability vanishes also as Q^2 goes to zero.

$P^{(01,01)0}$ polarizability

The multipole reads now:

$$H_{NB}^{(01,01)0} = \frac{1}{8\pi\sqrt{p_0 p'_0}} \sum_{\sigma, M} (-1)^{\frac{1}{2} + \sigma + 1 + M} \left\langle \begin{array}{cc|c} \frac{1}{2} & \frac{1}{2} & 0 \\ -\sigma & \sigma & 0 \end{array} \right\rangle \left\langle \begin{array}{cc|c} 1 & 1 & 0 \\ M & -M & 0 \end{array} \right\rangle \int d\hat{q}' d\hat{q} V_0^*(0, 1, M; \hat{q}') H_{NB}^{00} V_0(0, 1, M; \hat{q}) \quad (102)$$

since only $V_0(0, L, M; \hat{k}) \neq 0$ and the polarizability is:

$$P^{(01,01)0}(Q^2) = 2\sqrt{\frac{2}{3}} \sqrt{\frac{1+\tau}{1+2\tau}} \frac{T_2(0)T_2(Q^2)}{(m_p + M_r)^3} \quad (103)$$

where $\tau = \frac{Q^2}{4m_p^2}$. Note that this polarizability does not vanishes as Q^2 goes to zero.

$\mathbf{P}^{(11,11)0}$ polarizability

The definition of the multipole corresponding to this polarizability is:

$$H_{NB}^{(11,11)0} = \frac{1}{8\pi\sqrt{p_0 p'_0}} \sum_{\sigma, M} (-1)^{\frac{1}{2} + \sigma + l + M} \left\langle \begin{array}{cc|c} \frac{1}{2} & \frac{1}{2} & 0 \\ -\sigma & \sigma & 0 \end{array} \right\rangle \left\langle \begin{array}{cc|c} 1 & 1 & 0 \\ M & -M & 0 \end{array} \right\rangle \int d\hat{q}' d\hat{q} V_\mu^*(1, 1, M; \hat{q}') H_{NB}^{\mu\nu} V_\nu(1, 1, M; \hat{q}) \quad (104)$$

and the polarizability is:

$$P^{(11,11)0}(Q^2) = 2\sqrt{\frac{8}{3}} \sqrt{\frac{1+\tau}{1+2\tau}} \frac{T_2(0)}{(m_p + M_r)(m_p^2 - M_r^2)} (T_1(Q^2) + T_2(Q^2)) . \quad (105)$$

3.6 Dispersion relation formalism

In the previous sections, I have introduced the generalized polarizabilities of the proton and focused on their extraction when the energy of the outgoing photon is low. Unfortunately, VCS cross-sections are not very sensitive to the GPs at low energy. So it is better to go to higher photon energies. The purpose of this section is to describe a formalism, called dispersion relation (DR) formalism, that allows to extract GPs from data over a large energy range and with a minimum model dependence.

Let me remind that it is the same situation as in RCS (section 2.2) for which one uses a DR formalism to extract the polarizabilities at energies above pion threshold, with generally larger effects on the observables. Thus I will follow the same steps as for the description of the RCS dispersion relation formalism. I will make as many comparisons as possible with RCS, and often establish useful relations between RCS and VCS. Finally, I will discuss the extraction of the GPs from the data.

VCS amplitudes

For fixed (q, q', θ) , the VCS tensor can be parameterized in terms of twelve

independent amplitudes F_i [2] as:

$$H^{\mu\nu} = \sum_{i=1}^{12} F_i(Q^2, \nu, t) \rho_i^{\mu\nu} \quad (106)$$

where $\rho_i^{\mu\nu}$ are twelve independent gauge invariant kinematic tensors. The $F_i(Q^2, \nu, t)$ contain all the nucleon structure information and they are free of kinematical singularities and constraints, provided a good tensor basis is found. The amplitudes F_i are functions of ν and t as for the amplitudes A_i from RCS, plus the variable Q^2 that describe the virtuality of the incoming photon. They can be found in [31].

Nucleon crossing combined with charge conjugation provides the following constraints on the F_i :

$$F_i(Q^2, \nu, t) = F_i(Q^2, -\nu, t) \text{ for all } i \quad (107)$$

For $Q^2 = 0$ (RCS), we find $A_i(\nu, t) = A_i(-\nu, t)$, and the relations between the F_i at $Q^2 = 0$ and the A_i are given in [31].

Dispersion relations

Assuming analyticity and an appropriate high energy behavior, the amplitudes $F_i(Q^2, \nu, t)$ fulfill unsubtracted dispersion relations:

$$\text{Re}F_i(Q^2, \nu, t) = \frac{2}{\pi} \mathcal{P} \int_{\nu_{thr}}^{+\infty} \frac{\nu' \text{Im}F_i(Q^2, \nu', t)}{\nu'^2 - \nu^2} d\nu' \quad (108)$$

with the same notations as for Eq. 39.

The existence of Eq. 108, requires that the amplitudes $\text{Im}F_i$ drop fast enough at high energies ($\nu \rightarrow \infty$, t and Q^2 finite) so that the integral is convergent and the contribution at infinity from the semi-circle can be neglected.

In the Regge limit ($\nu \rightarrow \infty$, t and Q^2 finite), one can show [31] that for F_1 and F_5 , unsubtracted dispersion integrals do not exist, whereas the other ten amplitudes can be evaluated through unsubtracted dispersion integrals. This situation is similar to RCS where two of the six invariant amplitudes can not be evaluated by unsubtracted DR (section 2.2).

Evaluation of the amplitudes F_i

We have seen in the previous paragraph that the amplitudes F_i , with the index i not equal to 1 or 5, can be evaluated through unsubtracted Dispersion Relations (Eq. 108).

For the F_1 and F_5 invariant amplitudes for which one cannot write unsubtracted DRs, we proceed as in the case of RCS, that is to say perform the unsubtracted dispersion integrals along the real ν axis in the range $-\nu_{max} \leq \nu \leq \nu_{max}$, and close the contour by a semi-circle with radius ν_{max} (Fig. 5), with the result:

$$ReF_i^{NB}(Q^2, \nu, t) = \frac{2}{\pi} \int_{\nu_{thr}}^{\nu_{max}} \frac{\nu' ImF_i(Q^2, \nu', t)}{\nu'^2 - \nu^2} d\nu' + F_i^{as}(Q^2, \nu, t), i = 1, 5 \quad (109)$$

with $F_i^{as}(Q^2, \nu, t)$ the contribution of the semi-circle of radius ν_{max} . Then this latter term is parameterized by t -channel poles (for example, for $Q^2 = 0$, F_1^{as} corresponds to a σ exchange, and F_5^{as} corresponds to a π^0 exchange (cf. [31])).

Extraction of the GPs

We have seen in the previous sections that the Non-Born VCS tensor $H_{NB}^{\mu\nu}$ at low energy can be parameterized by six GPs, namely $P^{(01,01)0}(q)$, $P^{(11,11)0}(q)$, $P^{(01,01)1}(q)$, $P^{(11,11)1}(q)$, $P^{(11,02)1}(q)$ and $P^{(01,12)1}(q)$.

In the limit $q \rightarrow 0$ for the GPs, we have the following relations with the polarizabilities of RCS:

$$P^{(01,01)0}(0) = -\frac{4\pi}{e^2} \sqrt{\frac{2}{3}} \alpha_E \quad (110)$$

$$P^{(11,11)0}(0) = -\frac{4\pi}{e^2} \sqrt{\frac{8}{3}} \beta_M \quad (111)$$

$$P^{(01,12)1}(0) = -\frac{4\pi}{e^2} \frac{\sqrt{2}}{3} \gamma_{M2} \quad (112)$$

$$P^{(11,02)1}(0) = -\frac{4\pi}{e^2} \frac{2\sqrt{2}}{3\sqrt{3}} \gamma_{E2} \quad (113)$$

$$P^{(01,01)1}(0) = 0 \quad (114)$$

$$P^{(11,11)1}(0) = 0. \quad (115)$$

Since the limit $q' \rightarrow 0$ at finite q corresponds to $\nu \rightarrow 0$ and $t \rightarrow -Q^2$ at finite Q^2 , we will now use the amplitudes $\tilde{F}_i(Q^2)$ defined as:

$$\bar{F}_i(Q^2) \equiv F_i^{NB}(Q^2, \nu = 0, t = -Q^2) . \quad (116)$$

Then, the \bar{F}_i (for $i \neq 1, 5$) are evaluated through the unsubtracted DRs:

$$\bar{F}_i(Q^2) = \frac{2}{\pi} \int_{\nu_{thr}}^{+\infty} d\nu' \frac{Im F_i(Q^2, \nu', t = -Q^2)}{\nu'} . \quad (117)$$

Among the six GPs named above, we have four combinations for which unsubtracted DRs do exist:

$$P^{(01,01)0} + \frac{1}{2} P^{(11,11)0} = \frac{-2}{\sqrt{3}} \left(\frac{E+M}{E} \right)^{\frac{1}{2}} M \tilde{q}_0 \{ \frac{q^2}{\tilde{q}_0} \bar{F}_2 + (2\bar{F}_6 + \bar{F}_9) - \bar{F}_{12} \} \quad (118)$$

$$P^{(01,01)1} = \frac{1}{3\sqrt{2}} \left(\frac{E+M}{E} \right)^{\frac{1}{2}} \tilde{q}_0 \{ (\bar{F}_5 + \bar{F}_7 + 4\bar{F}_{11}) + 4M\bar{F}_{12} \} \quad (119)$$

$$P^{(01,12)1} - \frac{1}{\sqrt{2}\tilde{q}_0} P^{(11,11)1} = \frac{1}{3} \left(\frac{E+M}{E} \right)^{\frac{1}{2}} \frac{M \tilde{q}_0}{q^2} \{ (\bar{F}_5 + \bar{F}_7 + 4\bar{F}_{11}) + 4M(2\bar{F}_6 + \bar{F}_9) \} \quad (120)$$

$$P^{(01,12)1} + \frac{\sqrt{3}}{2} P^{(11,02)1} = \frac{1}{6} \left(\frac{E+M}{E} \right)^{\frac{1}{2}} \frac{\tilde{q}_0}{q^2} \{ \tilde{q}_0(\bar{F}_5 + \bar{F}_7 + 4\bar{F}_{11}) + 8M^2(2\bar{F}_6 + \bar{F}_9) \} \quad (121)$$

where $E = \sqrt{q^2 + M^2}$ denotes the initial proton center of mass energy, and $\tilde{q}_0 = M - E$ the virtual photon center-of-mass energy in the limit $q' = 0$.

Finally, these four combinations are evaluated in a framework of unsubtracted DRs using the integrals Eq. 117 for the corresponding $\bar{F}_i(Q^2)$. In practice, the dispersion integrals of Eq. 117 are evaluated by B. Pasquini *et al.* [31] using the MAID parameterization of the $\gamma^*p \rightarrow \pi N$ amplitude.

The asymptotic contribution to the amplitude F_5 along a semi-circle of finite radius in the complex plane is modeled by the approximatively ν -independent t -channel π^0 -exchange graph.

The asymptotic contribution to F_1 is obtained by the ansatz of an effective

t -channel σ exchange. The coupling to this effective exchange is a free (Q^2 dependent) parameter, related to $\beta(Q^2)$:

$$F_1^{NB}(Q^2, \nu, t) \simeq F_1^{\pi N}(Q^2, \nu, t) + \frac{1 + Q^2/m_\sigma^2}{1 - t/m_\sigma^2} \frac{4\pi}{e^2} \sqrt{\frac{2E}{E+M}} (\beta(Q^2) - \beta^{\pi N}(Q^2)). \quad (122)$$

In Eq. 122, $F_1^{\pi N}$ and $\beta^{\pi N}$ are the contributions from the dispersion integrals over the MAID photo-production amplitudes.

The dispersion integral for F_2 converges in principle. In practice, this term is expected to have a large contribution from $N\pi\pi$ intermediate states, not included in the MAID parameterization. For ν below 2π threshold, F_2 is described by the contribution from the πN dispersion relations, plus an energy independent constant evaluated at the $\nu = 0$ and $t = -Q^2$ point:

$$\begin{aligned} F_2^{NB}(Q^2, \nu, t) &\simeq F_2^{\pi N}(Q^2, \nu, t) + (\bar{F}_2(Q^2) - \bar{F}_2^{\pi N}(Q^2)) \\ &= F_2^{\pi N}(Q^2, \nu, t) + \frac{4\pi}{e^2} \sqrt{\frac{2E}{E+M}} \frac{\tilde{q}_0}{q^2} \frac{1}{M} \\ &\quad \left[(\alpha(Q^2) - \alpha^{\pi N}(Q^2)) + (\beta(Q^2) - \beta^{\pi N}(Q^2)) \right] \end{aligned} \quad (123)$$

$$(124)$$

The preceding formalism completely determines all polarizabilities, up to the specification of two Q^2 dependent functions: $\alpha(Q^2) - \alpha^{\pi N}(Q^2)$ and $\beta(Q^2) - \beta^{\pi N}(Q^2)$. For definiteness, these are parameterized with dipole form factors:

$$\alpha(Q^2) - \alpha^{\pi N}(Q^2) = \frac{\alpha(0) - \alpha^{\pi N}(0)}{(1 + Q^2/\Lambda_\alpha^2)^2} \quad (125)$$

$$\beta(Q^2) - \beta^{\pi N}(Q^2) = \frac{\beta(0) - \beta^{\pi N}(0)}{(1 + Q^2/\Lambda_\beta^2)^2}. \quad (126)$$

Results for $ep \rightarrow ep\gamma$ observables

A full study of VCS observables within a DR formalism requires all twelve amplitudes F_i that have been described in previous paragraphs. Then, the differential cross-section for $ep \rightarrow ep\gamma$ can be evaluated by taking account of the full dependence of the $ep \rightarrow ep\gamma$ observables on the energy q' .

Fig. 7 examines the differential cross-sections of the $ep \rightarrow ep\gamma$ reaction along with the calculable BH+Born contribution on the left side of the figure as a

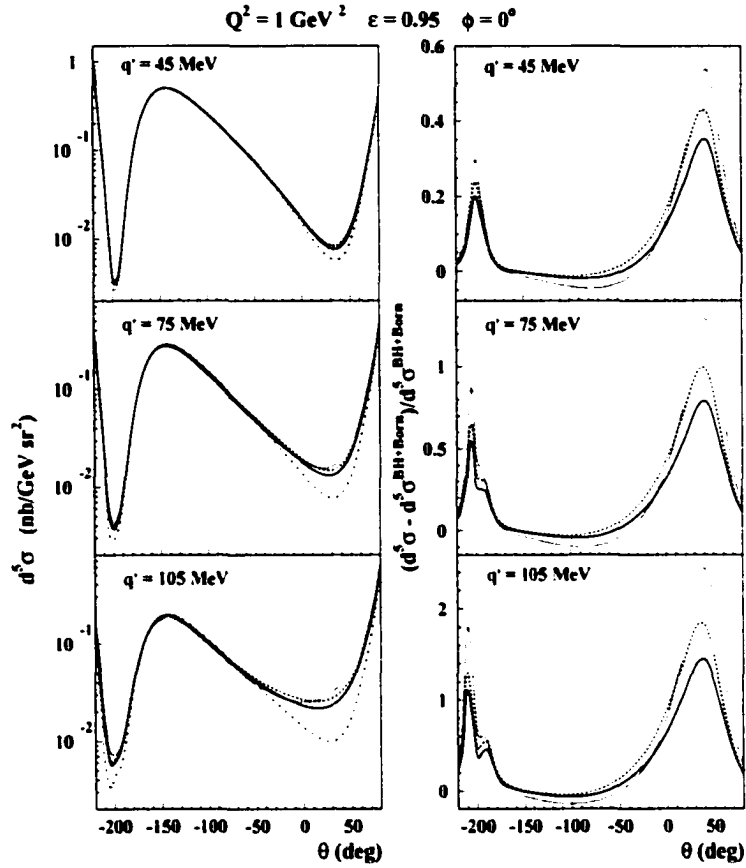


FIG. 7: Dispersion relation formalism predictions at $Q^2 = 1 \text{ GeV}^2$ (from [31]). Left three plots: the differential cross-section for the reaction $ep \rightarrow ep\gamma$ is plotted as a function of the photon scattering angle and at different values of the outgoing photon energy q' . Right three plots: ratio of cross-sections $(d\sigma - d\sigma^{BH+Born})/d\sigma^{BH+Born}$. The dashed-dotted curves on the left plots represent the BH+Born contribution. The DR results are displayed (on both left and right plots) with the asymptotic terms parameterized using the following values: $\Lambda_\alpha = 1 \text{ GeV}$ and $\Lambda_\beta = 0.6 \text{ GeV}$ for the full curves, $\Lambda_\alpha = 1 \text{ GeV}$ and $\Lambda_\beta = 0.4 \text{ GeV}$ for the dashed curves and $\Lambda_\alpha = 1.4 \text{ GeV}$ and $\Lambda_\beta = 0.6 \text{ GeV}$ for the dotted curves. Note that the DR formalism predicts significant deviations from the BH+Born cross-section (due to polarizability effects) for the presented kinematics in the two valley regions.

function of the photon scattering angle and for three values of the outgoing photon energy ($q' = 45, 75$ and 105 MeV). Note the logarithmic scale of these plots. The right plots present the relative ration of the two cross-sections. Any effect of the polarizabilities induces a deviation from the BH+Born cross-section. Such deviations are visible. The deviation is also growing with q' , an already expected result from the low energy expansion. Fig. 7 can also be compared to Fig. 89 of chapter 11 where a differential cross-section of the $ep \rightarrow ep\gamma$ reaction is also plotted after extraction of the polarizabilities with the low energy expansion method. In this latter plot, the Dispersion Relation results show a noticeable deviation from the low energy expansion results.

Fig. 8 presents results for the unpolarized structure functions $P_{LL} - P_{TT}/\epsilon$ (upper plots) and P_{LT} (lower plots) in the Dispersion Relation formalism as a function of Q^2 . The left plots present separately the dispersive πN contribution of the GP α (or β), the dispersive πN contribution of the spin-flip GPs and the asymptotic contribution of α (or β). The formulas for the three structure functions can be found in section 3.4 (Eq. 88, 89 and 90). The right plots present the sum of the previous contributions for several values of the parameters Λ_α and Λ_β . The RCS (from [23]) and MAMI (from [4]) data points are also displayed.

In this formalism, the spin-flip GPs contributions are always small in absolute but not in relative when Q^2 increases.

It is obvious from the bottom left plot that the structure function P_{LT} results from a large dispersive πN contribution and a large asymptotic contribution (both to β), with opposite sign, the former being paramagnetic while the latter is diamagnetic, leading to a relatively small net result. This net result is slightly dominated by the paramagnetic contribution that seems to fall off less rapidly in Q^2 and therefore more rapidly in space coordinates. This paramagnetic contribution could be related to the quarks while the diamagnetic contribution, extending further in space, could be related to the pion cloud.

In the upper left plot, one can see that, at $Q^2 \simeq 0$, all contributions have the same sign and therefore add, in contrast with the magnetic polarizability β . The asymptotic contribution to α clearly dominates over a large range in Q^2 .

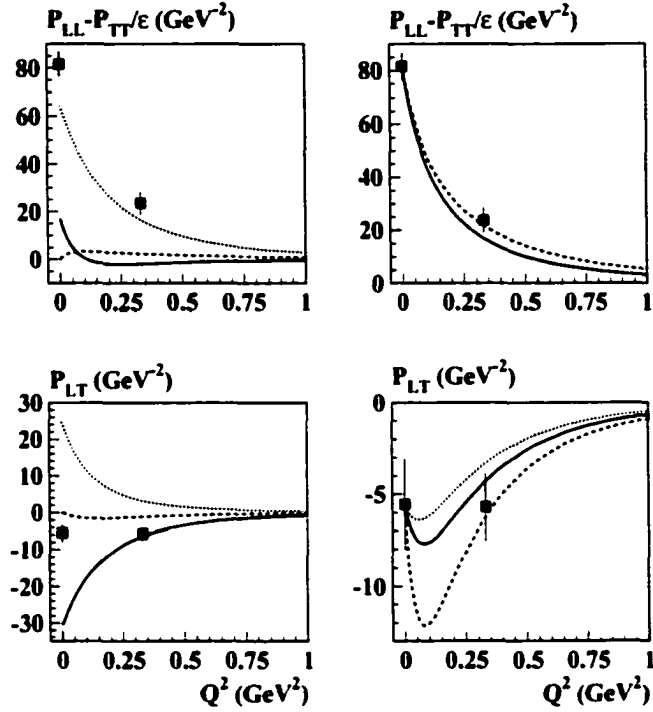


FIG. 8: Results for the unpolarized structure functions $P_{LL} - P_{TT}/\epsilon$ and P_{LT} for $\epsilon = 0.62$ in the Dispersion Relation formalism (from [31]). The RCS (from [23]) and MAMI (from [4]) data points are also displayed.

Upper left plot: dispersive πN contribution of the GP α (solid curve), dispersive πN contribution of the spin-flip GPs (dashed curve), and asymptotic contribution of α with $\Lambda_\alpha = 1$ GeV (dotted curve).

Upper right plot: sum of the previous contributions to $P_{LL} - P_{TT}/\epsilon$ when using $\Lambda_\alpha = 1$ GeV (solid curve) and $\Lambda_\alpha = 1.4$ GeV (dashed curve).

Lower left plot: dispersive πN contribution of the GP β (solid curve), dispersive πN contribution of the spin-flip GPs (dashed curve), and asymptotic contribution of β with $\Lambda_\beta = 0.6$ GeV (dotted curve).

Lower right plot: sum of the previous contributions to P_{LT} when using $\Lambda_\beta = 0.6$ GeV (solid curve), $\Lambda_\beta = 0.4$ GeV (dashed curve) and $\Lambda_\beta = 0.7$ GeV (dotted curve).

Chapter 4

VCS experiment at JLab

4.1 Overview

The E93-050 experiment proposed to investigate the field of Virtual Compton Scattering (VCS) at Jefferson Lab using the CEBAF accelerator and the Hall A High Resolution Spectrometers [1]. We will see indeed, in the next section, that this combination is necessary to observe VCS.

One of the main physics objectives of the experiment was to measure the VCS cross-section below pion threshold at $Q^2 = 1.0 \text{ GeV}^2$ ([32] and present work) and $Q^2 = 1.9 \text{ GeV}^2$ ([33]), in order to extract the generalized polarizabilities. The second goal was to investigate nucleon resonances by studying the $ep \rightarrow ep\gamma$ reaction in the resonance region at $Q^2 = 1.0 \text{ GeV}^2$ ([34], [35]).

For about a month spread between March and April 1998, data were collected in Hall A. The time allotted had to be shared between production data and calibration data. Indeed, as part of a commissioning experiment, a substantial fraction of the time had to be dedicated to data taking intended to calibrate the spectrometers. This calibration was especially requested for the Electron arm since it was used at high momenta and never been calibrated in that region by the few previous experiments. Consequently an effort had to be sustained to calibrate the spectrometers and better understand other parts of the equipment.

4.2 Experimental requirements

Because of the emitted photon, the VCS cross-section is suppressed by a factor $\alpha \simeq 1/137$ with respect to the elastic scattering case. A very high luminosity is then required to allow the smaller VCS cross-section to be measurable within a reasonable time frame. A luminosity of a few $10^{38} \text{ cm}^{-2} \cdot \text{s}^{-1}$ available at CEBAF was used during the E93050 experiment.

Moreover, we wanted to study VCS at high invariant four-momentum transfer squared values such as $Q^2 = 1.0$ and 1.9 GeV^2 . For that purpose, we used the highest available beam energy at the moment, which was 4 GeV.

Finally, the measurement of such an exclusive reaction required the detection of the electron and the proton in coincidence in the Hall A High Resolution Spectrometer pair. This high resolution detection, as well as the intrinsic high energy resolution of the beam, allowed the reconstruction of the so far missing photon and the selection of the $ep \rightarrow ep\gamma$ events by a missing mass technique as explained in section 4.4. The 100% duty cycle of the machine was also useful to lower the accidental to true coincidence fraction.

4.3 Experimental set-up

We realized $ep \rightarrow ep\gamma$ reactions by having the CEBAF electron beam (up to 100 μA) interact with a 15 cm liquid Hydrogen target. The scattered electron and the recoil proton were detected in coincidence in the two Hall A High Resolution Spectrometers as schematically represented in Fig. 9. Further details on these spectrometers as well as other parts of the experimental set up can be found in chapter 6 while chapter 5 presents first the CEBAF machine.

These spectrometers can move independently around the target in the horizontal plane in the experimental hall to take measurements at different angles. Nevertheless, for the data set at $Q^2 = 1.0 \text{ GeV}^2$ intended to extract polarizabilities, that will be the focus of this thesis, the Electron arm was kept at a fixed setting: central angle and momentum were $\theta_E = 15.42^\circ$ and $p_E = 3.433 \text{ GeV}$. The

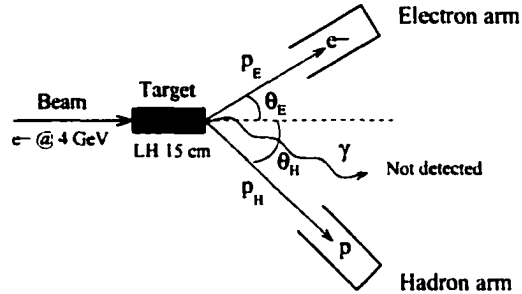


FIG. 9: Schematic representation of the experimental set up. The beam electrons scatter off the Hydrogen target. The scattered electrons are detected in the Electron arm. The recoil protons are detected in the Hadron arm. The emitted photon is actually not detected but its energy and momentum are reconstructed as being those of a missing particle and its photon nature determined by a missing mass technique.

Hadron arm swept through a series of angles and momenta as collected in Table I.

These settings were chosen to cover the majority of the $q' \times p'$ phase space below pion threshold. The proton kinematics are represented in Fig. 10 by rectangles which indicate the nominal acceptance.

4.4 Experimental method

As previously stated, only the scattered electron and proton are detected in coincidence. VCS events are then isolated without photon detection by using a missing mass technique.

This technique consists in calculating the mass of the undetected particle X (missing particle) in the $ep \rightarrow epX$ reaction, or more accurately, the mass squared. This last quantity is a relativistic invariant and is therefore frame independent. This missing mass squared M_X^2 reads:

$$M_X^2 = E_X^2 - \vec{p}_X^2 \quad (127)$$

where E_X and \vec{p}_X are the energy and momentum of the missing particle. These

TABLE I: Electron and hadron spectrometers central values for VCS data acquisition below pion threshold at $Q^2 = 1.0 \text{ GeV}^2$. Each setting is denoted da.1.X with X between 1 and 17.

Names	Electron spectrometer		Hadron spectrometer	
	p_E (GeV)	θ_E ($^\circ$)	p_H (GeV)	θ_H ($^\circ$)
da.1.1	3.433	15.42	0.935	-53.0
da.1.2	3.433	15.42	0.935	-50.0
da.1.3	3.433	15.42	0.935	-47.0
da.1.4	3.433	15.42	0.980	-53.0
da.1.5	3.433	15.42	0.980	-50.5
da.1.6	3.433	15.42	0.980	-48.0
da.1.7	3.433	15.42	0.980	-45.0
da.1.8	3.433	15.42	1.040	-52.0
da.1.9	3.433	15.42	1.040	-49.5
da.1.10	3.433	15.42	1.040	-47.0
da.1.11	3.433	15.42	1.040	-44.5
da.1.12	3.433	15.42	1.110	-50.5
da.1.13	3.433	15.42	1.110	-47.5
da.1.14	3.433	15.42	1.110	-44.5
da.1.15	3.433	15.42	1.190	-50.0
da.1.16	3.433	15.42	1.190	-48.5
da.1.17	3.433	15.42	1.190	-46.5

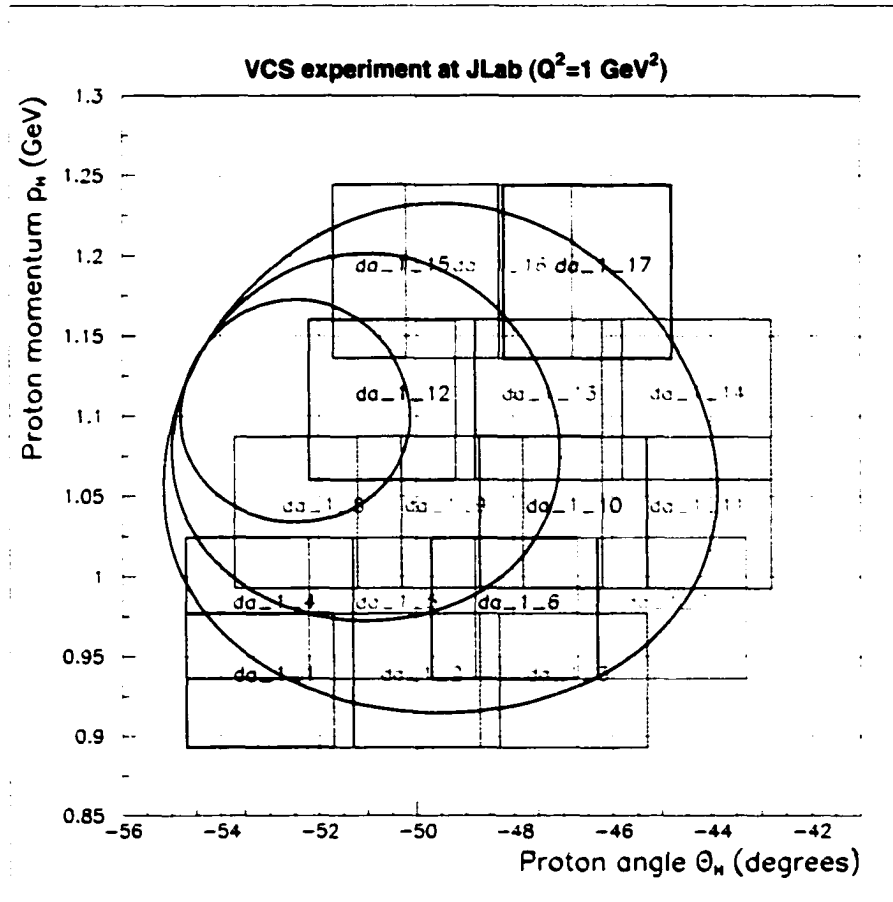


FIG. 10: Hadron spectrometer kinematic settings for VCS data acquisition below pion threshold at $Q^2 = 1.0 \text{ GeV}^2$. The curves approximately circular are contours of constant outgoing real photon energy in the VCS center of mass frame q'_{cm} at fixed $Q^2 = 1.0 \text{ GeV}^2$. From the inner curve to the outer curve, the values for q'_{cm} are: 45, 75 and 105 MeV. The boxes are the approximate Hadron arm acceptance for each setting.

latter quantities are obtained by energy and momentum conservation laws:

$$E_X = (E_e + E_p) - (E'_e + E'_p) \quad (128)$$

$$\vec{p}_X = (\vec{k} + \vec{p}) - (\vec{k}' + \vec{p}') . \quad (129)$$

The meaning of the notations is as follows: the incoming electron has energy E_e and momentum \vec{k} and the target proton has energy E_p and momentum \vec{p} while the prime is used for quantities after interaction.

The detection is performed in the Lab frame. The scattering angle and momentum magnitude are measured for both the scattered electron and recoil proton in the two spectrometers. All primed quantities are therefore known through measurement. In the Lab frame, the target proton is considered at rest implying $\vec{p} = \vec{0}$ and $E_p = m_p$. Finally, the beam energy and beam direction are also known quantities. Adding a correction on the incoming electron and detected particles for energy loss due to particle travel through experimental equipment, nothing prevents from reconstructing the missing particle and its missing mass squared.

VCS events are identified by $M_X^2 = 0 \text{ GeV}^2$ corresponding to the emitted photon mass. The next channel corresponds to the creation of a π^0 in the reaction $ep \rightarrow ep\pi^0$. This particle is the lightest meson. It has a mass of about 135 MeV. It is important to note that the $ep \rightarrow ep\pi^0$ reaction, where the π^0 primarily decays into two photons, creates a physical background which may prevent the extraction of the VCS signal. However, the resolution of Hall A spectrometers is good enough to separate the $ep \rightarrow ep\gamma$ and the $ep \rightarrow ep\pi^0$ events by the missing mass technique described above. A sample of missing mass squared histogram can be found in section 9.1.

Chapter 5

the CEBAF machine at Jefferson Lab

5.1 Overview

Thomas Jefferson National Accelerator Facility (TJNAF), or Jefferson Lab (JLab), is a research laboratory built to probe the nucleus of the atom to learn more about the quark structure of matter. It shelters the CEBAF machine (Continuous Electron Beam Accelerator Facility) towards that goal.

The lab is managed by a consortium of fifty three universities called the Southeastern Universities Research Association or SURA under contract of the Department of Energy. The first physics experiments to study nuclear matter at intermediate energies started in 1994.

JLab represents a \$600 million investment of the Federal Government, the State of Virginia, the City of Newport News, foreign contributors and the US nuclear physics research community. JLab has an annual operating budget of approximately \$70 million.

CEBAF is a superconducting electron accelerator with recirculation arcs. It is composed of two LINear ACcelerators (LINAC) linked by nine recirculation arcs (see Fig. 11) allowing the electrons to loop through the LINAC pair up to five times. The electron energy after sustaining five times the acceleration from both

LINACs is 6 GeV at the present time of this document. After acceleration, the beam can be extracted from the accelerator and directed to one of the three experimental halls (A, B and C). But CEBAF does more: it simultaneously provides up to three electron beams, possibly with different energies and different beam current intensities, to the experimental halls.

In this chapter, I will discuss in more details the operating mode of CEBAF, by describing successively the injector then the beam acceleration and transport. I will explain how it is possible to obtain different energies and different beam current intensities simultaneously in the three halls, and how CEBAF delivers a continuous beam.

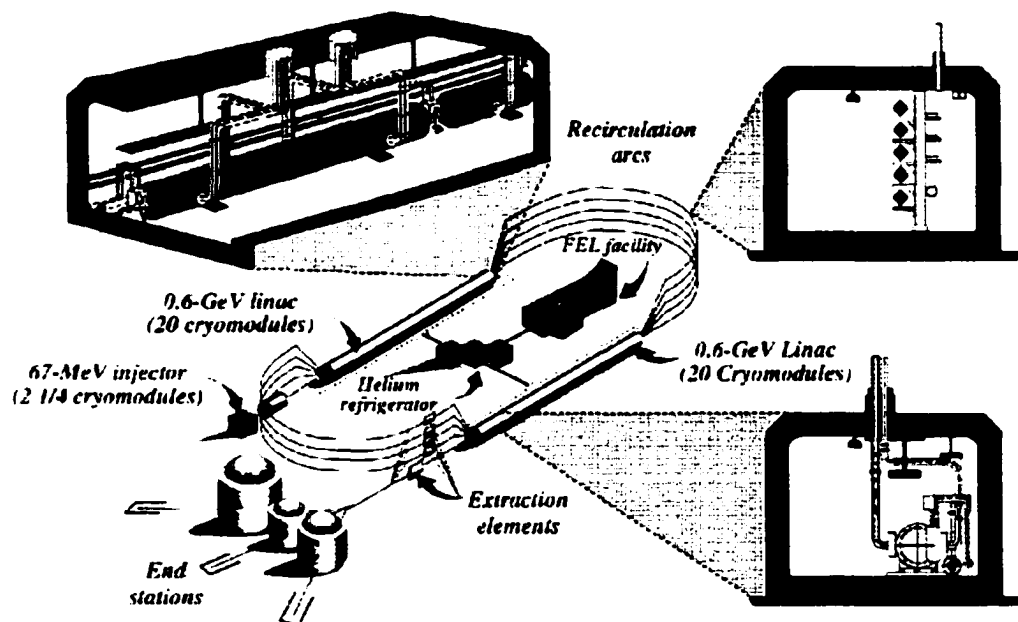


FIG. 11: Overview of the CEBAF accelerator. The electron beam is created in the injector. The beam is accelerated inside superconductive cavities in the LINAC sections. Recirculation arcs allow the beam to loop several time through the LINAC sections to increase further the energy. Finally, after up to five passes, the beam is extracted and sent to the experimental halls. This accelerator produces up to three electron beams delivered to three experimental halls. The machine has a 100% duty cycle and a reduced energy spread.

5.2 Injector

The electron beam's birth place is the injector. It is there that electrons are extracted and a first acceleration applied.

The injector can deliver both polarized and unpolarized beams. Two setups are yet necessary. Unpolarized beam is produced with a thermionic source (heated metal cathode). For polarized beam, by illuminating a semi-conductor source (GaAs) with a circularly polarized source of light adapted to the gap energy of GaAs, one can extract polarized electrons. At the time of our experiment, the thermionic gun delivered a continuous unpolarized beam.

The extracted electrons are accelerated to an energy of 100 keV by an electrostatic field. Then the continuous beam passes through a 499 MHz chopper. This chopper consists of two room temperature 499 MHz transverse chopping cavities, a set of four magnetic solenoid lenses, and three chopping apertures. The purpose of the chopper is to convert time (or phase) into position and then back into time (or phase). The beam is kicked transversely to pass through the chopping apertures in a circular pattern. At this point the beam is basically cut into three sets of electron bunches. It is there that the three beams intended for the three halls are being built. Moreover enlarging or reducing each chopping aperture enables the machine operators to set the beam intensity for each hall separately. Typically there are up to six orders of magnitude between the intensity delivered in Hall A and Hall C (100 μ A) and the intensity delivered in Hall B (100 pA). This wide dynamic range is unprecedented.

After this operation the three beams are recombined on the same trajectory. Two beam bunches to be delivered to the same hall are separated by 2 ns (1/499 MHz). But the frequency of bunches, and therefore of the accelerator as a whole, is three times higher ($3 \times 499 = 1497$ MHz) since three bunches of different intensities are created during one chopper period.

Finally the electrons are accelerated to 45 MeV (67 MeV in 2001) in a small LINAC section before being injected in the north LINAC, one of the two sections of the accelerator where the electrons are substantially accelerated.

5.3 Beam Transport

After their injection into the accelerator, the electrons travel in the first of the two 300 m LINACs. Their energy is increased by 600 MeV each time they circulate inside a LINAC. Such an acceleration is provided with 320 cavities in pure niobium frozen with liquid helium to 2 K. At this temperature, niobium is superconductive which minimizes calorific losses and allow an acceleration frequency of 1.497 GHz.

Electrons are directed from one LINAC to the other through a recirculation arc. There are in total nine recirculation arcs. Four are superposed at the west extremity and five at the east extremity (see Fig. 11). At the end of each LINAC, before the arc, the beam is split vertically (according to energy) by a magnet chicane. At the end of the arc, all beams (different energies) are recombined onto one trajectory before being reinjected in the opposite LINAC. A beam composed of electrons having once sustained acceleration by the two LINACs is qualified as a one pass beam. With each pass, the electrons follow a different arc. Electrons can circulate up to five times through the LINAC pair. The accelerator can then provide five different beam energies to the experimental halls.

At the end of the south LINAC, a radio-frequency separator allows to extract the electron beam. From a given bunch A, B or C from the sequence ABCABC... the electrons of a chosen energy (1 pass, 2 pass ... 5 pass energy) can be directed into one of the experimental halls.

The high frequency (electron bunches delivered in each hall are spaced by only 2 ns) and the use of superconducting technology makes the originality of CEBAF of delivering a continuous beam. Indeed this continuous wave (CW) feature is an advantage for data taking: for the same luminosity the peak current is much lower for a CW beam rather than for a pulsed beam. This allows a better density regulation when using a cryogenic target, but also a lower accidental rate (since proportional to I_{peak}^2) improving the signal over noise ratio. Finally note that the acceleration capabilities have been rapidly improved since our experiment (maximum beam energy of 4 GeV at that time) and that the whole accelerator is planned to be upgraded to 12 GeV in the forthcoming years.

Chapter 6

Hall A

The purpose of this chapter is to acquaint the reader with the basic equipment used in Hall A. I will nevertheless only mention the instrumentation used in the E93050 experiment setup and even further restrict the detector package description to detectors actually used in the analysis. Bear in mind that we want to scatter electrons off protons, detect the two outgoing particles and reconstruct the emitted photon as a missing particle.

I will successively describe what piece of equipment can be found along the beam line enclosing the electron beam up to the target, the cryogenic Hydrogen target itself where the studied reactions occur, the two spectrometers used to analyze the scattered electrons and recoil protons, and, at last, the detectors which will yield information on the detected particles. The acquisition trigger is then discussed followed by an overview of the data acquisition system.

6.1 Beam Related Instrumentation

This section deals with all the equipment that aims to a good monitoring of the beam from its trajectory to its energy to its intensity. Fig. 12 and Fig. 13 sketch the various devices. The latter is a continuation of the former. The unscattered electrons continue their course straight ahead until they reach a beam dump where they are stopped and collected.

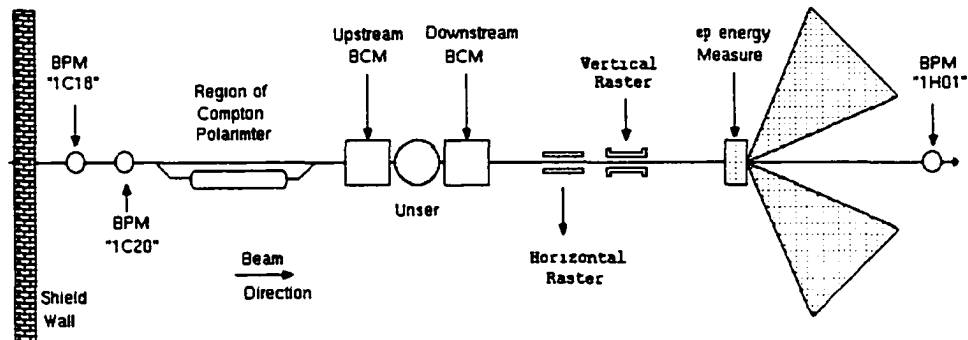


FIG. 12: The Hall A beamline elements from the shield wall to the e-p energy measurement system. The BCM and Unser monitors are beam current reading devices, downstream of which stand the two raster coils. (Elements not to scale.)

Let me succinctly mention the presence on the beam line of two polarimeters. Early on the beam line stands the Compton polarimeter which can monitor the beam polarization in real time. Further down is the Møller polarimeter which analyzes the beam in a destructive way. Of course those two instruments were not used during the VCS experiment since no polarized beam was requested. Nevertheless the quadrupoles of the Møller apparatus were used by the accelerator operators to focus the beam onto the target.

Beam positioning

The first real issue is the beam positioning on the target since the analysis of the experiment relies heavily on this knowledge: the vertical position of the reaction vertex is solely accessed by the vertical beam position while the horizontal beam position is used as a redundant measure for event selection purposes (*cf.* chapter 9).

The shield wall separates what one calls the Hall on the downstream side and the accelerator on the upstream side. There are five Beam Position Monitors (BPM) downstream of the shield wall and upstream of the target. As their name

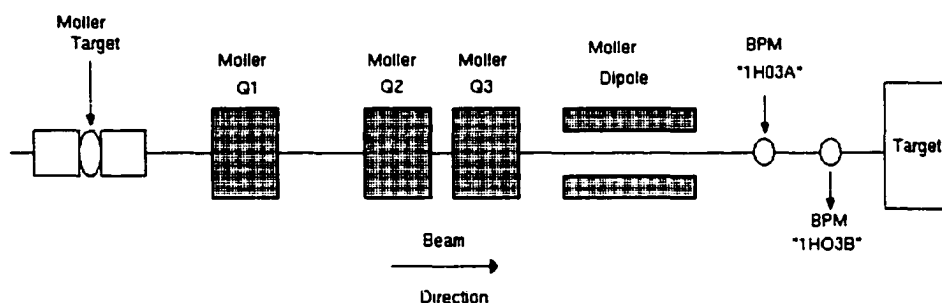


FIG. 13: Second part of the beamline elements schematic. The Møller target and magnets are represented on the left while the two BPMs used in the analysis for beam positioning come next. (The elements are not to scale.)

indicates, the use of these devices is dedicated to monitoring the beam orbit in the Hall A beam pipe. The measurement is non destructive and thus enables a continuous monitoring.

Each BPM is a cylindrical cavity with a four wire antenna array running parallel to its axis. Viewed in a cross-section perpendicular to the beam line direction (which is also supposed to be the cylindrical symmetry axis), the four wires are equally spaced around the center. As a resonant cavity, it is tuned so that the beam passing inside it excites the resonant modes. The asymmetry between the signals on two opposite wires is analyzed by the electronics and yields a position along the straight line joining those two wires. The intercept of the two straight lines from the two pairs of wire therefore locates the position of the centroid of the beam.

For data purposes, only the information from the last two BPMs, located 7.6 m and 1.4 m upstream from the target (Fig. 13), is recorded. The position of the beam at those two locations allows the determination of the trajectory of the beam as well. One can then extrapolate the impact of the beam on the target.

The need of beam rastering

The beam current intensity can reach values as large as $100 \mu\text{A}$ for unpolarized beam. The total beam power deposited in our liquid hydrogen target can then be up to 400 W. Even though the target was designed with several temperature regulation features, one has to expect that too much heat in too little area will induce local density changes. The density of scattering centers is a direct normalization factor for cross-sections. Controlling this factor is essential if one is to extract precise results. So, to prevent such local boiling, two sets of magnets are used to deflect the beam from its nominal position. They are located about 23 m from the target (see Fig. 12). The current in each of the coils was varied sinusoidally. The frequencies were chosen so as not to create special patterns on the target. The horizontal rastering frequency was set to 18.3 kHz and the vertical one to 24.6 kHz.

In addition to this density consideration, a security concern required moving the beam spot on the cryogenic target. A fixed beam spot could indeed drill a hole on the aluminum wall or at least weaken this end cap.

The raster device can also help us with beam positioning. The current from the coils can be read out. From there the kick imposed to the beam can be calculated and the position at the target be inferred knowing the average beam position.

Beam current monitoring and beam charge

Two Beam Current Monitors (BCM) are used in Hall A. They are placed 24.5 m upstream of the target (Fig. 12). A BCM is a resonant cavity, a cylindrical wave guide 15.48 cm in diameter and 15.24 cm in length (see Fig. 14). The resonant frequency is adjusted to the 1497 MHz frequency of the CEBAF beam by a stub tuner mounted on a micrometer that can be moved in and out of the cavity. The beam going through the BCM induces a magnetic field that is resonant in the cavity. This field induces a current in a coil (antenna) placed inside the cavity. This current is proportional to the induced field amplitude and therefore to the beam current. The BCMs provide a measure of the beam current with a good linearity over a wide range (0 to $120 \mu\text{A}$) with a negligible beam position

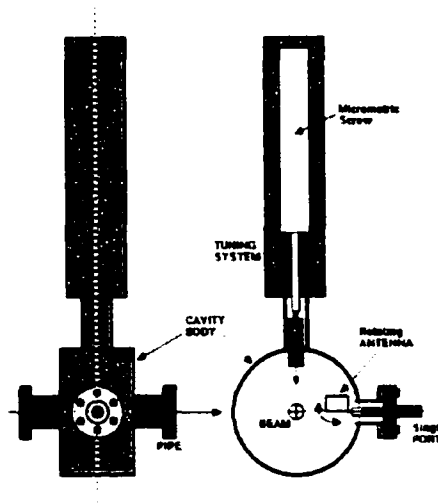


FIG. 14: BCM monitor. This device is a resonant cavity that picks up a signal proportional to the beam current. It is linear over a wide range of currents and is used for charge measurement. But this cavity is a relative measuring device and needs to be calibrated in absolute (against the Unser monitor).

dependence. These devices are used as the regular monitors of the beam current. But they are relative instruments (signal only proportional to beam current) and must be calibrated in absolute.

This calibration is made against the Unser monitor, a parametric current transformer (see Fig. 15). This type of monitor is able to provide accurate and high precision measurements of circulating beam currents over a dynamic range of 10^5 or greater. The method used for measurement is a zero flux method. Two primary toroidal cores with identical magnetic properties enclose the beam. Since the continuous beam current provides no time varying flux component to generate a signal by magnetic induction, a time varying flux component is added via the action of a magnetic modulator circuit: counter-phased windings around the cores powered by an external source drive the cores deep into saturation, alternating the polarities in time. In the absence of any continuous beam current, common-phased sense windings around each core read exact opposite signals leading to

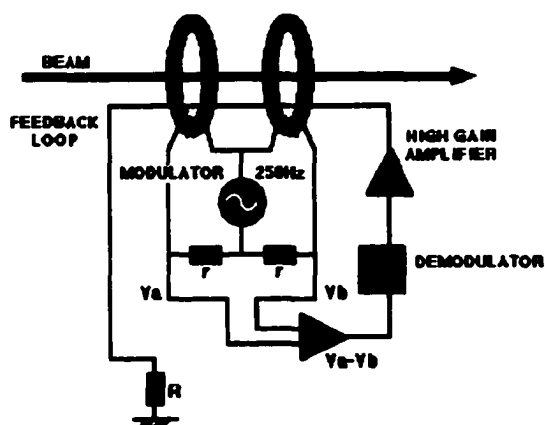


FIG. 15: Unser monitor. A feedback current compensates the effect of the beam in a zero flux method between two coils. Because of drift and noise, the device is not used for monitoring of the beam charge sent to the target. However the absolute magnitude of a change in current is reliable and is taken advantage of in the absolute calibration of the BCM monitors.

a zero net result. Now, when the beam flows through the cores, this balance is lost, each core reaching their saturation levels differently. The net result is a flux imbalance between the two cores. This discrepancy is then used in a feedback loop: a current is sent in the opposite direction of the beam to counter-balance the effect of the beam and restore the zero flux. A measure of this current through a voltage reading across a series of high precision resistors yields a measure of the beam current.

The calibration of the Unser monitor (with respect to changes in current) has been observed to remain very stable over a large period of time. However the Unser is susceptible to drift and noise in the measurement of current. This prevents its use as a charge monitor (current integral over time) in favor of the BCM monitor. An absolute change in current is nevertheless reliable and is used in the BCM absolute calibration procedure described in subsection 7.1.2.

Finally, all these current monitors are very sensitive to temperature and a careful thermal insulation and regulation is needed and provided.

6.2 Cryogenic Target and other Solid Targets

6.2.1 Scattering chamber

The scattering chamber is an Aluminum cylindrical vessel that shelters the targets. The bottom is fixed to the pivot of the hall. Several transparent windows can be used to visually inspect the inside.

The middle section of the chamber with an inner diameter of 104 cm and wall thickness of 5 cm is at beam level. The beam entrance and exit pipes are attached directly onto the chamber. The beam passing through the target therefore does not interact with the walls of the chamber.

Scattered particles exit the scattering chamber through exit windows. This is a special band of the chamber, 18 cm tall and only 0.4064 mm thick, that spans almost the totality of the scattering chamber's circumference so that particles can enter the spectrometers for a large range of positioning angles. Very forward scattering angles are not accessible because of the intrinsic size of the spectrometers. Backward angles are not accessible either because of other equipment stationed there (electronics racks, cryogenic target components other than the target cells which the beam interacts with, *etc.*). Otherwise only supports for the beam entry and exit pipes as well as a few other supports reduce a total visibility.

The chamber is also maintained under vacuum. This vacuum reduces multiple scattering on molecules that would otherwise be present in the chamber. But it also helps to keep the cryogenic target cold as a thermal insulator layer. The vacuum is carefully maintained at the 10^{-6} Torr level since an increase in that pressure is strongly correlated to a corresponding increase in target temperature.

6.2.2 Solid targets

On a target ladder are disposed, from top to bottom, the cryogenic targets, the dummy targets and finally the solid targets. Fig. 16 helps to visualize this array of targets.

The raster target with rectangular holes drilled in it was used for raster commissioning. The Carbon and Aluminum targets are 1.02 mm thick foil targets. They can be used for spectrometers studies when a thin target is preferred over an extended target. The Beryllium-oxide target is 0.5 mm thick and glows when the beam is incident on it. A video camera enables the viewers to visually check that beam is on target. The last solid target is called empty because it is essentially an Aluminum foil with a large circular hole and is used anytime no target should be on the beam path such as when the accelerator crew is adjusting the beam in the hall.

The dummy targets are simply composed of two flat plates of Aluminum separated by empty space. They simulate the end caps of the cryogenic targets. Three dummy targets are available. The spacing between the plates is respectively 10, 15 and 4 cm. They can be used to estimate the contribution of the cryogenic endcaps to the background. Data with beam incident on those targets were also taken during E93050 to calibrate the optics of the spectrometers for vertex reconstruction.

6.2.3 Cryogenic Target

Solid targets are perfect targets: they are easy to handle and compact. The density of molecules and therefore of nuclei is very high offering a high probability of interaction. That is fine when the intended target is for instance Carbon, Aluminum or Lead or even Oxygen (water target). But when the intended target is the proton itself, the situation gets more complicated. To be free of nucleus effects, a proton by itself is to be the target. That implies the use of the Hydrogen atom or molecule. Compound involving Hydrogen could be used but the analysis of the experiment would be much simpler if a pure Hydrogen target were available. Such a target exists in the form of the di-Hydrogen molecule, which is in gaseous phase in normal conditions of temperature and pressure.

The need for a liquid Hydrogen target arises when one wants to optimize the reaction rate of an experiment on Hydrogen. Indeed the density of scattering

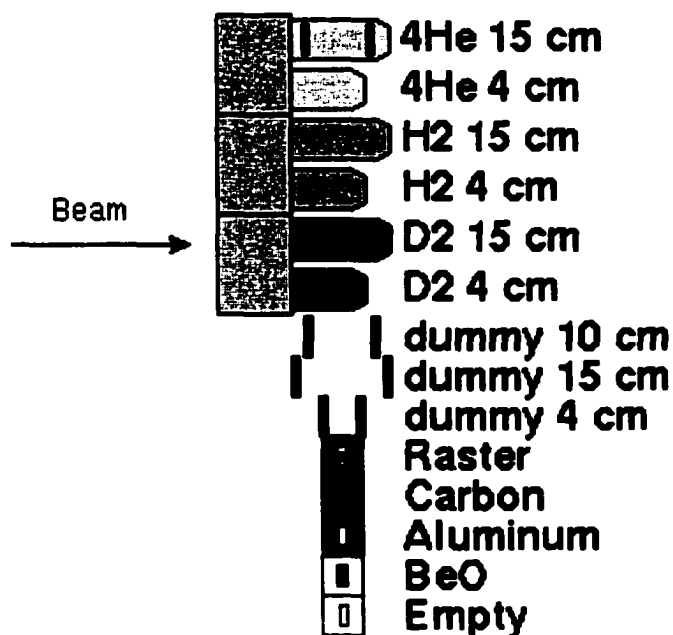


FIG. 16: Schematic of all available targets. Cryogenic targets (side view) are on top, then come the dummy targets (side view) and, at the bottom, the solid targets (front view).

centers is greatly increased when the target is in liquid phase. A factor of 1000 is to be expected. This reduces the required volume of the target by an enormous factor for a fixed reaction rate. Simply put, a compact Hydrogen target makes the experiment viable: a small target extension enables the use of spectrometers and a high density target reduces data taking duration thus reduces financial cost.

The target compactness is achieved by controlling the environmental conditions such as temperature. Extremely low temperatures, qualified as cryogenic, are yet necessary for the Hydrogen molecules to be in liquid phase.

The cryogenic portion of the Hall A target consists of three target loops, each of which has two target cells. These target cells are of lengths 15 cm and 4 cm (see Fig. 16). The second loop is primarily devoted to Hydrogen and was used

during the VCS experiment. The operating temperature and pressure were 19 K and 25 psia.

Despite the need of temperature regulation for operating and safety reasons, a good temperature control also allows a handle on the target density, a direct normalization factor of the experiment. Indeed, the target density is a proportional factor in the luminosity of the experimental setup (see section 8.5) and being able to evaluate this quantity for various operating conditions reduces the final uncertainty on the cross-sections. A study of target density dependence upon beam conditions (beam current intensity and beam rastering size) at fixed target operating condition is presented in section 8.4.

Target loop and target cryogen circulation

The main components of each target loop are the heat exchanger, the axial fan, the cell block, the heaters and the temperature thermometry. A diagram of one of the loops can be seen in Fig. 17.

The target loop at play during the VCS experiment is used in the following for further description. In operation mode, the loop is filled with liquid Hydrogen at 19 K. The axial fan makes the target cryogen flow from the heat exchanger to the cell block. This cryogen enters the lower cell, 4 cm long, exits back to the cell block only to enter the upper cell, 15 cm long. It flows then back to the heat exchanger. There, in the central part of the exchanger, it is pumped upwards by the fan. It is then diverted at the top to the outer part to flow back down around winding fin-tubing where heat exchange takes place. The use of the fin is for better heat exchange.

The target cells are thin cylinders made of Aluminum. They have a diameter of 6.48 cm and a sidewall thickness of 0.18 mm. The slightly rounded downstream endcap is monolithic with the sidewall. For the 15 cm cell of loop 2, this endcap was chemically etched to be 0.094 ± 0.005 mm thick. The other end of the target cell is soldered onto the cellblock. Inside each cell is a flow diverter that forces the cryogen into the beam path.

It is to be noted that each loop is an open system. Indeed at the heat exchanger

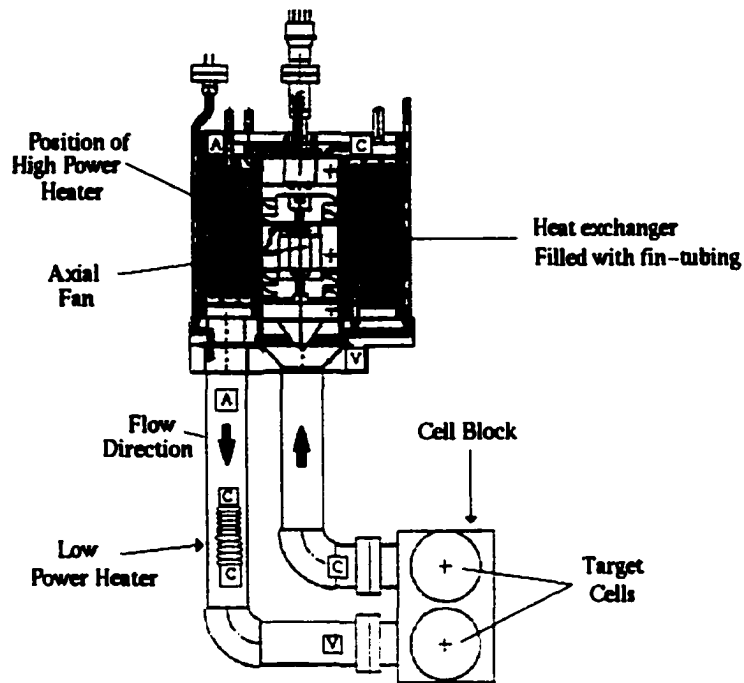


FIG. 17: Diagram of a target loop. The main components are shown. The letters in squares represent the three types of temperature sensors: (C)ernox, (A)llen-Bradley and (V)apor pressure bulbs.

level are attached the inlet and outlet pipes for Hydrogen. If the temperature were to increase, the gaseous Hydrogen could escape without the target blowing up, a large tank farther on the line stocking the gas for later re-use. Once the target loop is filled with liquid Hydrogen, no new amount of Hydrogen is let into the system though.

Cooling system and temperature regulation

For E93050 experiment, the VCS counting rate is tiny compared to elastic scattering. The rate is enhanced by a high beam current ($100 \mu\text{A}$) while the 100%

duty cycle of the CEBAF machine reduces the accidental coincidences level. The power thus deposited by the beam in the target can be evaluated in the following manner. It is the product of the electron flux times the energy loss by unit length for each electron (also called stopping power of Hydrogen) times the target length gone through:

$$P = \frac{I}{e} \times \frac{dE}{dx} \times \ell . \quad (130)$$

The electron flux, the number of electrons per second, is the ratio of beam current over the elementary charge. The energy loss of 4 GeV electrons can be considered constant over the whole target and at ionization minimum. It evaluates to 4 MeV·cm²/g (energy loss per unit length per unit density) for electrons in liquid Hydrogen [7]. The use of MeV units actually spares us the division by the elementary charge in the previous factor. The last factor is the target length: the 15 cm target was in use. One also has to multiply by the target density at the operating conditions since the energy loss was expressed per unit density. For this power estimation, the density is evaluated to 0.07 g/cm³. Thus we have:

$$P = \frac{100 \mu\text{A}}{e} \times 4 \text{ MeV} \cdot \text{cm}^2 \cdot \text{g}^{-1} \times .07 \text{ g} \cdot \text{cm}^{-3} \times 15 \text{ cm} \simeq 400 \text{ Watt} . \quad (131)$$

This energy transfer is soon converted into heat. This heat has to be extracted in order to maintain a constant temperature and thus a constant density. This task is fulfilled by the heat exchanger with a target cryogen set in motion by the fan.

Gaseous Helium coming from the on site Central Helium Liquefier plant (referred to as Helium refrigerator in Fig. 11) and entering the bottom of the heat exchanger at 15 K flows **inside** three layers of winding fin-tubing to the top (see Fig. 17) and serves as cold source in the heat exchange process. The target cryogen, on the other hand, flows in the other direction, downwards, and **outside** the fin-tubing.

The Helium return line goes to a second heat exchanger that serves the purpose of bringing down the Hydrogen temperature from 300 K (room temperature) to a temperature between 20 and 80 K during target cool down preparation, the loop heat exchanger being in charge, at that time, to liquify the Hydrogen.

The Helium flow rate is adjusted with beam off so as to maintain the Hydrogen temperature at 19 K as the last step in the cool down preparation period. The flow rate is then progressively increased again, still with beam off but now with target temperature regulation on. The computer process in charge of temperature regulation detects the decrease in Hydrogen temperature and turns on the high power heaters. They are Kapton encased wires embedded in the heat exchanger. Heat is released by the resistive Joule effect when current flows in the wires. The opening of the valves on the Helium inlet is stopped when the power released by the heater equals the power that the beam will deposit when turned on.

This prepares the target to receive beam. When the beam arrives, it deposits its energy. The regulation system detects an increase in temperature since the power balance between cooling power and heating power is not true anymore. Indeed the Helium cooling power is kept fixed and now two sources of heat are present in the target loop system: the high power heaters, which already compensated the cooling power, and the beam. The current intensity in the high power heater is then reduced by the computer in order to bring back the power balance.

This is also the mechanism for temperature regulation. A balance in cooling power from Helium flow rate and heating power from current flowing in the high power heaters is set. Anytime the beam is on, the high power heater is turned off automatically. Anytime the beam goes off, the high power heater is turned back on.

These two heaters are connected in parallel so that if one were to fail, there would be the other one left to operate before repair. Together they can provide more than 700 Watt of heat. One can then set the equilibrium setting such that, when the beam is on, the high power heaters are not completely off. A reasonable offset in residual heating power from the high power heaters is a good security margin, but unnecessary cooling power drain is to be avoided. This offset will also take care of fluctuations in cooling power.

A low power heater is also installed before the cell block to fine tune the temperature regulation. They provide up to 50 Watt and are used to compensate for small temperature variations.

Temperature sensors

The loop temperature is monitored by computer through the use of different types of sensors strategically located. As temperature is a critical factor in cryogenic equipment, an accurate monitoring is essential to ensure the system's integrity and proper functioning.

The first type of sensor is the Allen-Bradley resistor (from the manufacturer's name). They are semi-conductor resistors whose resistance varies with temperature. In our target, they are not used to precisely monitor the temperature, but instead give a redundant measurement and make sure the target is filled with liquid and not gas. There are two of them in a loop, one on top of the heat exchanger and one at the bottom, in the Hydrogen outlet to the target. For a visual check on the positions of these sensors, as well as the positions of the next sensors, please refer to Fig. 17.

The second type of sensor is called vapor pressure bulb. A bulb containing Hydrogen is partly immersed in the target Hydrogen. By heat transfer between the target Hydrogen and the bulb Hydrogen through the bulb wall, a thermodynamics equilibrium is established inside the bulb between the liquid and vapor phases. The pressure inside the bulb is then linked to the temperature of the Hydrogen by the vaporization curve. Knowing this curve, a reading of the pressure yields a measure of the temperature.

The last type of sensor is the Cernox resistor. They are commercial sensors, adapted to cryogenic temperatures. Their high resistance sensitivity to temperature is taken advantage of to carefully monitor the target temperature at various points. Each sensor is provided with its own calibration curve which is loaded in the readout device. This increases their dependability.

Security devices

There are several safety valves that are either automatic or operator controlled. They prevent excess pressure in the system mostly due to pressure fluctuations. If the pressure were to increase anomalously large and suddenly, a rupture disk would break and release the pressure. A large tank is also in the circuit to collect

the target material in its gaseous form in case of intentional or accidental warming up of the target.

Software

A dedicated computer runs a program that interfaces the operator with the hardware. The operator can visualize the temperature evolution in time, query some information about the operating conditions, remotely control some devices, *etc.* The program is also in charge of the automatic temperature regulation. This control system of the target was produced [36] entirely in the EPICS environment (Experimental Physics and Industrial Control System).

6.3 High Resolution Spectrometer Pair

Hall A is equipped with two arms labelled “Electron arm” and “Hadron arm” according to the type of particles the equipment mounted on them were first chosen to detect (Fig. 18). Both arms can be moved independently around the target. Due to their intrinsic size, the minimum detection angle is 12.5° with respect to the exit beam line for the Electron arm and -12.5° for the Hadron arm. Each arm supports a High Resolution Spectrometer (HRS) and a detector package. This configuration allows coincidence experiments such as VCS where the scattered electron and the recoil proton need to be detected in coincidence.

The role of the spectrometers is to perform a momentum selection on the particle type we want to detect in each of them. Both spectrometers were nominally identical in terms of their magnetic properties. Each includes a pair of superconducting quadrupoles (Q1 and Q2) followed by a 6.6 m long dipole magnet (D) with focusing entrance and exit faces, and including further focusing through the use of a field gradient in the dipole. Subsequent to the dipole is another superconducting quadrupole (Q3). This QQDQ configuration provides adequate resolution for both transverse position and angle required by high resolution experiment like VCS.

Q1 is convergent in the dispersive plane (vertical plane in the lab frame) while

Q2 and Q3 provide transverse focusing (horizontal direction). The effect of the dipole is to bend particle trajectories through a 45° angle in the vertical plane. Globally, each spectrometer provides point-to-point focusing in the dispersive direction and mixed focusing in the transverse direction.

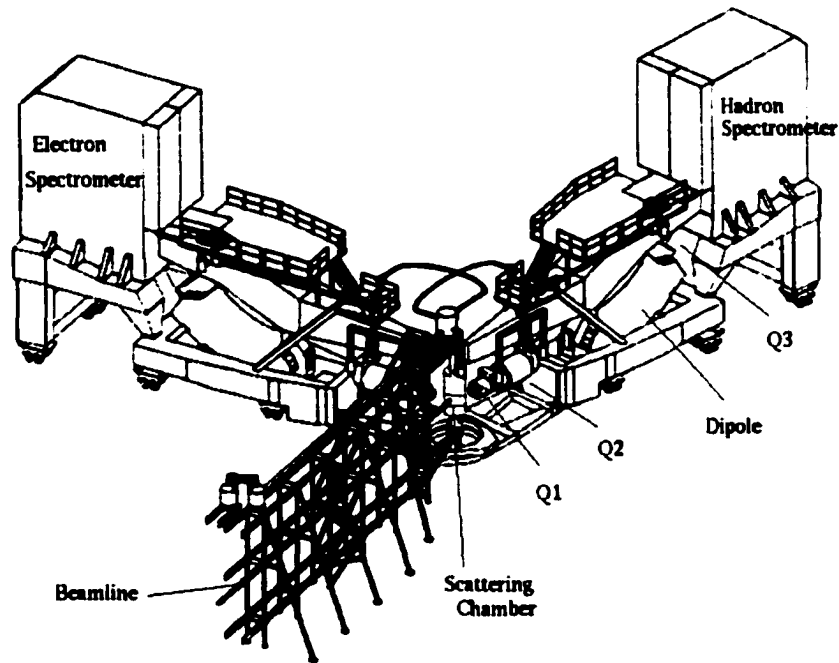


FIG. 18: The Hall A High Resolution Spectrometer pair sits in Hall A 53 m large in diameter. The beam line is indicated in which the beam propagates before interacting with the Hydrogen target contained in a target cell inside the scattering chamber. The scattered electron and recoil proton are then analyzed by the spectrometers that have a QQDQ configuration and bend the particle trajectories in the vertical plane with a 45° angle for central particles. Downstream, in the detector shielded houses, stand the detector packages.

The momentum resolution $\delta P/P$ thus achieved is a few 10^{-4} while the range is from 0.3 to 4.0 GeV/c. The momentum acceptance with respect to the central value is $\pm 4.5\%$. The angular acceptance is ± 60 mrad in vertical and ± 30 mrad in horizontal. All HRS characteristics are summarized in Table II.

TABLE II: Hall A High Resolution Spectrometers general characteristics [37].

Momentum range	0.3 - 0.4 GeV/c
Configuration	QQDQ
Bend angle	45°
Optical length	23.4 m
Momentum acceptance	± 4.5 %
Dispersion (D)	12.4 cm/%
Radial linear magnification (M)	2.5
D/M	5
Momentum resolution (FWHM)	1×10^{-4}
Angular acceptance	
Horizontal	± 28 mr
Vertical	± 60 mr
Solid angle	
(rectangular approximation)	6.7 msr
(elliptical approximation)	5.3 msr
Angular resolution (FWHM)	
Horizontal	0.6 mr
Vertical	2.0 mr
Transverse length acceptance	± 5 cm
Transverse position resolution (FWMH)	1.5 mm
Spectrometer angle determination accuracy	0.1 mr

The polarity of the magnets can be switched so as to change from positively charged particles detection to negatively charged particles detection independently for each arm.

For illustration purposes, a spectrometer could very well be compared to a complicated optical system (a series of lenses and other optic devices) that would use electrons instead of light. Since L. De Broglie, one knows about the wave-particle duality that particles can exhibit. So can light behave like particles in some conditions: photons represent the quantum aspect of light. Moreover the refractive index gradient of a medium traversed by light could be compared to the (electric and magnetic) field gradient the electrons are subject to. This possible

comparison is used in the terminology if not in the physics involved. For instance, one speaks of the spectrometer optics when speaking about the relation between the electron (or proton) variables before and after going through the spectrometer (variables at the target level and variables at the detector level).

In the same line of thinking, and just like one may want to restrict the sample of rays of light from an extended source, a collimator was used in the VCS experiment, placed at the entrance of each spectrometer. The purpose of this collimator was to better define the nominal acceptance of the spectrometers and perform a hardware selection on the scattered particles. We shall see in chapter 9 about VCS events selection that the collimator partially achieved its objective of better defining the acceptance.

The collimator defines a rectangular free space to the particles about twice larger in its vertical dimension than its horizontal one. The side presented to the target is actually slightly smaller than the other side that faces the inside of the spectrometer. Indeed the inside edges of the collimator have a slanting cut. The collimator material used is Heavy Metal, mostly Tungsten. Outside the band (approximately 17 mm wide) defined by the Tungsten material around the free space, Lead is otherwise the material used. The specifications of the Electron collimator are registered in Table III. The Hadron arm has the same collimator. The distance from the center of the target to the face of the collimator is nonetheless only 1100 ± 2 mm for this arm.

TABLE III: Electron spectrometer collimator specifications.

Thickness (mm)	80.0
Target side dimensions (mm × mm)	62.9 × 121.8
Spectrometer side dimensions (mm × mm)	66.7 × 129.7
Outer dimensions (mm × mm)	94 × 158
Distance target to face (mm)	1109 ± 2

6.4 Detectors

This section emphasizes the description of the detectors whereas their calibration will be discussed in the next chapter.

Of course particle detectors are essential in high energy or nuclear physics experiments for they are the ones that will actually react to particle passage (whence their name), yield electrical signals that will be manipulated and digitized by the associated electronics, be encoded and recorded to finally reach a computer at a later time for an off-line analysis. The latter will yield meaningful measurements which will help us understand what happened at the target and maybe the sought secrets of matter.

The sharpness of our understanding could not but be helped by good quality detectors. This global quality relies on the quality of the design, the materials used, the manufacturing, the associated electronics, *etc.* This translates into what one calls resolution. The better the resolution, the better the “image”.

An ambivalence inherent to detectors is due to the fact that detection requires interaction. In the case of our detectors, a first detector will have to alter at least one aspect of the particle, even so slightly, in order to yield information, leaving the next detector with an altered particle. A good detector would then be one that gives a strong signal but that is least disruptive to subsequent detectors, or as thick as needed to yield a strong signal but also as thin as possible not to degrade too much the particle’s characteristics.

Each Hall A arm supports a spectrometer and a detector package. Each detector package is composed of different detectors that fit different measurement needs. Those can be energy, trajectory, velocity, polarization, *etc.* For the VCS experiment, the needs were such that the two arms were loaded with about the minimum package. Each package contains two scintillator planes chiefly for data acquisition trigger and two vertical drift chambers (VDC) that allow for particle tracking. In addition to that, I shall mention an electromagnetic calorimeter (preshower-shower counters) on the Electron arm for particle identification that

can also be used for energy measurement and a gas Čerenkov detector for negatively charged pion/electron discrimination. Fig. 19 presents the Electron arm detector package while Fig. 20 gives the schematic view of the Hadron arm detector package.

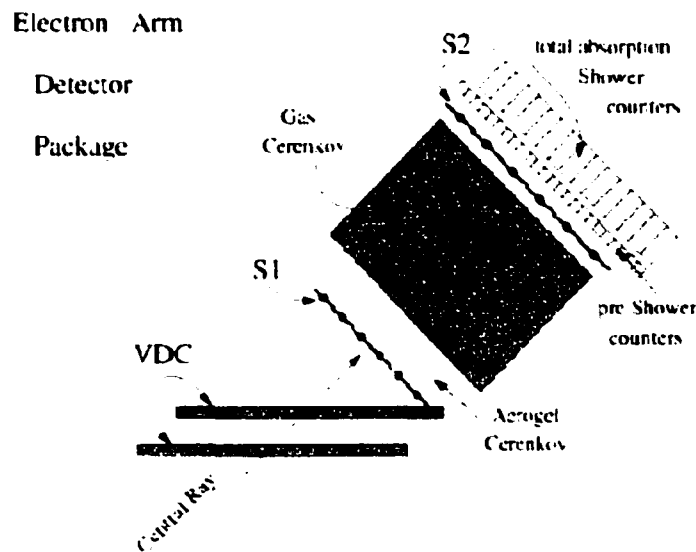


FIG. 19: Electron arm detector package. First on the trajectory of the particles stand the two vertical drift chambers that allow for trajectory reconstruction. Then come the two scintillator planes $S1$ and $S2$ used to trigger the data acquisition system. Finally the pre-shower and shower counters stop the electrons and yield a measure of their energy.

In the line of avoiding data acquisition for unwanted events triggered by background radiation (mainly particles not coming from the target through the spectrometer), the detectors dwell inside a shield house of metal and concrete. This protection also has the advantage to prevent degradation of good events. Indeed if an additional particle to the one triggering the data acquisition were to cross the detector package, some additional signals would be recorded and it would become less clear as what signals belong to the good particle. Said differently, the outside noise level is kept as low as possible by this shielding.

Let us also not forget that any kind of electronic equipment is very sensitive to radiation damage. The detector hut shielding offers a first step in preventing this kind of damage.

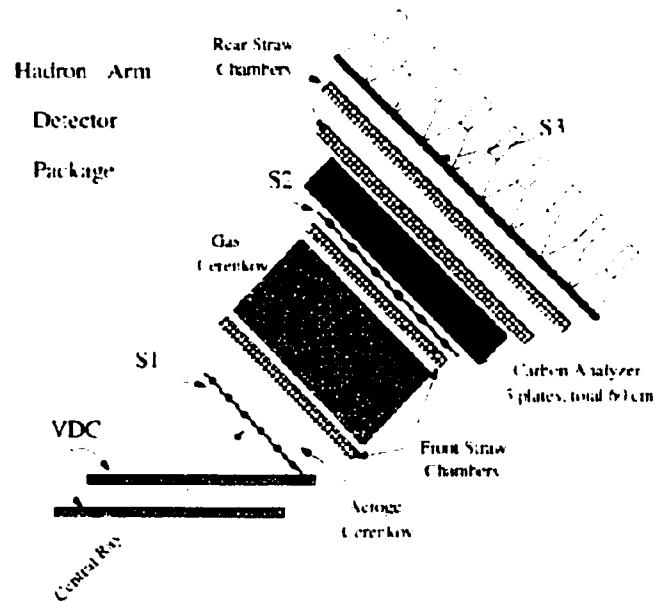


FIG. 20: Hadron arm detector package. Note that only the vertical drift chambers and the first two scintillator planes were used for the VCS experiment.

6.4.1 Scintillators

The primary goal of the scintillator detectors is to detect that a particle (at least one) traversed the detector package and thus to initiate recording the information from all the detectors. Nevertheless the decision making is left to the trigger electronics system (see next section). In addition these detectors provide the primary measurement of the time of passage.

We use two planes of scintillators, that I will refer as $S1$ and $S2$. $S1$, which comes first on the particle trajectory, is composed of six paddles made of Bicon BC-408 plastic with a 1.1 g/cm^3 density. Each paddle is a thin board, 0.5 cm

thick, of that particular plastic material. The active surface presented to particles is $36 \text{ cm} \times 30 \text{ cm}$, the largest dimension being horizontal also called transverse with an implicit reference to the spectrometer. The six paddles are positioned side by side in the dispersive direction. This assembly thus covers a $36 \times 180 \text{ cm}^2$ area and defines a plane which is perpendicular to the propagation direction of central particles which emerge from the spectrometer with a 45° angle with respect to the vertical. To avoid gaps between two consecutive paddles that is bound to happen due to ill positioning but, above all, to the fact that the 0.5 cm thick sides cannot be perfectly flat and active, we arrange the paddles so that they overlap a little bit (half an inch for $S1$). Therefore they do not perfectly lie within a plane. But this is no drawback given the fact that we now cannot miss any particle on the account of particles traveling undetected between paddles.

As far as the physics happening in this kind of detector is concerned, the principle could be apprehended with a comparison with the fluorescent property of some minerals. Particles flying through the detector material will lose a fraction of their energy. This transfer of energy will excite some of the atoms. They will decay soon to their ground state by emitting a photon of visible wavelength. This radiation of photons is called scintillation light, whence the name of the detector. The chemical structure of the plastic has been carefully engineered to maximize the light output (approximately 3% of the deposited energy is released as visible light) and minimize the pulse length (time constant of about 2.0 ns).

This light is nonetheless not emitted in any special direction. The goal is to collect as much of it as possible since one doesn't want to waste any part of what will contribute to the still future detection signal. Most of the light collection happens by total internal reflection. The light does not leave the scintillator material but bounces off the material boundaries to finally reach the collecting sides. But part of the light escapes. That is why the paddle is loosely wrap (loosely to preserve optical properties at the scintillator boundaries) with reflecting material that will send back the light inside. The wrapping also serves the purpose of keeping away any exterior light.

Everything is covered except the collecting sides where a light guide will collect

the light onto a photo-multiplier tube (PMT). There the photons will free some electrons from the photocathode on the inside of the PMT entrance window. The goal of the PMT is to create a true electrical signal: each freed electron of the window will free a lot more electrons in a cascade on the dynodes inside the tube. The gain is typically of one million to one.

The $S2$ scintillator plane is very similar except now the size of the paddles is $60\text{ cm} \times 37\text{ cm} \times 0.5\text{ cm}$. The increased covered area is due to spectrometer optical property (especially in the transverse direction). The distance between the two planes is 1.933 m in the Electron arm and 1.854 m in the Hadron arm.

Fig. 21 presents a possible arrangement of the overlapping paddles for the two scintillator planes. One can also see the shape of a paddle. Each side is linked to a light guide to collect the light onto a PMT (black end on the sketch).

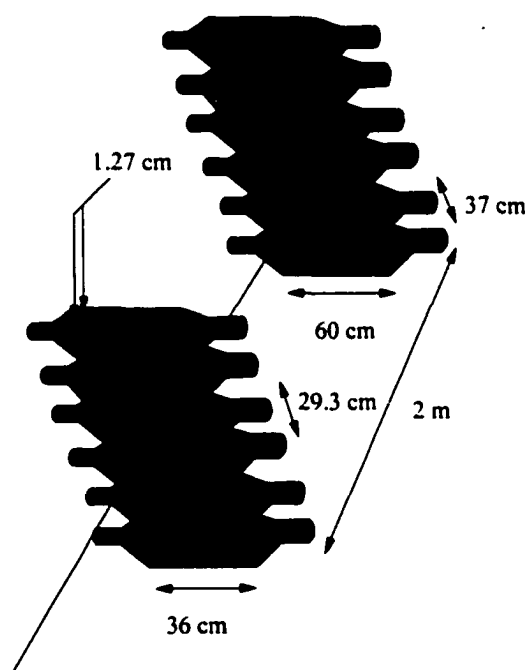


FIG. 21: Scintillator detector package. Note that the arrangement of the paddles may not reflect the actual positions with respect to each other. Note also that the size of the $S1$ scintillator should be read as $36\text{ cm} \times 30\text{ cm} \times 0.5\text{ cm}$.

6.4.2 Vertical Drift Chambers

These detectors are used for trajectory reconstruction of a particle traversing the detector package by measuring its position and angles near the spectrometer focal plane. This information is mandatory to determine the momentum vector of the detected particle after interaction in the target.

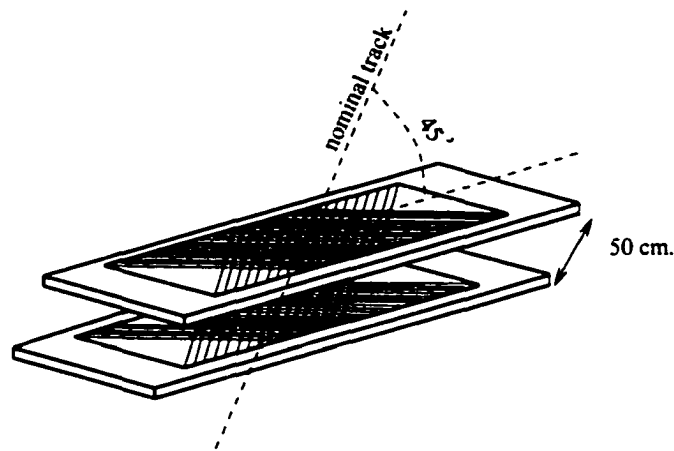


FIG. 22: VDC detector package. The wires of the four wire planes are drawn. The two wiring directions in each chamber are perpendicular while the chamber itself makes a 45° angle with central particle trajectories.

The drift chamber package, shown in Fig. 22, consists of two identical Vertical Drift Chambers (VDCs) of active surface $211.8 \text{ cm} \times 28.8 \text{ cm}$. The second VDC is placed 50 cm downstream. Each VDC is composed of two wire planes, denoted U and V, spaced by 2.6 cm. The wiring direction in one plane is perpendicular to the wiring direction of the other plane. Each plane contains 368 Gold-plated $20 \mu\text{m}$ diameter Tungsten wires spaced approximately every 5 mm. On both sides of a wire plane, at a distance of 1.3 cm, stands a high-voltage plane ($6 \mu\text{m}$ thick Gold-plated Mylar foil) at negative high-voltage -4 kV (while the wires are grounded). The chamber is closed by a window of aluminized Mylar $6 \mu\text{m}$ thick.

Inside the chamber, the wire planes are bathed with a gaseous medium composed of 65% argon for ionization and 35% ethane for quenching.

A charged particle going through a chamber ionizes the ambient gas. Electrons resulting from the gas ionization drift toward the wires because of the electric field present in the chamber. Getting closer to the wires, they are sensitive to a stronger electric field. Thus accelerated, they gain enough energy in their mean free path to ionize other atoms, inducing an avalanche process. In the meantime the positive ion cloud drifts away from the anode wire. This induces a negative pulse on the anode wire. After amplification, this pulse triggers a TDC which records the arrival time relative to a reference time from the *S2* scintillator.

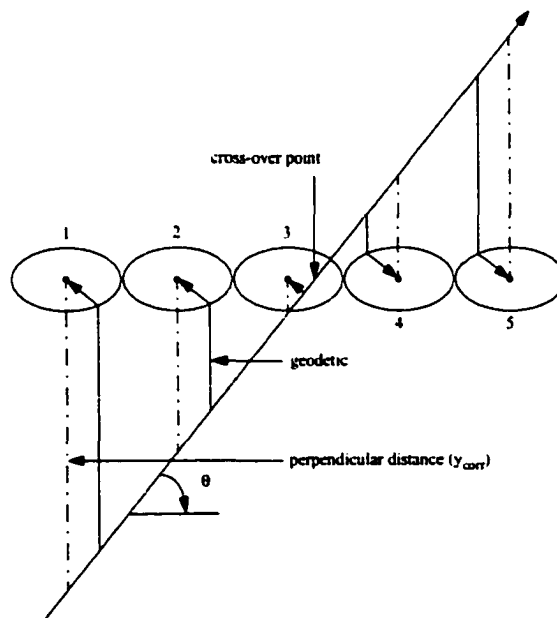


FIG. 23: The electrons of the gas mixture freed by ionization due to the energetic particle flying through the VDC drift along the electric field lines. These field lines are straight away from the anode wires but the electric field becomes radial and stronger closer to the wires inducing an avalanche phenomenon. The full arrowed line starting from the particle trajectory are samples of freed electron paths. The dashed dotted lines represent the reconstructed distances between the trajectory and each wire inferred from timing information. A fit to these distances yields the coordinates of the cross-over point. (cf. section 7.3)

A particle going through a wire plane with the nominal 45° track typically fires five wires (Fig. 23). By knowing the avalanche drift velocity in the gas and the timing of the processes, one can compute the particle crossing point. With the Hall A VDC package, the crossing point between the particle trajectory and the wire planes is known at a $225 \mu\text{m}$ level (FWHM) using both planes U and V, and the angular precision is about 0.3 mr (FWHM) using both VDC chambers.

6.4.3 Calorimeter

Only the Electron arm was equipped with preshower and shower counters at the time of the E93050 experiment. These detectors measure the energy loss of particles going through them, what further allows for particle identification (electron/negatively charged pion discrimination).

The preshower counter consists of forty-eight TF-1 lead glass blocks placed in two columns, each block representing 3.65 radiation lengths. The shower counter is made of ninety-six SF-5 blocks in six columns, each block representing here 15.22 radiation lengths. Finally, each block is coupled to a phototube. Fig. 24 presents a view on how the blocks are stacked up.

The principle of these detectors is the following: when a high-energy electron is incident on a thick absorber, it initiates an electromagnetic cascade: Bremsstrahlung photons and created e^+/e^- pairs generate more and more electrons and photons, but with lower and lower energy. This phenomenon is also called a shower, hence the name of these detectors. The shower develops and eventually the electron energies fall below a critical energy after which the electrons dissipate their energy by ionization and excitation rather than by generation of additional shower particles. If the material extension is large enough, all of the incident particle energy is deposited. High energy electrons and positrons (with velocity $\beta > 1/n$ with n the index of refraction of the medium) also create visible photons in a forward cone (defined with $\cos \theta_c = 1/n\beta$) by Čerenkov effect. The number of photons collected in the phototubes is proportional to the electron energy deposition. The shower counter present in the Electron arm is long enough

to be qualified as a total absorption calorimeter and indeed measures the total energy of the incident electrons.

On the opposite, heavier particles cannot create Bremsstrahlung or Čerenkov light as easily as electrons and they lose their energy only by ionization. In this case, the number of emitted photons is much smaller than in the case of electrons. Based on energy deposition, it is then possible to select electrons from all heavier particles.

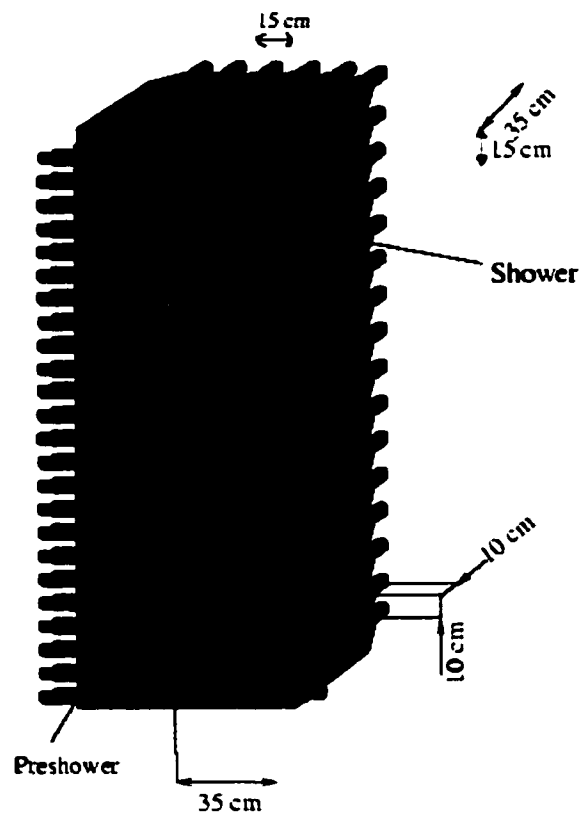


FIG. 24: Preshower-shower detector package. The arrangement of the blocks is shown. Every black area represents the PMT associated with each block.

6.5 Trigger

6.5.1 Overview

At a basic level, one wants to know how many reactions of an interesting type occurred out of all the possibilities including the special case of no reaction at all. Thus one faces a counting problem. To illustrate more quantitatively the problem, it can be said that the rate of interaction (for rare processes) is given by the product of the beam intensity, the target thickness and finally the cross-section, the latter being characteristic of the investigated reaction and the quantity to be determined. In its practical aspect, a cross-section evaluation relies on an event counting capability.

But before being able to count particles and analyze them, we must detect them. While particles are flowing through the spectrometer and the detectors, we actually do not know for sure if there is any yet that are doing so. Moreover, once we found a way to tell that particles are traveling through the spectrometer on an individual basis, we do not want to miss any of them for the purpose of accurate counting, even though we cannot or may not want to record information about every particle.

So we have to collect a minimal set of information, easy to handle and reliable, to decide, first, if this gathered information is coherent with a true particle, and then, decide to record what information. For a coincidence experiment, we also want to check if we have coincidences between two particles, one in each spectrometer, that would come the same reaction vertex. Moreover we need a fast answer to these questions. This deciding and first step sorting task has been assigned to the trigger system which is described in the following.

6.5.2 Raw trigger types

There are four main types of raw triggers called $S1$, $S2$, $S3$ and $S4$. The information coming from the scintillator phototubes is used to form those basic triggers. Additionally the Čerenkov detector is used on the Electron arm. A simplified

diagram of the trigger electronics is shown in Fig. 25.

Triggers $S1$ and $S2$ are related to what is happening in the Electron arm only. An $S1$ trigger is formed by a coincidence between the two scintillator planes $S1$ and $S2$ in a so-called S-ray configuration. It is supposed to indicate that a good electron went through the detector package. Explicitly, three requirements are necessary:

1. We have to have a valid signal out of both sides of any paddle in the first scintillator plane. In other words, we must have a clean signature of a particle going through one scintillator paddle.
2. We also have to have the same clean signature of the particle in the second scintillator plane.
3. The possible trajectories are restricted. As the good particles are supposed to arrive perpendicular to the scintillator planes, the label number of the paddle that fired should be the same in both planes. Nevertheless the case of contiguous paddles firing in the second plane is also accepted chiefly to account for deviations from perfect perpendicularity and paddle edge effects. (S-ray configuration)

Let me add a few comments on any of the first two requirements. A coincidence between the left and right sides of one paddle is a minimum requirement. Noise is tolerated: another signal from any other PMT can be present in the logic system. One or even several other left-right coincidences can also coexist.

By reference to Fig. 25, the logic process can also be understood. Any analog signal coming from a PMT with an amplitude greater than a constant threshold is transformed into a logic pulse by the associated discriminator. For each paddle, a left-right coincidence within a 40 ns time window is checked by an AND gate. (Only one paddle for each plane is sketched on the diagram.) Each result of this first check is sent to a Memory Lockup Unit (MLU). At this point, an OR operation is performed between the six logic signals from the AND gates related to the six paddles of one scintillator plane. A positive result is obtained if at least one

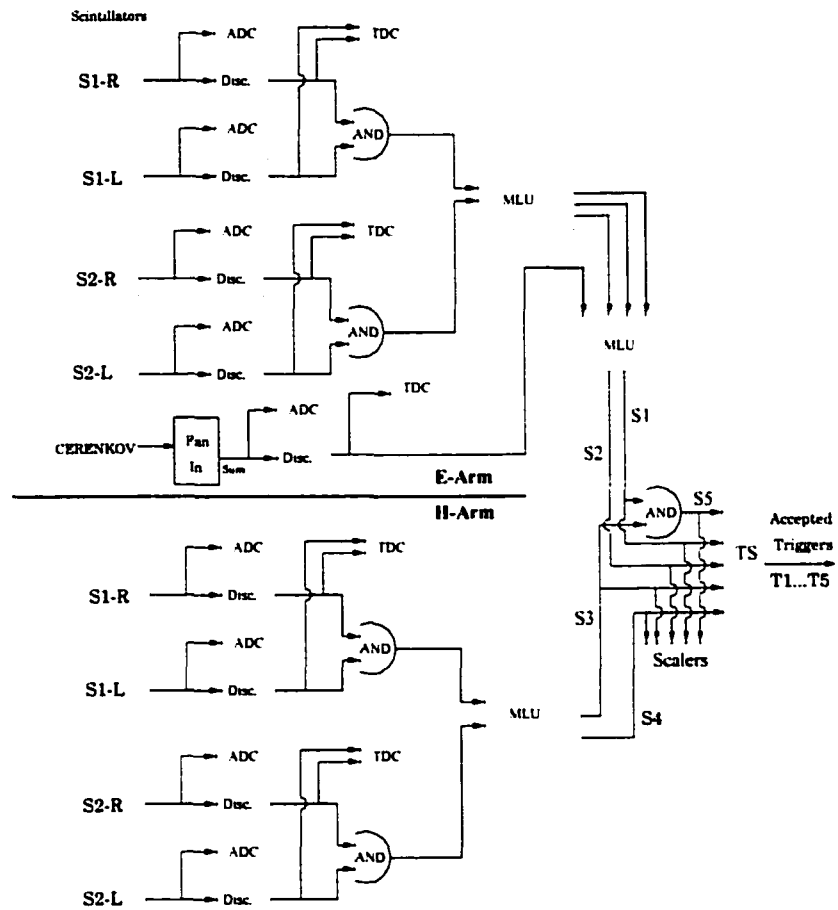


FIG. 25: Simplified diagram of the trigger circuitry. Only one paddle is referred for each scintillator plane of the two spectrometers. Left-right coincidences in the scintillator paddles are checked by MLU modules for each scintillator plane. The modules also check the S-ray configuration. The result is the formation of good triggers (S1 and S3) and bad triggers (S2 and S4). The trigger supervisor sorts all the triggers and starts the data acquisition for a sample of them.

left-right coincidence exists. Each scintillator plane is treated separately. The S-ray configuration is also checked at this stage. The output of this MLU is therefore composed of three logic results corresponding to the three above requirements.

This output is used as input for a second MLU. An additional signal line from the Čerenkov detector is also used as input. The decision made at this level is whether or not there is a definite signature of a particle, the fulfillment of the three previous requirements, in which case a trigger $S1$ signal is formed. If one of the three tests failed then another decision is taken, namely was the pattern close to being an $S1$ trigger signature. Three possibilities are to be given more consideration :

1. Maybe only the S-ray configuration was missing.
2. Maybe there was no coincidence in the $S1$ scintillator plane but there was one in the $S2$ plane and additionally a signal was detected in the Čerenkov and therefore it is highly probable that we should have had a coincidence in $S1$.
3. Same thing but in the $S2$ plane now.

In all those cases, an $S2$ trigger is formed. Any other pattern is not considered. Although the $S1$ triggers can be considered as the only relevant triggers, it would be a mistake to completely neglect the $S2$ triggers for part of them reflect inefficiencies in our exhaustive counting of particles going through the spectrometer. I refer the reader to section 8.2 for further details on scintillator inefficiencies.

$S3$ and $S4$ are equivalent to $S1$ and $S2$ respectively when the Hadron arm triggers are considered.

$S5$ triggers are formed if an $S1$ trigger and an $S3$ trigger are found to be in coincidence within a 100 ns time window.

All trigger types are counted in counting scalers. Note that the $S5$ scaler double count since an $S5$ trigger is first an $S1$ trigger and an $S3$ trigger as well and already counted as such.

6.5.3 Trigger supervisor

The central part of the electronic trigger system is the trigger supervisor. It is it which decides what type of trigger is accepted and consequently what information will be recorded.

Its first function is to scale down all raw trigger types. A prescale factor can be set for each trigger type. A prescale factor of N means that the trigger supervisor simply will not consider the first $(N-1)$ raw triggers of that type as far as its second function is concerned, triggering data acquisition.

After prescaling, the first raw trigger that arrives at the second level is accepted. Accepted triggers are called $T1$, $T2$, $T3$, $T4$, $T5$, $T8$ and $T14$ with reference to the raw trigger type names. If a second trigger arrives within 10 ns of the first one, an overlap occurs. That is how $T14$ triggers are formed. During E93050, the combination of raw trigger rates and prescaling made the $T14$ trigger rate negligible. Nevertheless $T5$ triggers might never be formed for an $S5$ trigger is always there because an $S1$ and an $S3$ triggers are there too. To avoid overlaps between the three and to ensure that $S5$ takes precedence and becomes a $T5$, the $S1$ trigger is delayed to arrive 22 ns after the $S5$ trigger whereas $S3$ is forced to arrive 40 ns after $S5$.

6.6 Data Acquisition

The aim of a nuclear physics experiment is to gather data about nuclear interactions. The data are collected from detectors which generate electrical signals. These signals encode information related to the nuclear interactions which took place. The data acquisition (DAQ) system formats and stores this information in a way which can be retrieved for later analysis.

The data acquisition system that was used for this experiment is based on the Jefferson Lab Common Online Data Acquisition (CODA) system, a modular, extensible software toolkit from which DAQ of varied complexity can be built. A

typical CODA system consists of a central module, the trigger supervisor, a program running on a Unix system for interface with the human operator and one or more “readout controllers”, known as ROCs, single board computers running the Vx Works real-time kernel. ROCs communicate with TDC and ADC FASTBUS modules, interfacing detectors and some of the beam line instrumentation (BPMs) to the Unix computer system.

Each time the trigger supervisor accepts a trigger, it sends a signal starting digitalization of TDC and ADC FASTBUS signals. After that, it asks the ROCs to read the FASTBUS modules values. At the same time, it warns the UNIX acquisition to be prepared to receive an event. Each ROC then sends data, through the network, to the Event Builder (EB). The EB collects bits and pieces of events arriving at different time from different places and packs them with other information (such as detector origin, detector part, trigger type, *etc.*) needed by the analysis. The event is then stored in a file on a disk, before being copied on a silo of huge capacity and equipped with robotic fast tape drives for later retrieval.

By default though, an ADC channel is not read out if the value is below the pedestal cut (See also section 7.2). ADC values below this cut are indeed useless since they only indicate that no electric signal was present at the ADC input line. The pedestal cut is usually ten channels above the actual pedestal. If the measurement of the actual pedestal is too noisy (sigma of distribution $> 10\%$ of peak position), the cut is set to zero, which means that, for that channel, there is no suppression. This typically occurs in 2 to 5% of channels. The pedestal suppression reduces the event size and readout time, thus reducing deadtime by typically a factor of two. (See section 8.1.3 about Computer deadtimes.)

In Hall A, data acquisition is enabled by the human operator. After a while or for any reason, the human operator can decide to stop data recording. The accumulated events form what is called a run.

Aside from the events introduced in the previous section and called Physics events, two additional event types are inserted in the datastream. First, Scaler events containing scaler countings since the beginning of the run are periodically inserted. Each arm has its own block of scalers, even though some scalers can be

found in both blocks. The Electron arm scalers are inserted every 20 s. So are the Hadron arm scalers but with an approximate offset of 10 s with respect to an Electron Scaler events. Among the scalers, one can find the VtoF scaler that will yield the accumulated beam charge (*cf.* section 7.1), a clock scaler and the raw triggers scalers. These scaler events are only approximately synchronized with the Physics events. A better synchronization procedure had to be found to relate the beam charge accumulated over a period of time to the Physics events that occurred during the same period of time (see also section 7.1).

The other “special event” type is the EPICS event type. Approximately every thirty seconds, a long list of EPICS variables from the slow controls is inserted into the datastream. These events contain such information as the magnetic fields of the spectrometer magnets and the high voltage of the detector PMTs. A shorter list is also inserted approximately every four seconds containing fewer information such as on line beam current.

Beside data recording, some visualization programs allow to check on-line the data quality. Histograms are formed to detect dead channels by use of software tools that access a real-time event buffer maintained by the CODA Data Distribution system (DD system). The reconstruction of a sample of events is also made for an on-line analysis.

Fig. 26 tries to lay out the Hall A data acquisition system.

The typical size of an event is 1 kB, and typical running conditions do not exceed 2 kHz with 20% deadtimes. During the E93050 experiment, 450 GB of raw data have been stored on tapes which includes 170 GB of data collected for the $Q^2 = 1 \text{ GeV}^2$ data set.

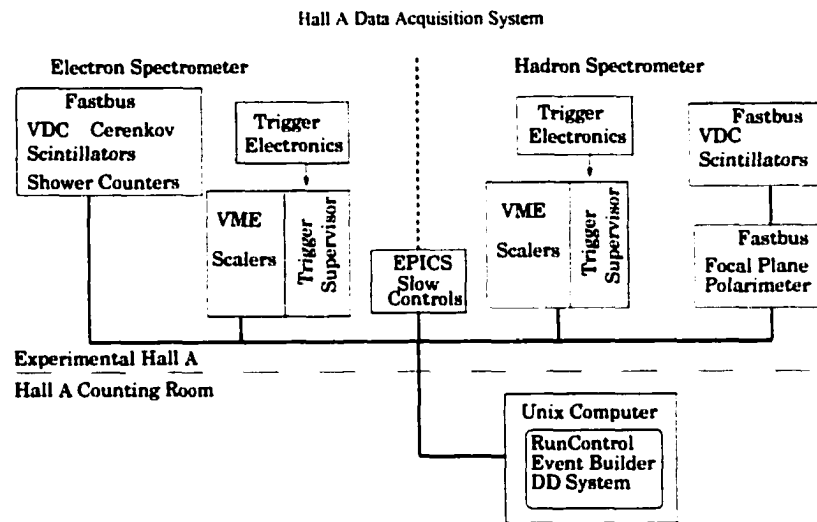


FIG. 26: Hall A data acquisition system. In this figure the Trigger Supervisor on the Electron side has to be understood as the electronics related to electron triggers, the real decision taking being made in the Trigger Supervisor on the Hadron side. A Unix computer centralizes information from the detectors in Physics events when requested by the Trigger Supervisor, counting scalers information in periodic Scaler events and finally information from the EPICS slow controls in periodic EPICS events.

Chapter 7

Calibrations

In the previous chapter, I emphasized the description and operating principle of the detectors and other useful instruments. But in order to obtain meaningful measurements and to translate the raw data into physical information, each device has to be calibrated.

The purpose of the present chapter is globally threefold. The first section is dedicated to charge evaluation. This quantity enters the luminosity, a normalization factor described in the next chapter for absolute cross-sections. A reliable evaluation is therefore necessary. The calibration of the current and charge measuring devices is studied and the charge evaluation method explained.

The next sections present a few aspects of the calibration procedures and results obtained for the detectors used in the experiment. The scintillators and the vertical drift chambers calibrations are considered first. The spectrometers calibration is then investigated succinctly even though of extreme importance. Indeed the transport tensor, subject of the calibration, relates measured quantities in the detectors to vertex variables. Finally the electromagnetic calorimeter (preshower and shower counters) calibrations is treated.

The last section examines the calibration of the coincidence time-of-flight, variable that allows to define time windows for accidental and true coincidences which enables an accidental subtraction under the true coincidence peak in the true coincidence time window.

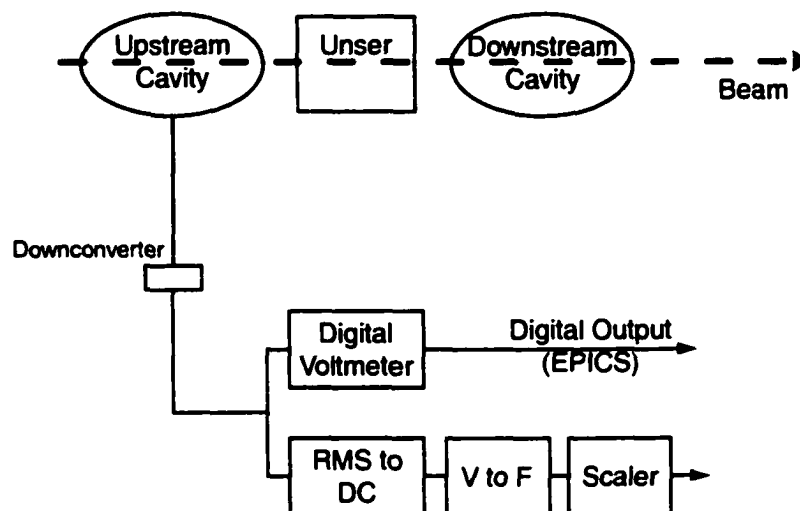


FIG. 27: Diagram of the current reading devices and readout electronics for the upstream cavity. The voltage signal from the cavity is treated by two electronics chains. The first chain (EPICS) yields a measure of the beam current after the voltage from the cavity is multiplied by an on-line current calibration coefficient. It is a sampled signal since a beam current value reflects the beam delivery over a one second period every four seconds. The second chain is a measure of a quantity proportional to the charge sent to the target as a counting scaler is incremented by pulses generated at a frequency proportional to the cavity voltage. The proportionality constant has to be calibrated.

7.1 Charge Evaluation

7.1.1 Calibration of the VtoF converter

Electronics layout

Fig. 27 lays out the current reading devices and the main components of the electronics chain that enables a voltage reading from a cavity. The signal coming from a cavity is first of all downconverted to lower the frequency (from 1.5 GHz to 1 MHz) for a proper analysis by different electronic modules. It is then split into two branches.

On the one hand, the signal is fed to a digital voltmeter. The signal is averaged over nearly one second and send to the Epics slow control system after a current calibration coefficient has been applied obtained from an on-line current calibration. This on-line current calibration coefficient is updated every day by a dedicated calibration run. A current reading is recorded into the Hall A datastream roughly once every four seconds. We are dealing here with a sampled signal of the beam current.

On the other hand, we have an RMS-to-DC converter. The output is a DC signal proportional to the root mean square (rms) of the incoming signal (voltages from the cavity) and therefore proportional to the beam current. This DC voltage is then fed to a logic pulse generator (VtoF: voltage-to-frequency converter) that generates pulses at a frequency proportional to the input voltage. The pulses are then simply counted by a counting scaler. We are dealing here with an integral proportional to the beam current.

Objective of the calibration and how to treat the cavity signals

The goal here is to calibrate the VtoF electronics branch. Indeed we are interested in evaluating the accumulated charge sent to the target during a run since the charge enters the luminosity normalization factor for the cross-sections (*cf.* section 8.5). The VtoF scaler just fits that need. Its readings (every 20 s) represent the series of an accumulation of counts. The counts are accumulated with a frequency (the output pulse frequency of the VtoF converter) proportional to the cavity voltage and therefore proportional to the beam current so that a reading of the VtoF scaler is a reading of a quantity proportional to the beam charge sent to the target. This constant of proportionality needs to be determined.

All we have at our disposal to calibrate the VtoF electronics branch is the other electronics branch, namely the EPICS branch. The variable to be used is the output voltages from the cavity. One could have thought that the current readings would have been a better choice (the quantities directly available in the datastream). But it is not since the current values from the EPICS signal are tainted by a not so good current calibration constant evaluated on-line that

transforms the voltage readouts from the cavity to an evaluation of the beam current. To make a long story short, it is better to remove this on-line current calibration constant from the EPICS signal and go back to the raw signal, the voltage readings from the cavity.

The calibration will then consist in relating the cavity voltages extracted from the EPICS signal with the counting rate of the VtoF scaler. We will need another calibration, namely the calibration that relates the cavity voltage to the actual beam current, and is the subject of the next subsection.

An additional difficulty in this calibration is the fact that the EPICS signal is a sampled signal of the cavity voltage that reflects what is happening to the beam current delivery over a one second period every four seconds while the VtoF scaler reflects everything happening to the beam current in a continuous way (no three second gaps every four seconds). Moreover, we only have at our disposal the readings of the VtoF scaler inserted in the datastream about every 20 s (the time elapsed between two scaler readings is actually evaluated by a clock scaler). We can therefore only build the average counting rate between two scaler readings. All these problems are avoided by averaging the EPICS signal and the VtoF rate over a period of time (at least several minutes) during which the beam current is assumed to remain constant.

Data used for the calibration

The regular production runs (also used to extract cross-sections) are used at this stage. A sample of runs is chosen on the sole basis that the sample of beam current delivered during all these runs spans a large interval in beam current and for statistics reasons (runs long enough).

Calibration procedure

In order to perform the calibration, we have to select some runs that seem appropriate. The runs have to be rather neat, without beam trips and with a constant intensity for the delivered beam since we want to restrict ourselves to periods of stable beam current delivery at one value of the current. It is not

exactly possible to find such runs. A bypass to the problem is to select a part of a run where the beam intensity was about stable according to the EPICS readout.

Once the runs have been selected to cover a large range of beam intensity (from $10 \mu\text{A}$ to $100 \mu\text{A}$ for instance), one selects the good parts. To do so, one looks at the beam current intensity from the EPICS signal and at the rate of the VtoF scaler. The simultaneous look at the two variables enables to select in time the good slices of run. One is left to evaluate a mean value of the current by averaging over the EPICS readouts and over the VtoF counting rates.

The error on these mean values is simply taken as the root mean square of the gathered data points, assuming implicitly the delivery of a constant beam current. Nevertheless there is no assurance that the beam intensity delivered by the accelerator crew was rock steady. Therefore this root mean square will include the real fluctuations in the beam delivery and the fluctuations in the readouts of the current due to the reading devices and their electronics chain. This will overestimate the actual errors assigned to the readings.

Fit of the data

Fig. 28 presents the averaged voltages from the upstream cavity as seen by the EPICS readout branch *versus* the averaged rate of VtoF from the VtoF readout branch obtained over the selected periods of runs. A linear fit of the data points has been performed. One can already realized that this fit is rather good. The straight line goes through all the data points at that plotting scale. A chisquare per degree of freedom of $4.5 \cdot 10^{-2}$ is another indication of the goodness of the fit (too good because of the overestimation of the errors: the beam was indeed not rock steady and its instability in current artificially increased the error bars.). This valid linear fit is not ultimately surprising either since we compare the same signal treated by two electronics chains built to be as linear as possible. The errors of the data points are actually plotted but are not visible because of the plotting scale and the intrinsic size of the points.

To go beyond and look at the validity of the fit more closely, a residual plot is created that will show the differences in the two average voltage estimations

as estimated from the EPICS signal and as inferred from the VtoF rates by the linear fit model.

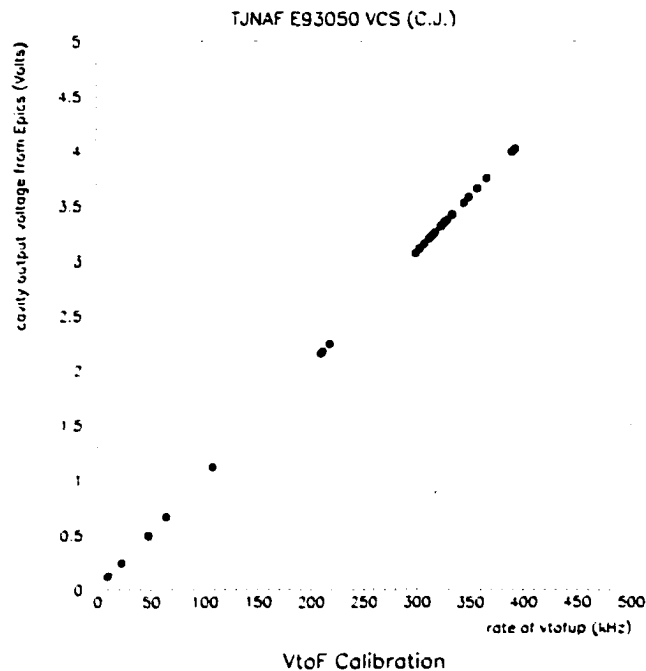


FIG. 28: VtoF converter calibration. The average voltage extracted from the EPICS signal is plotted *versus* the average counting rate of the VtoF scaler. The result from a linear fit is also displayed. This calibration is for the upstream cavity. No calibration for the downstream cavity was performed as it exhibited suspicious behavior.

Residual plot

The next plot (Fig. 29) is then the residual plot. This plot represents the difference between the estimations of the voltage from the cavity as measured from EPICS and as calculated from VtoF counting rates and the linear fit model results obtained in the previous step *versus* the second of these two estimations. The plotted error is the rms of the average EPICS current divided by the on-line current calibration constant.

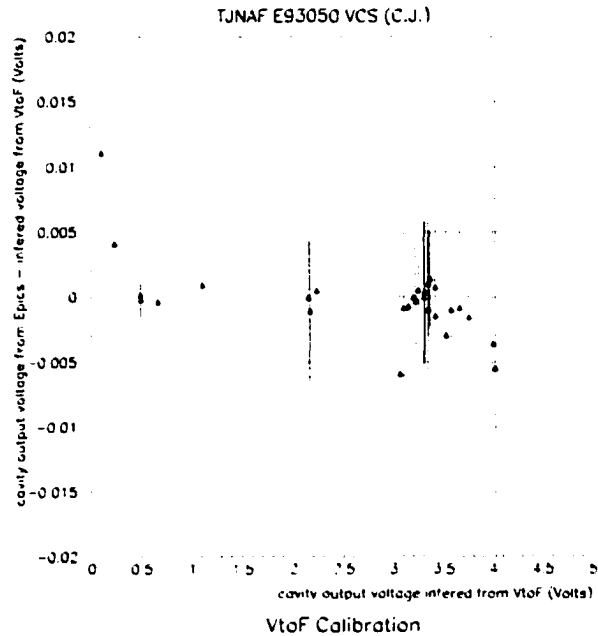


FIG. 29: Residual plot. The residues between the two average cavity voltage estimations (from EPICS and VtoF rates) is now plotted as a function of the voltage inferred from VtoF. The validity of the fit is confirmed as the points stand at very small values of the residues. The first two points depart from zero and is an indication of an expected nonlinearity of the VtoF electronics branch for very low currents.

Anticipating on the next subsection 7.1.2, the horizontal scale in Fig. 29 can be multiplied by about twenty-five to yield a beam current scale. A deviation from linearity for beam currents below $10 \mu\text{A}$ (cavity voltage of $\simeq 0.5 \text{ V}$) seems to appear. This deviation is actually expected.

In order to better check the previous deviation from linearity, Fig. 30 presents a relative residual plot. On this plot the vertical axis consists of the former differences of Fig. 29 but now divided by the values inferred from the VtoF counting rates. The deviation at low currents clearly appears: 10% deviation at $3 \mu\text{A}$ and 2% deviation at $6 \mu\text{A}$.

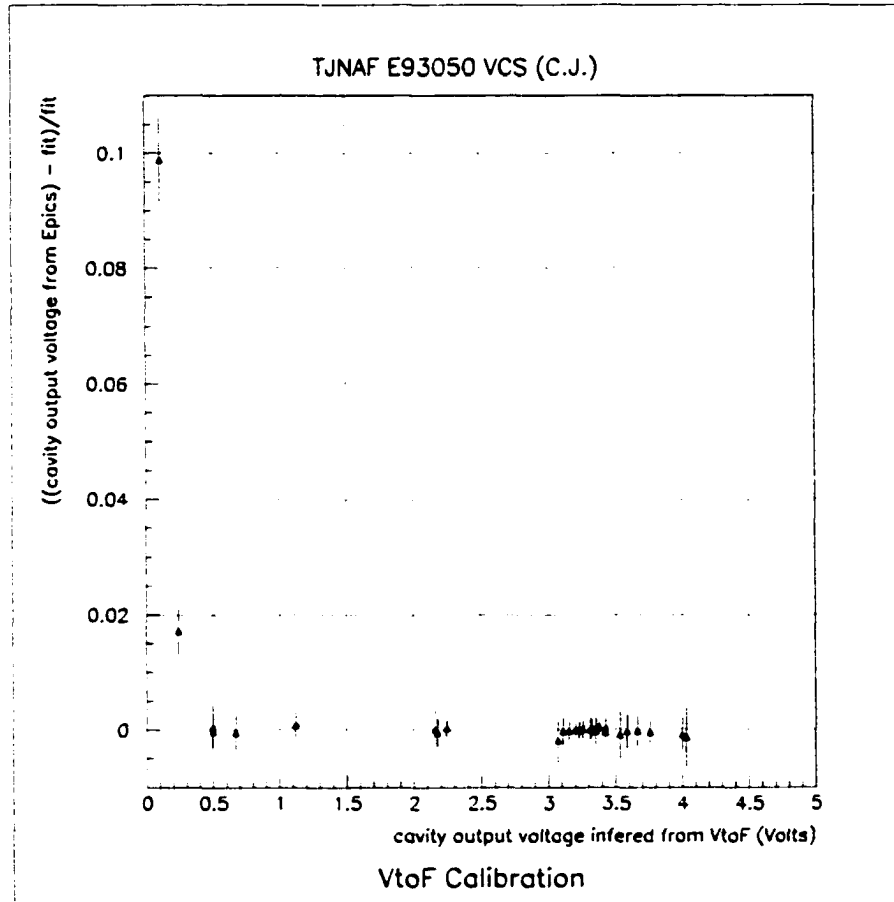


FIG. 30: Relative residual plot. The differences of Fig. 29 between the two cavity voltage estimations are now relative to the voltage estimation inferred from the VtoF rates. These relative differences are plotted as a function of the voltage inferred from VtoF. The linearity between the two electronics branch is obvious above $10 \mu\text{A}$ (cavity voltage of $\simeq 0.5 \text{ V}$) while the expected nonlinearity for low currents is also showing.

Results of the fit and summary

The VtoF electronics calibration has been performed by relating an average cavity voltage obtained from the EPICS information (after removal of the on-line current calibration factor) to the corresponding average VtoF counting rate.

The VtoF electronics branch has been designed to be as linear as possible over a large range of cavity output voltage. Indeed the VtoF scaler at the end of the VtoF electronics branch is dedicated to measuring the charge sent onto the target and a linear counting rate ensure the proportionality between the charge and the VtoF scaler counting.

Such a linearity has been checked. A linear fit of the following form has been used in the calibration:

$$v = \alpha f + \beta \quad (132)$$

where v is the cavity output voltage, f is the output frequency of the VtoF converter (the counting rate of the VtoF scaler) and α and β are the two coefficients of the linear fit. The numerical values and errors of the parameters are:

$$\alpha = (1.0194 \pm 6.0 \cdot 10^{-4}) \times 10^{-5} \text{V} \cdot \text{s} \quad (133)$$

$$\beta = (1.77 \pm 0.11) \times 10^{-2} \text{V} \quad (134)$$

for the slope and offset coefficients respectively. The correlation error coefficient between the slope and the intercept is found to be $\sigma_{\alpha\beta}^2 = -5.0 \cdot 10^{-11} \text{V}^2 \cdot \text{s}$.

The domain of validity of the linear fit has been checked to be for beam current intensities between 10 and 100 μA (anticipating the current calibration result of subsection 7.1.2 that transforms cavity voltage to beam current). The accumulated charge sent onto the target can therefore be evaluated over any period of time for which the beam current stayed within the previous limits. A stable beam intensity is not required thanks to the linearity of the VtoF electronics chain. On the other hand, any period of time for which the beam current lingered below 10 μA should be removed from the cross-section analysis. Periods of no beam fall into this category. Finally an upper limit in beam current for the linearity of the charge reading electronics has not been clearly determined. Such a limit is nevertheless expected.

7.1.2 Current calibration

Objective of the calibration

The purpose of the current calibration is to relate the cavity output voltage to the actual beam current since the BCM cavity offers an output signal only proportional to the beam current. Measures of the beam current are given by the Unser monitor which is used as an absolute reference. A description of the BCM cavities and of the Unser monitor is available in section 6.1.

Data

The data used for this present study were retrieved from the CEBAF accelerator archiver since no data pertaining the Unser monitor were inserted in the Hall A datastream and recorded at the time of our experiment. Only the interesting portions of the entire amount of data were actually retrieved and divided in what I will later refer as calibration runs. Most of these calibration runs simply correspond to periods of “official” BCM calibrations that were performed on-line during the VCS experiment. The rest of the calibration runs corresponds to periods of time when the beam has been tripping fairly often. I will explain in the calibration procedure the interest of these trips and how they can help us to calibrate the cavities.

A drawback of the retrieved data (*vs.* the on-line data) is the sampling rate: only 0.1 Hz. This corresponds to one data point every ten seconds. Each point is an electronic averaging over nearly one second. The on-line rate is ten times higher. So in the case of the accelerator archiver data, only 10% of the possible data are accessible.

To perform a BCM calibration one needs current readings from the Unser monitor for two values of delivered beam, or equivalently current readings at one beam current value and readings with no beam delivered, since the Unser monitor is most reliable for changes in beam current. One also needs the output information from the cavity to be calibrated, namely the cavity output voltage. This information is not directly available since only the product of the cavity voltage multiplied by the on-line current calibration coefficient is recorded. So in

a try to undo the on-line calibration (also proved to be not so good) and extract the necessitated cavity voltages, one also has to retrieve the on-line calibration coefficients for the two cavities updated during each on-line BCM calibration (performed approximatively once a day).

This operation of dividing the current readings by the on-line calibration coefficient is very easy in theory: one just has to divide a current reading by the corresponding calibration coefficient. But in practice, a lack of synchronization among the readings of the devices and with the updates of the current calibration coefficients makes the operation a bit more complicated. That is also the reason for the averaging in the off-line calibration procedure (of next paragraph).

BCM Calibration procedure

This paragraph aims at explaining what a BCM calibration procedure is. The first requirement is to have some low and high current plateaux. The low current phases are necessary to determine the offset in the Unser that fluctuates on a time scale longer than minutes. The duration of each plateau is about one minute. A succession of a low current and high current plateaux lasts then about two minutes during which time the Unser does not drift too much. It is then possible to evaluate the change in the Unser current readout between beam on and beam off. This will be used as a measure of the current delivered by the accelerator.

We can now compare the beam current intensity to the output voltages from the cavities by forming the following quantity:

$$C = \frac{\Delta u}{\Delta v} = \frac{u_+ - u_-}{v_+ - v_-} . \quad (135)$$

A second quantity can also be formed: $C' = \frac{\Delta u}{v_+} = \frac{u_+ - u_-}{v_+}$. In these two quantities, u_+ and u_- are the averaged current reading from the Unser monitor on a high plateau and on a beam off plateau respectively. Similarly v_+ and v_- are the averaged output voltage from a cavity on a high plateau and on a low plateau respectively.

This averaging over the plateaux is a different technique than the one used

on-line. Instead of using every single current value obtained every second to compute a calibration coefficient and then average the obtained coefficients (on-line technique), the off-line technique averages first the current and voltage readings over the plateaux with an error for each reading obtained with the rms of the data points and then forms the quantity C or C' .

The use of C or C' is determined by the nature of v_- . In the first case (use of C), it is treated as an offset whereas in the second case it is considered as a noise term. It turned out that the tiny value of v_- yields negligible discrepancies between C and C' .

The general procedure repeats this low-step/high-step five times which is a compromise between taking potential beam time (the procedure is indeed invasive for the three halls) and increasing the statistics of the measurement and its reliability.

In order to obtain independent measurements, one should use only the ascending (or only descending) transitions. Yet the results ought to be the same.

Beam trips after which the beam is not restored immediately can very well simulate the needed transitions between a low current and a high current to yield also a calibration coefficient.

Fit of the data

Fig. 31 is a plot of the current calibration coefficient values obtained for the upstream cavity using only the step up transitions (from low to high current) as a function of time expressed in hours since March 12th 1998 00:00. Note on this plot the dilated vertical scale: less than 1% around the central plotting value.

The first way to analyze the results of Fig. 31 is to try to fit by a constant. The χ^2 per degree of freedom is 0.6 for 31 degrees of freedom. It seems once again that the errors were overestimated because the errors used are the rms values of the regrouped data points that also reflect fluctuations of actual beam current delivery. It is expected for the current calibration coefficient to remain constant within certain limits. The error on the average of the current calibration coefficient is 0.04% in this case.

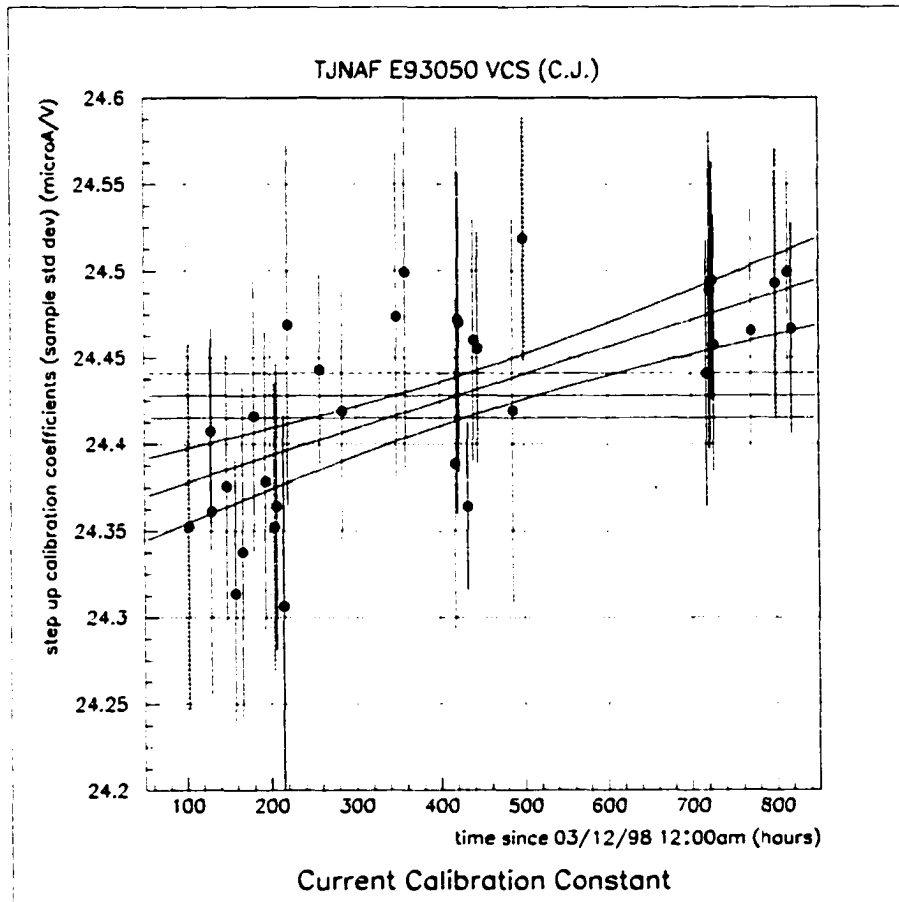


FIG. 31: Current calibration coefficient for the upstream BCM cavity. The results for each calibration run are displayed as a function of time. The time axis represents the time elapsed since March 12th 1998 00:00 expressed in hours. Note that the vertical axis for the coefficient values spans a short range ($< \pm 1\%$ around the central plotting value). A fit by a constant and a linear fit along with their error bands are also displayed.

A second analysis would be a linear fit in time. The χ^2 per degree of freedom is reduced: 0.3 for 30 degrees of freedom. It seems to be a better fit except that there is no good physical explanation for a linear drift in time for this current calibration coefficient.

The last analysis would be to say that the coefficient undergo a jump at about $t = 200$ hours. Before that time, the coefficient has a given first value whereas afterwards the coefficient has another value. A maintenance operation could explain this jump, but there is no reported indication of such a thing in the experiment logbook. Moreover the downstream cavity does not reflect this behavior.

The last remark that can be made is that the maximum difference between the linear fit and the fit by a constant is 0.3%.

Results of the fit and summary

As a global conclusion, the current calibration coefficient of the upstream cavity is taken as a constant value ($C = 24.43 \mu\text{A}/\text{V}$) with a relative error of 0.3% to reflect the incertitude on its behavior in time. The downstream cavity was not calibrated as it exhibited unreliability during the experiment.

7.1.3 Charge determination

After performing the two previous calibrations, the beam current intensity can now be evaluated from the VtoF scaler information too. Its expression is:

$$I = C (\alpha \text{Rate_VtoF} + \beta) \quad (136)$$

where *Rate_VtoF* stands for the counting rate of the VtoF scaler. In the case where the current calibration coefficient C is believed to remain constant, the integrated charge sent onto the target over a period of time defined as between two readings of the scalers can be expressed by the following formula:

$$Q = C (\alpha \Delta \text{VtoF} + \beta \Delta t) \quad (137)$$

where:

- $\alpha = (1.0194 \pm 6.0 \cdot 10^{-4}) \times 10^{-5} \text{ V.s.}$
- $\beta = (1.77 \pm 0.11) \times 10^{-2} \text{ V}$,
- $\Delta V_{toF} = V_{toF_{final}} - V_{toF_{initial}}$,
- Δt is the time in seconds elapsed between the two scaler readings, and
- $C = (24.43 \pm 0.07) \mu\text{A/V}$.

The formula for the error on the charge evaluation is:

$$\begin{aligned}
\sigma_Q^2 = & \left(\frac{Q}{C}\right)^2 \sigma_C^2 \\
& + (C \Delta V_{toF})^2 \sigma_\alpha^2 + (C \Delta t)^2 \sigma_\beta^2 + 2 C^2 \Delta V_{toF} \Delta t \sigma_{\alpha\beta} \\
& + (C \alpha)^2 (\sigma_{V_{toF_{initial}}}^2 + \sigma_{V_{toF_{final}}}^2) \\
& + (C \beta)^2 (\sigma_{t_{initial}}^2 + \sigma_{t_{final}}^2) .
\end{aligned} \tag{138}$$

In the above formula (Eq. 138), the first term on the first line accounts for the error on the current calibration constant C and represents the main contribution to the error on the charge. The next three terms on the second line accounts for the errors on the linear fit coefficients of the VtoF electronics chain calibration and their correlation error ($\sigma_{\alpha\beta}^2 = -5.0 \cdot 10^{-11} \text{ V}^2\text{s}$). The last four terms on the third and fourth lines represent the errors due to the individual initial and final readings of the VtoF and time scalers. For periods of time longer the a few minutes, the relative global error on the charge is less than 1% and can reach values such as 0.5%. Thus the charge evaluation does not represent a significant source of uncertainties in cross-section evaluation.

But in order to reach this order of accuracy on the charge, the price to pay is to reduce the analysis to events that actually occurred between the initial and final instants of hardware reading of the scalers. This is not such an obvious task to perform since the physics events and the scaler events are not inserted in the recorded datafile in a synchronized manner. Fortunately one of the scalers, read and recorded at the same time as the VtoF scaler, counts the total number of events written in the datafile since the start time of the run. The reading of this

scaler counting the physics events written on file is therefore enough to locate the first and last events to be included in the analysis that correspond to the start and end times of a period over which an accurate evaluation of the charge sent onto the target is possible.

7.2 Scintillator Calibration

In this subsection, the scintillator calibration is discussed. To be more specific, this calibration concerns the ADC and TDC converters which are the true devices that are read out. As described in chapter 6, one photomultiplier (PMT) is attached to each side of each scintillator paddle. The signal from the photomultiplier is sent to one ADC and one TDC as well as the trigger supervisor. That is a total of twelve converters of each kind for one scintillator plane and therefore forty-eight total for each arm that are to be calibrated.

7.2.1 ADC calibration

The first step in calibrating is to deal with the ADC converters. One has first to determine the pedestals, the reading of the ADC converters when no true signal is fed as input (empty reading). This is achieved by taking data without pedestal suppression. Examples of pedestal histograms can be found in Fig. 34.

Then comes the gain matching operation. Each photomultiplier has its own gain which may vary as the PMT ages for instance. Same thing for the internal gain of each ADC. The combined gain is therefore different from one ADC to the next, implying that different ADC readings would be obtained for the same scintillation signal (same amount of collected light). The idea here is to smooth out such discrepancies between any two ADCs by use of an additional gain for each ADC. Practically, this additional gain takes the form of a multiplicative constant g which is applied to the raw reading of each ADC:

$$adc_new = g \times (adc - ped) \quad (139)$$

where adc is the actual reading of the converter, ped is the pedestal value and g the effective gain of the ADC.

7.2.2 TDC calibration

The ADCs calibration is most useful when one wants to use the scintillators as a particle identification detector. For E93050, the scintillators were mostly used to trigger the data acquisition system. The extension of this role is timing. The purpose of the TDC calibration is to ensure a good timing between all the sides of all the scintillator paddles of the two scintillator planes. At this stage the timing is still restricted to each arm. The main objective is to make all time related information clean of any delay not due to the particle path in the spectrometer. The ultimate goal is to use the timing information from the two arms to be able to claim that both detected particles came from the same reaction vertex. The variable invoked for this affirmation is called coincidence time-of-flight and will be the subject of its own section (*cf.* section 7.6).

All signals coming from the PMT to be input into the TDCs are delayed in cables. Those cables have different lengths. The point of this delaying is to let the trigger supervisor decide first whether or not the information from various sources is coherent enough to be worth recording as an event. If so, a common start signal is sent to every TDC. This reference signal is actually the signal from the right PMT of the paddle that made the coincidence that triggered the system. The individual delays are calibrated by aligning time-of-flight spectra obtained between each scintillator paddle and one other detector element.

7.3 Vertical Drift Chambers Calibration

The Vertical Drift Chambers package has been presented in subsection 6.4.2. The description of the calibration of these drift chambers is undertaken in the present section for a deeper understanding.

A high energy particle traveling through the drift chambers ionizes the gaseous

medium surrounding the wires of the chambers. The freed electrons are attracted by the sense wires because of the electric field maintained in the chamber while the positive ions drift towards the cathode planes. For central particles, there typically are five wires that sense the initial high energy particle which information is to be obtained from. Each wire is connected to a discriminator that yields a start signal for a Fastbus multi-hit TDC if the collected signal on the wire is above a constant threshold. This TDC and any other from other wires that may have fired are commonly stopped by the delayed event trigger (signal from the $S2$ scintillator).

Fig. 32 presents a typical TDC spectrum obtained for one wire plane. This spectrum corresponds to times elapsed between an initial ionization and the induction of a signal on a sense wire, called drift times. The time spectrum is reversed since the TDC has a common stop from the trigger (and not commonly started) and each channel is started by an individual wire signal. Indeed, if a particle were to travel close to a wire, the electrons from ionization would soon be on the wire, the TDC associated with the wire would soon be started and would stay on for a long time before the delayed signal from the scintillator triggers the stop on the TDC. On the other hand, if the track went further away from the wire, the electrons would require more time to reach the wire, leaving less time between the start and stop signals on the corresponding TDC. It is therefore to be understood that the highest values in the TDC spectrum of Fig. 32 correspond to the shortest drift times. The peak centered at channel 1800 corresponds to wires that fired because of a particle track passing in the region where the electric field is radial. This case is pictured in the middle cell of Fig. 23 in subsection 6.4.2. The plateau on the left of the previous peak correspond to other cases (other four cells in Fig. 23) and indicates that the drift velocity is about constant away from the wires.

The TDC spectrum of Fig. 32 is obtained after a t_0 optimization. The quantity t_0 is the shortest allowed drift time. This parameter is to be optimized for each group of sixteen wires since the wires are cabled and bundled in groups of sixteen. The cable lengths and other timing delays are different for each group hence the need of a calibration.

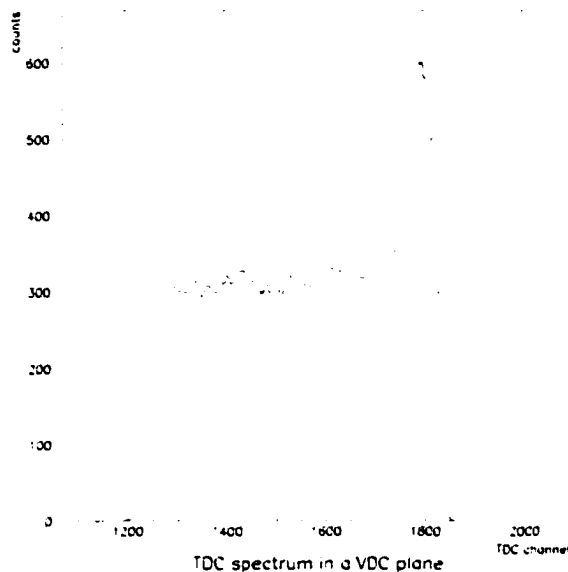


FIG. 32: Drift time spectrum in a VDC plane. The resolution of the TDC converters is 0.1 ns/channel. The drift time is the time elapsed between an initial ionization due to the high energy particle crossing the VDC chambers and the induction of a signal on a sense wire. A particle traveling close to a sense wire will have a short drift time but will appear in the peak on the right side of the plot since the TDCs are commonly stopped by the trigger signal.

The next optimization regards the drift velocity. This drift velocity translates the drift times into drift distances. Each wire plane uses its own drift velocity as it might be different for each of them. Fig. 33 presents a drift velocity spectrum after optimization. The peak value is used as the drift velocity.

Finally the drift distances and perpendicular distances (*cf.* Fig. 23) are evaluated using a parameterization of the geometry of the electric field, the drift times and the drift velocity. A fit to the perpendicular distances yields the cross-over point in each wire plane. The results from the four chambers enable the reconstruction of the trajectory of the particle that emerged from the reaction vertex, went through the spectrometer and is under analysis.

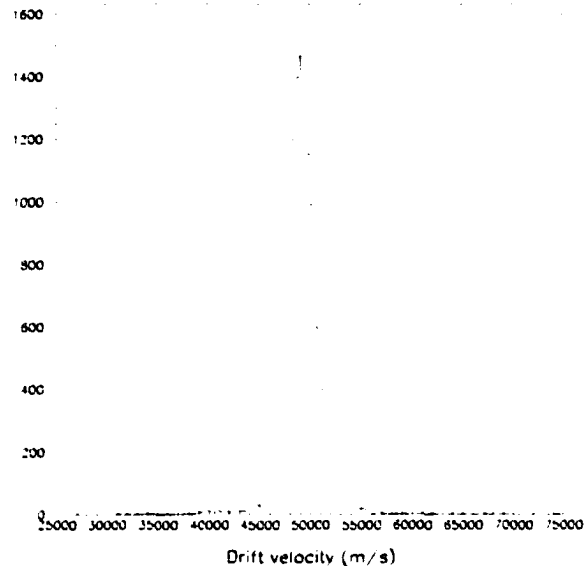


FIG. 33: Drift velocity spectrum in a VDC plane.

7.4 Spectrometer Optics Calibration

Even though the calibration of the optics part of the spectrometer is crucial in extracting physics from the recorded data, it shall not be very detailed in this document. I refer the reader to other VCS thesis [33][34] for further information.

The principal idea in this calibration is to establish relations between measured quantities in the detectors located after the spectrometer to physics variables related to the analyzed particle just after reaction in the target, therefore before the entrance of the spectrometer.

The first step consists in relating variables (two angular and two spatial coordinates to resolve the trajectory) measured in the detectors (VDC chambers) to variables defined in a new frame, called focal plane coordinate system, that restores the symmetries of the spectrometer. This already necessitates a simultaneous optimization of the polynomial expansion of three of the new variables upon

the fourth. Special data has to be recorded in particular conditions to increase the number of experimental parameters under control. The new variables are called y_{fp} , x_{fp} , θ_{fp} and ϕ_{fp} .

The second step concerns the optic tensor itself also known as the transport tensor. It links the focal plan variables, calculated in the previous step, to the target variables. We actually have the desire to evaluate five variables at the target: two spatial and two angular coordinates to resolve the trajectory of the scattered electron (or the recoil proton) as well as its momentum. To reduce this number to four for calibration purposes, as we only have four variables at the focal plane level, one of the five variables, the vertical position of the vertex, is chosen to be set to zero within a 100 μm interval of the origin.

The four remaining variables are expressed in the target coordinate system and have simple physical meanings. The z axis of this coordinate system is defined as the line perpendicular to the sieve-slit surface and going through the center of the central sieve-slit hole. The positive z direction points away from the target. The x axis runs parallel to the sieve-slit surface and points downwards (it follows gravity for a perfectly horizontal spectrometer (which is the assumption)). The y axis is such that the unit vectors of x, y and z axis define a right-handed system ($\vec{u}_x \times \vec{u}_y = \vec{u}_z$). The origin of the coordinate system is defined to be the point on the z axis at a fixed distance from the sieve-slit such that the latter stands at a positive z value. This distance is 1183 mm for the Electron arm target coordinate system and 1174 mm for the Hadron arm target coordinate system. y_{tg} is the horizontal position of the vertex in this system. θ_{tg} is the vertical angle of the particle trajectory or the angle with respect to the z axis in the z-x plane ($\tan \theta_{tg} = \Delta x / \Delta z$). ϕ_{tg} is the horizontal angle of the particle trajectory or the angle with respect to the z axis in the z-y plane ($\tan \phi_{tg} = \Delta y / \Delta z$). The last remaining variable is δ , in relation with the particle momentum as defined further below.

In a first order approximation, the optic tensor reduces to a simple matrix. Furthermore, due to symmetry of the spectrometer magnetic properties, this matrix is block diagonal implying that the four variables actually decouple in two

independent sets of two variables: (δ, θ_{tg}) and (y_{tg}, ϕ_{tg}) .

In practice, the expansion of the target variables upon the focal plane variables is performed up to the fifth order. The transformation is described by a set of tensors, Y_{ijkl} , T_{ijkl} , P_{ijkl} and D_{ijkl} , according to :

$$y_{tg} = \sum_{ijkl} Y_{ijkl} x_{fp}^i \theta_{fp}^j y_{fp}^k \phi_{fp}^l \quad (140)$$

$$\theta_{tg} = \sum_{ijkl} T_{ijkl} x_{fp}^i \theta_{fp}^j y_{fp}^k \phi_{fp}^l \quad (141)$$

$$\phi_{tg} = \sum_{ijkl} P_{ijkl} x_{fp}^i \theta_{fp}^j y_{fp}^k \phi_{fp}^l \quad (142)$$

$$\delta = \sum_{ijkl} D_{ijkl} x_{fp}^i \theta_{fp}^j y_{fp}^k \phi_{fp}^l \quad (143)$$

where any angle θ or ϕ really stands for the tangent of the same angle and δ stands for $\frac{P-P_0}{P_0}$ where P is the measured momentum of the particle and P_0 is the central momentum of the spectrometer.

I should also take the opportunity to specify that this expansion is made possible because all the focal plane variables are relative to some nominal values and therefore render small deviations from those nominal values (spectrometer setting). Another consequence is that the higher the exponent, the less significant in the sum the term is.

Mid-plane symmetry of the spectrometer already mentioned requires $(k + l)$ to be odd for Y_{ijkl} and P_{ijkl} and the same sum to be even for D_{ijkl} and T_{ijkl} .

With suited sets of data, one can perform the optimization of y_{tg} (thin foils target data), then the angles θ_{tg} and ϕ_{tg} , and finally δ (sieve slit data).

7.5 Calorimeter Calibration

The calorimeter has been described in subsection 6.4.3. It is composed of forty eight preshower blocks and ninety six shower blocks. Each of these blocks is associated with an ADC fed by a PMT. The first step in calibrating this detector is to determine the position and width of all the ADC pedestals. The next step is to optimize the gains of the ADCs.

Even though the data acquisition runs in a pedestal subtracted mode to reduce deadtimes, this affects the scintillators information but not the calorimeter information. For every Electron trigger, the readings of all the ADCs of the 144 blocks are recorded. It is therefore possible to extract the pedestal information in any production data run. There is no need for a dedicated pedestal calibration run.

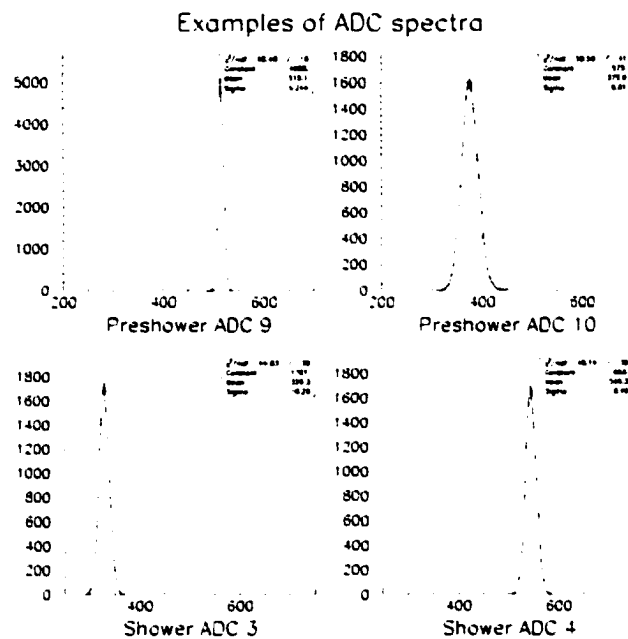


FIG. 34: This figure presents four examples of ADC pedestal spectra. The two top spectra are obtained from ADC number 9 and 10 of the Preshower counter, the two bottom spectra from ADC number 3 and 4 of the Shower counter. The pedestal or empty readings of the ADC devices exhibits a Gaussian shape. The width of the distribution as well as the mean value vary from one ADC to the next.

Fig. 34 presents four examples of pedestal peaks. The two top plots are the ADC spectra obtained from ADC number 9 and 10 of the Preshower counter. The two bottom spectra are obtained from ADC number 3 and 4 of the Shower counter. The spectra are extracted from the raw data file and a Gaussian fit

applied. These examples illustrates that the empty readings of the ADCs, *i.e.* the pedestals, is mostly Gaussian and that the position of the mean value and the width of the distributions may vary from one ADC to the next. While the width of the Preshower ADCs can be characterized by a sigma value of about five ADC channels, it happens that this width goes up to 16.6 channels (ADC 10). The usual sigma of the shower ADCs is 11 channels. The mean value of the peaks ranges from channel 300 to channel 600.

For each event, the total energy deposited in the Preshower and Shower counters is given by the sum of the energy deposited in the cluster of blocks around the reconstructed particle track. The deposited energy in a block is calculated by multiplying the block's ADC signal subtracted by the pedestal mean value by a calibration constant. The second step of the calorimeter calibration consists in determining these calibration constants. A uniform illumination of the focal plane by electrons provides best results. The calibration coefficients are fitted by minimizing the functional

$$\chi^2 = \sum_{k=1}^N \left[\sum_i C_{PSi} (A_{PSi}^k - P_{PSi}) + \sum_j C_{SHj} (A_{SHj}^k - P_{SHj}) - P^k \right]^2 \quad (144)$$

where N is the number of calibration events, i represents the index running on the Preshower blocks included in the Preshower cluster reconstructed in the k^{th} event, j the index of the Shower blocks included in the Shower cluster reconstructed in the k^{th} event, P_{PSi} and P_{SHj} stand for the pedestal mean values determined in the previous step, A_{PSi}^k and A_{SHj}^k are the actual readings of the ADC i of the Preshower and j of the Shower in the k^{th} event, P^k is the electron momentum as reconstructed by a spectrometer analysis, while C_{PSi} and C_{SHj} are the calibration coefficients that are adjusted to minimize the χ^2 of Eq. 144.

Fig. 35 is obtained after calibration. It presents the energy deposited in the Preshower counter as a function of the energy deposited in the Shower counter for Electron triggers. Most of the events stand close to a line corresponding to a constant total energy ($E \simeq 3500$ MeV). Fig. 36 is a spectrum of the energy over momentum ratio. The energy E is obtained by summing the energies in

the Preshower and Shower counters while the momentum p is extracted by spectrometer analysis. A clear peak centered at the value $E/p = 1$ corresponding to electron events can be seen while a background tail extends to small values. The main conclusion, and primary objective of this calibration, concerns the absence of a π^- peak at $E/p = 0.3$, π^- particles that would be created by interactions in the target and travel through the spectrometer up to the detectors. It can therefore be concluded that our VCS kinematics are free of negatively charged pions and only electrons are observed in the Electron arm spectrometer.

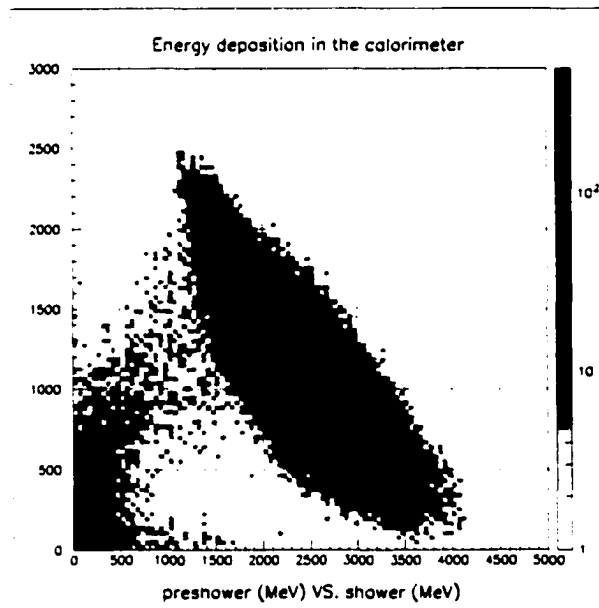


FIG. 35: This figure is a 2-D plot of the energy deposited in the Preshower counter (vertical axis) *vs.* the energy deposited in the Shower counter (horizontal axis). Both axes are expressed in MeV units. The density of events is color coded: the darker the region, the higher the density. The main feature of the picture is that the events are mostly distributed along a line close to the center of the plot. These events correspond to electrons traveling through the spectrometer from the target. The other populated region is at low energy deposition (below 500 MeV in both coordinates). These events belong to a background distribution and are to be rejected. As confirmed by Fig. 36, there is no significant sign of π^- pollution in the Electron arm that would be defined by an energy deposited in the Preshower less than 300 MeV.

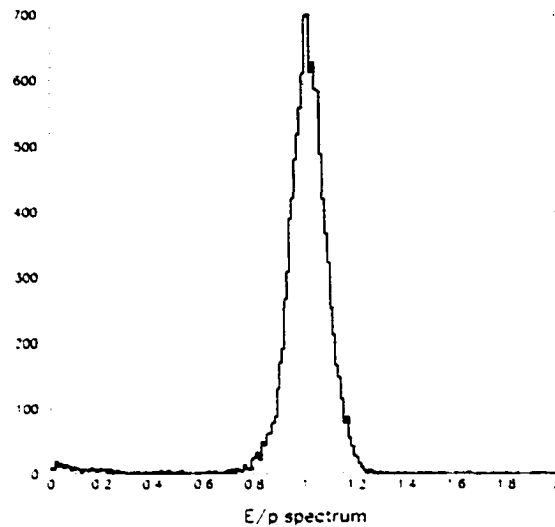


FIG. 36: This figure presents an E/p spectrum. The energy E is the total energy deposited in the Preshower and Shower counters. The momentum p is obtained with the expression $P_0(1 + \delta)$, where $P_0 = 3433$ MeV is the central value of the Electron spectrometer, and δ comes from particle trajectory analysis. The ratio of the previous energy over momentum should be one for electrons. We do observe such a peak centered at one. Except for a small background, there is no other peak centered at 0.3 that would correspond to π^- particles generated in the target and triggering the data acquisition system. The VCS kinematics are then free of π^- in the Electron spectrometer.

7.6 Coincidence Time-of-Flight Calibration

In our VCS experiment, we wish to detect the scattered electron in coincidence with the recoil proton. That means to detect each of the two particles separately and then, due to timing consideration, to try to make sure the two particles actually come from the same reaction vertex in the target.

In practical terms and as the electron always reaches the detectors first in our kinematics, a coincidence time window of 100 ns is opened by the electron trigger.

If any hadron trigger comes within that window, a coincidence trigger is formed by the trigger supervisor (*cf.* section 6.5).

A measure of the time elapsed between the electron and hadron triggers is achieved by means of a coincidence TDC, started by the electron trigger and stopped by the hadron trigger. This is a raw measure though, and corrections to this quantity called coincidence time-of-flight have to be applied for a better use of this timing information to select true coincidences. Indeed, because of competitive reactions like elastic scattering, hadron triggers uncorrelated with electron triggers (different reaction vertices) can fortuitously fall into the coincidence time window. Those events, called accidental coincidences, are treated by the hardware as any valid coincidence triggers. For proper analysis this background must be removed and/or subtracted. Note that the 100% duty cycle of the CEBAF machine is a first hardware try to reduce the ratio of accidental to true coincidences. Chapter 9 and especially subsection 9.1.1 offers more information on accidental coincidences and their subtraction.

The corrections to be applied to the raw measure of the coincidence time-of-flight can be divided into corrections due to particle momentum (and therefore path length in the spectrometer) and corrections due to other effects. These other effects involve fluctuations in the scintillator TDCs compensated by averaging the left and right readings, light propagation effects (dependence on where the particle crossed the scintillator paddle), signal pulse height effects (the discriminators work on a constant threshold mode: a weak signal fires the discriminator later than a strong signal which triggers the discriminator on its sharp rising edge) and overall timing offsets.

The acceptance of each of the spectrometers is large enough to allow detection of particles within a range of momentum what entails slight differences in arrival times on the scintillators and therefore on the trigger times. Indeed, according to the particle momentum, the path inside the spectrometer and the detector package varies with respect to the central trajectory. The path length also varies for the same reason. In an attempt to take that effect into account in the calculation of the coincidence time-of-flight, a parameterization upon the focal plane variables

is undertaken. It takes the following form where $\Delta\ell$ is the path length difference between the actual path length and the path length of particles following the central trajectory:

$$\Delta\ell = \sum_{ijkl} L_{ijkl} x_{fp}^i \theta_{fp}^j y_{fp}^k \phi_{fp}^l \quad (145)$$

following the idea used to obtain target variables (*cf.* section 7.4).

The impact of the previous optimization can be encompassed in Fig. 37 and Fig. 38. The former figure is a *tc_cor* spectrum over a large range of time while the latter figure spans a narrower range. The variable *tc_cor* is the coincidence time-of-flight corrected for all the effects discussed in the paragraphs above. The first thing to be noted on Fig. 37 is a sharp peak standing at a value close to 190 ns that roars far above the ripples on either side of it. This peak corresponds to true coincidence events. The series of smaller peaks correspond to accidental coincidences. This background of accidentals is not flat but is instead an image of the internal structure of the beam. Indeed, a bunch of electrons is delivered on the target every 2 ns, the spacing between two consecutive peaks as can be best seen on Fig. 38. Every event belonging to one of those peaks of accidentals is a coincidence between a scattered electron from one beam bunch and a recoil proton from a reaction vertex induced by an electron from another beam bunch. Accidental coincidence events between two consecutive bunches appear in the first peak of either side of the true coincidence peak, the side depending on which one of the beam electrons associated with the electron trigger and the hadron trigger came first into the experimental hall. The more bunches that separate the two electrons, the further away from the true coincidence peak the event will fall. Note that we also have accidental coincidences within the same bunch that also have to be removed. Finally it is a remarkable success to be able to see the microstructure of the beam so clearly in the coincidence time-of-flight variable.

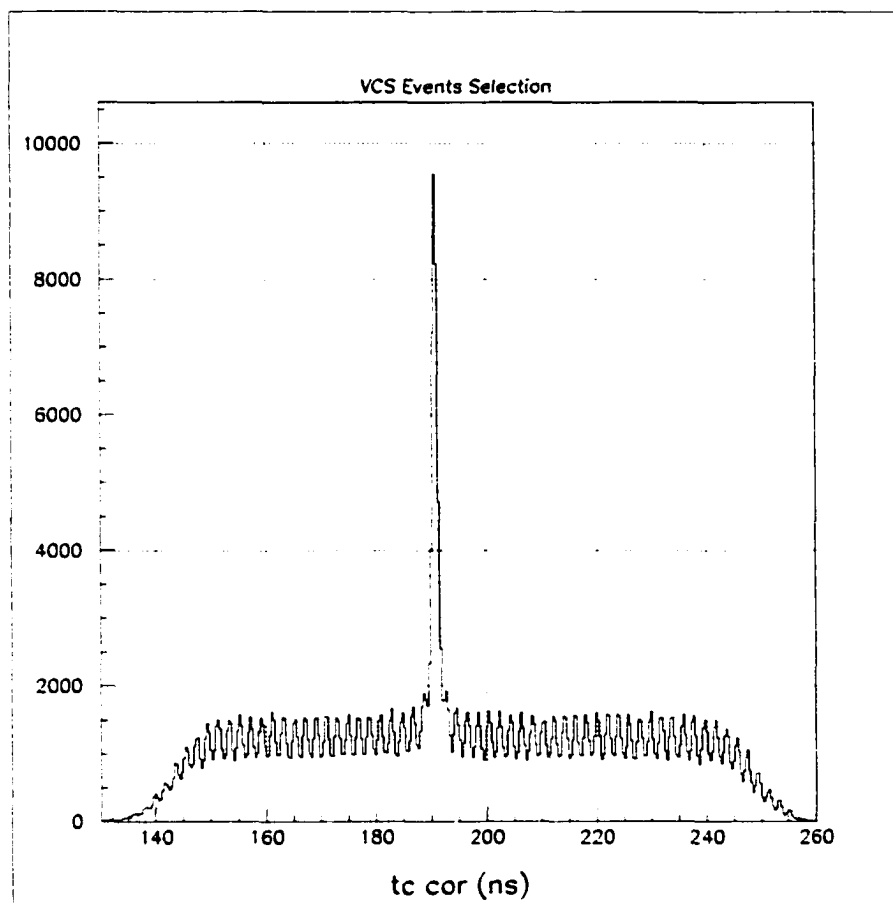


FIG. 37: tc_cor spectrum for run 1589. The true coincidence peak at $tc_cor = 190.3$ ns roars above the accidental coincidence peaks. The latter peaks are due to the time structure of the beam: a beam bunch arrives on the target every 2 ns.

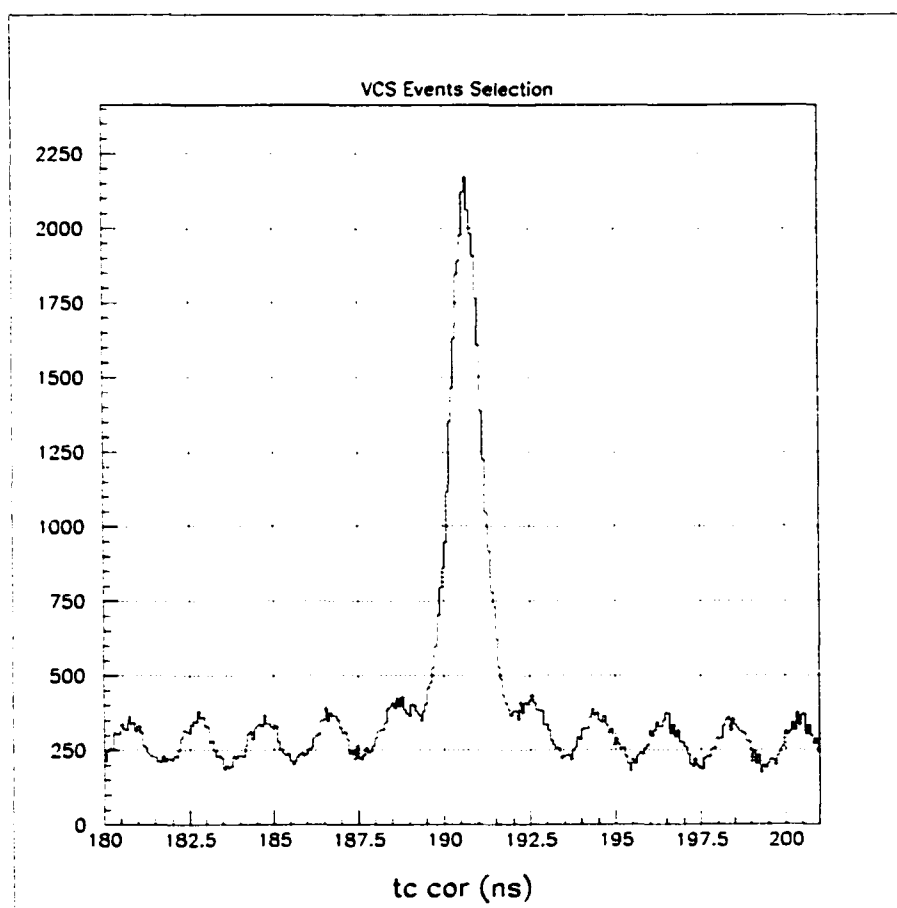


FIG. 38: Zoom of Fig. 37 around the true coincidence peak.

Chapter 8

Normalizations

The goal of this chapter is to treat various corrections that are to be applied in order to correctly evaluate cross-sections. Experimentally a cross-section is evaluated by counting the number of times a reaction under study is observed and then by normalizing with several factors.

A piece of equipment is hardly operational at all times. A first type of hardware limitation that leads to a miscounting is deadtime in the electronic hardware dedicated to data handling. Some events are just dropped or simply ignored because the system is already busy. Computers too have limitations! This study is divided in two parts: trigger electronics deadtime and computer deadtime presented in a first section.

After describing and calibrating the detectors in chapter 6 and 7, we have reached the stage of actual use of those detectors. It is likely that they will not behave perfectly all the time and statistically not react when they should have. We speak of inefficiency. We end up missing some events. Our events counting becomes incorrect. So we have to account for this lack of efficiency to restore a correct counting. The scintillators inefficiencies is treated first. The vertical drift chambers and tracking algorithm efficiency is examined as a global correction in the following section.

The third developed main subject emphasizes the target density effect correction. Even though we regulate the target temperature, local temperature cannot

be maintained. This is especially true along the beam path. The beam electrons going through the liquid Hydrogen material deposit energy by collisions. This is soon transformed into heat, all of which might not be extracted quickly enough. The expected consequence is a density dependence upon beam current intensity. As we ran at various beam current and to take into account this dependence, the normalization factor due to the target density was not treated as a constant and a correction was implemented on each run or part of run collected at a given beam current. The results from a study of target density is reported in the next to last section. This density correction is actually part of a more global normalization factor called luminosity treated in the last section of this chapter.

8.1 Deadtimes

8.1.1 Electronics Deadtime

The correction addressed in this subsection belongs to the category of corrections that aim to correct for trigger undercounting due to valid triggers that actually never made it as such. The first reason for that is scintillator inefficiencies. One or more PMT failed to provide a detection signal leading to a failure in forming a valid data acquisition trigger. I shall detail how we recover from this phenomenon in section 8.2.

For the moment, I want to concentrate on the fact that the trigger electronics system itself can fail to form valid triggers on the account of high input rates. Indeed when the system treats one event, it is busy trying to resolve it. Any other event coming too soon on the input lines cannot be integrated and information is discarded. This is called electronics deadtime.

Each arm has a first stage trigger related analysis by electronics independent of the other arm. Therefore a correction factor exists for each of the two arms. In Fig. 39, the electronics deadtimes in the Electron arm and for the Hadron arm are displayed on the same plot as a function of run number.

First, it can be checked that the Hadron arm deadtime is lower than the

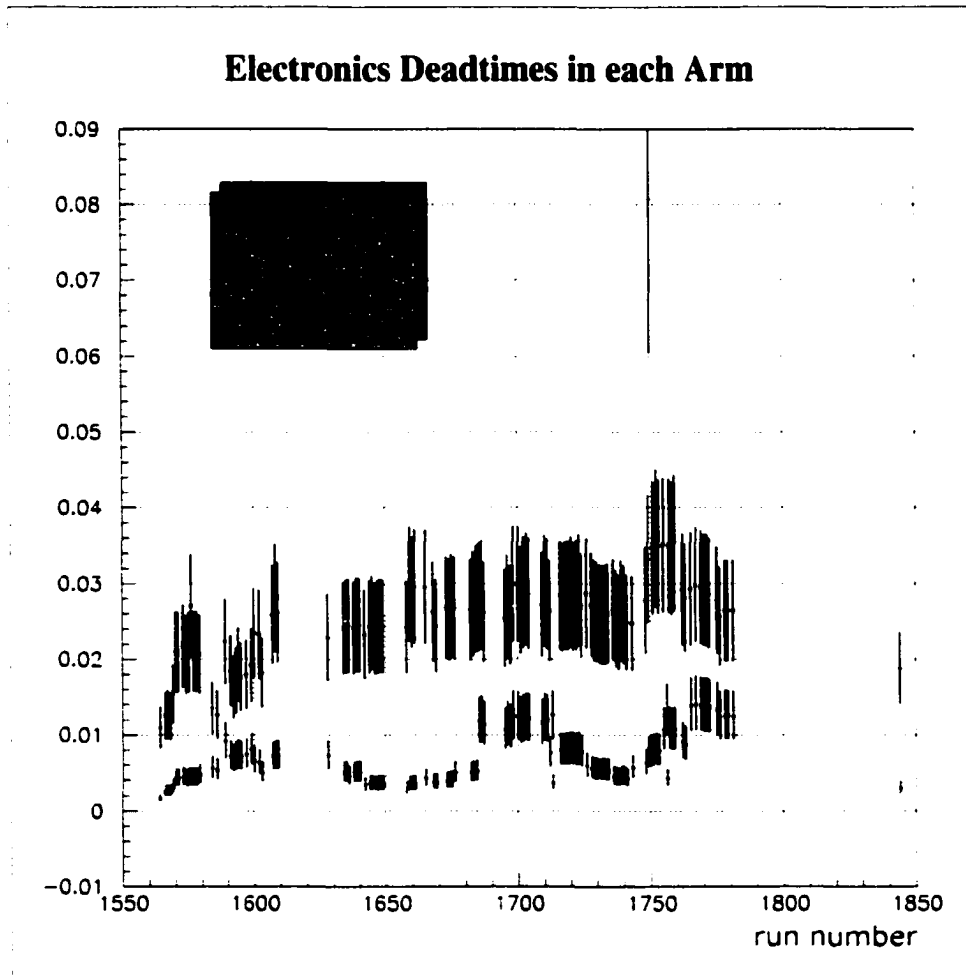


FIG. 39: Electron and Hadron arm electronics deadtimes (E edt and H edt) as a function of run number. The Electron arm deadtime ranges between 1 and 4% while the Hadron deadtime stays below 1.5%.

Electron arm deadtime implying that the input rates at the trigger system in the Hadron arm is lower. This is to be expected since the elastic scattering process is within the acceptance of the Electron arm inducing large raw counting rates while the Hadron spectrometer settings have been chosen to emphasize VCS kinematics and reduce overflow from elastic and radiative elastic events (Bethe-Heitler process especially). Thus no large raw counting rates are expected in the Hadron arm.

The range of the Electron deadtime is about 2% between 1 and 4% inducing a correction of the same order. The Hadron deadtime spans between 0.2 and 1.4 %.

When analyzing in single arm, only one of these deadtimes would have to be corrected for, depending on which arm is being investigated. But for a VCS analysis, coincidence events are required and both deadtimes have to be incorporated.

Another quick but interesting study that was performed is the dependence of these deadtimes upon beam current intensity. The results can be seen on Fig. 40. It can be checked on the top plot that the deadtime in the Electron arm follows a nice linear dependence except for a few runs. The errors are apparently overestimated since the χ^2 value of the fit is very small.

On the other hand, the Hadron arm deadtime does not follow such a linear fit (middle plot in Fig. 40). That is an indication that the counting rate in this arm is not solely induced by the beam. Some setting dependence starts to appear here. This might also be a first introduction to the “punch through” problem: some protons go into the acceptance of the Hadron spectrometer and therefore to the detector package whereas they should not do so. This leaking into the acceptance is one of the biggest pollution in the analysis. (*cf.* chapter 9.)

8.1.2 Prescaling

In the previous section, counting problems occurring before the trigger supervisor were considered. In this subsection and the next, everything happening at and after the trigger supervisor is investigated.

First of all, the data acquisition system cannot handle every single event due to the time needed to read out the detectors, format the information and then

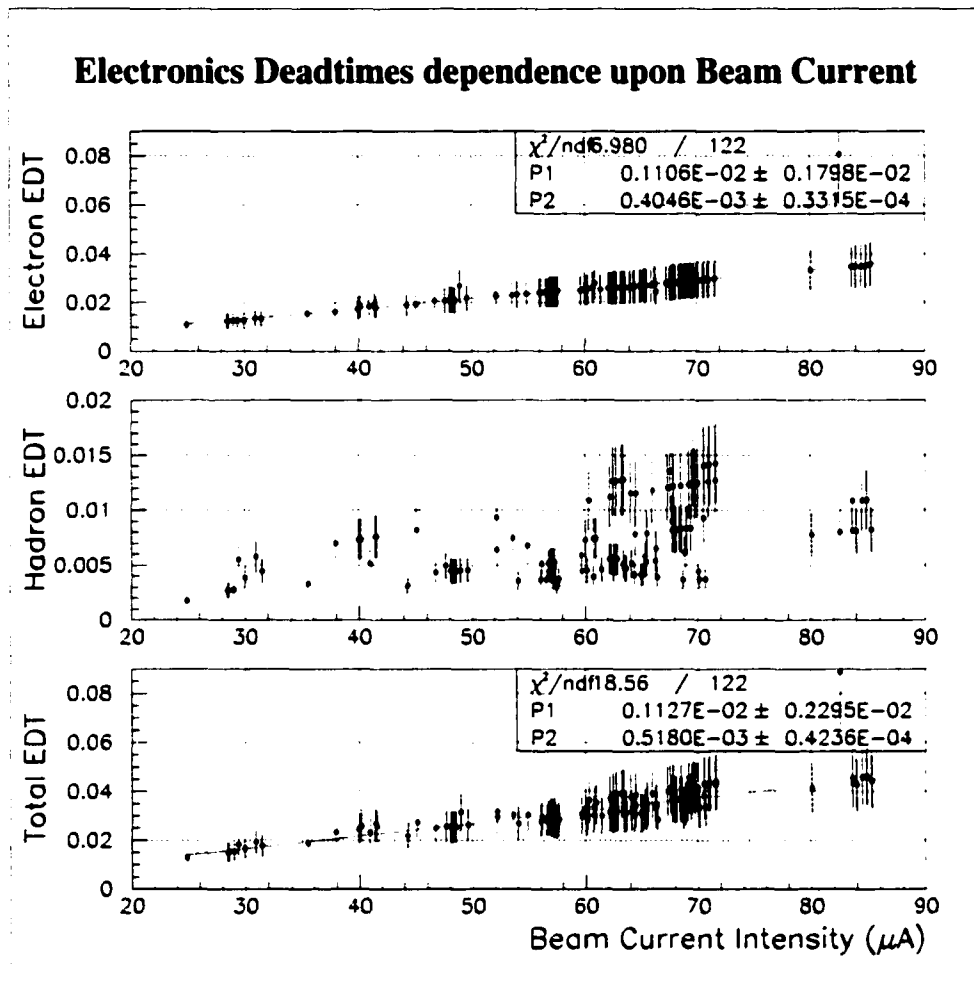


FIG. 40: Electron arm, Hadron arm and total electronics deadtimes as a function of beam current intensity. The Electron arm deadtime (top plot) follows a nice linear fit (intercept of 0.1% and slope of 4% per 100 μA). The Hadron arm deadtime (middle plot) does not show such behavior. The bottom plot displays the combined deadtime.

write it out into a data file. So a first sampling occurs at the trigger supervisor. This intentional decrease of the number of events is achieved with prescale factors. Each trigger type S_i has its own prescale factor and a set value psi means that only the psi^{th} event of type S_i is let through the rest of the acquisition chain.

The other flexibility allowed by those prescale factors is the possibility to favor more or less one trigger type with respect to the other types in the recorded data file. A high value for one given trigger type will clearly reduce the number of recorded event of that type as only one out of psi events are considered for recording.

T_2 and T_4 events are recorded mainly for scintillator efficiency study and are not especially favored since not containing clean physics information. The T_1 portion is also greatly reduced because of high raw counting rate that would otherwise lead to an overflow of the coincidence events which are the true interesting events in coincidence experiments such as VCS. Note that in addition to the previous facts and other hardware preferentialism, the T_5 prescaler is set to one so that no T_5 event (coincidence event) would be discarded.

The set of prescale values can be chosen on a run-by-run basis. A compromise is made for a good balance between all trigger types according to the needs of the analysis and for an overall event rate that do not overwhelm the data acquisition. Nevertheless the average event rate is not reduced too much so as to have a data acquisition system always working and never idle. Doing so the later system sustain deadtime which is called Computer Deadtime in this analysis.

8.1.3 Computer Deadtime

The number of events actually recorded onto file does not match the number of events accepted at the trigger supervisor. This is due to an intentional slight overload of the data acquisition system. The resulting deadtime can also be due to other factors like network and data acquisition computer activity. Glitches or short periods of increased deadtime has been observed.

Once again, in order to restore a precise counting for cross-section purposes,

the computer deadtime has to be evaluated and corrected for. The method of estimation consists in evaluating the average number of missing events over a period of time. This is achieved thanks to counting scalers. Indeed events fed into the trigger supervisor are counted before treatment. (*cf.* section 6.5) Those numbers, one for each raw trigger type S_i , when divided by the corresponding prescale factor, yield the number of events that should be in the raw data file in absence of deadtime. A difference with the number of events actually present in the data file is enough to obtain the number of missing events and therefore the deadtimes.

One has to be cautious though to the fact that accepted (or recorded) trigger types T_i are exclusive. In particular, a T_5 event is formed after a coincidence in both arms but is not counted as a T_1 or T_3 whereas this same event was counted as an S_5 but also as an S_1 and S_3 . Keeping that in mind, we can express the five livetimes LT_i as:

$$LT_1 = \frac{ps1 T1}{S1 - S5} \quad (146)$$

$$LT_2 = \frac{ps2 T2}{S2} \quad (147)$$

$$LT_3 = \frac{ps3 T3}{S3 - S5} \quad (148)$$

$$LT_4 = \frac{ps4 T4}{S4} \quad (149)$$

$$LT_5 = \frac{ps5 T5}{S5} \quad (150)$$

The deadtimes DT_i are just $DT_i = 1 - LT_i$ and the correction factors for each trigger type are:

$$\frac{1}{LT_i} = \frac{1}{1 - DT_i} \quad (151)$$

For illustration, the five computer deadtimes are plotted as a function of run number on Fig. 41. No particular dependence upon beam current can be observed and the correction factor has to be applied on a run-to-run basis.

As a result of the prescale factors, the deadtime correction factors are different for different trigger types. Indeed, for a trigger type with a unit prescale factor,

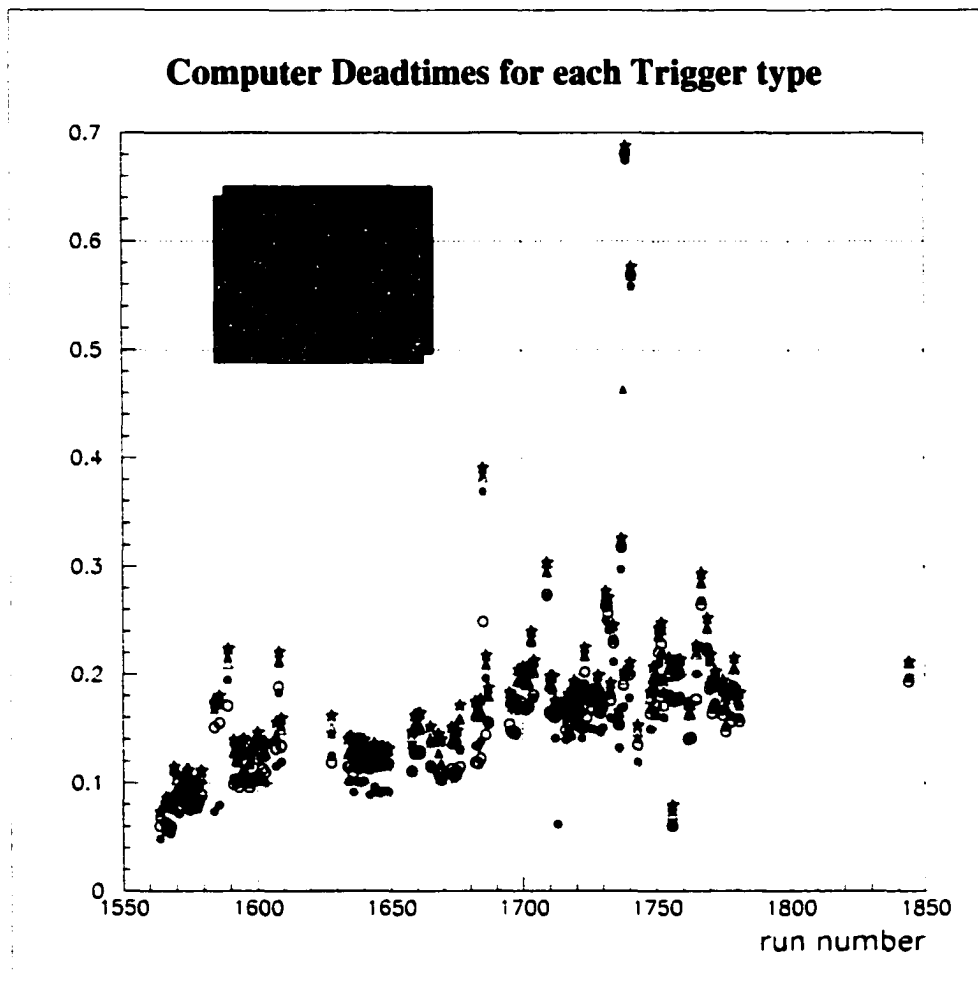


FIG. 41: The computer deadtimes for each of the five main trigger types are displayed as a function of run number. Runs with excessive deadtimes are rejected for the analysis. The deadtimes range from 5 to 30%.

the time distribution between events is:

$$P(t, 1) = \frac{1}{\tau} e^{(-\frac{t}{\tau})} \quad (152)$$

where τ is the mean time to wait between two triggers. For a trigger type with a prescale factor ps , the time delay distribution is:

$$P(t, ps) = \frac{1}{\tau} \left(\frac{t}{\tau}\right)^{ps-1} \frac{1}{(ps-1)!} e^{(-\frac{t}{\tau})} \quad (153)$$

with a mean time $ps\tau$ between triggers. This gives a lower deadtime correction, even at the same rate.

8.2 Scintillator Inefficiency

8.2.1 Situation

The scintillator efficiency correction is part of a bigger correction, namely the trigger efficiency correction. In order to accurately evaluate an absolute cross-section, it is necessary to count the good events and to account for anyone missing. What we want to correct for here, is the fact that a valid trajectory could fail to form a trigger due to scintillator inefficiency.

As already described in subsection 6.4.1, scintillation light is emitted when a particle travels through the scintillator material. This light is collected and the signal amplified by a PMT. The PMT signal is then sent to a discriminator which creates a logic pulse or not depending on whether or not the signal amplitude is greater than a threshold value. Each side of each paddle is associated with a PMT. Thus, each side of each paddle can be checked for a logic signal. Each scintillator plane should have a signal on each side of one of its paddles and the two hit paddles should be in an S-ray configuration in order for the logic system to label the event as good. If for any reason (PMT weakening with age, deteriorated scintillator material, *etc.*) at least one of the four required signals is missing, a good trigger will not be formed. For any such event, the scintillator inefficiency label will be invoked.

To measure this inefficiency, data are recorded even though the trigger logic decided not to label those events as good. A special trigger was created to record a sample of events without a valid $T1$ trigger configuration. Those events are of type $T2$ in the Electron arm and $T4$ in the Hadron arm. (*cf.* section 6.5 for further details.)

In a first approach to the problem, let us consider each scintillator plane as a whole. From the trigger point of view, we have an inefficiency if one or both planes failed to fire. It is actually more precise to say that the logic system failed to find a left-right coincidence in one or both planes. As a reminder, a left-right coincidence happens when the signals from the left side and the right side of one paddle are strong enough to make it past the discriminator threshold. The trigger inefficiency can then be written as:

$$\eta_{trigger} = p(\mathcal{S}1 \downarrow, \mathcal{S}2 \uparrow) + p(\mathcal{S}1 \uparrow, \mathcal{S}2 \downarrow) + p(\mathcal{S}1 \downarrow, \mathcal{S}2 \downarrow) \quad (154)$$

where $p(\mathcal{S}1 \downarrow, \mathcal{S}2 \uparrow)$ is the probability of having scintillator $\mathcal{S}1$ inefficient and scintillator $\mathcal{S}2$ efficient for instance. Similarly, the trigger efficiency can be written as:

$$\epsilon_{trigger} = p(\mathcal{S}1 \uparrow, \mathcal{S}2 \uparrow) . \quad (155)$$

One has to keep in mind that the S-ray configuration has to be imposed on the geometry of the track. This condition does not appear in the previous formal equations simply because it is imposed on all terms. One can check that no case has been left out and we do have:

$$\epsilon_{trigger} + \eta_{trigger} = 1 . \quad (156)$$

The trigger efficiency correction factor due to scintillator inefficiency can then be expressed as:

$$te_{C_{trigger}} = \frac{1}{\epsilon_{trigger}} = \frac{1}{1 - \eta_{trigger}} . \quad (157)$$

Denoting η_1 the inefficiency of scintillator $\mathcal{S}1$ and ϵ_1 its efficiency and using similar notations for $\mathcal{S}2$, we have:

$$\eta_{trigger} = \eta_1 \epsilon_2 + \epsilon_1 \eta_2 + \eta_1 \eta_2 \quad (158)$$

$$\epsilon_{trigger} = \epsilon_1 \epsilon_2 \quad (159)$$

$$teC_{trigger} = \frac{1}{\epsilon_1 \epsilon_2} = \frac{1}{1 - \eta_1} \times \frac{1}{1 - \eta_2} \quad (160)$$

Basically this is showing that we need to know both inefficiencies (or efficiencies) if we want to correct for trigger undercounting due to the scintillator inefficiency. On the other hand, those two inefficiencies are uncorrelated. One can just determine one and then the other independently with whatever method pleases. Nevertheless it is very tempting to use one scintillator plane to calibrate the other one. Indeed if one plane fires, it is already a hint that the other plane did or should have fired. The actual method used to determine inefficiencies exposed in this document follows this idea of using one plane to evaluate the inefficiency of the other one and is exposed in the next subsection.

8.2.2 Average efficiency correction

In an attempt to address this scintillator efficiency correction, a first study was conducted using the following method.

Of course raw information from the trigger is used: $T1$ are good events and $T2$ are potentially good events for which one can be assured that there already is one left-right coincidence in one plane and that the gas Čerenkov detector fired, improving chances that the event is formed after a real electron going through the system. ($T3$ and $T4$ are used for Hadron arm efficiencies.)

We restrict our sampling to events for which one plane was efficient to evaluate the inefficiency of the other plane. Indeed $T2$ events do not include events with double inefficiency for they look too much like garbage events that one does not want to waste computing time on. So we use a subset of the whole populations of $T1$ and $T2$ triggers, namely the subset of events where $S2$ was efficient when $S1$ inefficiency is evaluated and the subset of events where $S1$ was efficient when $S2$ inefficiency is evaluated. This does not bias the results since the probability of $S1$ being inefficient is independent of what is happening in $S2$.

We even further restrict the sampling to events with a very clean signature in the not investigated plane. We request on the $T1$ events that only one paddle was

hit, *i.e.* only one PMT fired on the left side of the reference scintillator and the corresponding right PMT alone fired as well. The principal use of this software cut is to ensure a perfect coincidence when digging out among the $T2$ events for which the eventual coincidence proof from the logic electronics has been lost. This also helps to impose the S-ray configuration pattern on the $T2$ triggers.

Finally it has been decided to apply the scintillator inefficiency correction on an event-by-event basis instead of a global correction. Doing so local inefficiency differences are taken into account. Such local variations are, for instance, due to a specific weak paddle or geographical variations within a paddle (edges, weak spot, *etc.*).

A grid divides a scintillator plane into two-dimensional bins. Each bin has its own correction coefficient. The width of the bins in the non dispersive direction is uniform. In the dispersive direction, it is not the case and the bins are smaller at the edges of the paddle to take into account the fact that the edges are less efficient. Tracking information helps figuring out what specific bin the particle went through.

The inefficiency of one bin in the $S1$ scintillator plane can be written as:

$$\eta_1(x_i, y_j) = \frac{N(S1 \downarrow, S2 \uparrow)}{N(S1 \uparrow, S2 \uparrow) + N(S1 \downarrow, S2 \uparrow)} \quad (161)$$

where, for instance, $N(S1 \downarrow, S2 \uparrow)$ stands for the number of events for which the tracking indicates a trajectory intersecting that bin, $S2$ is efficient, $S1$ is not and the S-ray pattern is validated. A more practical formula would be :

$$\eta_1(x_i, y_j) = \frac{ps2 \times N_{T2}}{ps1 \times N_{T1} + ps5 \times N_{T5} + ps2 \times N_{T2}} \quad (162)$$

where N_{Ti} stands for the number of trigger of type Ti that passed the software cuts:

- For $T2$ events: only one paddle in $S2$ was hit, the trajectory is reconstructed through the bin in the $S1$ plane, one signal from the paddle in $S1$ that corresponds to the bin is missing and the S-ray configuration is validated).
- For $T1$ or $T5$ events: the trajectory goes through the bin and only one paddle in $S2$ fired.

The prescale factors psi take care of restoring the actual numbers of events that arrived at the input of the trigger supervisor since only a fraction of one out of psi triggers of type Si are considered for being written on file.

The main results of this study consist in the following facts:

- Some paddles worked less efficiently than others.
- Even within a paddle, local efficiency variations are observed (edges less efficient).
- The hadron arm planes were very efficient and the corresponding correction could easily be neglected.
- A time dependence is observed.

The only visual result shown here is the time evolution of the partial trigger efficiency correction factor (tec) for each of the four planes averaged over each plane (weighted average over the bins). Fig. 42 displays the four coefficients as a function of run number. Only runs belonging to the Polarizabilities data set at $Q^2 = 1 \text{ GeV}^2$ were used.

8.2.3 A closer look

Presented here is a closer look at the spatial distribution of the scintillator inefficiency.

As shown in the previous subsection, only the Electron arm scintillator planes present a substantial need for correction even though, on average, the correction does not exceed 2% for the data set studied in this document.

In this subsection, the inefficiencies will be averaged on the transverse coordinate y (along one paddle) in order to concentrate on the distribution along the dispersive coordinate x where most of the variations have been observed so far.

Except for a finer binning, this study also incorporate specific computer dead-times. Each trigger type events are not discarded in the same proportion. As a reminder, this discarding happens when the computer in charge of events recording

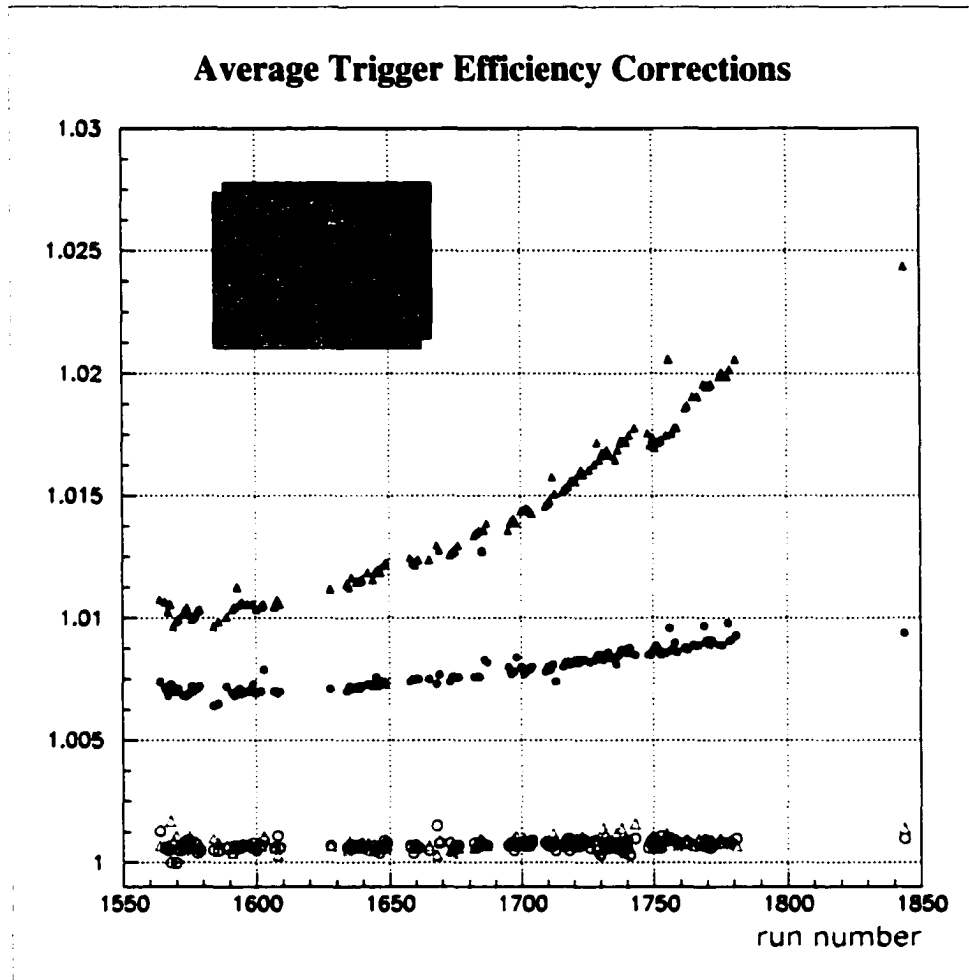


FIG. 42: Time evolution of the four partial trigger efficiency coefficients averaged over each plane. The corrections in the Hadron arm can be neglected on the grounds of being very small. They indeed stay below 0.1%. The corrections in the Electron arm do not exceed 2% for most of the runs but a time evolution is clearly visible. These runs span five days of data taking. This somehow rapid deterioration is attributed to an Helium leakage that induced a rapid deterioration of the coating of the PMT entrance windows.

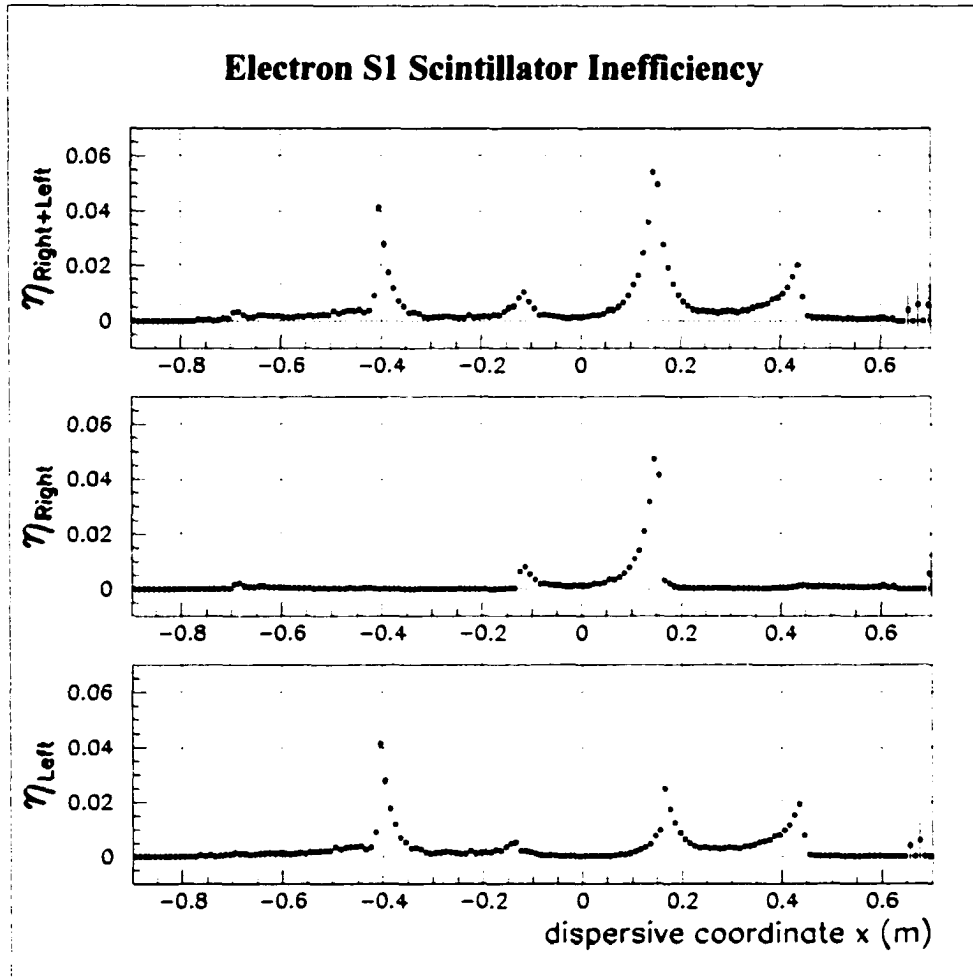


FIG. 43: Electron $S1$ scintillator inefficiencies as a function of the x coordinate. The inefficiencies are averaged over the non dispersive direction y . The top plot presents the inefficiencies where no distinction is made whether the left side or the right side was inefficient. The middle plot presents the inefficiencies due to the right side only while the bottom plot is for the left side only. On these plots the paddle edges can be located because of an increase of inefficiency. Only one paddle was inefficient from the right side point of view. The inefficiencies go up to 6% at some edges: local variations are big.

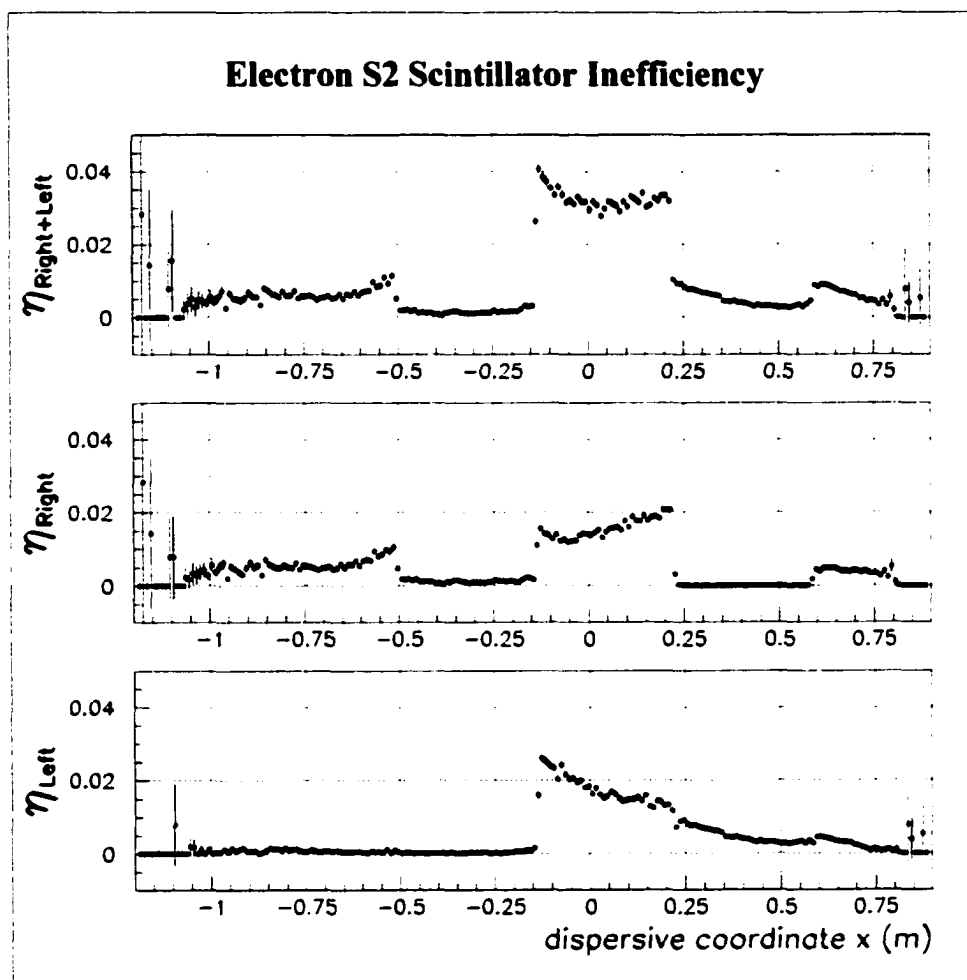


FIG. 44: Electron $S2$ scintillator inefficiencies as a function of the x coordinate. We again see the edges of the paddles because of sudden change in efficiency. In contrast with the $S1$ plane, the inefficiencies do not reach values greater than 4% but paddle 4 was consistently inefficient. The PMTs of that paddle were changed later in the experiment.

cannot catch up with the rate it is asked to write out events (*cf.* subsection 8.1.3 about computer deadtime). This deadtime has to be corrected for and one could implement it as a correction to the prescale factors. Indeed the ratio of the number of raw triggers, formed by the trigger system and counted in scalers, with respect to the number of events accepted by the trigger supervisor and actually written onto tape depends on the trigger type. This ratio can be written as the product of the prescale factor times the computer deadtime correction. Stated formally by an equation, we have:

$$\frac{\text{formed } S_i}{\text{recorded } T_i} = \frac{psi}{1 - cdt_i} \quad (163)$$

where cdt_i is the computer deadtime of trigger type S_i . These effective prescale factors defined by Eq. 163 replace the prescale factors in Eq. 162 of the inefficiency

Fig. 43 illustrates the behavior of the Electron scintillator plane $S1$ while Fig. 44 is for the $S2$ plane. The inefficiencies of the right side, left side and both sides combined are plotted as a function of the dispersive x coordinate at the scintillator while averaging on the non dispersive direction y . It can be observed that the edges of the paddles are less efficient than the middle sections (especially in $S1$). There was also one bad paddle in $S2$ whose PMTs were changed. This restored the efficiency. Even if globally the inefficiency was less than 2%, big discrepancies with that averaged value are locally observed.

The presence of overlap regions between two paddles can also be checked. Fig. 45 is a spectrum of the position of the tracks in the $S2$ plane for events for which two consecutive paddles fired. The presence of overlap regions can also be checked in the $S1$ plane in the same way.

In these overlap regions, the inefficiency is not given by only one paddle anymore but is driven by the coupling of the two overlapping paddles. Indeed if one fails to register the track, maybe the other did not. In order to have an inefficiency in the overlap regions, both paddle must fail to fire. This double requirement of detection failure translates into the fact that, in these overlap regions, the inefficiency of the scintillator plane is the product of the inefficiencies of both paddles. Of course that reduces the inefficiency of the detection in these regions. A drop

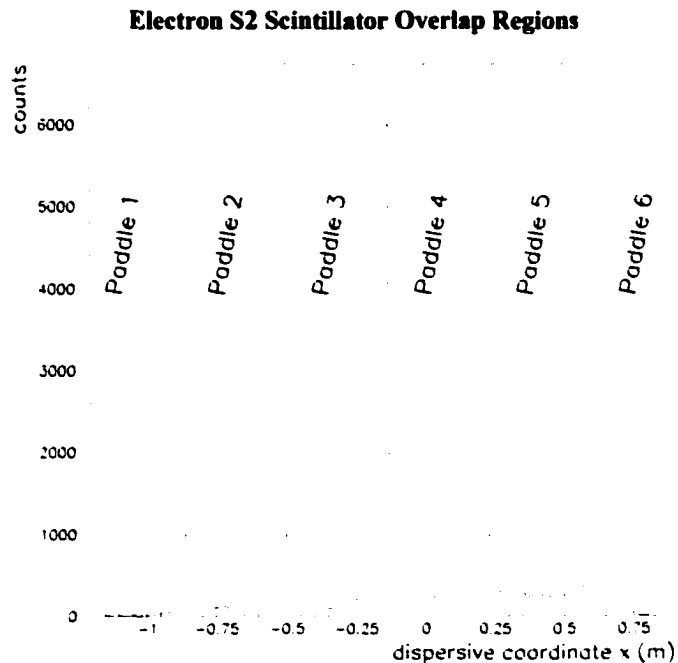


FIG. 45: Spectrum of the position of the tracks in the $S2$ plane for events for which two consecutive paddles fired. The presence of overlap regions is confirmed by the sharp peaks on this spectrum.

in inefficiency should therefore be visible on graphs such as those on Fig. 43 and Fig. 44 when the binning in the variable x is increased. On these latter plots, one can already guess this effect but Fig. 46 zooms in the overlap region between paddle 4 and 5 in the Electron $S1$ plane and the effect is clearly visible. Indeed, on this last figure, a slow decrease of the inefficiency due to paddles starting to overlap is visible (starting at $x \simeq 15.3$ cm). Then the inefficiency reaches a minimum value. It stays low if the next paddle is totally efficient (case of the right side inefficiency pictured in the middle plot). If not (case of the left side pictured in the bottom plot), the scintillator inefficiency rises again until the paddles start to stop overlapping.

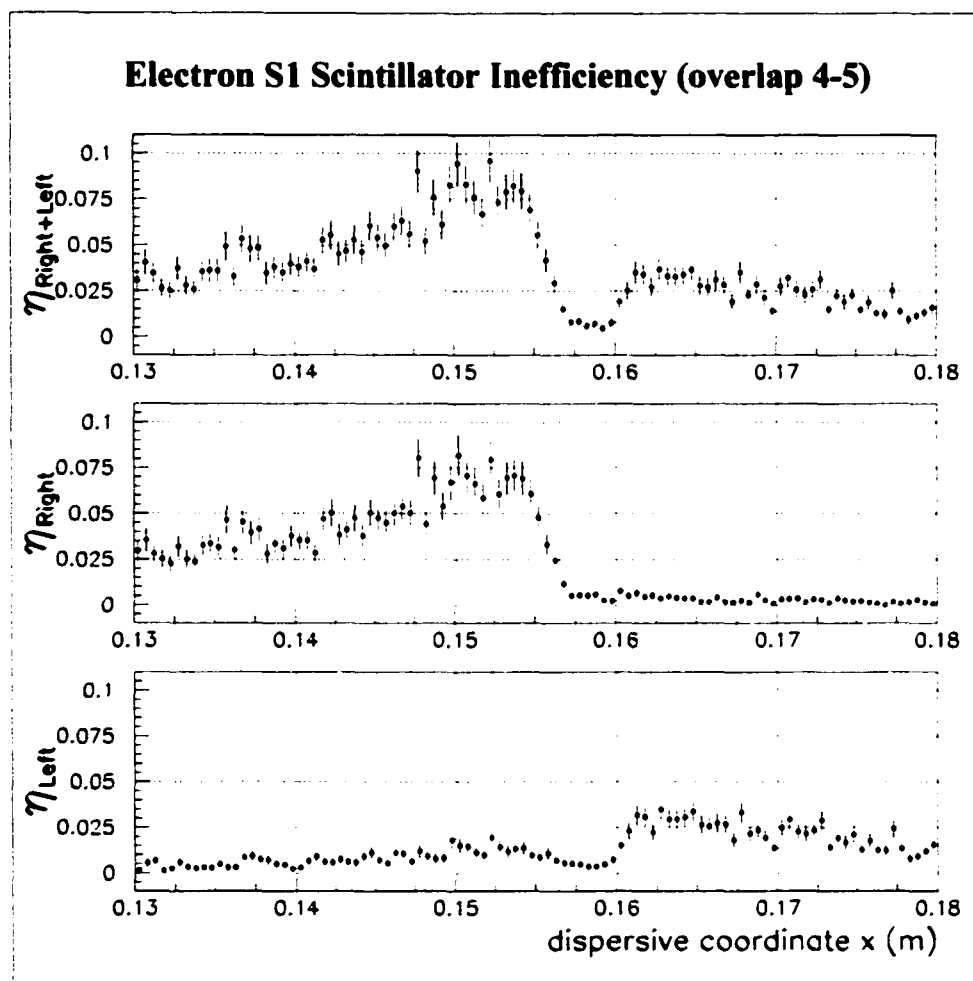


FIG. 46: This figure presents the inefficiencies of the Electron $S1$ plane when zoomed in an overlap region between paddles (overlap region between paddle 4 and 5). the top plot is the inefficiency plot as a function of the dispersive coordinate x when no distinction is made whether the missed trigger is due to the right PMT or the left one failing to fire the discriminator. The middle plot is for the right side of the scintillator only while the bottom plot is for the left side. A decrease in inefficiency is obvious when the paddles overlap. One can even observe a slowly decrease when the paddle start to overlap and a minimum before the inefficiency rises again until the paddles start to not overlap anymore. Note that inefficiencies can reach 10% very locally.

8.2.4 Paddle inefficiency and fitting model

In the previous subsections, we studied the inefficiency of each scintillator considered as a whole with an inefficiency averaged over the plane. We concluded that the Hadron scintillator planes presented very low inefficiencies and that a correction was not mandatory. Concerning the Electron scintillator planes, low (less than 2%) but not negligible average inefficiencies were observed and had to be corrected for. A time dependence was also observed requiring at least a run-to-run correction. A somewhat coarse grid was defined to correct also for spatial dependence. The scintillator efficiency correction was then implemented on an event-by-event basis.

We then refined the grid. Inefficiency dependence upon the x coordinate was carefully studied, averaging only on the y coordinate of the particle trajectories at the scintillator plane. We concluded that the paddles behave differently, that the right and left sides of each paddle can also behave differently, that we can observe reduced inefficiencies where two paddles overlap and finally that inefficiencies can reach high values such as 10% locally in the Electron $S1$ scintillator plane.

In the present subsection, a study of the inefficiency dependence upon the y coordinate is investigated. The left and right sides are studied separately as they correspond to different PMTs which can be deteriorated differently. A fine grid is defined and the inefficiency values observed as a function of both x and y coordinates. Fig. 47 present the results obtained for the right side of paddle 4 of the Electron $S1$ scintillator.

After investigating the inefficiency distributions in the Electron $S1$ plane and especially in paddle 4, it was found that an exponential shape was relevant for the y dependence. The method was the following. For each bin in y in a grid such as that of Fig. 47, the x distributions were extracted. One x distribution was chosen as reference and the other ones normalized to it. A weighted average of the previous relative inefficiencies was calculated for each bin in y . The results were plotted as a function of the central y value of the bins and this distribution fitted by an exponential.

To explain the fact that the paddle edges are less efficient than the central

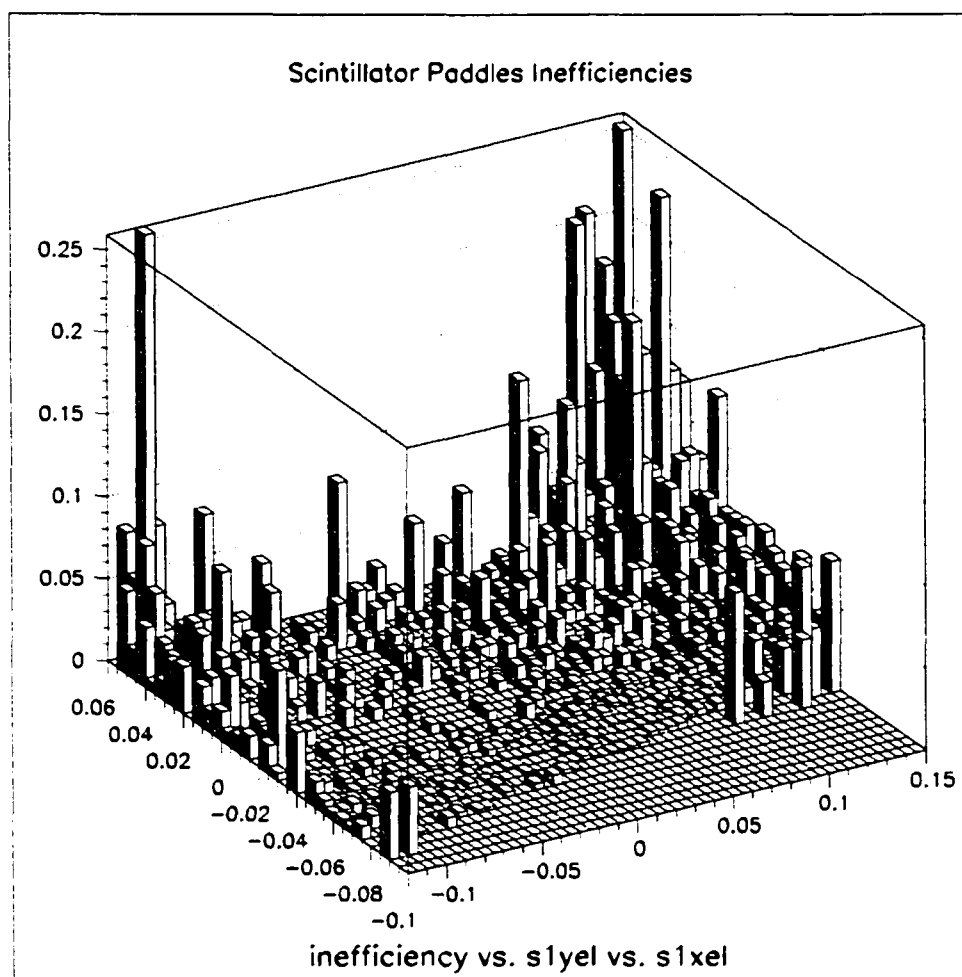


FIG. 47: This figure is a 2-D plot of the inefficiency of the right side of paddle 4 of the Electron $S1$ scintillator as a function of both x and y trajectory coordinates expressed in meters. The vertical axis is dedicated to inefficiencies. $s1yel$ stands for the y position of the particle when it crossed the scintillator plane. The graduation marks of its axis are located in the bottom left corner. The span in y is divided into 32 bins 5 mm wide. The x position axis is the almost horizontal axis on the plot. The overlap regions between paddles have been removed since relevant of two paddles. The remaining extension is divided into 54 bins 2.5 mm wide. The spatial variations of the inefficiency can be visualized. One can see high inefficiencies on the edges of the paddle. The inefficiencies also increase with the y value as we move further away from the right PMT. Locally, in the corner at large positive values for x and y , the inefficiency can reach 10, 15 or even 20%.

part at constant y value, the parameterization of the inefficiency has the following form:

$$\eta(x, y) = A(x) e^{\beta y} \quad (164)$$

where β parameterizes the y dependence and where the x dependence of the inefficiency is explicitly contained in the normalization constant $A(x)$. A direct fit of $A(x)$ in a given y bin proved to be too difficult. The following idea was then investigated. Every bin in x has the same y dependence parameterized by β . The x dependence is implemented as an offset to y such that the inefficiency reads:

$$\eta(x, y) = A e^{\beta(y - y_{off}(x))} . \quad (165)$$

The offset y_{off} depends on x such that a given inefficiency is reached at a varying position in y for varying x positions. An iso-inefficiency curve can then be built. The inefficiencies are evaluated in bins centered at (x_i, y_{0i}) where there is a lot of statistics and where i runs on the number of bins in x . These inefficiencies are noted η_{0i} . We can now write the inefficiency parameterization as:

$$\eta(x_i, y) = \eta_{0i} e^{-\beta y_{0i}} e^{\beta y} . \quad (166)$$

A reference bin in x is chosen. The inefficiency value is η_{0ref} at y_{0ref} in that bin. The inefficiency is therefore $\eta_0 = \eta_{0ref} e^{-\beta y_{0ref}}$ at $y = 0$. we can then solve for y_i , the y value for which the inefficiency in bin i in the x coordinate is η_0 , in the following equation:

$$\eta(x_i, y_i) = \eta_{0i} e^{-\beta y_{0i}} e^{\beta y_i} = \eta_0 = \eta_{0ref} e^{-\beta y_{0ref}} . \quad (167)$$

We obtain the set of values:

$$y_i = y_{0i} - y_{0ref} - \frac{1}{\beta} \ln \left(\frac{\eta_{0i}}{\eta_{0ref}} \right) \quad (168)$$

that are plotted as a function of x_i . A polynomial fit yields the iso-inefficiency curve $y_{off}(x)$. The inefficiency function is now:

$$\eta(x, y) = \eta_0 e^{-\beta y_{off}(x)} e^{\beta y} . \quad (169)$$

The distribution in y is then rebuilt by weighting every events available over the paddle area (multiplying by $e^{\beta y_{off}(x)}$). The distribution is fitted by an exponential function and values for β and η_0 are extracted.

We then rebuild the iso-inefficiency curve with the new value of the β parameter. We evaluate again the weighted distribution in y with the new iso-inefficiency curve to extract better fitting values for β and η_0 . Iterations can be made.

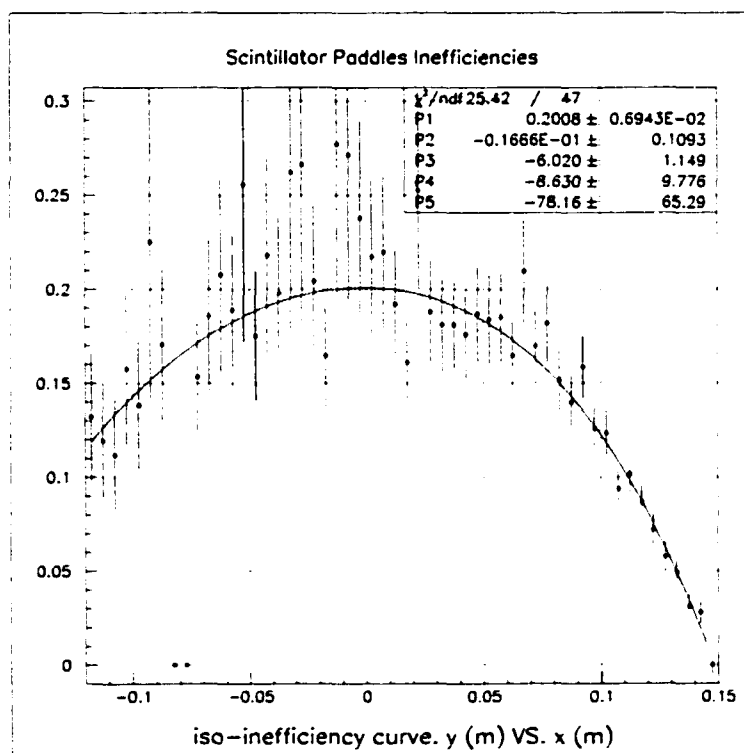


FIG. 48: Iso-inefficiency curve for the right side of paddle 4 of the Electron scintillator $\mathcal{S}1$ obtained after one iteration. The coefficients P_i of the polynomial fit ($y_{off}(x) = \sum P_i x^i$) are displayed at the right corner of the plot. The last bin in x on the right has been chosen as bin of reference. The inefficiency at $x = 0$ cm is the same as that at $x = 15$ cm if moving about 20 cm further away from the PMT ($y_{off}(0) \simeq 20$ cm).

Fig. 48 is the iso-inefficiency curve obtained for the right side of paddle 4 of the Electron scintillator $\mathcal{S}1$. The result of a polynomial fit is displayed. The even

power of the polynomial is imposed on the grounds that the inefficiency is greater on the sides than in the central part and should not decrease again further away if the overlap regions have been removed from the data set used. For this particular paddle side, the iso-inefficiency curve indicates that a region at $x = 0$ cm is as inefficient as a region at $x = 15$ cm if the distance in y between them is about 20 cm.

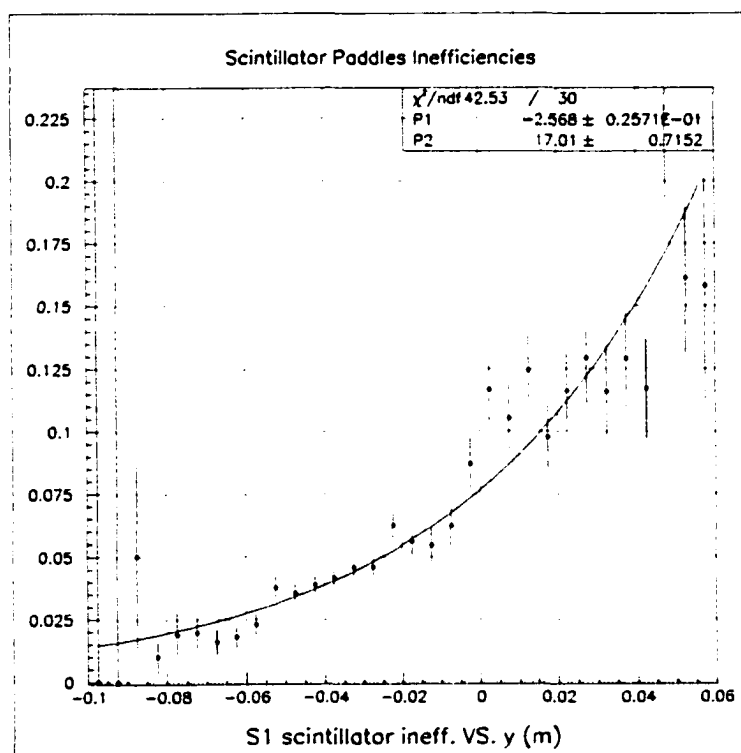


FIG. 49: Weighed y distribution for the right side of paddle 4 of the Electron scintillator S1 obtained with the iso-inefficiency curve of Fig. 48. An exponential fit is applied and the resulting coefficients are displayed in the right corner. The parameterization is of the form e^{P1+P2y} . This corresponds to a β value given by $P2$ and a η_0 value given by e^{P1} which evaluate then to 17.0 and 0.0765 respectively in the case presented.

Fig. 49 is the y distribution obtained using the iso-inefficiency curve of Fig. 48. The result of an exponential fit is displayed. This fit agrees with the distribution

(the reduced χ^2 is about 1.4). The last two points on the left at large negative y values are obtained with very low statistics.

Fig. 50 is a 3-D plot of the inefficiency as a function of the variables x and y as obtained with the model parameterization.

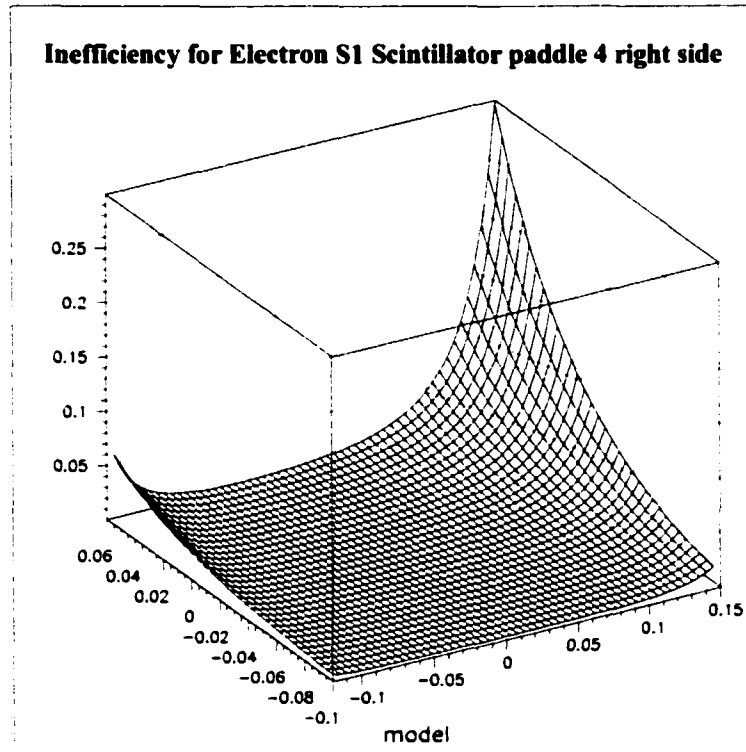


FIG. 50: Inefficiency model for the right side of paddle 4 of the Electron scintillator $S1$. This parameterization is obtained by merging three consecutive runs to improve the error bars. Each run is weighted by its relative duration while its own prescale factor and computer deadtime is used. The iso-inefficiency curve obtained with the three runs has improved error bars inducing a slightly different parameterization. The plot in this figure can be compared with the plot in Fig. 47.

Once each side of each paddle has been parameterized, the whole scintillator inefficiency can be parameterized. Indeed if the particle track goes through a region where two paddles do not overlap then the parameterization is already available. If the track goes through an overlapping zone then the inefficiency is

obtained by combining the previous inefficiencies of the two overlapping paddles extrapolated to the overlapping region.

For regions where only one paddle is at play, the efficiency of the paddle (and therefore of the scintillator) is the product of the left and right efficiencies:

$$\epsilon_{scint} = \epsilon_{paddle} = \epsilon_L \epsilon_R \quad (170)$$

since both sides have to be efficient for the paddle to be efficient. The inefficiency then reads:

$$\eta_{scint} = \eta_{paddle} = 1 - (1 - \eta_L)(1 - \eta_R) \quad (171)$$

where η_L and η_R are the inefficiencies of the left and right sides, each of the form of Eq. 169.

For overlapping regions, the inefficiency of the scintillator can be written in the following manner:

$$\eta_{scint} = \eta_P \eta_{P'} \quad (172)$$

since the scintillator is inefficient if and only if both paddles P and P' are inefficient. Each of the terms η_P and $\eta_{P'}$ has the form of Eq. 171.

The efficiency and inefficiency of the scintillator are now defined analytically by intervals. The same work has to be done for both scintillators.

Finally, an event with a track intersecting the scintillators $\mathcal{S}1$ at $(x1, y1)$ and $\mathcal{S}2$ at $(x2, y2)$ has to be weighted by the following trigger correction factor due to scintillators inefficiency:

$$tec_{trigger}(x1, y1, x2, y2) = \frac{1}{\epsilon_{trigger}(x1, y1, x2, y2)} \quad (173)$$

$$= \frac{1}{\epsilon_{S1}(x1, y1) \epsilon_{S2}(x2, y2)} \quad (174)$$

$$= \frac{1}{(1 - \eta_{S1}(x1, y1))} \frac{1}{(1 - \eta_{S2}(x2, y2))} \quad (175)$$

since both scintillators have to be efficient.

8.3 VDC and tracking combined efficiency

In this subsection a rapid overview of a study about the VDC efficiency and the tracking algorithm efficiency is presented. These two efficiencies are actually studied as a whole combined efficiency.

When a particle travels through the VDC chambers, its presence is detected by sense wires (*cf.* subsection 6.4.2). Several consecutive wires sense the particle. In the tracking algorithm, these wires are regrouped and labelled as a cluster. Several clusters can be present in a wire plane due to noise, secondary particles, background particles, *etc.* The tracking algorithm is in charge of sorting out these clusters in each plane, of fitting locally the trajectories based on timing information, and finally of relating clusters in the four planes and form a track. For the same reason as there can be several clusters in a wire plane, there can be several tracks found by the tracking algorithm. The most probable is selected based on timing information and quality of the fit.

Table IV presents the proportions of zero-track events (no track found by the tracking algorithm), one-track events and multi-track events (2, 3 or 4 tracks found) in the Electron arm for three runs.

The zero-track events concerns a small fraction of the total number of recorded events (1.3%). It was checked that most of these events ($\geq 80\%$ of the previous fraction) have no cluster at all in any wire plane. These events do not represent an inefficiency. Cosmic rays triggering the system could be invoked for an explanation. The tiny remaining fraction of events could be explained by noise and inefficiency but their fraction is negligible. It results that the combined efficiency of the hardware coupled with the tracking algorithm is almost 100% and no correction is implemented.

The one-track event proportion was relatively constant over the data set period and was about 90%. It was checked that most of these events ($\simeq 80\%$ of the total population) have one and only one cluster per plane, being therefore the cleanest.

The proportion of the multi-track events was found between 8 and 10% of the total population. Within the multi-track sample, the proportion of two-track,

TABLE IV: This table presents the proportions of zero-track, one-track and multi-track events as reconstructed by the tracking algorithm in the Electron arm for three runs. Additionally for the two extreme runs (the first is early in the data set and the last is towards the end), the proportions of zero-track events with no cluster at all and of one-track events with only one cluster per wire plane are quoted. All figures are with respect to the total number of recorded events for each run.

Tracking type		run 1571	run 1597	run 1771
0-track	total	1.3%	1.3%	1.3%
	no cluster at all	1.2%	-	1.0%
1-track	total	90.4%	90.8%	89.4%
	one cluster per plane	80.4%	-	78.8%
multi-track	total	8.3%	7.9%	9.3%

three-track and four-track events are respectively about 70%, 20% and 10%.

As a general conclusion, 80% of the recorded events are reconstructed as one-track events with one cluster per wire plane, another 10% are also one-track events but with less clear cluster signature, and finally 10% of the events are multi-track events.

By looking more closely to the figures, one could draw the conclusion that the VDC chambers grew more noisy with time (reduction of zero-track events with no cluster at all, slight reduction of one-track events with only one cluster per wire plane and slight increase in the number of multi-track events).

As far as the analysis is concerned, only the one-track events are kept. The zero-track events are rejected and no correction is applied since the part of these events due to inefficiency is negligible. The multi-track events are rejected for fear of deteriorated vertex variables reconstruction or wrong track chosen by the tracking algorithm. A run-by-run statistical correction is implemented to correct the cross-section for these multi-track events not being counted in the analysis assuming that each multi-track event corresponds to only one good event. The

correction factor is therefore:

$$\textit{tracking_correction} = \frac{N_{1\text{-track}} + N_{\textit{multi-track}}}{N_{1\text{-track}}} \quad (176)$$

where $N_{1\text{-track}}$ and $N_{\textit{multi-track}}$ are the numbers of recorded one-track events and multi-track events respectively.

A similar study was performed on the Hadron arm and a similar correction is also applied to account for the rejection of Hadron multi-track events.

8.4 Density Effect Studies

8.4.1 Motivations

The density effect study described in this section matured over time and the version presented here is automated and finalized. Improvement is always possible but this study, based on the data it is using (the VCS experiment production runs of the $Q^2 = 1$ GeV data set), has reached its limit.

A boiling study aims at understanding how the target cell density varies under different beam conditions even though the global target temperature is maintained constant and therefore so is the global density. Indeed when the beam goes through the liquid target material (Hydrogen in this experiment), it deposits some energy by interaction with the molecules. This is soon transformed into heat which leads to a local raise of the temperature. The amount of heat could be large enough to not only increase the temperature but also make the liquid Hydrogen undergo a change of phase and become gaseous locally.

The beam current intensity is the most obvious parameter of the problem: the more particle are sent per second, the more energy is transfered. A more refined parameter is actually the beam current density, the number of electrons per unit time and unit area. The intrinsic beam size has therefore its importance but the rastering amplitude is also part of the problem. Indeed the beam path is changed so that the beam spot never stays exactly at the same place, increasing the area swept and therefore reducing the current density. Typically for this experiment,

the beam sweeps an area 10 mm wide horizontally and 8 mm wide vertically, in the almost sole sake of avoiding local boiling.

The other parameter of the situation, on the target side this time, is the target fan frequency which is directly related to how fast the liquid Hydrogen is being brought back to the heat exchanger and therefore to how fast the heat is extracted.

The purpose of this present study is twofold. Firstly, the target cell density has to be evaluated as it enters an absolute cross-section through the scattering center density, one of the normalization factors of the counting rate of the measured process. Secondly, and this second purpose is intertwined with the procedure of the test, the density evaluation is also used as a consistency test over the whole collected data set ($Q^2 = 1 \text{ GeV}^2$). Indeed the Electron arm setting was kept fixed: fixed positioning angle and fixed magnets fields. Thus a measure of elastic cross-section in single arm data should yield a consistent result run by run.

At this stage, we are not interested in any particular physics variable dependence but we want a quick check of consistency with minimal analysis. As the elastic process dominates, an integrated cross-section over the whole acceptance of the spectrometer by mean of raw trigger counting seems enough. In practice, the yield of the number of raw electron trigger (called $S1$ in this thesis) divided by the integrated beam charge in under study in the following subsections. Once again it is proportional to the elastic cross-section and should remain constant run by run.

8.4.2 Data extraction

In order to automatize boiling data analysis, a UNIX script has been written. It creates several files among which a file with a specific format that is used when submitting requests for the allocation of a processor in the computing batch farm (a remote not interactive PC) available through the Computer Center at Jefferson Lab. The other necessary file created in the process is another UNIX script that contains the list of actions the remote processor will have to perform.

When the remote processor is allocated, the raw datafile is extracted from the

silo and copied over to the local disk associated with the processor, and finally all the needed executable codes copied over through the network. The execution script starts to process the data on the local disk.

A first code finds its way among the scalers banks contained in the raw datafile and extracts the needed information. In this discussion, we can limit the interesting information to the readings of the scaler counting the raw electron triggers, the VtoF scaler used for charge determination, a clock scaler used to measure time elapsed since the beginning of the run, and finally the scaler that reads the number of events accepted by the trigger supervisor and recorded on file used to synchronize physics events with scaler events. It also calculates on the fly the corresponding rates and the second order time derivative of the scalers that will help to visualize the time evolution of the rates themselves.

A second code scans the output file of the previous code and selects scaler events belonging to slices of run during which the variations in time of the raw trigger rate is below a given threshold while the beam is on. The goal here is to remove any periods of time when the beam was off, when the target temperature was not stabilized (after beam recovery) and finally select periods of time when the operating conditions have been stable for more than a given duration (set to a minimum of three minutes).

A first output file contains information which, when processed and current calibration coefficients applied, yields the ratios of raw trigger count divided by beam charge, both quantities being calculated between two scaler events separated by about twenty seconds. As a result, one obtains a series of values proportional to the elastic cross-section, each value being an average over about twenty seconds.

The next output file is used for beam position extraction since it has been found that the previous yields expose a beam position dependence. The file contains information needed to run ESPACE (Event Scanning Program for Hall A Collaboration Experiments) in order to extract beam positions on an event-to-event basis and calculate averaged beam positions between two successive scaler blocks belonging to the previously determined run slices.

8.4.3 Data screening, boiling and experimental beam position dependence

Analysis of run 1636

I first present the analysis of run number 1636 that exhibits many interesting aspects. Fig. 51 shows the raw counting rates in the two arms and the raw coincidence counting rate as a function of time. Aside from giving an example of raw counting rates in the experiment (beam current of $60 \mu\text{A}$), one can notice two beam trips. The first beam loss occurred about sixteen minutes (960 s on the plot). the beam was restored between 35 and 40 seconds later. At about $t = 2000$ s. a second beam loss happens, but the beam is soon restored. One may then notice that, after about one minute after beam restoration, the rate in the Hadron arm goes to zero, indicating a hardware problem. Indeed it can be checked that the scintillators high-voltage went off.

These simple plots from scaler information yield valuable information in the sense that they enable us to locate and later reject any portion of a run where some hardware problem occurred. Those problems can be related to spectrometer magnets problems or trigger problems (especially from the scintillators). This is nevertheless insufficient since problems happening in the other important detectors, the vertical drift chambers, are not pointed out.

The other source of data rejection is boiling. Indeed whenever the beam goes away, the temperature regulation of the target increases the current in the high power heaters so that the heat created by Joule effect in those heaters compensates the heat from beam energy deposition. When the beam comes back, the high power heaters are switched off, but the temperature is not stabilized instantaneously. The relaxation time is typically between one and two minutes, depending on the operating conditions of the target, on the beam current intensity and how the beam is restored (beam off duration, restoration of the beam at full current or by steps).

The concern was raised that if the beam losses occur too frequently, then the measured VCS cross-section could become biased at the percent level. To be on

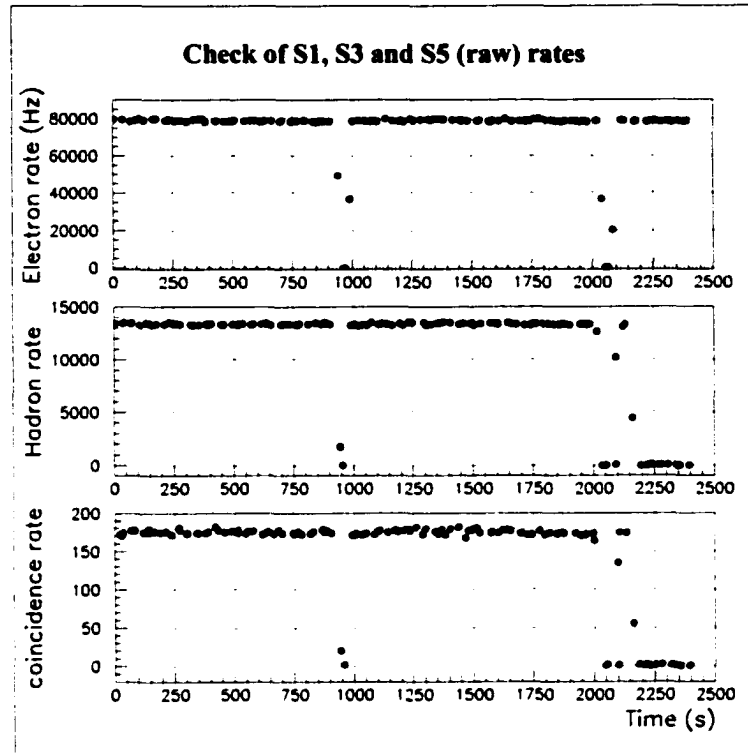


FIG. 51: These three plots show the raw counting rate in the Electron arm (top plot), in the Hadron arm (middle plot) and finally in coincidence (bottom plot) as a function a time. (Note that there is a shift in the time axis in the two last plots as the time defined in the Hadron arm starts about ten seconds later than in the Electron arm.)

the safe side, it has been decided to remove any portion of the data when the temperature is not stabilized. This also became the removal of portion of data from the last scaler event preceding the beam loss moment until the next scaler event during which the temperature was stable.

This is achieved thanks to the time derivative of the Electron rates: if the rate were to increase or decrease by an amount above a threshold value (determined *ad hoc* to reject boiling periods) while the beam is on, the corresponding times of unstable rates are cut away.

In Fig. 52, one can see the result of this boiling screening. On those two plots, the vertical axis is the yield of the Electron raw counting rate divided by the beam current intensity in $\text{Hz}/\mu\text{A}$. In practice, it is the yield, in units of $\text{counts}/\mu\text{C}$, of the difference in Electron raw triggers counts between two consecutive scaler events divided by the charge cumulated during the same period.

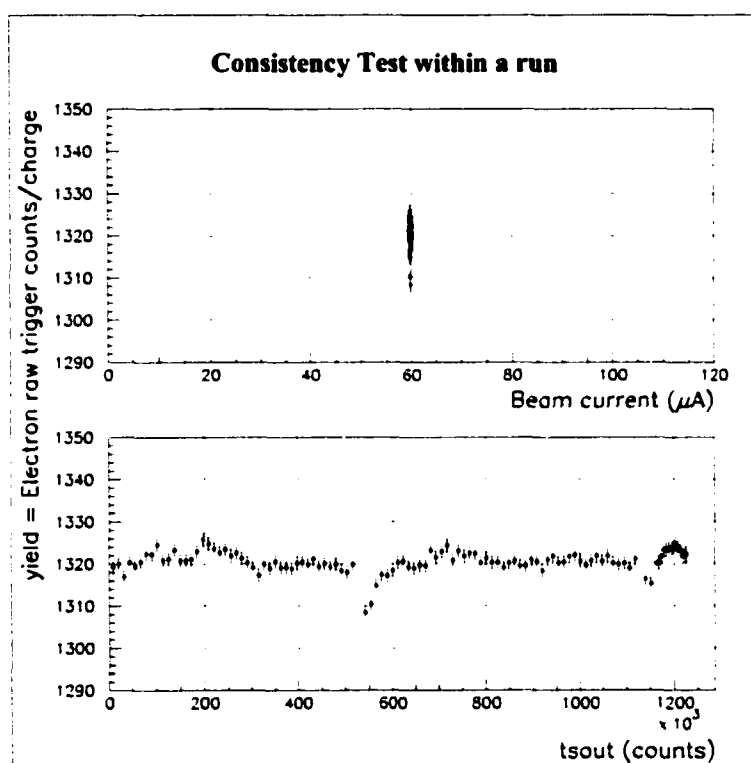


FIG. 52: On these plots one can see the result of boiling screening obtained for run 1636. While the beam current was steadily at $60 \mu\text{A}$, the yield presents some variations over time, induced by residual boiling effect and average beam position dependence.

The top plot shows that the beam current was steadily at $60 \mu\text{A}$ while the bottom plot shows the yield as a function of $tsout$, the number of triggers accepted by the trigger supervisor and written on file since the beginning of the run. $tsout$ can be thought of as a replacement for time since, in stable data taking situation, $tsout$ increases linearly in time. However, at the end of this run, we saw that the

Hadron arm rates dropped to zero, implying that the number of accepted triggers is reduced to the Electron triggers, whence the higher density of points on the right of the plot.

Nevertheless, the attention is drawn to the middle of the plot, after the first beam trip, where it seems that a residual boiling effect still shows up. Moreover the yield presents some other variations due to beam position.

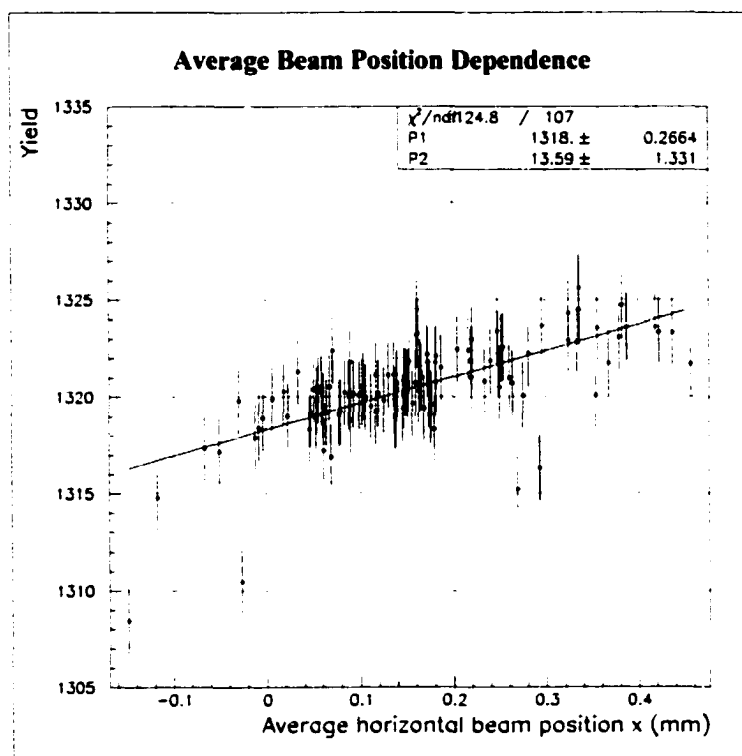


FIG. 53: Visualization of the average beam position dependence and linear fit results for run number 1636.

Fig. 53 shows how the yield is distributed as a function of average beam position. A linear fit is performed to investigate the dependence of the yield as a function of average beam position.

The result of the fit gives a value for the slope of 13.59 ± 1.33 units/mm and an intercept at $x = 0$ mm of 1318.3 ± 0.3 . While the χ^2 per degree of freedom of

the fit is 1.17, indicating that it is a reasonable fit, the relative error on the slope parameter is 10%.

Using this dependence, a beam position correction can then be implemented. The new value for the yield is:

$$yield_{new} = yield_{old} - slope \times x . \quad (177)$$

The beam position correction is applied and the result can be visualized on Fig. 54.

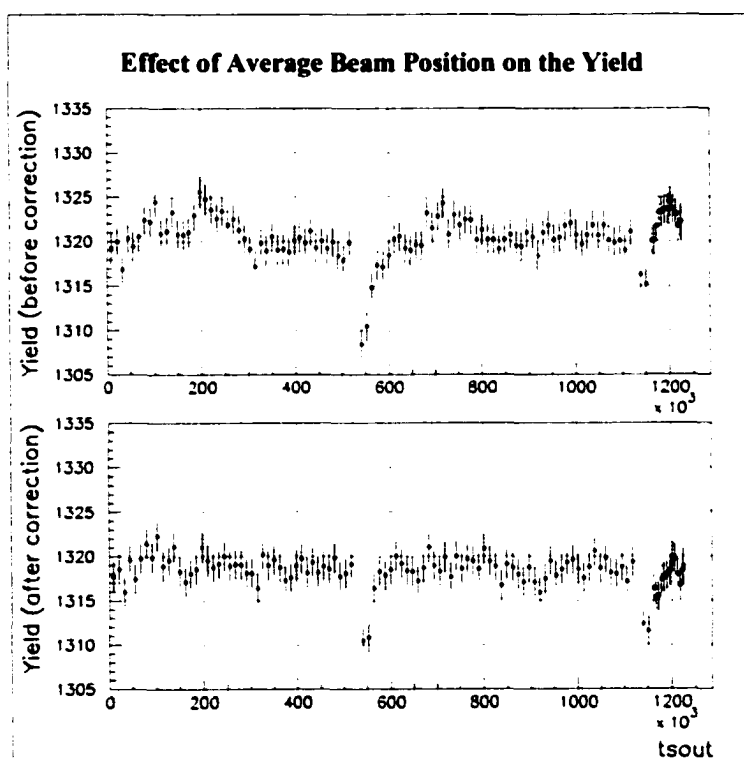


FIG. 54: Comparison of the yield before and after average beam position correction for run number 1636.

The top plot shows the situation before correction and the bottom plot shows what the yield becomes after correction. One can see that the yield offers a smoother behavior. A few scaler events stand aside though. They are remaining part of the boiling effect. On the other hand, the relative discrepancy is fairly low:

the difference in yields between the average value and the low points divided by the average value is of the order of 0.5% while the low points concern 3 to 4% of the run duration or even less when a cut before the second beam trip is applied.

Analysis of run 1687

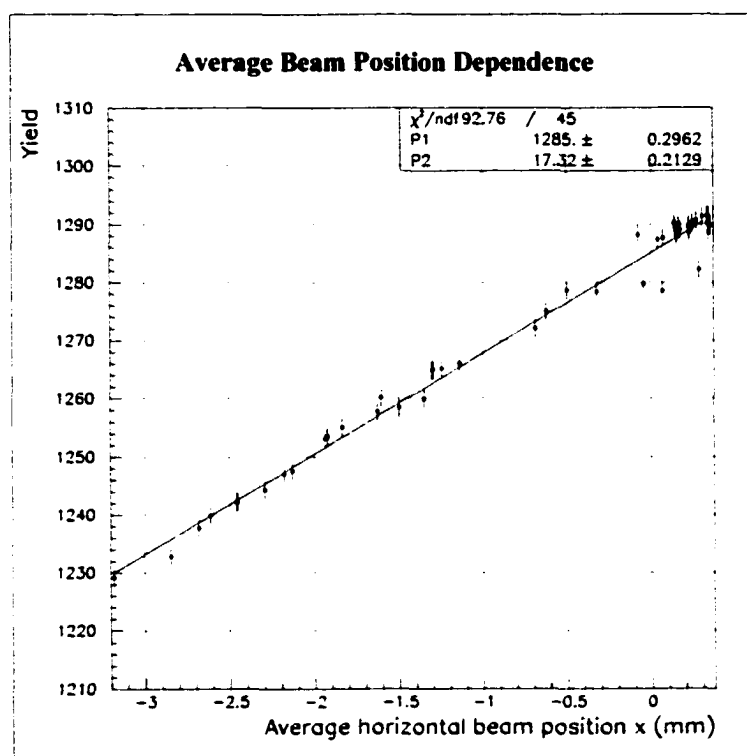


FIG. 55: Determination of the beam position dependence for run number 1687.

During production data taking on which this study is based, the beam was requested to remain within 0.25 mm of the nominal beam position. The lever arm in the determination of the slope of the yield as a function of the beam position is therefore small (of the order of 0.5 mm). This is part of the explanation why the error on the slope is so large. As a consequence, for most runs, the result of the fit does not yield valuable information. For one run though, the beam excursion is large enough to allow for better fitting conditions.

Fig. 55 presents the yield for run 1687 as a function of the average beam position and the fit results obtained. The value of the slope is different from that of run 1636. The value is 17.3 ± 0.2 units of yield per mm. This value is used to implement the beam position dependence in the boiling plots of next subsection.

Finally note that the correction for beam position dependence does not exceed 0.5% most of the time, or half this value when the beam is kept within 0.25 mm of the nominal beam position.

8.4.4 Boiling plots and conclusions

In this subsection, boiling plots are presented. Fig. 56 presents the ratios of the number of raw electron triggers $S1$ over the accumulated charge obtained for good slices of run (every detector is working, the beam is stable at one value of beam current intensity and the target density is also stable). A correction for average beam position is implemented in the evaluation of the previous ratios as explained in the previous section. These yields are plotted as a function of the beam current intensity. Three values of target fan frequency were used during the VCS data taking at $Q^2 = 1 \text{ GeV}^2$.

It seems that the target density depends on the beam current since lower values for the yield are obtained for higher values of beam current. But an inconsistency is visible: the red stars obtained with a target fan running at a frequency between 72 and 75 Hz are below the blue circles obtained with a target fan frequency of 60 Hz. Indeed a higher fan frequency means a faster flow of the liquid Hydrogen target and therefore that the heat due to the energy deposition by the beam is extracted faster.

Fig. 57 presents the yields of Fig. 56 corrected for scintillator efficiency and Electron electronics deadtime. The previous inconsistency between the data points is still present. Moreover the Electron electronics deadtime seems to overcorrect the boiling effect.

By looking more closely at when the runs were taken, it turns out that the runs taken with a fan frequency of 80 Hz were taken first. Then the runs with

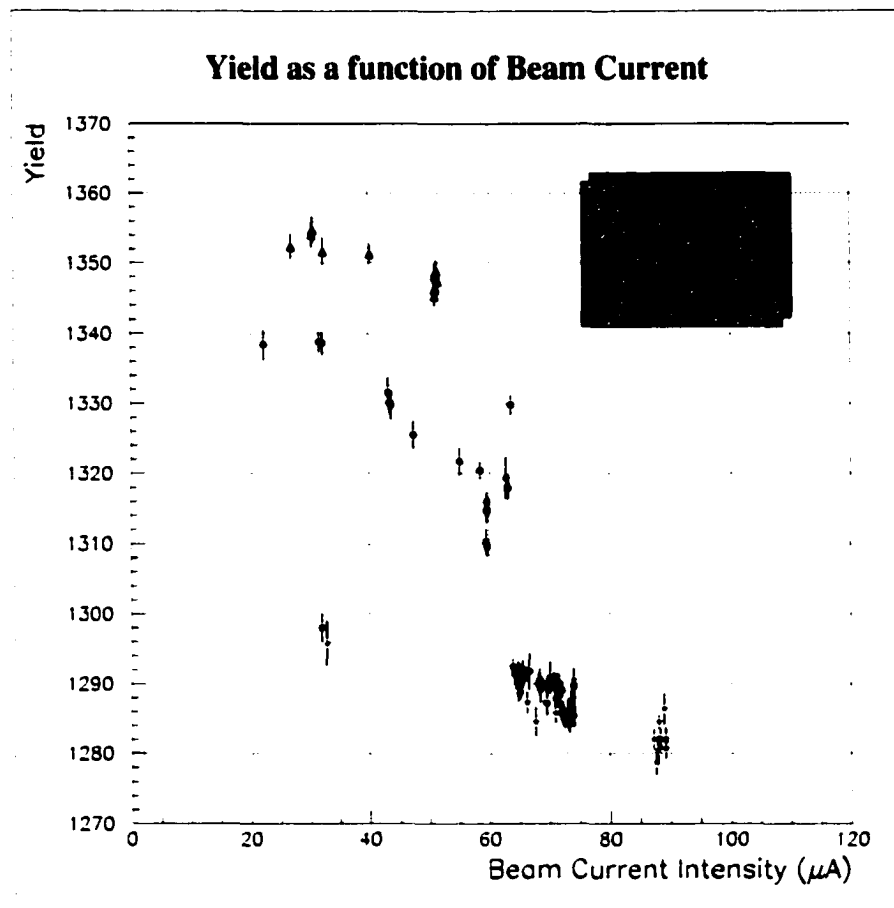


FIG. 56: Raw boiling plot. Note the narrow range on the vertical axis. The target density seems to depend on the beam current. An inconsistency is visible though: the red stars obtained with a target fan running at a frequency between 72 and 75 Hz are below the blue circles obtained with a target fan frequency of 60 Hz which contradicts the fact that a higher fan frequency helps to extract the heat due to the beam more easily.

a fan frequency of $ff = 60$ Hz were collected and the data set ends with runs collected at $ff \simeq 70$ Hz. It can be noted that a significant drift in the yield can be observed starting after about one fourth of the data at $ff = 60$ Hz were taken. Indeed runs at low beam current were taken first and the current was increased up to $I = 63 \mu\text{A}$. Then for additional runs at $I = 60 \mu\text{A}$, the yields show a tendency to be reduced with respect to the previous ones taken at about the same current. The drift in the yield continues as data were taken at beam current between 65 and 75 μA , still at the same fan frequency. For one of those last runs, it was also possible to extract a yield at $I \simeq 30 \mu\text{A}$ that stands really below the points obtained in the beginning (*cf.* Fig. 56 or Fig. 57). The runs at $ff \simeq 70$ Hz were then taken and the yields are similar to those of the end period of the previous fan frequency set whereas they should be above because of a higher fan frequency.

No valid explanation was found to explain the drift in the raw counting rate in the Electron arm. This prevents a coherent and detailed interpretation of the boiling study.

Nevertheless if we were to admit such a drift and correct for it, the points at $ff = 70$ Hz would stand between the points obtained at $ff = 80$ Hz and the first points obtained at $ff = 60$ Hz, yielding a tiny dependence of the cross-section on the fan frequency parameter (0.07%/Hz over the range [60;80] Hz).

The Electron electronics deadtime was evaluated empirically from a later experiment using also the Hydrogen target. Thus, the Electronics deadtime correction may include an empirical boiling correction. This could explain the local positive slopes in Fig. 57. If this deadtime correction is removed, the clusters of points in Fig. 57 exhibit a slope of $-2\%/100\mu\text{A}$ for the beam current dependence.

Finally the variations in Fig. 57 are not correlated to changes in the raster amplitude. The raster pattern was never smaller than about 10 mm in total horizontal amplitude (± 5 mm from the average position) and about 8 mm vertically.

Without an explanation for the source of the drift, we are left with the conclusion that the cross-section normalization due to the target density is known to 1.1%, the root mean square fluctuations of the points in Fig. 57.

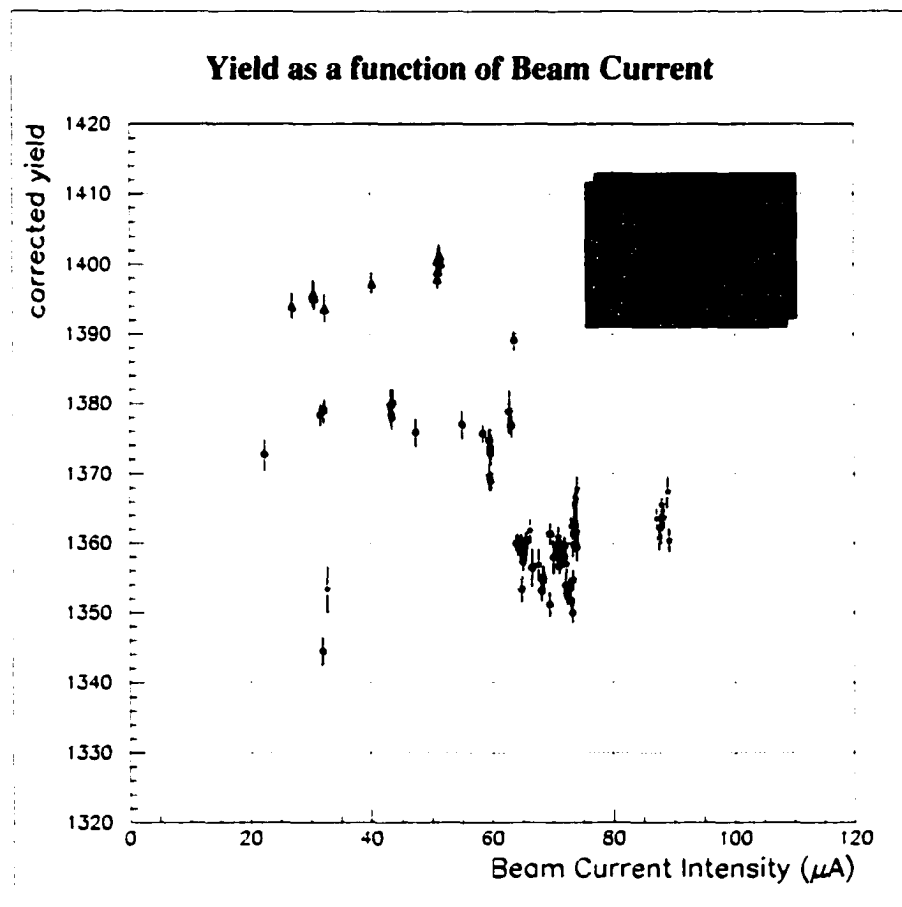


FIG. 57: Corrected boiling plot. The raw boiling plot of Fig. 56 is now corrected for scintillator efficiency and Electron electronics deadtime.

8.5 Luminosity

The $ep \rightarrow ep\gamma$ cross-section can be evaluated by dividing the number of times the electron did interact through the $ep \rightarrow ep\gamma$ process by the number of times the electron had the opportunity to interact, whether it interacted through the studied process, through any other process or did not interact at all.

The integrated luminosity \mathcal{L}^{exp} is defined to be the total number of opportunities of interaction. It is the factor that normalizes the number of counts observed in the detectors and corrected for inefficiencies, radiative effects and phase space. The integrated luminosity is totally independent of the reaction studied. It only depends on the characteristics of the target and of the beam.

The beam may have a small incident angle on the target. Nevertheless the spatial extension of the target (long longitudinal and large transverse extensions with respect to the rastering size of the beam) makes almost no difference in the volume of target material the beam goes through. In the following we consider that the beam arrives perpendicularly to the target transverse area.

Let us consider an elementary volume of target $d\tau$. The elementary luminosity from that volume $d\mathcal{L}$ is the product of the electron flux density through the elementary transverse area (number of electron per unit area per unit time) times the number of scattering centers (number of target protons) in the volume dN_{centers} . The electron flux density is the current density divided by the elementary charge e , a current intensity being by definition the flux of the current density ($I = \iint \vec{j} \cdot d\vec{S}$). The number of scattering centers in $d\tau$ can be rewritten as the density of scattering centers times the elementary volume. Finally $d\tau$ can be written as the transverse area times the longitudinal extension. Thus we have:

$$d\mathcal{L} = \frac{dN_{\text{centers}}}{d\tau} \frac{\vec{j} \cdot d\vec{S}}{e} dz \quad (178)$$

$$= \frac{dN_{\text{centers}}}{d\tau} \frac{j dS}{e} \cos(\theta_{\text{incident}}) dz \quad (179)$$

$$= \frac{dN_{\text{centers}}}{d\tau} \frac{j}{e} d\tau \quad (180)$$

since we assume the incident angle on the target to be zero.

The number of di-Hydrogen molecules per unit volume in the considered elementary volume $d\tau$ is the ratio of the mass density ρ by the mass of one molecule. The mass of one molecule is the molar mass of the Hydrogen molecule M_{H_2} divided by the number of entities per mole, the Avogadro number \mathcal{N} :

$$\frac{N_{H_2 \text{ molecules}}}{\text{Volume}} = \frac{\rho}{\frac{M_{H_2}}{\mathcal{N}}} = \frac{\rho \mathcal{N}}{M_{H_2}}. \quad (181)$$

The molar mass M_{H_2} is actually twice the molar atomic mass A_H of the Hydrogen element since a molecule of di-Hydrogen contains two Hydrogen atoms. The number of scattering centers (number of protons) contained in $d\tau$ is also twice the number of Hydrogen molecules, so that the density of scattering centers is:

$$\frac{dN_{\text{centers}}}{d\tau} = 2 \frac{\rho \mathcal{N}}{2A_H} = \frac{\rho \mathcal{N}}{A_H}. \quad (182)$$

The integrated luminosity can now be written as the integral over time and the target extension of the elementary luminosity $d\mathcal{L}$:

$$\mathcal{L}^{\text{exp}} = \int_{\text{time}} \iiint_{\text{target}} \frac{\rho \mathcal{N}}{A_H} \frac{j}{e} d\tau dt. \quad (183)$$

The beam electrons do not interact enough in the target to make j change along the longitudinal extension z . Moreover, for lack of heat convection model implementation, the target density is assumed to be uniform in the volume swept by the beam. We can therefore easily integrate along the z direction. The integration over the transverse directions is also reduced to the rastering area.

$$\mathcal{L}^{\text{exp}} = \frac{\mathcal{N}}{eA_H} \int_t \ell \iint_{\text{Raster}} \rho j dS dt \quad (184)$$

$$= \frac{\mathcal{N}\ell}{eA_H} \int_t \rho I dt \quad (185)$$

$$= \frac{\mathcal{N}\ell}{eA_H} \int_t \rho_0 (fan)(1 + \beta_{\text{boiling}} I) I dt \quad (186)$$

where ℓ is the target length (15 cm). In Eq. 186, a phenomenological model for target density as a function of beam current I and fan frequency fan is implemented. ρ_0 stands for the target density with no beam at fan frequency fan .

To go further, one has to cut on periods of time when the beam current was about stable, calculate the luminosity on each of these periods and sum them up. The luminosity over the experiment can therefore be written as:

$$\mathcal{L}_{\text{total}}^{\text{exp}} = \frac{\mathcal{N}\ell}{eA_H} \rho_0 \sum_{i=1}^{N_{\text{periods}}} (1 + \beta_{fan} fan_i)(1 + \beta_{boiling} I_i) Q_i \quad (187)$$

where i runs from 1 to N_{periods} , the total number of periods of about stable beam current intensity, I_i is the average current for slice i , Q_i the accumulated charge over the slice and finally fan_i is the fan frequency for slice i .

Note that the results, presented in the previous section 8.4, from a target density study for the data set of the VCS experiment studied in this document, yield the values $\beta_{boiling} = (0 \pm 1) \%/100 \mu\text{A}$ and $\rho(fan) = \rho_0 \pm 1\%$ for the parameters of the previous phenomenological model. For VCS cross-section extraction, we used $\rho_0 = 0.0723$.

Chapter 9

VCS Events Selection

In this chapter, the cuts used to perform a VCS events selection are explained. This selection relies on three main cuts.

The first cut is based on a time of coincidence between the Electron and Hadron triggers. The raw time of coincidence is corrected for particle propagation times in the spectrometers to yield a variable called *tc_cor* that stands for corrected coincidence time (*cf.* section 7.6). The true coincidences lie under a sharp peak.

The second main cut is based on the collimator size. Indeed collimators were placed at the entrance of both spectrometers. As a direct consequence, the reconstructed trajectories of the particles should be found inside the free space defined by the collimator edges.

The last main cut is based on a spatial coincidence. The vertex coordinate x perpendicular to the beam direction and horizontal in the Lab frame is reconstructed using both spectrometers. The corresponding variable is called *twoarm_x*. If the vertex is correctly reconstructed and the two particles really emerged from the same vertex point, then this variable should coincide with the beam position, called *beam_x*, extracted from beam position monitors. The difference d between the two, $d = \text{twoarm}_x - \text{beam}_x$, should therefore be zero. But due to resolution effects of the detectors and other devices, the variable is distributed in a peak centered at zero.

9.1 Global aspects and pollution removal

9.1.1 Coincidence time cut

***tc_cor* spectrum and accidental subtraction procedure**

The variable *tc_cor* enables us to select coincidence events that, from a **timing** point of view, seems to correctly relate a trigger in the Electron arm to a trigger in the Hadron arm implying that both particles are issued from the same reaction vertex. Fig. 58 displays a histogram of this *tc_cor* variable.

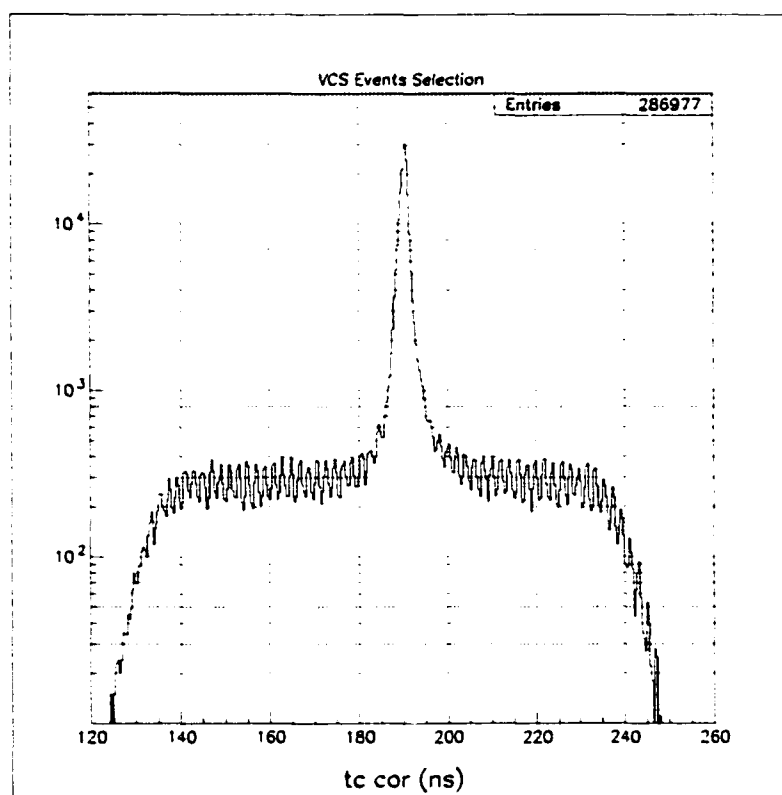


FIG. 58: This *tc_cor* spectrum exhibits the 500 MHz time structure of the beam: a beam bunch arrives in the Hall every 2 ns. The coincidences in time show in the central peak while the presence of accidental coincidences can be checked on each sides. (They are randomly distributed in the entire spectrum while convoluted with the beam time structure.)

In Fig. 58, the true coincidence events lie in the main peak centered at about 190.5 ns. It roars far above the accidental coincidences randomly distributed in this spectrum (but with a convolution with the beam structure as described below). Since the ratio of true to accidental coincidences is about 100, a logarithmic scale is applied on the vertical axis so as to better see the accidentals. One can notice an accidental peak every 2 ns. This structure corresponds to the beam structure: a bunch of beam electrons arrives in the Hall every 2 ns (see chapter 5 about the accelerator and section 7.6).

After all other event selection cuts are applied, a Gaussian fit to the central region of the true coincidence peak yields a sigma value of 0.5 ns. For the VCS events selection a time window of ± 3 ns around the central value of the peak is used (three beam bunches). This window will be referred to as the true coincidences time window.

In the previous window, not only can we find the true coincidences, but some accidental coincidences as well. Even under the true coincidences peak lie some of these accidental events. In order to statistically subtract those to the true coincidences, two other windows, one on each side of the main peak are selected. The events belonging to these two windows are merged. The ratio of the width of the true coincidences time window divided by the sum of the widths of the two accidentals time windows is used as a weighting factor. This weight is applied to the accidentals distributions in any variable and the result is subtracted from the distributions obtained with events selected by the true coincidences time window.

For further study, a time window of ± 5 ns around the true coincidence peak is defined.

d spectrum and pollution of the VCS events

For this run (run 1660) and others, the width of the main *tc_cor* peak is anomalously large. In order to figure out why the coincidence peak is so wide, a 2-dimensional plot of *d* versus *tc_cor* is shown in Fig. 59. An histogram projection of *d* is displayed on the side, while the projection on the *tc_cor* axis stands below. The density of events on the 2D plot is color-coded.

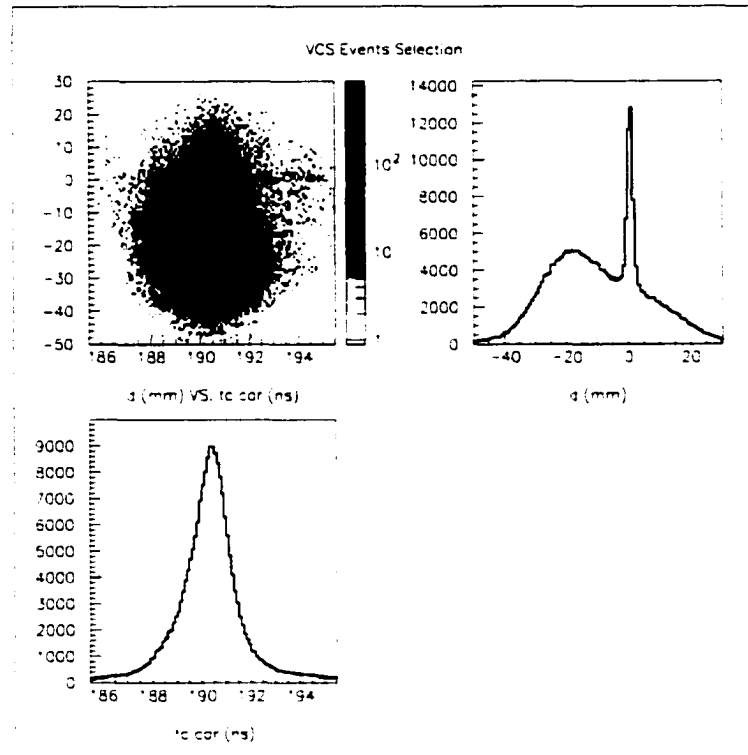


FIG. 59: Two populations overlap. The good events population which is centered at $tc_cor = 190.5$ ns and $d = 0$ cm is highly contaminated even though the vast majority of the pollution events (second population centered at $tc_cor = 190.3$ ns and $d = -2$ cm) are easily removable by a cut in d .

It is clear that the overwhelming majority of the events are true time coincidences: they stand in the peak in the tc_cor spectrum for true time coincidences. Nonetheless, the d spectrum shows that most of the events are not reconstructed to have a vertex position identical to the instantaneous beam position (broad distribution in the d spectrum not centered at zero).

The 2D plot gives a broader view of the problem by linking the two variables tc_cor and d on the same plot. One can see two overlapping populations on this plot. The first population centered at $tc_cor = 190.5$ ns and $d = 0$ cm corresponds to perfectly good events, good in timing and in vertex reconstruction. The other

population is approximately centered at $tc_cor = 190.3$ ns and $d = -2$ cm. This last value indicates there is a problem in the vertex reconstruction. The distributions of those last events are so wide that they spread far in all directions. The good events are contaminated at a high level. It is also interesting to notice that if the removal of that pollution is not perfect, it may bias the distribution of the good events in tc_cor by leaving a tail on the left side of the final peak. Note again that the broad off-centered peak in d is not due to time accidentals (too little time accidentals to explain the effect).

9.1.2 Collimator cut

What's happening at the collimators

Fig. 60 displays the distribution of the events at the entrance of the two spectrometers in the collimator planes. Note that the two plots have the same scales. On both plots the vertical axis is used for the vertical position of each particle at the collimator while the horizontal axis is for the horizontal position. Both plots

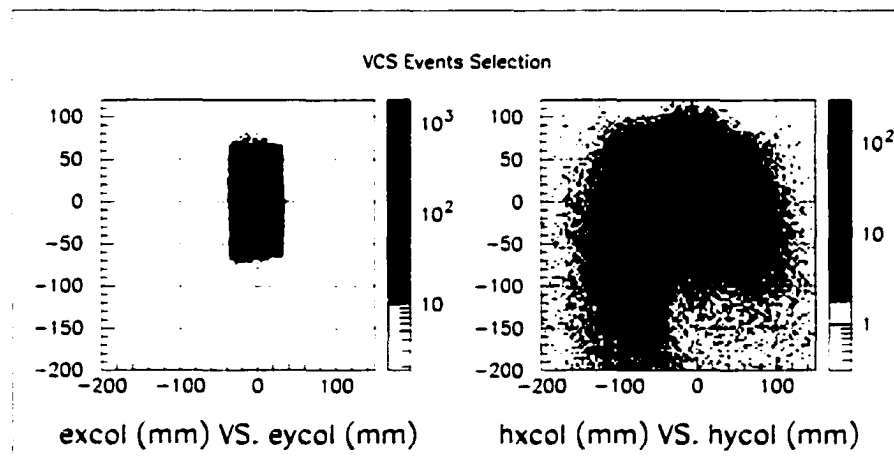


FIG. 60: 2D plots of the Electron collimator variables $excol$ vs. $eycol$ (left plot) and of the Hadron collimator variables $hxcol$ vs. $hycol$ (right plot). Note the same scales are used on these two plots. Most of the Electron events are reconstructed inside the collimator free space while this is not the case in the Hadron arm.

also include a frame box that represents the collimator size.

One can check that only a tiny fraction of the events are located outside the Electron collimator. On the other hand, a very substantial part of the events are located outside the Hadron arm collimator.

Cutting on the collimator variables

It is easy to check that the events reconstructed outside the Hadron collimator also have a wrong d value, an indication that an interaction of the protons with the collimator material occurred. I leave for section 9.2 a more detailed explanation. For the general discussion, I will only say that a cut on the collimator size greatly improve the VCS events selection. This fact can be checked in Fig. 61. The spectrum in black in this figure is obtained by implementing the coincidence time window cut and the following additional cut on the Hadron collimator variables: $-25 \text{ mm} < hycol < +25 \text{ mm}$ and $-60 \text{ mm} < hxcoll < +60 \text{ mm}$. When comparing the spectrum with the d spectrum in Fig. 59, the effect is obvious: the broad distribution peaked on the left of the good events belonging to the sharp peak centered at 0 mm is so largely reduced that the remaining pollution is now much more tolerable.

9.1.3 Vertex cut

The vertex cut corresponds to a cut in the variable d . After imposing that we have a time coincidence (cut in $tc.cor$) and that the reconstructed particle tracks go through the free space defined by the collimators (cut in the Hadron collimator variables), we now want to select events for which the reconstructed reaction vertex position coincide with the measured position of the beam. A window is defined for that purpose by the following interval: $-3 \text{ mm} < d < +3 \text{ mm}$. Note that this cut may reject valid events but the same cut will be applied in the simulation. If the resolution of the simulation reproduces well the resolution of the experiment, no bias is induced (*cf.* section 10.3).

An additional cut in the variable s can also be applied to remove additional pollution. This corresponds to the removal of elastic events that should not be in

the acceptance (*cf.* section 9.2). The cut to be applied in the variable s is defined by: $s > 0.9 \times 10^6$. Since the energy of the outgoing photon in the center of mass frame is $q' = (s - m_p^2)/2\sqrt{s}$, the previous cut in s also cuts photons energies below 10.4 MeV. But these photons are too soft and are not used for cross-section extraction anyway. The red spectrum in Fig. 61 shows the improved selection. Nevertheless, a remaining pollution contaminates the good events selected in the window $-3 \text{ mm} < d < +3 \text{ mm}$, at the 5 to 10 % level.

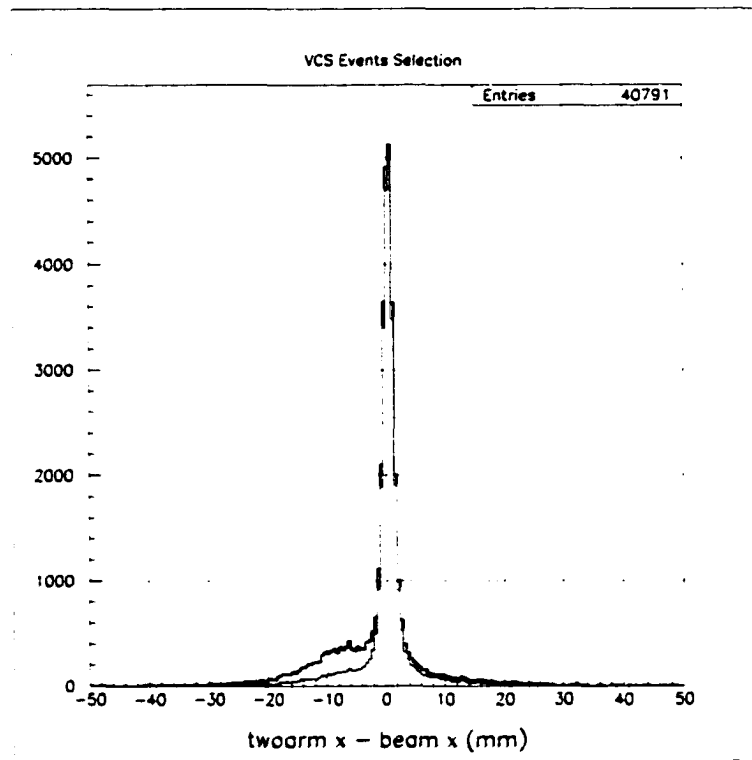


FIG. 61: d spectra. The spectrum in black is obtained with a coincidence time cut and the Hadron collimator cut. The red spectrum is obtained with an additional cut in s . This last cut improves the pollution removal on the left side of the peak. Note the drastic reduction in the number of events selected for the black spectrum (upper right corner) with respect the Fig. 58.

9.1.4 Missing mass selection

On Fig. 62, one can check the effect of the successive cuts on the missing mass variable: the red spectrum is obtained with the coincidence time window cut only, the green spectrum is obtained when adding the Hadron collimator cut, the blue spectrum is obtained by implementing the space coincidence cut (cut in the variable d) in addition to the previous two, and finally, the black curve is obtained by implementing the additional s cut. The Hadron collimator cut makes the VCS peak visible and the d and s cuts further shape the VCS and pion peaks by reducing the pollution. By adding the cut in the Hadron collimator

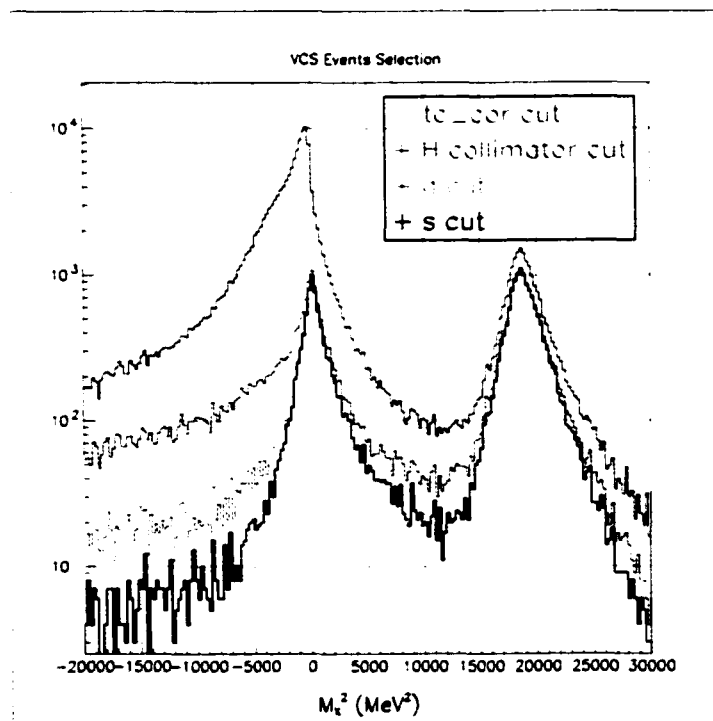


FIG. 62: M_X^2 spectra. The spectrum in red is obtained with the coincidence time window cut. The green spectrum is obtained with the additional cut on the Hadron collimator. The blue spectrum is obtained by implementing the cut in d in addition to the previous two. And finally, the black spectrum is obtained with all the above cuts plus the additional cut on s . Note the logarithmic scale used for the vertical axis.

variables to the tc_cor cut, we reject most of the events at missing mass squared equals zero that pollute the $ep \rightarrow ep\gamma$ events that stands there (VCS peak). The rejection ratio is much less in the single neutral pion production case (the other peak in fig. 62 that stands at $M_X^2 = m_{\pi^0}^2 \simeq 18200 \text{ MeV}^2$). This is an additional confirmation that we indeed reject pollution events at $M_X^2 = 0 \text{ MeV}^2$.

Fig. 63 shows the missing mass spectrum with all the above cuts in a linear scale. The $ep \rightarrow ep\gamma$ and $ep \rightarrow ep\pi^0$ peaks are clearly separated. It is one of the first times that an experiment achieves a so clean separation. Finally a missing mass squared window is used to select the VCS events. Its definition is: $-5000 \text{ MeV}^2 < M_X^2 < +5000 \text{ MeV}^2$.

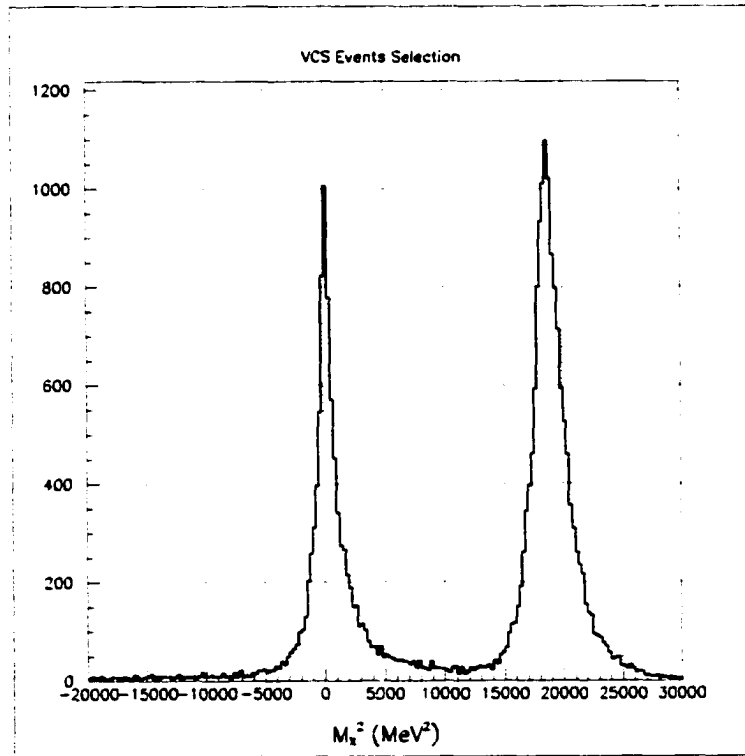


FIG. 63: M_X^2 spectrum with all cuts applied. The peak near $M_X^2 = 0 \text{ MeV}^2$ corresponds to the $ep \rightarrow ep\gamma$ reaction while the peak near $M_X^2 = 18200 \text{ MeV}^2$ corresponds to the $ep \rightarrow ep\pi^0$ reaction.

9.2 Chasing the punch through protons

This section is a more detailed study of the punch through protons pollution. It aims at a better understanding of the pollution rather than a search for the most effective way of pollution removal. Three different aspects of this problem are investigated. This investigation is done with the data run 1660 that offers the possibility of studying the three aspects.

9.2.1 Situation after the spectrometer in the Electron arm

As we saw in section 7.5 and in the left plot of Fig. 60, most of the Electron triggers correspond to well reconstructed electrons traveling from the target, through the spectrometer, to the detectors. It can be further checked that indeed the electron variables are well reconstructed at all levels and that the information that solely comes from the Electron arm side can be trusted.

The left plot of Fig. 60 presented the collimator variables in the Electron arm. The situation after the spectrometer is now investigated. The left plot in Fig. 64 is a 2-D plot of the electrons positions in the first scintillator plane (the intersection of the reconstructed trajectories with this scintillator plane) for coincidence events (type T5). The vertical axis of the plot is the vertical position in the plane (dispersive direction of the spectrometer). Likewise, the horizontal axis is the horizontal position (non dispersive direction). The plot is therefore, more or less, the momentum of the electron *versus* the scattering angle.

With a little imagination one can see a gun with a bullet below. The barrel of the gun stretches across the focal plane. This straight line can be identified with elastic events even though no such events should be accepted in coincidence. The handle of the gun corresponds to Bethe-Heitler events and the bullet corresponds to events in neutral pion production kinematics.

The elastic line is used as a new x-axis. The pointing direction is chosen to be from left to right. The perpendicular direction to the new x-axis defines the direction of a new y-axis that is chosen to point downwards. The right plot

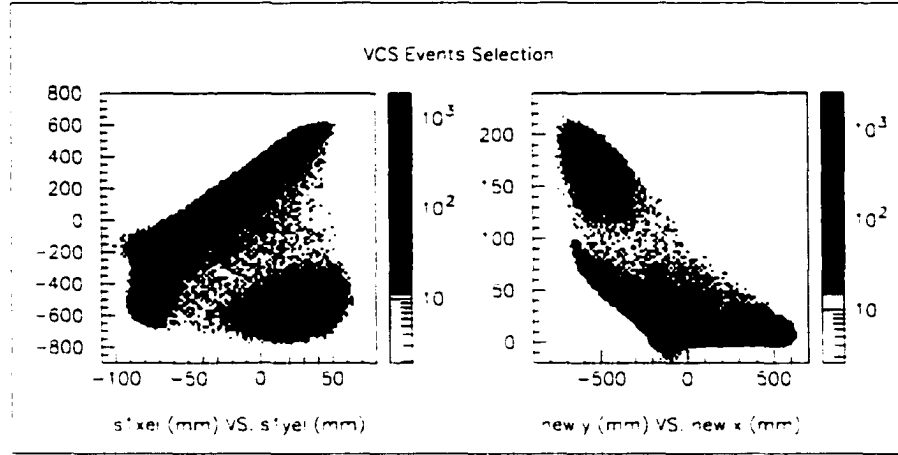


FIG. 64: The left plot presents the dispersive coordinate of the electrons at the first scintillator plane as a function of the non dispersive coordinate. The right plot is a rotation of the left plot with an additional inversion of the pointing direction of the new vertical axis. This last plots is used to define three regions of the focal plane that will be investigated separately (see the text for the definition of the new axes and the three squared areas.).

presents the situation when expressing the coordinates of the electrons in this new frame.

This latter plot will help visualize three zones of the focal plane that will be investigated separately. The first zone is defined by:

$$\begin{aligned} 0.1 \text{ m} &< (s'ye + 6.5 \times s'xe + 0.06)/6.576 < 0.6 \text{ m} \\ -0.02 \text{ m} &< (-s'xe + 6.5 \times s'ye + 0.39)/6.576 < 0.11 \text{ m} \end{aligned} \quad (188)$$

or equivalently by:

$$\begin{aligned} 100 \text{ mm} &< \text{new x} < 600 \text{ mm} \\ -20 \text{ mm} &< \text{new y} < 110 \text{ mm} \end{aligned} \quad (189)$$

This zone is a square box located in the bottom right corner of the right plot in

Fig. 64. The second zone corresponds to the bottom left corner and is defined by:

$$\begin{aligned} -800 \text{ mm} < \text{new } x < -250 \text{ mm} \\ -20 \text{ mm} < \text{new } y < 110 \text{ mm} \end{aligned} \quad (190)$$

Finally the third zone, corresponding to the upper left corner, is defined by:

$$\begin{aligned} -1000 \text{ mm} < \text{new } x < 0 \text{ mm} \\ 110 \text{ mm} < \text{new } y < 240 \text{ mm} \end{aligned} \quad (191)$$

Each of these three zones will now be investigated successively in the order they were defined above.

9.2.2 Zone 1: elastic

Preselection

On Fig. 65 four histograms are displayed. The top-left is the histogram of *twoarm_x*, the x-coordinate position of the reaction as seen by the two spectrometers. The top-right plot represents the variable *d*. For good events, one should see a peak centered at zero. The bottom-left is a missing mass squared histogram. And finally the bottom-right plot histograms the variable *s*. No cut except the one that defines this zone in the Electron focal plane is applied.

The *twoarm_x* spectrum (top-left) offers a one peak shape and not the double peak shape of the raster which is what one would have expected to obtain. Indeed the beam was not rastered beyond about 5 mm on either side of zero and the much larger values of vertex coordinate *x* reached by *twoarm_x*, reconstructed by using information from the two spectrometers, is a clear indication that something is wrong in this reconstruction.

The *d* spectrum (top-right) offers the same statement but in a more quantitative way: this spectrum presents a small peak at zero sitting on top of a mountain of events. This small peak contains the good events, the ones for which the reconstructed position is identical to that of the beam. The remaining vast majority of the events simply exhibits unphysical vertex position.

The missing mass squared spectrum (bottom-left) rendering the square of the mass of the missing particle, it presents a dominance of negative values which are also unphysical for an emitted real particle. This corroborates the fact that the reconstruction of the vertex variables is flawed for most of the events.

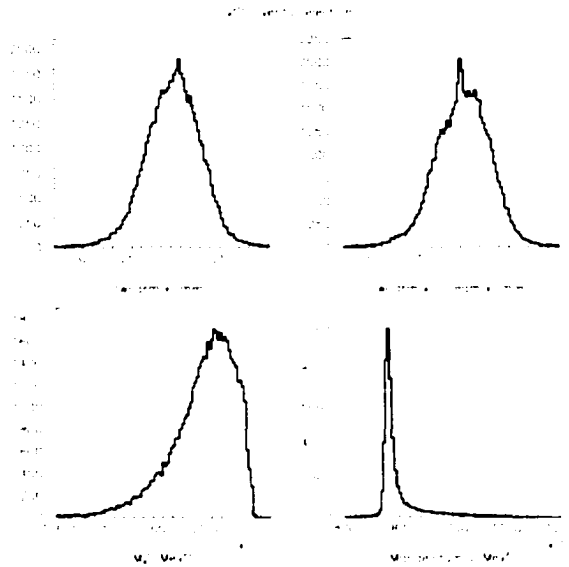


FIG. 65: *twoarm_x*, *d*, M_X^2 and *s* spectra without any cut applied except for a selection in the Electron focal plane (zone 1). The *s* spectrum indicates that most of the events are formed with electrons from elastic scattering. The potential VCS events are barely visible (small peak at zero in the *d* spectrum on top of a much wider distribution), overwhelmed by those elastic triggers in the Electron arm. The unphysical values in the first three spectra can be understood considering the fact that a large fraction of these events corresponds to events for which uncorrelated electron and proton triggers are associated to form coincidence events. An accidental coincidences explanation comes immediately to mind but this is not the whole story (see Fig 66).

The histogram of *s* (bottom-right) is typical of elastic electron scattering off a proton target. The sharp peak sits at about $s = m_p^2 = (938 \text{ MeV})^2 = 0.88 \times 10^6 \text{ MeV}^2$, the square of the proton mass.

It was checked that the Electron arm does not show any sign of corruption.

The variable s is calculated using only Electron arm information and therefore can be trusted. This leads to the interpretation that the majority of the events currently looked at are composed of elastic electrons. These electrons are recorded as coincidences with a Hadron arm trigger. But the Hadron triggers cannot be elastic protons since the Hadron arm spectrometer was not set to accept any elastic events. So, what are these events composed of elastic electrons and not elastic protons? With regard to that point, let us note that no cut has been implemented on the variable tc_cor . Accidental coincidences are not rejected yet. They can very well associate an electron trigger from elastic scattering, the dominant cross-section in our experimental conditions, to any proton trigger yielding unphysical values for vertex variables.

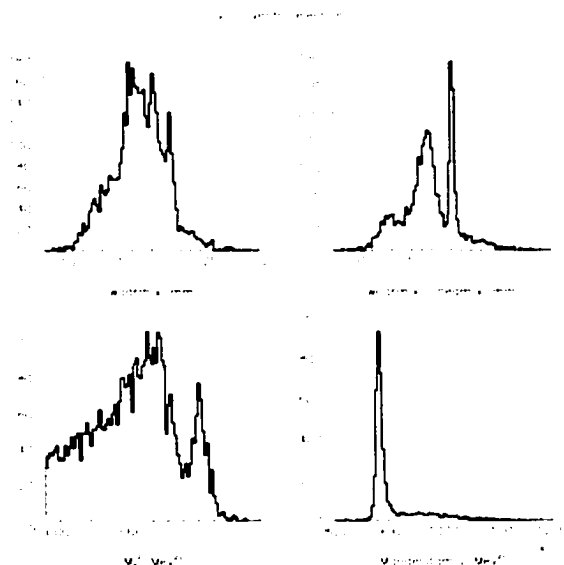


FIG. 66: Same spectra as in Fig 65 obtained now with the following preselection cut: $185.5 < tc_cor < 195.5$ and $-10,000 < M_X^2$. Most of the accidental coincidences have been suppressed. We are left with events in true coincidence. The majority of the events still presents the characteristics of elastic events with corrupted Hadron variables.

Let us now remove the accidentals. Fig. 66 contains the same histograms as

Fig. 65 but a preselection cut has been applied to the events. This cut now rejects events with a tc_cor value of less than 185.5 ns or greater than 195.5 ns, rejecting then most of the accidental coincidences. It also rejects events with a missing mass squared less than $-10,000 \text{ MeV}^2$.

The s spectrum still shows a preponderance of elastic events. Those events can also be found on the missing mass squared spectrum at still large negative values, on the left of the VCS peak that starts to appear centered at zero. I previously said that negative values in missing mass squared are unphysical. I should now temper this statement in two cases. The first case is for the VCS events: due to resolution effects in the detectors in general, the discrete value zero is transformed into a peak centered at zero with a finite extension. The second case is for well reconstructed elastic events. Indeed, in that case, there is no missing particle and therefore a missing mass squared spectrum presents a peak centered at zero with negative values allowed because of resolution and radiation effects.

In the $twoarm_x$ spectrum, the two characteristic horns of the raster on both side of zero starts to appear. They still stand on top of a remaining wide distribution. The situation is even clearer on the d spectrum where the peak centered at zero really shows escorted by other events mainly on its left side.

Even though the accidentals have been rejected for the most part, we still observe a dominant pollution of the VCS events by events involving elastic electrons. Even if the situation is now clearer, the separation between the VCS events and the pollution in the d and M_X^2 variables is still to be improved and so is the pollution removal under the peaks.

True coincidences and accidentals distributions

Fig. 67 is a 2-D histogram of d versus tc_cor after the preselection cut. The d and tc_cor spectra are unfolded in this 2-D plot. One can see the good events zone at $d = 0 \text{ mm}$ and tc_cor between 189 ns and 192 ns. The elastic events pollution can also be visualized in the same range of tc_cor but at negative values for d . One can also only guess the accidentals bunches every 2 ns since the lack of statistics does not make them very clear. This exact fact leads to the following remark:

the pollution does **not** come from the accidental coincidences. Even though an accidental subtraction is to be performed since some accidental events have values of d close to zero and therefore pollute the good events, this subtraction will not change much the final result.

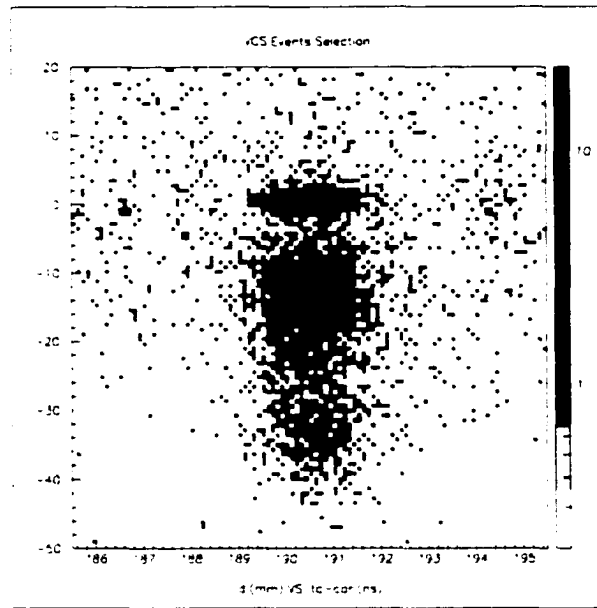


FIG. 67: This 2-D plot of d vs. tc_cor shows that the observed pollution comes from events in coincidence, the accidentals being almost inexistent offering an inexpedient explanation for the pollution.

Fig. 68 yields a further insight of the pollution, the good events and the accidentals. A 2-D plot of d versus s and of missing mass squared M_X^2 versus s are displayed on the left side for the events after preselection cut. The right side is for the accidentals, selected with the same preselection cut except the time window is now not the true coincidence time window but the accidental time window (on the left and right sides of the true coincidences in the tc_cor histogram of Fig. 58). A left-right comparison should only be qualitative since no weighting ratio has been applied for the accidentals.

The main remarks to be made are: the accidentals are mainly due to elastic

scattering and so is most of the remaining pollution (s value at the proton mass squared). But let us get more information on this pollution by finally looking at collimator variables in the Hadron arm.

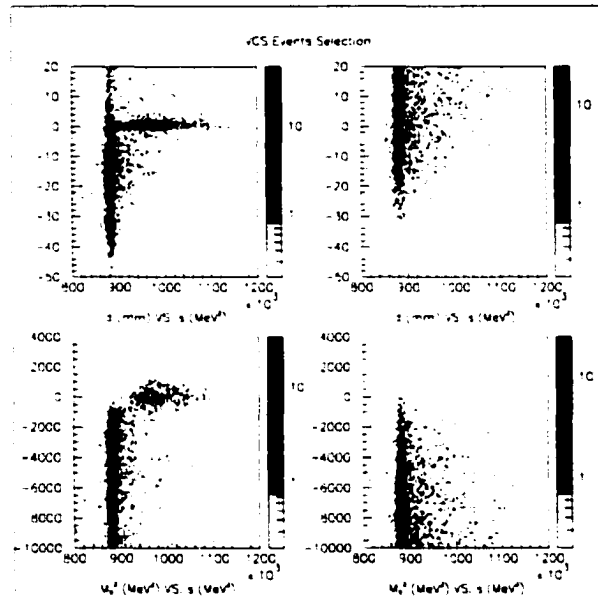


FIG. 68: The left panels concern the true coincidence events whereas the right ones are for accidentals. No quantitative comparison should be made since no weighting ratio has been applied to the accidentals. Both accidentals and the pollution events are from elastic scattering. The VCS events almost stand apart. A cut in s and/or d could really improve the VCS selection. But let us try first to better understand the pollution by studying Hadron collimator variables.

Punch through protons

Let us now invoke the Hadron collimator variables. The left plot in Fig. 69 is a 2-D plot of Hadron arm collimator coordinates obtained with the preselection cut. The range of the variables is the same as for Fig. 60 of the general discussion. As we saw there, some events lie outside the collimator at negative $hycol$ values ($hycol < -33$ mm) but now, in this particular zone of the Electron focal plane, there is almost no event beyond the collimator inner dimension at positive $hycol$

values ($hycol > 33$ mm). The edge of the collimator is also clearly visible as a dark region at $hycol \simeq -33$ mm. The vertical edges at $hxcol \simeq \pm 65$ mm are also distinguishable. The vertical coordinate is not fruitful to distinguish the good

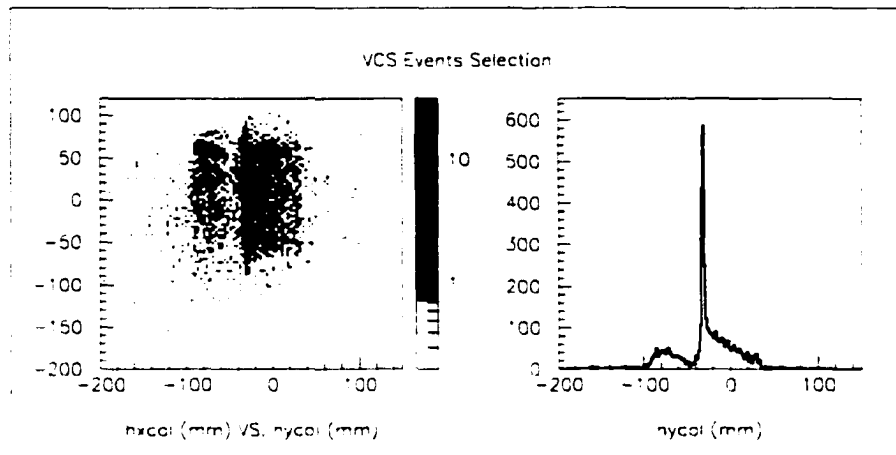


FIG. 69: The left plot is a 2-D plot of the vertical coordinate ($hxcol$) in the collimator plane *versus* the horizontal coordinate ($hycol$) while the right plot is a projection on the horizontal axis. The square shape of the free space defined by the collimator appears: almost no events are located beyond the collimator inner dimension on the right side of the plot ($hycol \simeq 33$ mm) while the right edge of the collimator (at $hycol \simeq -33$ mm) is visible (high density of events).

events from the bad ones. Indeed we do not have two independent measures of the vertical position of the vertex. We only have information from the beam and it is used to constrain the vertical vertex position. We therefore cannot form a difference like d is for the horizontal position. (That would have been very helpful though.) As the horizontal coordinate is discriminative, a profile in this horizontal coordinate is displayed on the right side of the figure. On this profile plot, we once again clearly see the extremity at the positive $hycol$ value of the collimator (sudden drop in the number of events), the other extremity as well because of the huge sharp peak and a bump of events in the left side of the plot.

The left plot in Fig. 70 finishes to give the interpretation of the pollution. This plot is a 2-D histogram of d *versus* $hycol$. The good events stands at $d = 0$ mm

and between the collimator edges ($-33 < hycol < 33$ mm). A region of pollution events stands at $hycol \simeq -33$ mm and negative d values that extends inside the band between the collimator edges. Another region of pollution events stands at large negative d and $hycol$ values. It can be noted that a band defined by $-50 < hycol < -33$ mm is more depleted of pollution. This band corresponds to the width of the collimator made of Heavy Metal (mainly Tungsten) that stops more efficiently the protons than Lead, the material used beyond the Heavy Metal band. Finally a cut in d and $hycol$ is very efficient in removing the pollution but the distribution of the pollution extends to the region of good events and therefore the pollution cannot be totally removed.

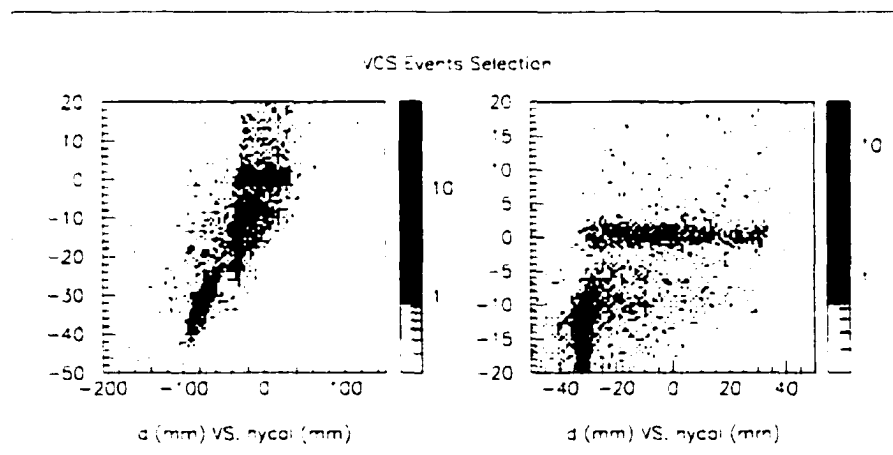


FIG. 70: These 2-D plots of the variables d and $hycol$ allow for a visual discrimination of three populations of events. First there are the punch throughs at large negative d and $hycol$. The second population is composed of the elastic protons that hit the collimator edge and bounced off it. The third population involves the good events located around $d = 0$ mm and between the two edges of the collimator. We note that a sole cut on d is not completely satisfactory as some events have a good value in d but not in the collimator variable. A cut in $hycol$ is also insufficient as a lot of events with negative d values and very certainly related to the elastic protons population bouncing off the edge of the collimator would be accepted. The right plot is a close up of the left one.

The right plot of Fig. 70 is a close up on the good events region. The good

events and the pollution from the edge of the collimator almost separate. The left plot of Fig. 71 is a projection of this close up on the d axis while the right plot presents a missing mass squared with a cut on d that accepts events with $-3 < d < 3$ mm.

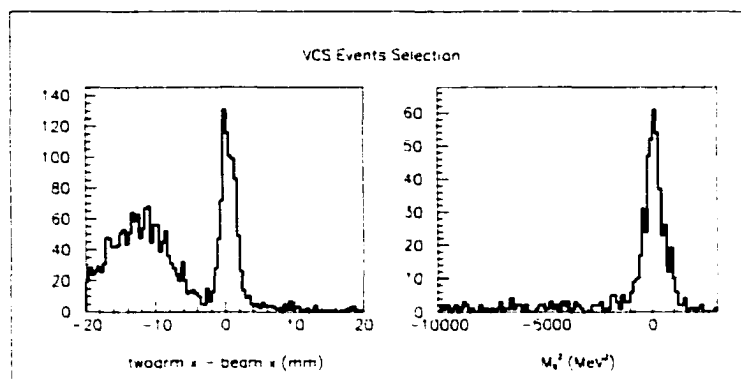


FIG. 71: The left plot is a projection on the variable d . The good events peaks almost stands apart for the pollution on its left. The right plot is a missing mass squared spectrum after the cuts $-33 < h_{ycol} < 33$ mm and $-3 < d < 3$ mm. The VCS peak is very clear.

Interpretation of the pollution origin

After the description of the good events and the pollution, the interpretation of the origin of the pollution can be made. It goes as follows. Some protons issued from an electron-proton elastic scattering process hit the edge of the collimator, bounce off it and are brought back into the acceptance of the spectrometer, the collimator in place not doing its role of cleanly defining a reduced acceptance. The spectrometer optics tensor reconstructs them correctly as from the edge of the collimator though. But the goodness stops here as the variables at the vertex in the target are not reconstructed correctly leading for instance to a negative missing mass squared or a negative value for d .

Other elastic protons interact “differently” at the edge of the collimator, are brought back into the acceptance but now are reconstructed as coming from inside

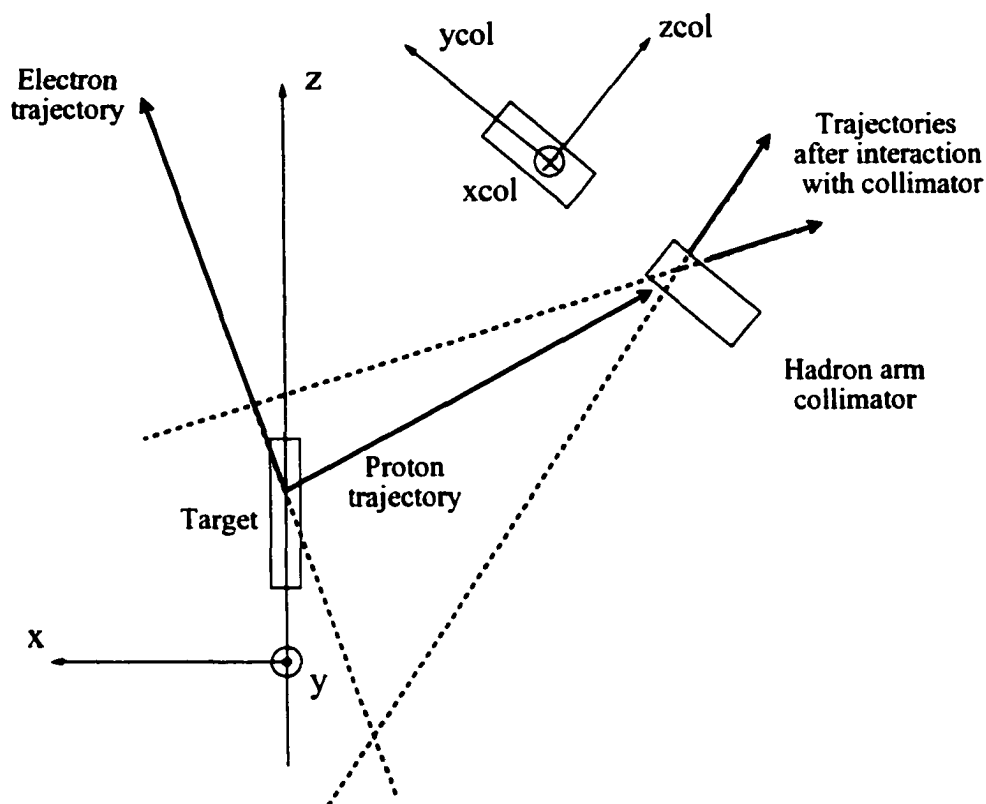


FIG. 72: Protons issued from electron elastic scattering off the target protons interact with the collimator matter. By combination between multiple scattering in the collimator or scattering off the edges, energy loss by going through the collimator matter, and acceptance functions of the spectrometer, we end up with a lot of them reaching the focal plane, triggering the system. They are reconstructed as primarily coming from the edge of the collimator or the right side matter of it, as pictured. Most of them have also negative values for d . As a reminder d is the difference between the x coordinate components of the intersection of the electron trajectory with the proton trajectory and the measured position of the beam. This is a question of acceptance: trajectories bended towards the center of the acceptance are more likely to stay within the acceptance (angular acceptance or acceptance in momentum). A cut on the collimator inner size is not enough to remove all of pollution. Indeed some of the events are reconstructed as coming from inside the collimator free space. Most of those can be removed with an additional cut in d . But even with a cut on d to remove them we are still bound to have a pollution for the selected good events by continuity of the phenomenon.

the collimator free space. They are the trickiest just because they seem to have an allowed trajectory. If it were not for a bad value in the d variable, they could easily be taken for perfectly valid events. An additional explanation is that they interacted in the top or bottom edges of the collimator. By losing energy in that process and by property of spectrometer in the dispersive direction, they are mixed with valid events for which the protons have lower momentum. Their horizontal collimator variable could be almost perfectly fine but not the vertical one leading to a corruption of the vertex variables.

Yet another class of elastic events seems to interact in the collimator matter, go through it and by multiple scattering inside the collimator matter, are brought once again in the acceptance.

It seems that all these events tend to be reconstructed at negative values of d , close to the edge of the collimator or further inside the collimator matter. But this is an acceptance bias: the scattering angle in the collimator reaction could have a wide range allowing also positive values of d . The latter values are less numerous simply because of a reduced acceptance value. Fig. 72 is a picture that offers a graphical understanding of this interpretation of the pollution.

Conclusion

In this zone of the focal plane, we saw that most of the accidental coincidences are due to elastic electron scattering off the proton. After investigation of the two other zones, we will conclude that most of the accidentals everywhere in the focal plane are due to elastic scattering.

We also saw that the removal of these accidentals is not enough to isolate the VCS events. Indeed the majority of the true (from a timing point of view) coincidences are also due to elastic scattering. The interpretation for this presence is linked to the collimator at the entrance of the Hadron spectrometer. This collimator does not correctly play its role of defining a reduced acceptance of the spectrometer. The energetic protons from elastic scattering are not stopped by the collimator but rather punch through it. The VCS kinematics being very close to the elastic kinematics, an intrinsic experimental difficulty of VCS, also allows

elastic protons to bounce off the edges of the collimator. We end up with a lot of elastic events polluting the VCS events.

Their removal is nevertheless possible for the most part. Indeed in their interaction with the collimator, the original vertex variables of the proton are affected. Protons still in the nominal acceptance of the spectrometer (*i.e.* acceptance without collimator) after interaction in the collimator are reconstructed correctly by the optics tensor at the collimator plane, at least in the non dispersive direction (position and angle). A cut on the reconstructed trajectories at the collimator can therefore remove the vast majority of the pollution. This cut does not remove all the pollution though and the diagnostic in the variable d has to be invoked. Unfortunately this latter cut is not enough for a total pollution removal since the tail of the pollution distributions extends in the region of actual good events. The variable s provides yet another cut that slices into the pollution. All cuts applied, the remaining pollution does not contaminate the good events by more than a few percent, a nice result considering the overwhelming proportion of the pollution before event selection.

9.2.3 Zone 2: Bethe-Heitler

Fig. 73 presents the four spectra of the four variables $twoarm_x$, d , M_{χ}^2 and s for all coincidence events. Fig. 74 presents the same spectra obtained with the preselection cut define in the previous subsection that mainly remove accidental coincidences (the 10 ns window centered around the true coincidences peak and a cut that removes large negative missing mass squared values). A comparison between the two figures indicates that there were not much accidental coincidences in the first figure. The d spectra present the sharp peak at zero of the good events while a wider distribution stands on its left. Like in the previous focal plane zone, the good events are polluted by events with an unphysical vertex position but with a good timing. The M_{χ}^2 spectra peak at zero. If it were not for the d values, one could easily take all the events for good VCS events. The s values indicate that the electrons are not from elastic scattering.

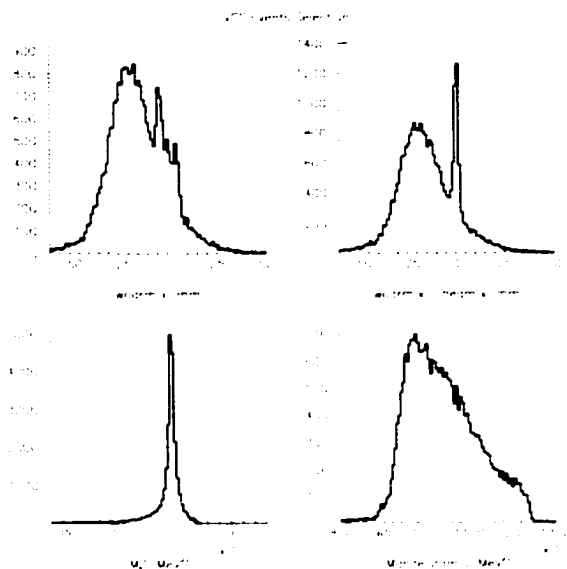


FIG. 73: To be compared with Fig. 65 and Fig. 80.

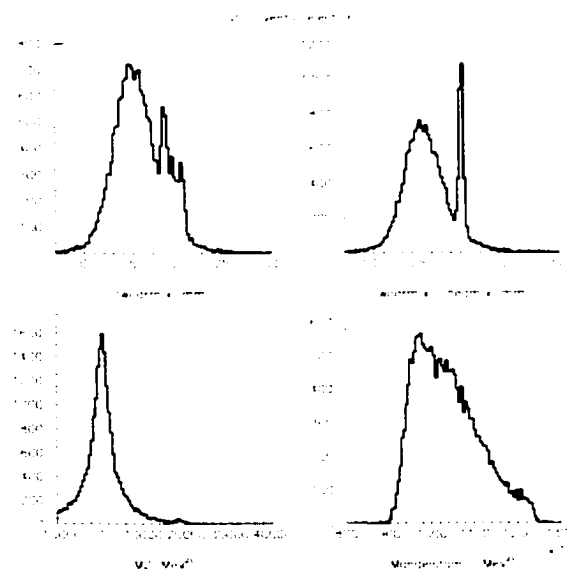


FIG. 74: To be compared with Fig. 66 and Fig. 81.

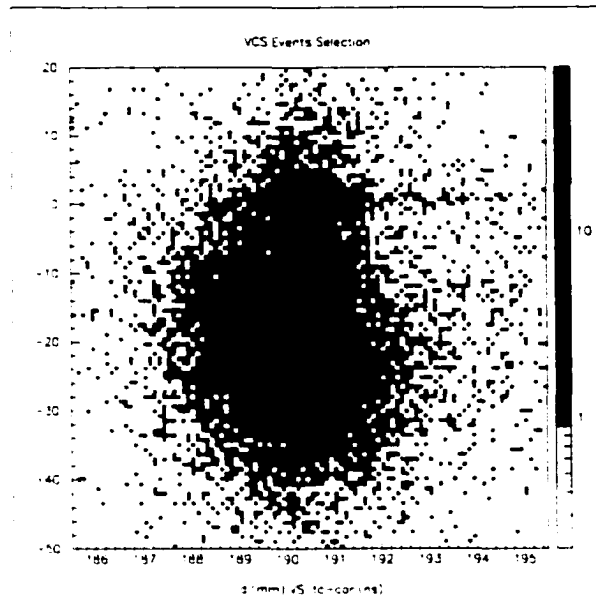


FIG. 75: To be compared with Fig. 67 and Fig. 82.

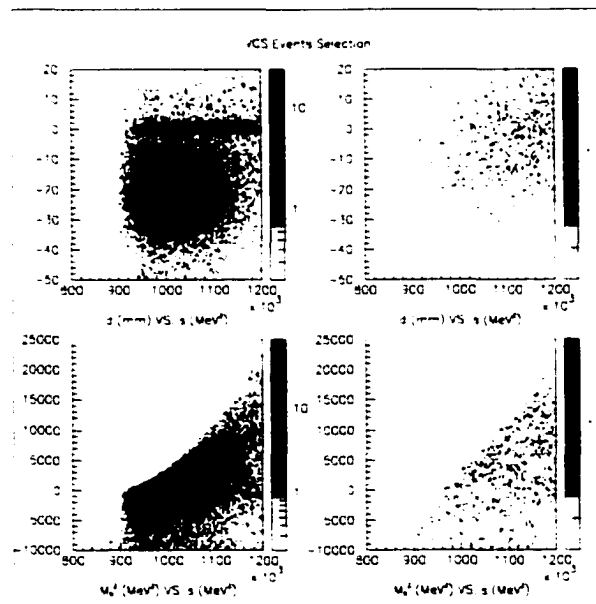


FIG. 76: To be compared with Fig. 68 and Fig. 83.

Fig. 75 presenting the variable d versus tc_cor confirms the fact that there is a pollution of the good events by events in the true coincidence peak with unphysical vertex positions. A cut in d can remove most of the pollution but not the tails that extend in the good events region.

Fig. 76 presents the 2-D plots of d and M_X^2 versus s for the true coincidence events on the left and for the accidentals on the right. Again there are not much accidentals. Furthermore the variable s is not discriminative anymore like it was in zone 1 of the focal plane.

Fig. 77 includes a 2-D plot of the collimator variables and a projection of this last plot on the horizontal axis, yielding a spectrum in $hycol$. The situation is very similar with that of zone 1. One can see a sharp peak locating on edge of the collimator, a lot of pollution on its left and not so much pollution on the other side of the collimator.

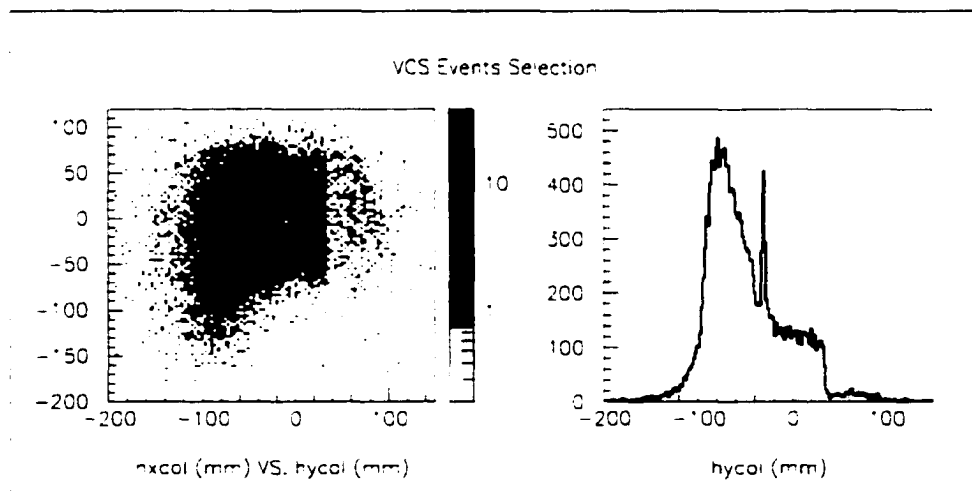


FIG. 77: To be compared with Fig. 69 and Fig. 84. From these plots of collimator variables, the same observations can be made as for zone 1 of the focal plane: the collimator edges are distinguishable by the reduced number of events on the right side and by the sharp peak on the left. Most of the events are outside the band of valid values for $hycol$.

Fig. 78 presents two 2-D plots of the discriminative variables d and $hycol$, the

right plot being a zoom on the good events. The conclusion is the same as for Fig. 70, namely that a cut on these two variables removes the majority of the pollution but not all of it. A slightly different aspect with respect to the previous focal plane zone is that the pollution contributes more in the good events peak.

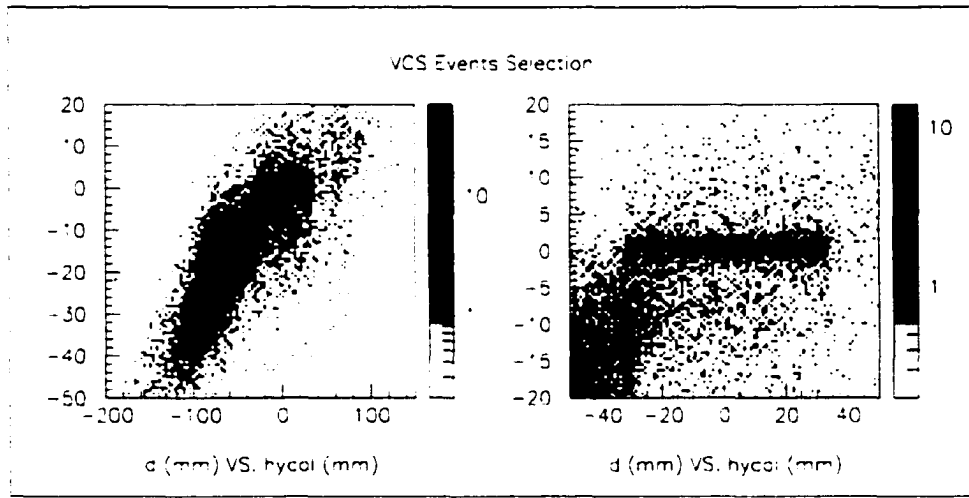


FIG. 78: To be compared with Fig. 70 and Fig. 85. These 2-D plots of d vs. $hycol$ unfold the $hycol$ spectrum of Fig. 69: most of the pollution (negative values of d) stands outside or on the edge of the free space defined by the collimator but it also trails inside and reaches the good events standing at $d = 0$ mm.

Finally Fig. 79 presents a d spectrum after the preselection cut and a cut on the nominal dimension of the collimator are applied. (It does not cut slightly inside as for the actual VCS events selection.) The pollution clearly reaches below the peak of the good events. The pollution removal cannot be total. The right plot is a missing mass squared spectrum when applying the previous cuts and the cut $-3 < d < 3$ mm. The VCS events are standing in the peak located at $M_X^2 = 0$ MeV². The pion peak starts to appear at 18200 MeV². The radiative tail of the VCS peak is also present.

From the previous observations, we conclude that the VCS events are polluted by events for which the proton interacted with the collimator just like in the previous focal plane zone. This leads to an unphysical reconstruction of vertex

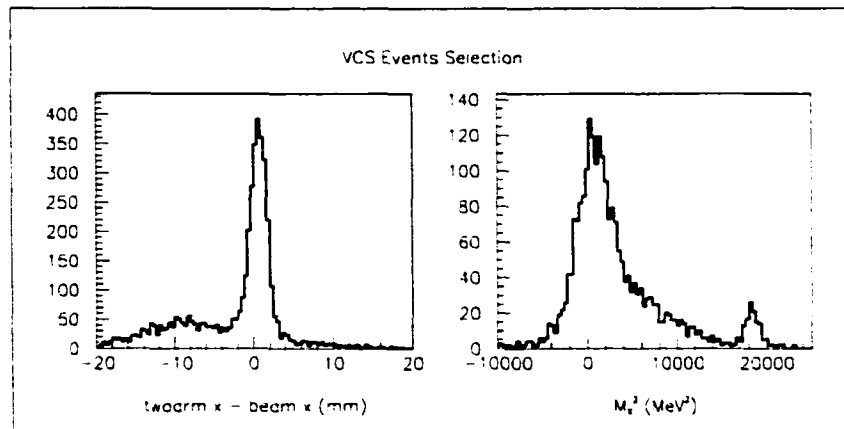


FIG. 79: To be compared with Fig. 71 and Fig. 86. A cut on the nominal inner dimension of the collimator is not enough to remove all the pollution as indicated by the d spectrum (left plot). An additional cut on this d variable eliminates another good fraction of the pollution and the M_X^2 spectrum on the right side is then obtained. The VCS peak and its radiative tail can be seen along with a rising pion peak.

variables and especially d . Fig. 72 still offers a graphical interpretation for the pollution. The pollution is removable for the very most part using the same set of cuts as in the previous zone: cut in tc_cor to select true coincidence events, cut in collimator variables to remove most of the pollution and cut in d to finish to prepare the VCS events selection in missing mass squared.

One main difference with the previous zone is that the electrons which triggered the coincidences belonging to the present focal plane zone are non longer purely elastic electrons but are located below the elastic line and therefore with a lower momentum. This fact is confirmed by the values of the variable s which are above the peak of purely elastic scattering events. Considering the existence of the Bethe-Heitler process, which has a stronger cross-section than the VCS process, and which corresponds to elastic scattering with radiation of a photon by the electron, then this process could be invoked to explain the pollution coincidences of the present zone.

9.2.4 Zone 3: pion

The figures presented here are obtained with events selected in the third zone of the electron focal plane. Fig. 80 is obtained before accidentals rejection while Fig. 81 has most of the accidentals removed. The pollution is less dramatic than for the two previous zones but can be more consequent in other VCS kinematics settings such as da_1_11 for instance (*cf* Fig. 10 regarding the VCS settings.).

The pollution is now located mostly on the right aisle of the good events peak in the d spectra. Most of the events are issued from the $ep \rightarrow ep\pi^0$ reaction as indicated by the peak in the missing mass squared spectra standing at the mass squared of the neutral pion.

As can be seen on Fig. 82 the accidentals are negligible in this zone and the pollution, once again, comes from true coincidences. The distributions in d , s and M_X^2 of the accidentals can be checked on the right panels of Fig. 83, the left plots being obtained with the true coincidences. Like in zone 2 but in contrast with zone 1, the variable s is not discriminative.

Fig. 84 offers a nice picture of the collimator. The pollution is now mostly on the right of plot. Fig. 85 displays 2-D plots of the discriminative variables d and $hycol$. The pollution can be seen outside of the free space defined by the collimator. By continuity of the phenomenon that induces the pollution, we are also bound to have some pollution inside but the observed values of d are such that it is very difficult to differentiate the good events from the pollution. The right plot is only a zoom on the region of good events.

A cut on the collimator inner dimension yield the left spectrum of d in Fig. 86. An additional cut on d allowing values at most 3 mm away from zero yield the missing mass squared spectrum on the right. Even if the VCS peak does not rise very high, it is well separated from the π^0 peak.

The interpretation of the pollution present in this zone of the electron focal plane is similar of that of the previous zones. The pollution is due to pion production reactions whose protons hit the collimator, punch through it and are still in the nominal acceptance of the spectrometer after interaction. The left side of the collimator is now at play in contrast with the previous two cases.

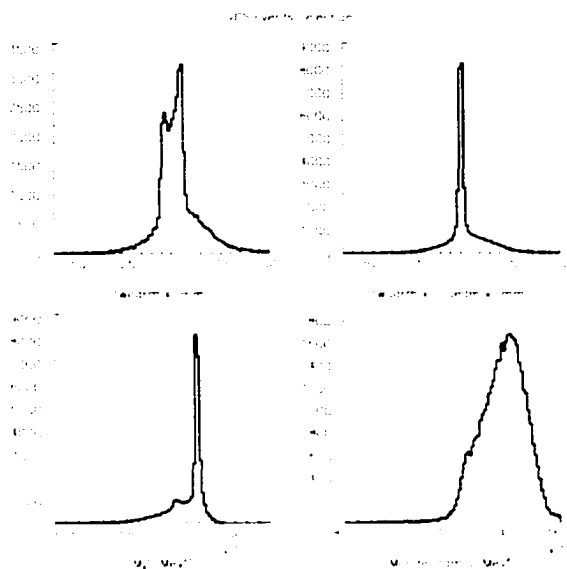


FIG. 80: To be compared with Fig. 65 and Fig. 73.

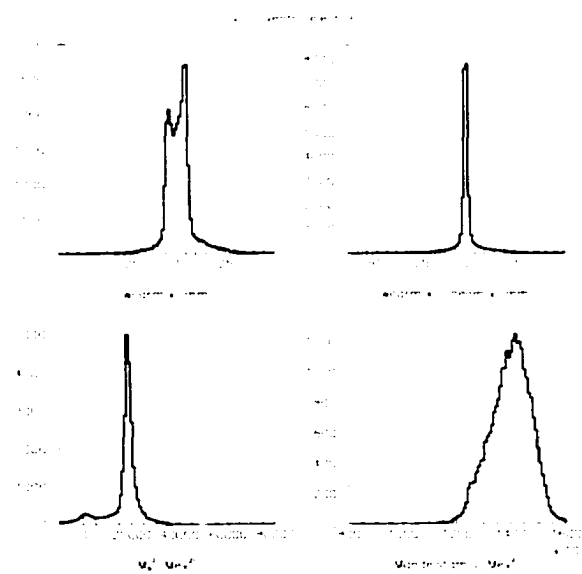


FIG. 81: To be compared with Fig. 66 and Fig. 74.

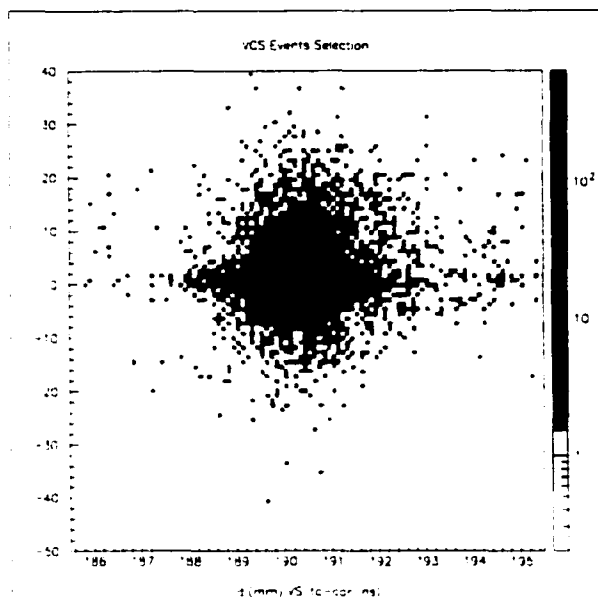


FIG. 82: To be compared with Fig. 67 and Fig. 75.

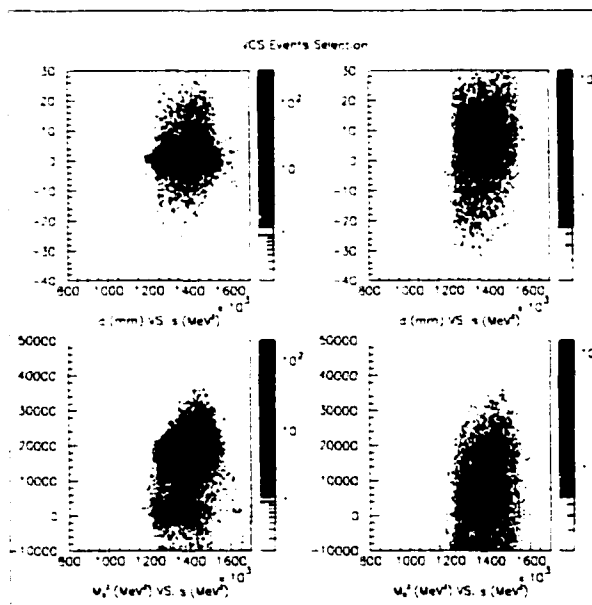


FIG. 83: To be compared with Fig. 68 and Fig. 76.

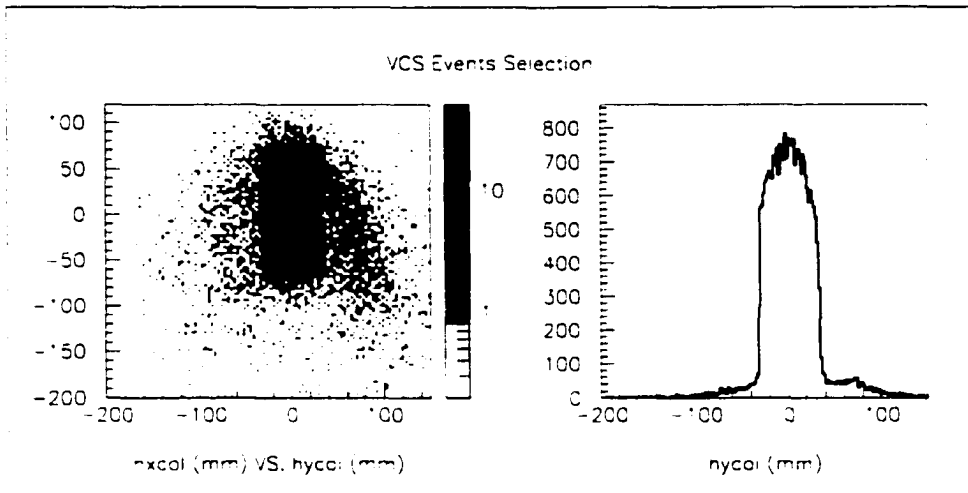


FIG. 84: To be compared with Fig. 69 and Fig. 77.

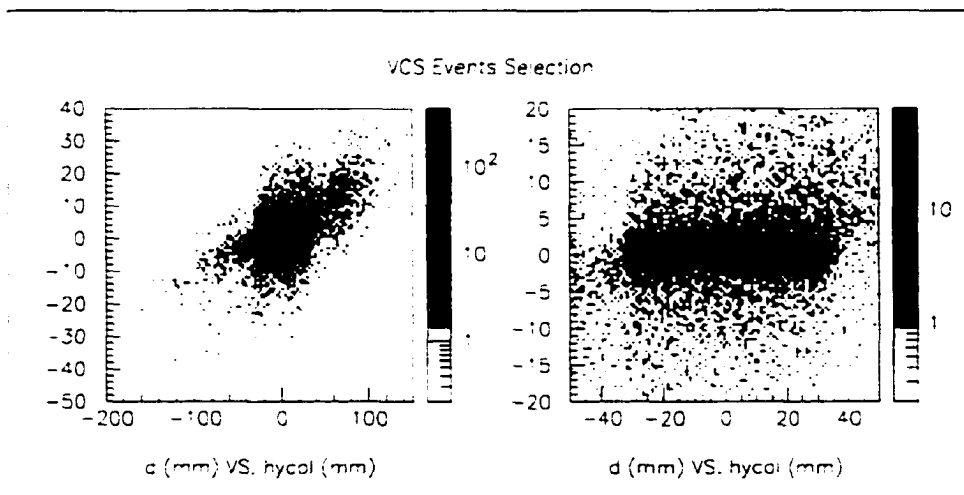


FIG. 85: To be compared with Fig. 70 and Fig. 78.

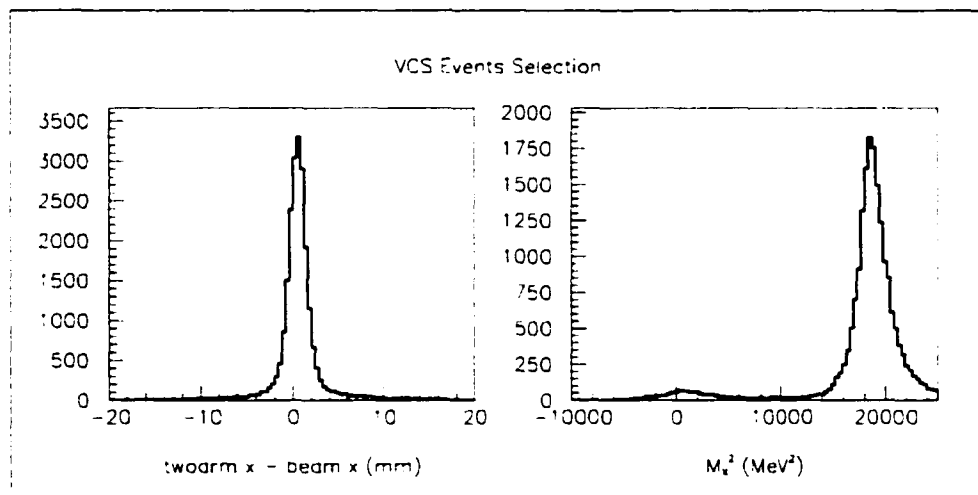


FIG. 86: To be compared with Fig. 71 and Fig. 79.

Chapter 10

Cross-section extraction

10.1 Average *vs.* differential cross-section

Most generally, a cross section evaluation is performed by first counting the number of reactions induced by the process under investigation. Those events can be arranged in bins. A one-dimensional bin is defined by a central value and a range. The total interval spanned by a given variable upon which the cross-section depends can be subdivided into smaller intervals, called bins. The practical size of the bin is mostly dictated by the number of counts measured in that bin. But the cross-section behavior restricts its width since the cross-section should not vary too much over the range of the bin. The size of the bins are therefore a compromise between a necessary finite size because of experimental constraints (counting rate, instrumental resolutions, *etc.*) and a not too big extension because of cross-section behavior (even though one could deal with rapid variations with a realistic simulation that includes a cross-section model that reproduces the true cross-section behavior).

A division of the number of counts in a bin (N_{bin}^{exp}) by the integrated luminosity (\mathcal{L}^{exp}), which is totally independent of the process under study and only depends on the target and beam characteristics, yields the integrated cross-section over the accessed phase space (geometric ranges of the variables convoluted with the

acceptance functions of the spectrometers):

$$\frac{N_{\text{bin}}^{\text{exp}}}{\mathcal{L}^{\text{exp}}} = \int d\sigma \quad (192)$$

This can also be written to define the cross-section averaged over the bin:

$$\left\langle \frac{d^5\sigma}{dk' d\Omega_e d\Omega_{\gamma^* \gamma}^{CM}} \right\rangle_{\text{bin}}^{\text{exp}} = \frac{N_{\text{bin}}^{\text{exp}}}{\mathcal{L}^{\text{exp}} \Delta^5(k', \Omega_e, \Omega_{\gamma^* \gamma}^{CM})}. \quad (193)$$

In this expression, $\Delta^5(k', \Omega_e, \Omega_{\gamma^* \gamma}^{CM})$ is the nominal acceptance of the bin in five variables which define the final state of the $ep \rightarrow ep\gamma$ reaction.

However this approach faces several limitations in a multi-dimensional phase space situation. Once the size of the bins are made large enough to accumulate significant statistics, the acceptance of the apparatus bisects many of the bins. The kinematics of the final photon ($\Omega_{\gamma^* \gamma}^{CM}$) are further convoluted by the experimental acceptance in missing mass squared M_X^2 (a finite acceptance is necessary in order to define a VCS event). For these reasons $\left\langle d^5\sigma / (dk' d\Omega_e d\Omega_{\gamma^* \gamma}^{CM}) \right\rangle_{\text{bin}}^{\text{exp}}$ (Eq. 193) is highly dependent on the experimental conditions.

We prefer an analysis strategy that will extract a differential cross-section that depends only on the physics and not on our apparatus. For that purpose, we rewrite Eq.192 to obtain an experimental differential cross-section as follows:

$$\frac{N_{\text{bin}}^{\text{exp}}}{\mathcal{L}^{\text{exp}}} = \left(\frac{d^5\sigma}{dk' d\Omega_e d\Omega_{\gamma^* \gamma}^{CM}}(P_0) \right) \left[\frac{\int d\sigma}{\left(\frac{d^5\sigma}{dk' d\Omega_e d\Omega_{\gamma^* \gamma}^{CM}}(P_0) \right)} \right] \quad (194)$$

where P_0 is a point in phase space (inside the bin or even outside the bin range).

In the above equation, Eq. 194, everything in square bracket has the dimension of the phase space and will be evaluated by a simulation. Doing so, we can now define:

$$\Delta_{\text{eff}}^5(k', \Omega_e, \Omega_{\gamma^* \gamma}^{CM}) \equiv \left[\frac{\int d\sigma}{\left(\frac{d^5\sigma}{dk' d\Omega_e d\Omega_{\gamma^* \gamma}^{CM}}(P_0) \right)} \right]^{\text{sim}}. \quad (195)$$

The experimental differential cross-section can then be defined from Eq. 194 as:

$$\left(\frac{d^5\sigma}{dk' d\Omega_e d\Omega_{\gamma^*}^{CM}}(P_0) \right)^{\text{exp}} \equiv \frac{N_{\text{bin}}^{\text{exp}}}{\mathcal{L}^{\text{exp}} \Delta_{\text{eff}}^5(k', \Omega_e, \Omega_{\gamma^*}^{CM})}. \quad (196)$$

The simulation of the effective phase space Δ_{eff}^5 (Eq. 195) must take into account possible migrations of events from one bin to the next. These migrations are caused by resolution deteriorations effects such as energy losses in the target material, energy losses through other materials along the particle path, multiple scattering when going through matter, spectrometer resolution and also by radiative effects that are very important in VCS (radiation of a second photon).

10.2 Simulation method

The Monte Carlo simulation used in this thesis has been developed in Gent, Belgium by L. Van Hoorebeke. It was first written for the VCS experiment at MAMI and then adapted to the VCS experiment at Jefferson Lab. It is in fact a package of three separate Fortran codes. The first part, named VCSSIM, simulates all processes happening in the target up to the entrance of the spectrometers. The second code, named RESOLUTION, takes care of applying all resolution deteriorations. Finally the third step consists in analyzing the previous output events. Events selection cuts can be applied and physics observables extracted. This code is named ANALYSIS. In short, this whole procedure yields simulated events which distributions can be compared to the actual data distributions. The simulation is divided in three codes to allow flexibility. Indeed the first step is very computer time consuming. It can be done once and the two other operations can be repeated at will.

The simulation technique uses a Sample-and-Reject method to generate an ensemble N^{sim} of events whose distribution within the bin models the physical cross section. Therefore the integrated cross section $[\int d\sigma]^{\text{sim}}$ of Eq. 195 is obtained in the same way as in Eq. 192:

$$\left[\int d\sigma \right]^{\text{sim}} = \frac{N_{\text{bin}}^{\text{sim}}}{\mathcal{L}^{\text{sim}}}. \quad (197)$$

Generation of N^{sim} events

This paragraph describes how the events are generated. First the code VC-SSIM samples a beam energy in a Gaussian distribution (beam energy resolution) and generates a beam position on the target following the rastering parameters. Then it samples an interaction point uniformly along the beam axis. It then applies multiple scattering and energy loss by collision in the target as well as real external and internal radiative effects on the incident electron. From there it samples uniformly in the phase space variables (k' , $\cos\theta_e$, Φ_e , $\cos\theta_{\gamma^*}^{\text{CM}}$, Φ). The method of Sample-and-Reject is then applied: events are accepted according to a cross-section behavior. A event at point P is accepted only with probability

$$p = \frac{d^5\sigma(P)}{dk' d\Omega_e d\Omega_{\gamma^*}^{\text{CM}}} \bigg/ \frac{d^5\sigma(P_{\text{ref}})}{dk' d\Omega_e d\Omega_{\gamma^*}^{\text{CM}}}, \quad (198)$$

where $d^5\sigma(P_{\text{ref}})$ is a reference cross section (if $p > 1$, the event is rejected also).

In a first pass analysis the BH+B cross-section is used (coherent sum of Bethe-Heitler and Born processes (*cf.* chapter 3)). This cross-section is relevant since the measured cross-section is a deviation from this BH+B cross-section. Refinements are accomplished for next passes (first evaluation of polarizability effects, Dispersion Relations). If the event is accepted, multiple scattering and energy loss by collision in the target materials (walls and liquid Hydrogen) along the way of the outgoing particles is applied, as well as real external and internal radiative effects on the outgoing electron. Finally an experimental acceptance check validates the event or not. (For completeness, although the following aspect will be further addressed in the next section, the RESOLUTION code smears the focal planes variables according to some parameterization and projects back to the target to obtain the new vertex quantities.) The total number of events accepted by both the sample-and-reject method and experimental acceptance in the phase space bin is $N_{\text{bin}}^{\text{sim}}$.

Calculation of \mathcal{L}^{sim}

Each event in the simulation before the sample-and-reject selection is imposed represents a beam-target interaction. \mathcal{L}^{sim} is the integrated luminosity necessary

to produce this number of interactions. \mathcal{L}^{sim} is calculated in parallel with the generation of N^{sim} , by Monte-Carlo integration of the cross section.

The spectrum of incident electron energies at the vertex extends from the incident beam energy k_0 all the way down to zero energy. To avoid dealing with the low energy tail of this distribution, we first calculate the simulation luminosity for incident electrons of energy $k > k_0 - 5$ MeV. In the following, the subscript '5 MeV' denotes this restriction on the event sample.

A reference phase space $\Delta_{\text{ref}}^5(k', \Omega_e, \Omega_{\gamma^* \gamma}^{CM})$ is defined such that for incident electrons with vertex energy $k > k_0 - 5$ MeV, the VCS process is physically allowable and the VCS cross section is less than the reference cross section (Eq. 198) everywhere inside Δ_{ref}^5 . The number of events accepted in Δ_{ref}^5 is $N_{5\text{MeV}}^{\mathcal{L}}$. The simulation luminosity is defined from Eq. 192 as:

$$\mathcal{L}_{5\text{MeV}}^{\text{sim}} = N_{5\text{MeV}}^{\mathcal{L}} / \left[\int_{\Delta_{\text{ref}}^5} d\sigma \right] \quad (199)$$

The integrated cross section is calculated by Monte-Carlo integration from the sample $N_{5\text{MeV}}^{\text{ref}}$ of events generated at random (before the sample-and-reject is applied) in Δ_{ref}^5 :

$$\left[\int_{\Delta_{\text{ref}}^5} d\sigma \right] = \frac{\Delta_{\text{ref}}^5(k', \Omega_e, \Omega_{\gamma^* \gamma}^{CM})}{N_{5\text{MeV}}^{\text{ref}}} \sum_{i=1}^{N_{5\text{MeV}}^{\text{ref}}} \frac{d^5\sigma(i)}{dk' d\Omega_e d\Omega_{\gamma^* \gamma}^{CM}} \quad (200)$$

The total simulation luminosity is then obtained by normalizing Eq. 199 by the ratio of all electrons generated in the beam N_{total} by the number $N_{5\text{MeV}}$ of events generated with $k > k_0 - 5$ MeV:

$$\mathcal{L}^{\text{sim}} = \frac{N_{\text{total}}}{N_{5\text{MeV}}} \mathcal{L}_{5\text{MeV}}^{\text{sim}}. \quad (201)$$

Effective phase space

The effective phase space Δ_{eff}^5 (Eq. 195) is therefore:

$$\Delta_{\text{eff}}^5 = \frac{N^{\text{sim}}}{\left(\frac{d^5\sigma}{dk' d\Omega_e d\Omega_{\gamma^* \gamma}^{CM}}(P_0) \right)^{\text{sim}} \mathcal{L}^{\text{sim}}}. \quad (202)$$

With this result from the simulation, the experimental differential cross-section of Eq. 196 is evaluated.

10.3 Resolution in the simulation

The simulation includes multiple scattering, energy loss straggling, and also bremsstrahlung effects. However, the experimental resolution was not as good as the simulation distributions. To improve the agreement between the simulation and experiment, additional Gaussian smearing was added to the focal plane variables in the simulation. The smeared coordinates were then projected back to the reaction vertex. In addition, the experimental distributions are observed to have long tails, including several percent of the total events. These tails were modelled in the simulation by including a second, broader distribution to the focal plane angle variables for a few percent of the events in the simulations, selected at random. The widths and strengths of these distributions were defined by examination of the `angle_diff` variable, which is the difference in the angle measured in one VDC compared to the angle measured with the two VDCs.

Fig. 87 shows a comparison of experimental data and the simulation for a missing mass distribution, after all event selection cuts, as defined in chapter 9.

10.4 Kinematical bins

One needs five independent kinematic variables to describe the reaction under study. Thus one has to extract the cross-sections into 5-dimensional kinematic bins.

Usually, one uses the following five independent quantities: the outgoing electron momentum, k' , the polar and azimuthal angles of the outgoing electron, θ_e and Φ_e respectively, the polar angle between the incoming virtual photon and outgoing real photon in the γ^*p center of mass, $\theta_{\gamma^*\gamma}^{CM}$, and the azimuthal angle of the outgoing real photon around the virtual photon polar axis, Φ . Note that Φ can also be seen as the angle between the leptonic and hadronic planes as shown in Fig. 88.

However, it is interesting to study the behavior of the cross-sections as a function of $\theta_{\gamma^*\gamma}^{CM}$ and q'_{CM} at fixed Q^2 . Then one can change from the variable pair

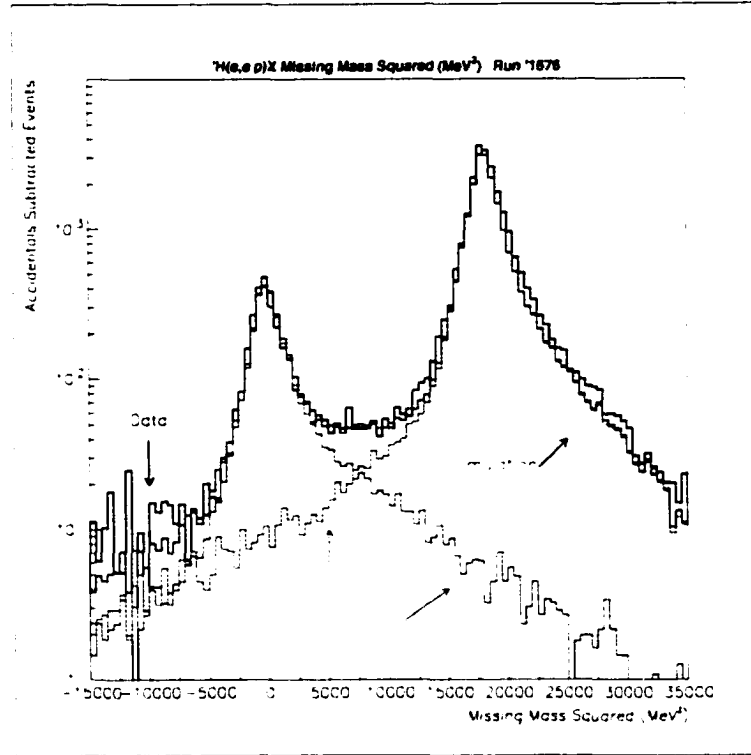


FIG. 87: Comparison between simulation and experimental data. A good agreement is found. The black histogram is obtained with the experimental data while the blue one is from the simulation. The red and green histograms separate the VCS events from the π^0 production events obtained by simulation.

(k', θ_e) to the set (Q^2, q'_{CM}) using the following relations:

$$Q^2 = 4EE' \sin^2(\theta_e/2) \approx 4kk' \sin^2(\theta_e/2) \quad (203)$$

neglecting the electron mass.

and

$$q'_{CM} = \frac{s - m_p^2}{2\sqrt{s}} \quad \text{with} \quad s = (q + p)^2 = -Q^2 + m_p^2 - 2m_p(k - k') \quad (204)$$

neglecting again the electron mass.

Now bins and central values have to be defined for Q^2 , q'_{CM} , Φ_e , $\theta_{\gamma^* \gamma}^{CM}$ and Φ .

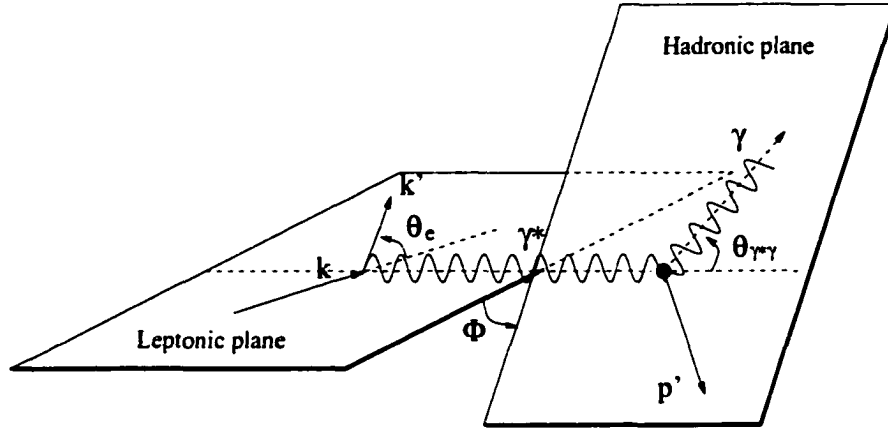


FIG. 88: VCS in the laboratory frame. The leptonic and hadronic planes are represented. The kinematical variables are also displayed.

In the analysis, all values of the azimuthal angle Φ_e of the electron reaction plane are used. All values of Q^2 of this data set is also used. The range is: $0.85 < Q^2 < 1.15 \text{ GeV}^2$. However, cross-sections are evaluated at $Q^2 = 1 \text{ GeV}^2$. It is the same situation for variable Φ , where we need to use all values to evaluate the cross-sections at $\Phi = 0^\circ$, since we want to make a study in the leptonic plane. Note that the leptonic plane is also characterized by $\Phi = 180^\circ$, but as a convention, we define $\theta_{\gamma^* \gamma}^{CM}$ to be negative and $\Phi = 0^\circ$ when in fact $\Phi = 180^\circ$.

The range of q'_{CM} is limited to [30 MeV, 120 MeV] and is divided in 3 bins: [30 MeV, 60 MeV], [60 MeV, 90 MeV] and [90 MeV, 120 MeV]. Cross-sections are evaluated in the middle of each bin, *i.e.* for $q'_{CM} = 45 \text{ MeV}$, $q'_{CM} = 75 \text{ MeV}$ and $q'_{CM} = 105 \text{ MeV}$.

Then, one has chosen to divide the 360° range of the variable $\theta_{\gamma^* \gamma}^{CM}$ into twenty bins of 12° in width, leading to twenty cross-section values, one for each bin in $\theta_{\gamma^* \gamma}^{CM}$, as we will see in the next chapter.

Finally VCS events were selected inside a window in missing mass squared: $-5000 \text{ MeV}^2 < M_X^2 < 5000 \text{ MeV}^2$.

10.5 Experimental cross-section extraction

General expression

The $ep \rightarrow ep\gamma$ experimental cross-section is calculated as follows:

$$\left(\frac{d^5\sigma}{dk' d\Omega_e d\Omega_{\gamma}^{CM}}(P_0) \right)^{\text{exp}} = \Gamma_{\text{radcor}} \frac{N^{\text{exp}}}{\mathcal{L}^{\text{exp}} \Delta_{\text{eff}}^5} \quad (205)$$

where:

- N^{exp} stands for the number of events remaining after event selection procedure corrected for various factors,
- \mathcal{L}^{exp} is for the integrated luminosity,
- Δ_{eff}^5 is the effective phase space,
- Γ_{radcor} represents the normalization factor due to radiative effects not taken into account in the simulation.

All those factors are discussed in the following paragraphs.

Filtering data

The operation of data filtering is to discriminate good portions of runs from periods when hardware problems occurred. These periods have to be rejected since they bias a cross-section evaluation.

Some of these problems can be identified as high voltage failure of VDCs or scintillators electric alimentation while the beam is still on. In both cases, no trajectory reconstruction is possible. Therefore, we cannot determine to which kinematic bin the unreconstructed event belong. Our evaluation of the number of events per bin is then inexact.

Another source of problem is spectrometer magnets drift: at the time of the experiment, no automatic feedback was implemented to regulate the magnets fields by means of magnet current regulation. In addition, spectrometer magnet currents can be lost. Here, the path of the particles in the spectrometers is not

what we assume it is and the vertex reconstruction is not correct. This leads to a mis-sorting of events in kinematic bins.

Beam restorations induce target temperature fluctuations that bias the luminosity evaluation (*cf.* subsection 6.2.3). Let me mention here that the boiling study can reveal any significant change in raw counting rates and thus diagnose some of the problems described above (*cf.* subsection 8.4.3).

Finally, for about 20% of the runs, a BPM asynchronization problem occurred: the information coming from the BPMs is not in phase with the physics events anymore.

As a consequence, we are not able to reconstruct the beam variable *beam_x* used in the event selection nor the variable *beam_y* used in reconstructing the target variables. It is possible to locate the exact event which starts the asynchronous period and thus to either cut the bad periods, or re-synchronize the BPMs information [38].

Determination of N^{exp}

N^{exp} is determined by applying a weight factor to each event selected by the cut procedure (see chapter 9). This weight factor is in charge of correcting for electronics deadtime, trigger prescaling factor, computer deadtime, scintillators inefficiencies, VDCs and tracking combined inefficiency. Please refer to chapter 8 for a description of each of the above corrections. Finally, note that the accidental subtraction is considered to be part of the events selection.

Determination of \mathcal{L}^{exp}

The integrated luminosity \mathcal{L}^{exp} is calculated according to section 8.5 for each of the good portions of runs.

Determination of Δ_{eff}^5

The effective phase space factor Δ_{eff}^5 is calculated using the simulation as in section 10.2 of the current chapter.

Determination of Γ_{radcor}

The last correction to apply is a global renormalization factor due to radiative effects not taken into account in the simulation.

The radiative corrections on the electron side of the interaction can be classified in two main types. The first type is called external radiative corrections. This is the Bremsstrahlung radiation emitted by the incoming and outgoing electrons in the surrounding electromagnetic fields other than that of the scattering proton. This correction is included in the simulation and therefore no correction has to be made for the experimental cross-section.

The second type of radiative corrections is called internal radiative corrections. They take into account the emission of additional real photons (real internal radiation) and the emission and re-absorption of additional virtual photons (virtual internal radiation) at the scattering proton. A part of the real internal radiation correction depends on the cut in missing mass squared applied in the VCS events selection procedure that truncates the radiative tail on the right side of the VCS peak. This seems to require a correction but the same cut is applied in the simulation when evaluating the effective phase space factor Δ_{eff}^5 and finally no correction has to be applied for the experimental cross-section. The remaining part of the real internal radiation correction only depends on the kinematics and was found to be nearly constant over the considered phase space. The virtual internal radiation correction was also found to be nearly constant over the considered phase space.

Finally an additional radiative correction has to be applied. It takes into account the virtual radiative corrections on the proton side, the two-photon exchange correction and the soft photon emission from the proton correction (Bremsstrahlung radiation from the proton).

The values for the three renormalization factors are extracted from Ref. [39] (see also Ref. [40] and Ref. [41]):

–18.3% for the virtual internal radiation on the electron side

+26.7% for the real internal radiation on the electron side (cut-off independent)

–1.3% for the remaining corrections.

The global correction factor is therefore $\Gamma_{\text{radcor}}=0.931$.

Chapter 11

Cross-section and Polarizabilities Results

11.1 Example of polarizability effects

Fig. 89 shows two plots for the purpose of presenting the Bethe-Heitler and Born (BH+Born) cross-section and the effects of the polarizabilities.

The left plot displays three models of the cross-section as a function of $\theta_{\gamma^*\gamma}^{CM}$, the angle between the two photons in the Center-of-Mass frame of the VCS reaction. The horizontal axis is for this angular variable. The range is 360° , spanned between -220° and 140° . This configuration has been preferred over the much more usual $[-180^\circ;180^\circ]$ to bring the interesting part of the curves closer to the middle and better display the zone of actual effects of the polarizabilities. The Bethe-Heitler peaks have therefore been shifted to the right of the plot. In this plot, the polar angle θ is positive when the azimuthal angle $\Phi = 0$, and θ is negative when $\Phi = \pi$. The BH peaks occur when the emitted photon is nearly collinear with the beam or scattered electron directions. Notice that in our convention for Φ , this occurs for positive values of θ . Note also that the vertical axis used for cross-section values is expressed in a logarithmic scale. Indeed the cross-sections shrink by three or four orders of magnitude between the Bethe-Heitler region and the rest of the interval.

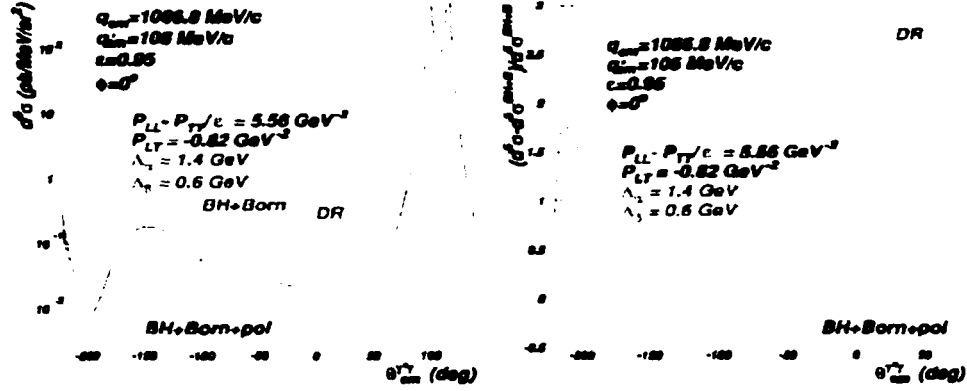


FIG. 89: Example of polarizability effects on the theoretical VCS cross-section $d^5\sigma/[dk'd\Omega_e]_{lab} d\Omega_{\gamma^*\gamma}^{cm}$. The magenta curve is the BH+Born calculation. The blue curve includes the polarizability effects in the first Non-Born term of the low energy expansion. The green curve is the Dispersion Relation curve of B. Pasquini *et al.*

The magenta curve is the coherent sum of the Bethe-Heitler and Born amplitudes. In addition to the sharp BH peaks, this curve displays a broad peak dominated by the approximately dipole (Larmor) radiation pattern of the Born amplitude (proton bremsstrahlung). The blue curve is the same as the magenta, with the inclusion of the contribution from the polarizabilities listed in the figure. The green curve is the full Dispersion Relation (DR) calculation of Pasquini *et al.* [31]. In the DR calculation, two parameters are needed (in addition to the dispersion analysis of the single pion production data). These parameters are the Q^2 dependent electric and magnetic polarizabilities. For convenience in the calculation, these polarizabilities are parameterized as follows:

$$\begin{aligned} \alpha_E(Q^2) - \alpha_E^{\pi N}(Q^2) &= [\alpha_E(0) - \alpha_E(0)^{\pi N}] / [1 + Q^2/\Lambda_\alpha^2]^2 \\ \beta_M(Q^2) - \beta_M^{\pi N}(Q^2) &= [\beta_M(0) - \beta_M^{\pi N}(0)] / [1 + Q^2/\Lambda_\beta^2]^2. \end{aligned} \quad (206)$$

In these expressions, $\alpha_E^{\pi N}(Q^2)$ and $\beta_M^{\pi N}(Q^2)$ are the contributions calculated from the dispersion integrals over the MAID parameterizations of the $\gamma^*N \rightarrow \pi N$

amplitudes. Note that the dispersion integrals for $\alpha_E^{\pi N}(Q^2)$ and $\beta_M^{\pi N}(Q^2)$ converge, even though the integrals for the complete α_E and β_M do not. The values $\Lambda_\alpha = 1.4$ GeV and $\Lambda_\beta = 0.6$ GeV were adjusted to fit the MAMI data at $Q^2 = 0.33$ GeV². The values $P_{LL} - P_{TT}/\epsilon = 5.56$ GeV⁻² and $P_{LT} = -0.82$ GeV⁻² were adjusted to the values of Λ_α and Λ_β .

The right hand side plot in Fig. 89 shows the relative deviation of the Low Energy Expansion and of the Dispersion Relation calculations from the BH+Born calculation. The effects of the Non-Born terms are important throughout the entire kinematic range displayed in the figure, except for the immediate vicinity of the BH peaks.

11.2 First pass analysis

The first pass analysis was realized as described in chapter 10. The obtained results, including all 17 settings discussed in section 4.3, are shown in Fig. 90.

In this figure, the six panels represent the experimental cross-sections values as a function of $\theta_{\gamma^* \gamma}^{CM}$. All these cross-sections have been evaluated at $Q^2 = 1$ GeV², and integrated over Φ_e . In the left plots, we consider all Φ values within the experimental acceptance, while in the right plots, only a small range around the leptonic plane considered, namely the leptonic plane $\pm 30^\circ$. Finally, the top, middle and bottom plots show the results for $q'_{CM} = 45$ MeV, $q'_{CM} = 75$ MeV and $q'_{CM} = 105$ MeV, respectively.

Extracted experimental values are compared to the theoretically calculated BH+Born ones (magenta curve in Fig. 90). Globally, the model reproduces well the data. Now looking at forward angles, one observes a small deviation of the data from the BH+Born model when q'_{CM} increases. This is believed to be the sign of the polarizabilities effect as discussed in section 11.1.

Initially, we were interested in extracting cross-sections values in the leptonic plane ($\Phi = 0^\circ, 180^\circ$). For $\theta_{\gamma^* \gamma}^{CM} > 0$, most of the data we collected were out of plane due to acceptance effect. That's why when we restrict ourselves to a small range around the leptonic plane (right plots in Fig. 90), errors bars are bigger.

However, taking into account these errors bars, one sees that the deviation of the data from the BH+Born model is roughly the same for all $\theta_{\gamma\gamma}^{CM}$ and q'_{CM} bins compared to the left plots.

This last observation is perhaps more clearly shown in Fig. 91, which presents the relative difference between the calculated BH+Born cross-sections and the experimental cross-sections shown in Fig. 90. The difference is displayed as a function of $\theta_{\gamma\gamma}^{CM}$ for the 3 values of q'_{CM} in the same scheme as for Fig. 90. Red points refer to the case we consider a large range around the leptonic plane, and the green points refer to the case where only a small range around the leptonic plane is considered.

Now that cross-sections have been extracted and seem to indicate a sign of polarizability effect, we are going to proceed to their extraction in the next section.

11.3 Polarizabilities extraction

The procedure to extract polarizabilities from the data is directly related to Eq. 86 which I recall here using the kinematical variables newly defined in chapter 10:

$$d^5\sigma_{ep\rightarrow e\gamma} = d^5\sigma^{BH+Born} + \Psi q'_{CM} \mathcal{M}_0^{NonBorn} + \mathcal{O}(q'^2_{CM}) \quad (207)$$

with (Eq. 87):

$$\mathcal{M}_0^{NonBorn} = v_{LL}[P_{LL}(q_{CM}) - P_{TT}(q_{CM})/\epsilon] + v_{LT}P_{LT}(q_{CM}) \quad (208)$$

Then, one first needs to make sure that the difference $d^5\sigma_{ep\rightarrow e\gamma} - d^5\sigma^{BH+Born}$ is consistent with zero when q'_{CM} is getting small in order to be able to use Eq. 207. Actually, this is what we just have concluded from Fig. 91, so we can proceed to the next step.

In Fig. 92 ΔM^{exp} is extracted directly from the data at $q' = 105$ MeV by

$$\Delta M^{\text{exp}} = [d^5\sigma_{ep\rightarrow e\gamma} - d^5\sigma^{BH+Born}] / [\Psi q'_{CM}] \quad (209)$$

In the limit that the $\mathcal{O}(q'^2_{CM})$ terms can be neglected:

$$\Delta M^{\text{exp}} \rightarrow \mathcal{M}_0^{NonBorn} \quad (210)$$

A study of $\mathcal{M}_0^{NonBorn}/v_{LT}$ (where the value of the numerator is known from the previous step) as a function of v_{LL}/v_{LT} , gives us access to $P_{LL}(q_{CM}) - P_{TT}(q_{CM})/\epsilon$ and $P_{LT}(q_{CM})$ (Eq. 208) with $P_{LL}(q_{CM})$, $P_{TT}(q_{CM})$ and $P_{LT}(q_{CM})$ being linear combinations of the generalized polarizabilities. For precisions on that point see section 3.4.

In Fig. 92, $\Delta M^{exp}/v_{LT}$ is plotted as a function of v_{LL}/v_{LT} . Again two cases have been considered, the first one including the whole range around the leptonic plane (left plot), and the second one over a smaller range (right plot). The numbers close to the data points indicate the value of $\theta_{\gamma^* \gamma}^{CM}$ for which they have been calculated. In the end, the linear fit applied is represented by the solid line. The results for $P_{LL}(q_{CM}) - P_{TT}(q_{CM})/\epsilon$ and $P_{LT}(q_{CM})$ are also given.

By looking at χ^2 values, one foresees that in order to extract polarizabilities from the data, it is again better to restrict ourselves to a relatively small range around the leptonic plane. Indeed, the effect of the polarizabilities is not necessarily the same over the whole range in Φ , and projecting them on the leptonic plane might lead to some additional systematic errors.

In any case, to improve the obtained results, it is necessary to perform an iteration in the analysis that I will present in the next section.

11.4 Iterated analysis

The iterated analysis consists in using the first guess of the polarizabilities effect obtained in the previous section to run a new Monte Carlo simulation. In this simulation the cross section model includes the BH+Born terms and the $\mathcal{O}(q')$ contributions from the polarizabilities, as extracted in the previous analysis. The resulting effective phase space from the simulation is used to extract revised values of the experimental cross sections in each bin. From these new cross sections, the polarizability analysis of the previous section is repeated.

The operation described above has been performed twice, and the results in Fig. 93 through Fig. 95 are issued from the second iteration. In Fig. 93, similar plots as in Fig. 90 are presented, but the model to evaluate the effective phase

space used in the calculation of the experimental cross-section includes now the polarizability effect. Fig. 94 is the second iteration plot similar to that of Fig. 91. In these two new figures, one notices that the deviation of the data from the BH+Born model is significantly accentuated after iterations, this for all q'_{CM} bins. even at the lowest value. This comes from the fact that cross-sections in the simulation are more realistic.

After a second iteration, the extraction of the polarizabilities is presented in Fig. 95. One can see that the data points are much better aligned compared to Fig. 92. It is confirmed by the χ^2 values: 2.6 and 2.2 to be compared to 6.5 and 3.5. This is a strong indication of the need of doing such an iterated analysis.

11.5 Discussion

In the previous sections, we have seen that the polarizabilities definitely exist even if it is difficult to measure them. We have also shown that a low energy analysis can give a value for these polarizabilities, at least a set of combination of them.

Fig. 96 shows cross-section values obtained after iteration 2 in comparison with various models. The magenta lines represent as usual the BH+Born model. The blue lines represent the cross-section values containing the polarizabilities effect as found in Fig. 95. As such, this model describes better the data points than the BH+Born model alone. As for the green lines, they are the result of a dispersion relation formalism calculation as described in section 3.6. One sees the data are quantitatively consistent with such a calculation.

That being said, a refinement in this analysis would be to include a dispersion relation formalism code in the simulation. Another improvement that could be done is to revise the binning to explicitly select out of plane events. At the present stage, we can determine a systematic error band for the two structure functions at $\bar{Q}^2 = 0.93 \text{ GeV}^2$ extracted at $q' = 105 \text{ MeV}$ as follows:

$$P_{LL} - P_{TT}/\epsilon \in [4, 7]\text{GeV}^{-2} \quad (211)$$

$$P_{LT} \in [-2, -1]\text{GeV}^{-2} . \quad (212)$$

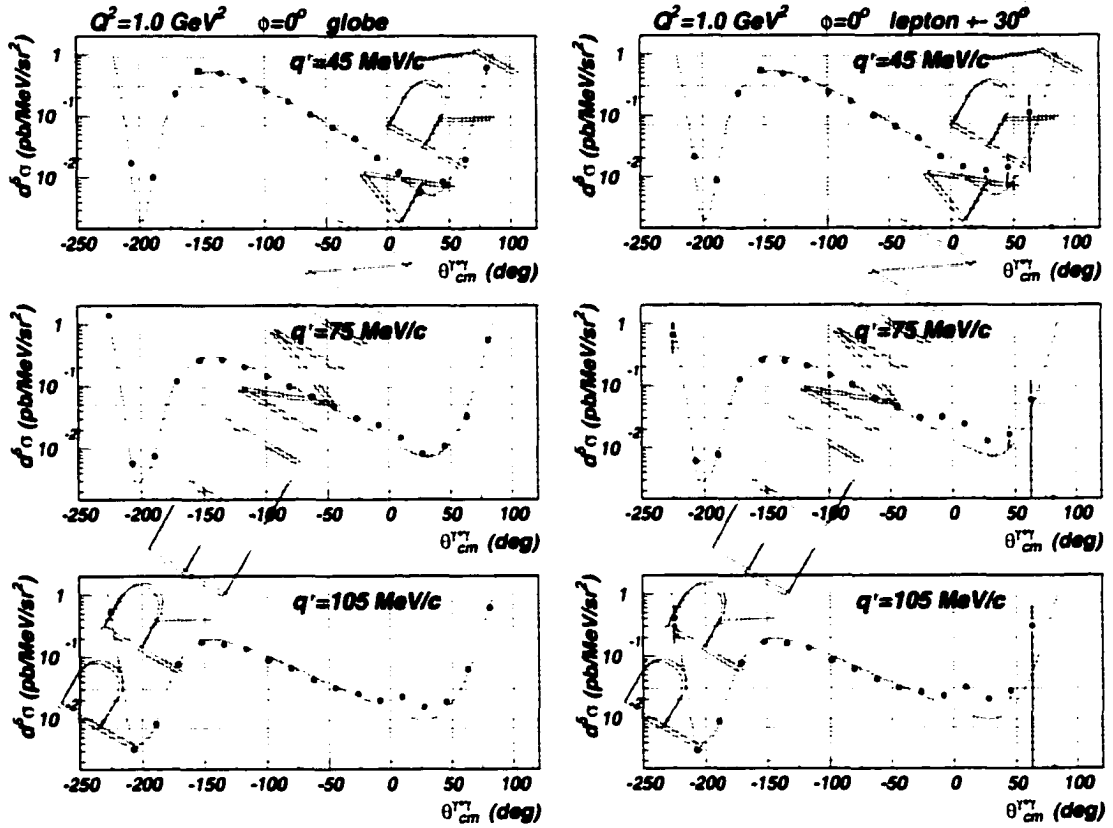


FIG. 90: $ep \rightarrow ep\gamma$ cross-sections as a function of $\theta_{\gamma^*}^{CM}$ for the three values of q'_{CM} . Q^2 is fixed to 1 GeV^2 , the results are integrated over Φ_e and over a large (small) range around the leptonic plane, left (right) plots. The points are experimental values while the magenta curves are the result of a calculation using the BH+Born model.

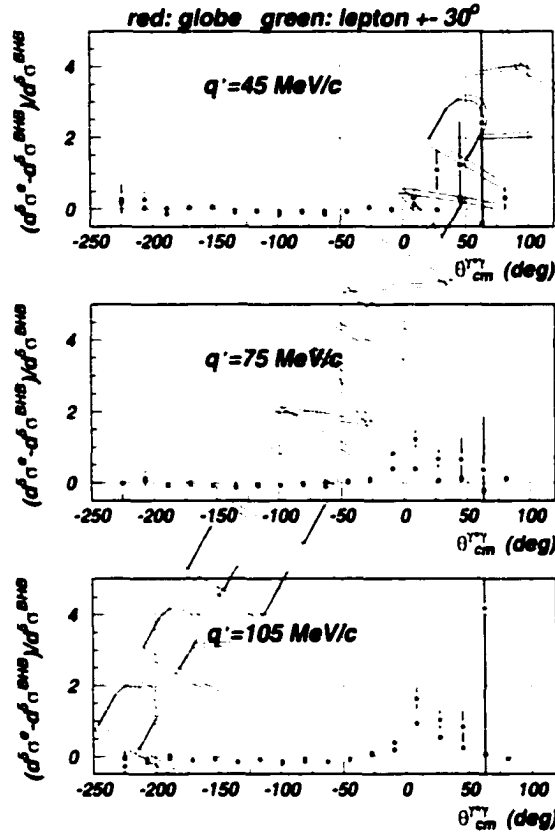


FIG. 91: Relative difference between the experimental cross-sections values and the calculated BH+Born cross-sections values as a function of $\theta_{\gamma\gamma}^{CM}$ for the three values of q'_{CM} . Q^2 is fixed to 1 GeV^2 , the results are integrated over Φ_e and over a large (small) range around the leptonic plane, red (green) dots.

$$\text{Step 3: } \frac{\Delta \mathcal{M}_0 - \Delta \mathcal{M}_0^{BH+B}}{v_{LT}} = [P_{LL}(q) - \frac{1}{\epsilon} P_{TT}(q)] \frac{v_{LL}}{v_{LT}} + P_{LT}(q)$$

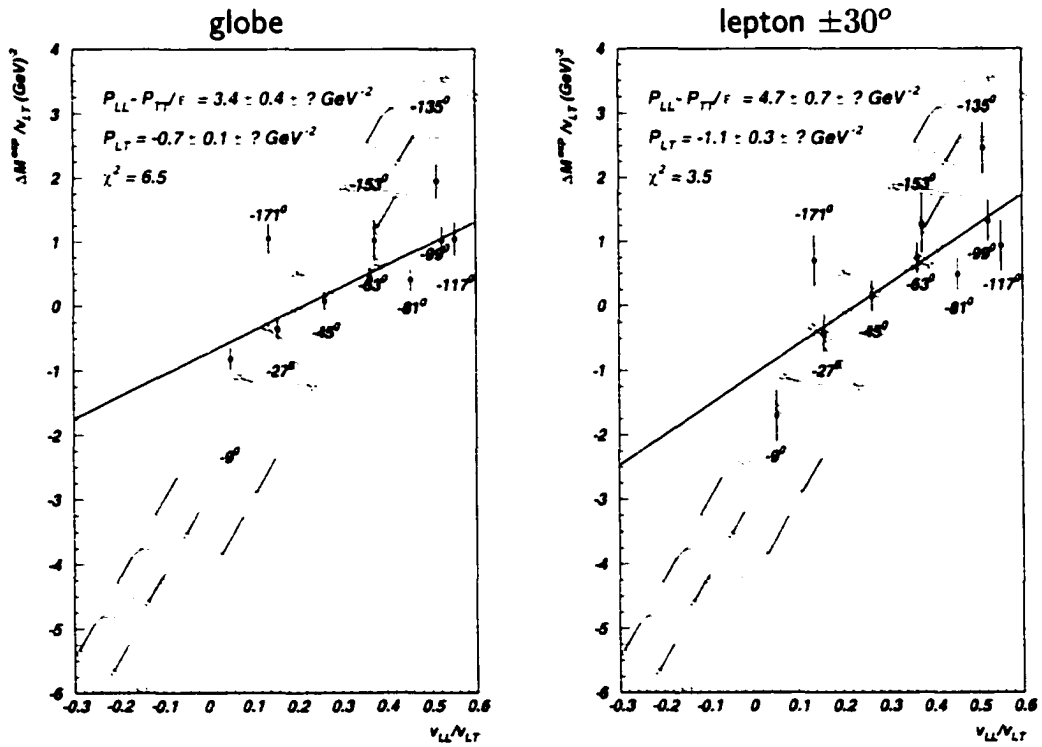


FIG. 92: $\Delta M^{exp}/v_{LT} = (\mathcal{M}_0 - \mathcal{M}_0^{BH+Born})/v_{LT}$ as a function of v_{LL}/v_{LT} . For each data point, the value of $\theta_{\gamma\gamma}^{C.M.}$ is indicated. The solid line is the linear fit to the data points. Resulting coefficients as well as obtained χ^2 are mentioned too. Left plot considers the whole range around the leptonic plane. Right plot considers events that are in the leptonic plane $\pm 30^\circ$.

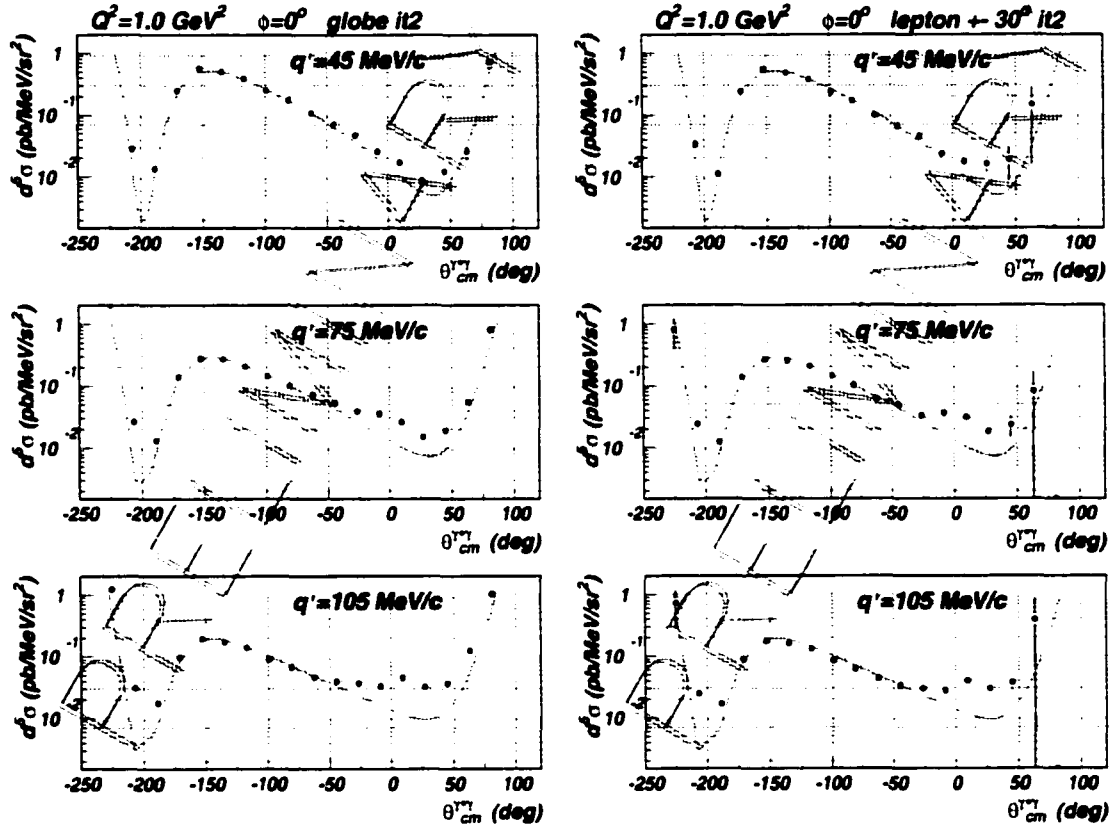


FIG. 93: $ep \rightarrow ep\gamma$ cross-sections after iteration 2 as a function of $\theta_{\gamma\gamma}^{CM}$ for the three values of q'_{CM} . Q^2 is fixed to 1 GeV^2 , the results are integrated over Φ_e and over a large (small) range around the leptonic plane, left (right) plots. The points are experimental values while the magenta curves are the result of a calculation using the BH+Born model.

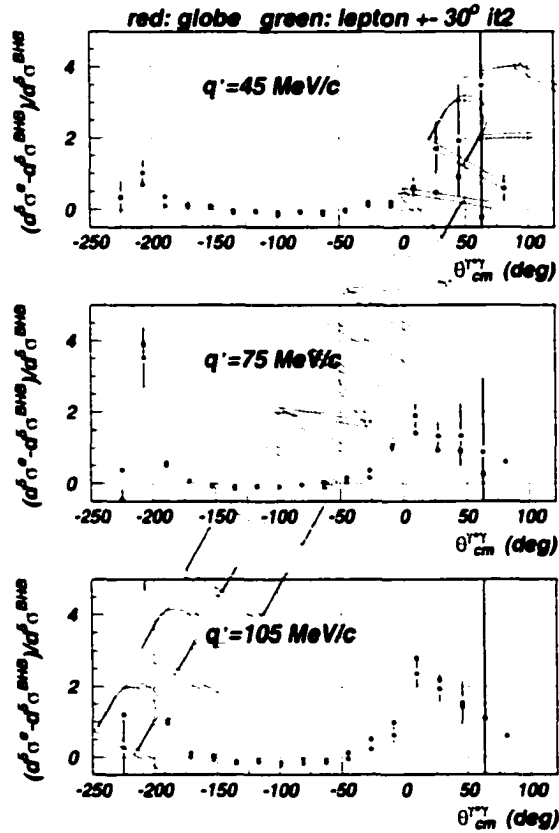


FIG. 94: Relative difference between the experimental cross-sections values after iteration 2 and the calculated BH+Born cross-sections values as a function of $\theta_{\gamma\gamma}^{\text{CM}}$ for the three values of q'_{CM} . Q^2 is fixed to 1 GeV^2 , the results are integrated over Φ_e and over a large (small) range around the leptonic plane, red (green) dots.

$$\text{Step 3: } \frac{\Delta \mathcal{M}_0 - \mathcal{M}_0^{BH+B}}{v_{LT}} = [\mathbf{P}_{LL}(\mathbf{q}) - \frac{1}{\epsilon} \mathbf{P}_{TT}(\mathbf{q})] \frac{v_{LL}}{v_{LT}} + \mathbf{P}_{LT}(\mathbf{q})$$

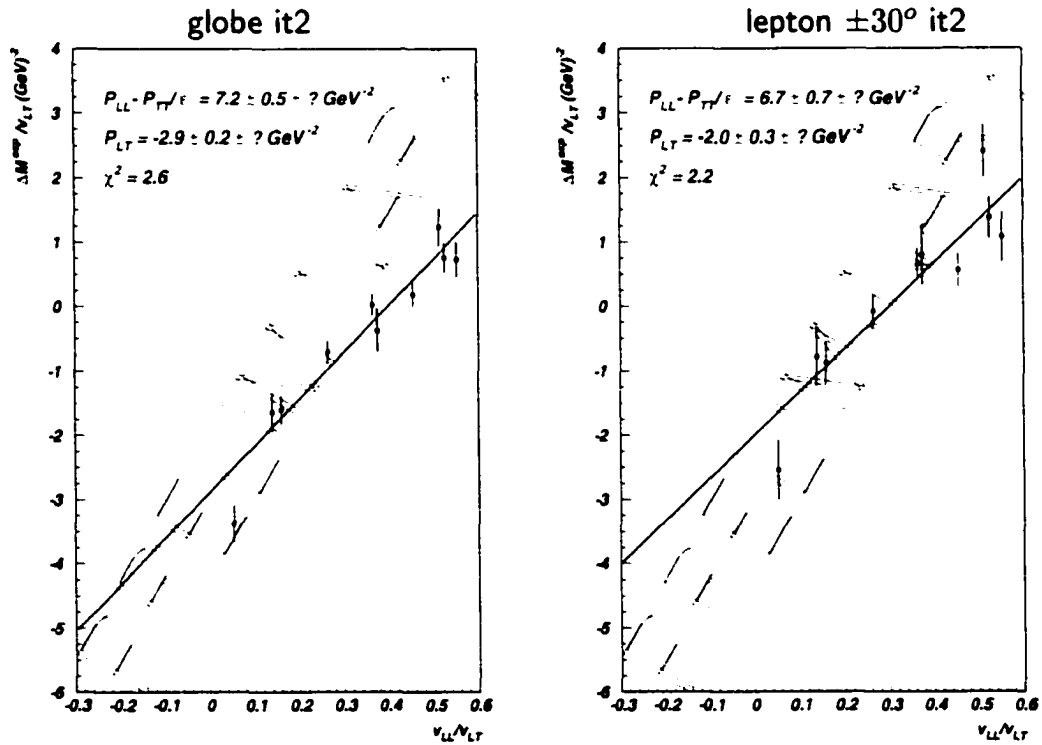
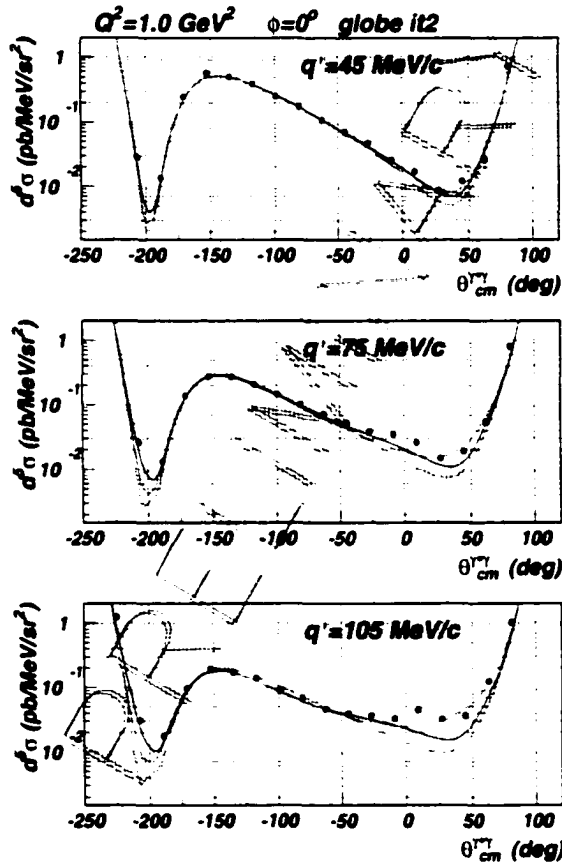


FIG. 95: $\Delta M^{exp}/v_{LT} = (\mathcal{M}_0 - \mathcal{M}_0^{BH+Born})/v_{LT}$ after iteration 2 as a function of v_{LL}/v_{LT} . For each data point, the value of $\theta_{\gamma\gamma}^{C,M}$ is indicated. The solid line is the linear fit to the data points. Resulting coefficients as well as obtained χ^2 are mentioned too. Left plot considers the whole range around the leptonic plane. Right plot considers events that are in the leptonic plane $\pm 30^\circ$.



$$P_{LL} - \frac{1}{\epsilon} P_{TT} = 6 \text{ GeV}^{-2}$$

$$P_{LT} = -2 \text{ GeV}^{-2}$$

$$\Lambda_n = 1.4 \text{ GeV}$$

$$\Lambda_3 = 0.6 \text{ GeV}$$

FIG. 96: $ep \rightarrow ep\gamma$ cross-sections after iteration 2 as a function of $\theta_{\gamma\gamma}^{CM}$ for the three values of q'_{CM} . Q^2 is fixed to 1 GeV^2 , the results are integrated over Φ_e and over a large range around the leptonic plane. The points are experimental values while the curves are the result of calculations: the magenta corresponds to the BH+Born model, the blue corresponds to BH+Born + polarizabilities effects and the green is the result of the dispersion relation formalism calculation.

Chapter 12

Conclusion

The experiment analyzed in this thesis is a new and original experiment and aims at studying the proton response to an electromagnetic perturbation, how the constituents in a large sense readjust (the proton being a composite object) and what are the new distributions in charge and magnetization. This study is achieved through the Virtual Compton Scattering (VCS) process $\gamma^* + p \rightarrow \gamma + p$, itself experimentally accessed through the electroproduction of photons off a proton target $e + p \rightarrow e + p + \gamma$. The Q^2 quantity is used to quantify the virtuality of the incoming virtual photon. It represents the square of the four-momentum transfer from the electron to the proton. In other words, Q^2 is the difference between the momentum transfer squared and the energy transfer squared. The Q^2 dependence of Generalized Polarizabilities (GPs) that parameterize the response of the proton constitute the actual subject of investigation. More technically, they parametrize the transition from a proton in its ground state to a proton state where the proton is coupled with an electric or magnetic dipole or quadrupole perturbation.

VCS off the proton brings to knowledge additional experimental information on the internal structure of the proton. Indeed Elastic Scattering is “restricted” to the elastic electric and magnetic form factors whose Q^2 dependence describes the spatial distribution of charge and current in the nucleon in its ground state. A RCS experiment is also “restricted” by essence to the $Q^2=0$ $(\text{GeV}/c)^2$ value.

Now, by contrast, VCS allows to independently vary the energy transfer and the momentum transfer and to probe the proton with virtual photon of any accessible virtuality Q^2 .

Only one such VCS experiment has been published prior to this work. For this latter experiment, the MAMI accelerator was used and the invariant four-momentum squared value was $Q^2 = 0.33 \text{ (GeV/c)}^2$. Another experiment has subsequently run at the MIT-Bates site at $Q^2 = 0.05 \text{ (GeV/c)}^2$.

On the theoretical point of view, VCS has been a subject in rapid expansion in several regimes. In this thesis, the theoretical approach is based on the theoretical framework of P.A.M. Guichon [2][25] using a low energy expansion upon the momentum of the outgoing photon. But the very promising Dispersion Relations formalism [31] was also discussed.

Our data were collected at Jefferson Lab in Hall A between March and April 1998. The data set under study in this document is below pion threshold at $Q^2 = 1. \text{ (GeV/c)}^2$. Another set of data was taken at $Q^2 = 1.9 \text{ (GeV/c)}^2$ below pion threshold, while data in the resonance region were collected as well in a third set. The facility was a new facility with a small emittance of the electron beam compared to other facilities, a 100% duty cycle to reduce the accidental level and a high luminosity (beam current intensity can be varied from very low values up to $120 \mu\text{A}$), all these ingredients enhancing the feasibility of a VCS experiment. One might also note that three independent experiments can run simultaneously in three different experimental halls.

Both the scattered electron and the recoil proton in the $e + p \rightarrow e + p + \gamma$ reaction are analyzed with a High Resolution Spectrometer. Since the incident particles are also resolved, a missing mass technique is used to isolate the VCS photon events. Due to the high resolution of the spectrometers, the separation between the VCS photon events and the neutral pion creation events from the first opening channel is very clear.

As part of a commissioning experiment of Hall A, a lot of efforts had to be involved in calibrating the equipment. The primary effort concerns the optics calibration of the spectrometers.

With regard to other difficulties, the primary problems in isolating the VCS events comes from the overwhelming pollution by the punch through protons. They are protons that end up being detected whereas they should have been stopped in the collimator at the entrance of the Hadron spectrometer. Their origin is attributed to elastic, radiative elastic and neutral pion creation kinematics. Their corrupted reconstructed vertex variables makes their removal possible.

Despite these difficulties, a cross-section was extracted but is still a preliminary result. A range for the two combinations $P_{LL} - P_{TT}/\epsilon \in [4, 7] \text{ GeV}^{-2}$ and $P_{LT} \in [-2, -1] \text{ GeV}^{-2}$ of polarizabilities was also extracted at $\tilde{Q}^2 = 0.93 \text{ GeV}^2$.

Fig. 97 is a summary of the present thesis results added to the MAMI results, the RCS results and the Dispersion Relation predictions. Two plots are presented: the structure functions P_{LL}/G_E and P_{LT}/G_E are displayed as functions of Q^2 . The points at $Q^2 = 0 \text{ (GeV/c)}^2$ are the RCS results while the points at $Q^2 = 0.33 \text{ (GeV/c)}^2$ are the VCS at MAMI results. The error bands at $Q^2 = 0.93 \text{ (GeV/c)}^2$ show the confidence limits of the present analysis.

The plots show a strong cancellation between the dispersive and asymptotic contributions to both $\alpha_E(Q^2)$ and $\beta_M(Q^2)$. Although the Q^2 dependence of $\alpha_E(Q^2)$ is very similar to the proton electric form factor G_E , each of the individual dispersive and asymptotic contributions have a much slower fall-off with Q^2 than G_E . The small value of P_{LT} relative to P_{LL} and its weak Q^2 dependence is indicative of a strong cancellation between para- and dia-magnetism in the proton. The Dispersion Relation formalism offers, in the facts, a separation between para- and dia-magnetism. In this frame, the para-magnetism of the proton is due to resonance contributions to the magnetic polarizability β , while the higher energy contribution, or asymptotic contribution, is dia-magnetic.

From the Q^2 dependence of the GPs, we learn about the spatial variation of the polarization response. We note that the Q^2 dependence of the electric (G_E) and magnetic (G_M) elastic form factors of the proton are not the same. Similarly the Q^2 dependence of the generalized electric (α_E) and magnetic (β_M) polarizabilities of the proton are also different. We are now seeing the differential motion of charge and magnetization inside the proton.

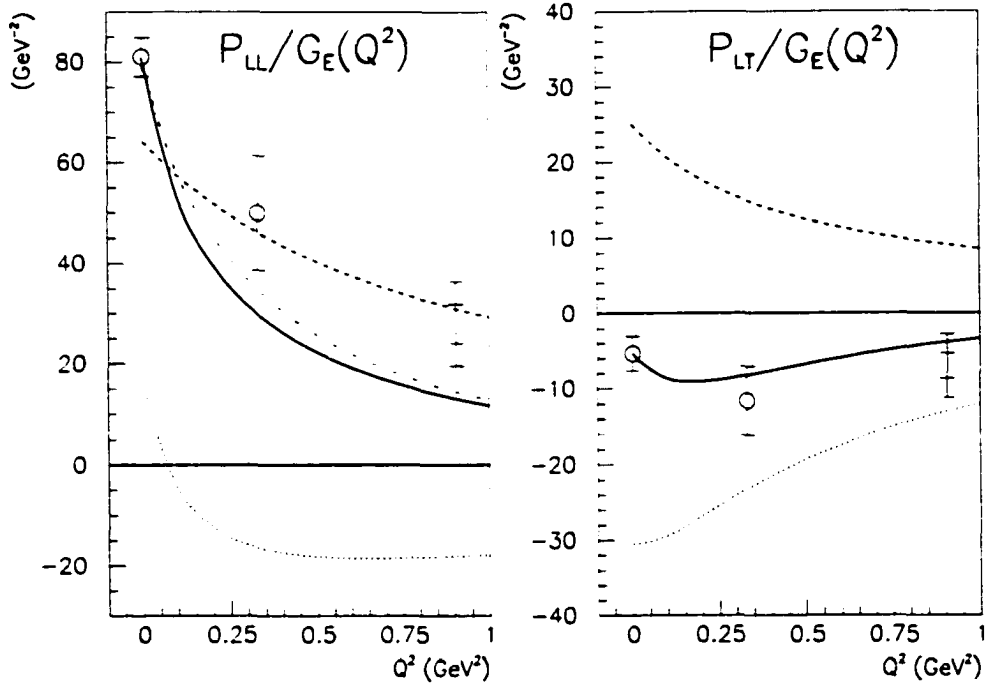


FIG. 97: The structure functions P_{LL}/G_E and P_{LT}/G_E are displayed as functions of Q^2 (solid curves). The data points for P_{LL} are obtained by adding the Dispersion Relation result for P_{TT}/ϵ to the experimental values for $P_{LL} - P_{TT}/\epsilon$, at the ϵ value of each datum. The points at $Q^2 = 0$ and 0.33 (GeV/c)² are the RCS and VCS at MAMI results while the error bands at $Q^2 = 0.93$ (GeV/c)² show the confidence limits of the present analysis. The dotted curves are the contributions fully predicted by the Dispersion Relations. The dashed curves are the phenomenological asymptotic contributions parameterized by the dipole forms of Eqs. 125 and 126 with $\Lambda_\alpha = 0.92$ GeV and $\Lambda_\beta = 0.66$ GeV. The red dot-dashed curve represents the assumption of a Q^2 dependence of the charge polarizability α_E identical to that of the elastic electric form factor G_E and normalized to the RCS point.

Appendix A

Units

In this appendix, the system of units used in this thesis is discussed. The special case of α_{QED} and its expression is detailed. The impact of the particular choice of units on other formulas is also undertaken.

As mentioned in section 2.1 of chapter 2, α_{QED} is the measure of the strength of the electromagnetic interaction. It is a dimensionless quantity. It is chosen to be the ratio of the electrostatic energy of repulsion between two electrons separated by a distance \hbar/mc divided by the rest energy of an electron mc^2 . Its expression in terms of quantities expressed in SI units is therefore:

$$\alpha_{QED} = \frac{e^2}{4\pi\epsilon_0\hbar c} . \quad (213)$$

The values of ϵ_0 , \hbar and c are totally set by nature. On the other hand, the charge of an electron $-e$ is not that constant and is intrinsically linked to α_{QED} . Without going too deep into quantum field theory, renormalization and charge screening (bare charge does not exist because always surrounded by vacuum fluctuations), it can be said that the running coupling constant α_{QED} and e depend on Q^2 : the deeper one tries to probe, the higher the charge appears. The charge of an electron can nevertheless be defined as the one measured in any long range electromagnetic interaction and, for instance, in Thomson scattering where an electron is probed with real photons at low energy. The Q^2 evolution of α_{QED} is

very slow. In the $Q^2 = 0$ limit,

$$\alpha_{QED} \simeq \frac{1}{137.0} . \quad (214)$$

This value is used for most experiment. As a reference, $\alpha_{QED} \simeq \frac{1}{128}$ at $Q^2 = m_W^2 \simeq 80^2 = 6400 \text{ GeV}^2$ [7].

When using the Heaviside-Lorentz system of electromagnetic units, the 4π factors appear in the force equations rather than in the Maxwell equations and ϵ_0 is set equal to unity. Like the latter constant, \hbar and c are also set equal to unity in this thesis: instead of using units of length (L), mass (M) and time (T), units of action (\hbar is one unit of action (ML²/T)), velocity (c is one unit of velocity (L/T)) and energy (ML²/T²) are in use most of the time. To be exhaustive, a fourth basic unit is necessary in order to be able to express any quantity and is commonly a unit of current.

The previous choice of units leads to a reduced expression of α_{QED} :

$$\alpha_{QED} = \frac{e^2}{4\pi} . \quad (215)$$

The choice of setting \hbar and c to unity, mostly to alleviate notations in equations, unites for instance mass, energy and momentum of a particle, all expressed in units of energy. The unit of energy that will be commonly used in this thesis is the MeV unit (or GeV when needed), where 1 eV is the energy acquired by an electron subject to a potential difference of 1 V. Numerically and in SI units.

$$1\text{eV} = 1.602 \cdot 10^{-19} \text{J} . \quad (216)$$

In an attempt to convert quantities expressed in the new system of units to the SI system, one should keep in mind that a mass quantity expressed in MeV should be divided by c^2 , a length quantity expressed in MeV⁻¹ should be multiplied by $\hbar c$, a time quantity expressed in MeV⁻¹ should be multiplied by \hbar and, in all cases, eV translated in Joule with Eq. 216. For a cross-section conversion, a multiplicative factor $(\hbar c)^2$ has to be applied with the use of the numerical value from Eq. 214 for α_{QED} to respect its dimensionless. In all cases a dimensional analysis always restores the right dimension.

Finally, here is a list of useful values:

$$\hbar = 1.055 \cdot 10^{-14} \text{ J.s} \quad (217)$$

$$c = 2.998 \cdot 10^8 \text{ m.s}^{-1} \quad (218)$$

$$\hbar c = 197.3 \text{ MeV.fm} \quad (219)$$

$$(\hbar c)^2 = 0.3894 \text{ GeV}^2 \cdot \text{mbarn} \quad (220)$$

$$e = 1.602 \cdot 10^{-19} \text{ C} \quad (221)$$

$$1 \text{ fm} = 10^{-15} \text{ m} \quad (222)$$

$$1 \text{ barn} = 10^{-28} \text{ m}^2 . \quad (223)$$

Appendix B

Spherical harmonics vector basis

The spherical harmonics vectors are defined by

$$\vec{y}_{LM}^l(\hat{q}) = \sum_{m,\lambda} \left\langle \begin{matrix} l & 1 \\ m & \lambda \end{matrix} \middle| \begin{matrix} L \\ M \end{matrix} \right\rangle Y_l^m(\hat{q}) \vec{\epsilon}(\lambda) \quad (224)$$

The multipole vector spherical harmonics are:

$$\vec{\mathcal{M}}_{LM}(\hat{q}) = \vec{y}_{LM}^L(\hat{q}) \quad (225)$$

$$\vec{\mathcal{E}}_{LM}(\hat{q}) = \sqrt{\frac{L+1}{2L+1}} \vec{y}_{LM}^{L-1}(\hat{q}) + \sqrt{\frac{L}{2L+1}} \vec{y}_{LM}^{L+1}(\hat{q}) \quad (226)$$

$$\vec{\mathcal{L}}_{LM}(\hat{q}) = \sqrt{\frac{L}{2L+1}} \vec{y}_{LM}^{L-1}(\hat{q}) - \sqrt{\frac{L+1}{2L+1}} \vec{y}_{LM}^{L+1}(\hat{q}) \quad (227)$$

The 4-vector spherical harmonics are defined as follows :

$$V^\mu(0LM, \hat{q}) = (Y_{LM}(\hat{q}), \vec{0}) \quad (228)$$

$$V^\mu(1LM, \hat{q}) = (0, \vec{\mathcal{M}}_{LM}(\hat{q})) \quad (229)$$

$$V^\mu(2LM, \hat{q}) = (0, \vec{\mathcal{E}}_{LM}(\hat{q})) \quad (230)$$

$$V^\mu(3LM, \hat{q}) = (0, \vec{\mathcal{L}}_{LM}(\hat{q})) \quad (231)$$

Bibliography

- [1] P.Y. Bertin, P.A.M. Guichon and C.E. Hyde-Wright, co-spokespersons, *Nucleon structure study by Virtual Compton Scattering*, CEBAF proposal PR93050 (1993).
- [2] P.A.M. Guichon, G.Q. Liu and A.W. Thomas, *Nucl. Phys. A* **591**, 606 (1995).
- [3] N. D'Hose *et al.*, MAMI proposal (1994).
- [4] J. Roche *et al.*, *Phys. Rev. Lett.* **85**, 708 (2000).
- [5] F. Halzen and A.D. Martin, *Quarks and Leptons*, John Wiley and Sons (1983).
- [6] T. De Forest and J.D. Walecka, *Adv. Phys.* **15**, 1-109 (1966)
- [7] C. Caso *et al.*, Particle Data Group, *Eur. Phys. J. C* **3**, 1 (1998).
- [8] M.N. Rosenbluth, *Phys. Rev.* **79**, 615 (1950).
- [9] R. Hofstadter, *Ann. Rev. Nucl. Sci.*, 231 (1957).
- [10] M. Jones *et al.*, *Phys. Rev. Lett.* **84**, 1398 (2000).
- [11] O. Gayou *et al.*, arXiv:nucl-ex/0111010 (2001).
- [12] P.E. Bosted, *Phys. Rev. C* **51**, 409-411 (1995).
- [13] W.A. Bardin and W.-K. Tung, *Phys. Rev.* **173** 1423 (1968).

- [14] M. Gell-Mann and M.L. Goldberger, Phys. Rev. **96**, 1433-1438 (1954).
- [15] F.E. Low, Phys. Rev. **96**, 1428 (1954).
- [16] J.D. Jackson, *Classical Electrodynamics*, John Wiley & sons, (1975).
- [17] D. Babusci *et al.*, Phys. Rev. C **58**, 1013-1041 (1998).
- [18] A.M. Baldin, Nucl. Phys. **18**, 310 (1960).
- [19] A.I. L'vov, V.A. Petrun'kin and M. Schumacher, Phys. Rev. C **55**, 359-377 (1997).
- [20] D. Drechsel *et al.*, Phys. Rev. C **61**, 015204 (2000).
- [21] S. Gerasimov. Yad. Fiz. **2** 598 (1965). *Sov. J. Nucl. Phys* **2** 930 (1966).
- [22] S.D. Drell and A.C. Hearn, Phys. Rev. Lett. **16**, 908 (1966).
- [23] V. Olmos de Leon *et al.*, Eur. Phys. J. A **10**, 207-215 (2001).
- [24] G. Galler *et al.*, Phys. Lett. B **503**, 245-255 (2001).
- [25] P.A.M. Guichon and M. Vanderhaeghen. Prog. Part. Nucl. Phys. **41**, 125 (1998).
- [26] F.E. Low. Phys. Rev. **110**, 974 (1958).
- [27] A. Edmonds. *Angular Momentum in Quantum Mechanics*. Princeton University Press, Princeton N.J, (1957).
- [28] C. Jutier, VCS internal report *Extraction of polarizabilities from a resonance model of the VCS amplitude* (2000).
- [29] L. Todor, Proceedings of N^* workshop, Jefferson Lab, January 2000.
- [30] Private communication with Dr. W. Roberts.
- [31] B. Pasquini, M. Gorchtein, D. Drechsel, A. Metz and M. Vanderhaeghen, Eur. Phys. J. A **11**, 185-208 (2001).

- [32] N. Degrande, Ph.D. thesis, Gent University (Gent, Belgium), (2000).
- [33] S. Jaminion, Ph.D. thesis, Blaise Pascal University (Clermont-Ferrand, France), DU 1259 (2000).
- [34] L. Todor, Ph.D. thesis, Old Dominion University (Norfolk, Virginia, USA), (2000).
- [35] G. Laveissière, Ph.D. thesis, Blaise Pascal University (Clermont-Ferrand, France), in preparation.
- [36] K. McCormick, Ph.D. thesis, Old Dominion University (Norfolk, Virginia, USA), (1999).
- [37] <http://www.jlab.org/Hall-A>.
- [38] G. Laveissière, VCS internal note *Asynchronization problems of the BPM/Raster ADC for E93050* (1999).
- [39] H. Fonvielle, VCS internal note *Practical use of radiative corrections to measured cross-sections $d^5\sigma(ep \rightarrow ep\gamma)$* (2000).
- [40] D. Lhuillier, Ph.D. thesis, DAPNIA/SPhN-97-01T, (1997).
- [41] D. Marchand, Ph.D. thesis, DAPNIA/SPhN-98-04T, (1998).

Vita

Christophe Jutier
Department of PHYSICS
Old Dominion University
Norfolk, VA 23529

Joint degree, **Ph.D.** in Physics, December 2001
Old Dominion University, Norfolk, VA, USA and
Université Blaise Pascal, Clermont-Ferrand, France
Dissertation: *Measurement of the Virtual Compton Scattering below pion threshold at invariant four-momentum transfer squared $Q^2 = 1. (GeV/c)^2$*

Research Associate, Old Dominion University Physics Department, 1996-2001

Diplôme d'Etudes Approfondies, Subatomic Physics, June 1996
Université Blaise Pascal, Clermont-Ferrand, France

Maîtrise ès-Sciences degree, Physics, June 1995
Université Blaise Pascal, Clermont-Ferrand, France

Typeset using L^AT_EX.